Tunable diode laser absorption tomography for spatially resolved concentration measurements

Vom Fachbereich Maschinenbau
an der Technischen Universität Darmstadt
zur
Erlangung des Grades eines Doktor-Ingenieurs (Dr.-Ing.)
genehmigte

D i s s e r t a t i o n

vorgelegt von

M.Sc. Anne Seidel

aus Frankfurt am Main

Berichterstatter:	Prof. Dr. rer. nat. V. Ebert
1. Mitberichterstatter:	Prof. Dr.-Ing. A. Kempf
2. Mitberichterstatter:	Prof. Dr. rer. nat. A. Dreizler
Tag der Einreichung:	06. Mai 2014
Tag der mündlichen Prüfung:	22. Juli 2014

Darmstadt 2015

D17

Eidestattliche Erklärung

Hiermit erkläre ich an Eides statt, dass ich die vorliegende Dissertation selbstständig verfasst und keine anderen als die von mir angegebenen Hilfsmittel verwendet habe. Ich erkläre außerdem, dass ich bisher noch keinen Promotionsversuch unternommen habe.

Anne Seidel

Darmstadt, den 06. Mai 2014

Das Gras wächst nicht schneller, wenn man daran zieht.

Afrikanisches Sprichwort

Contents

Nomenclature

Upper-case Latin letters		Unit
B_{12}	Einstein coefficient of induced absorption	s^{-1}
D	discrete total variation prior	–
E_1, E_2	lower and upper energy levels of a molecule	$\mathrm{J} = \mathrm{kgm}^2\mathrm{s}^{-2}$
E	intensity of background emission	$\mathrm{W/m}^2$
$\mathcal{E}$	expectation value	$\mathrm{W/m}^2$
F	Fourier transformed image function	m^{-1}
$\mathcal{F}$	Fourier transform	–
G	number of pixel neighbours	–
I	intensity	$\mathrm{W/m}^2$
$\mathbf{I}$	unity matrix	–
L	Cholesky-factorization of Γ	–
$\mathcal{L}$	discrete Laplace operator	–
M	number of measured path-integrals	–
N	number of pixels	–
$\mathcal{N}$	normal distribution	–
N_A	Avogadro constant	–
O	objective functions of TV prior minimization problem	–
OD_e	optical density	–
$\mathcal{P}_{12}$	probability of induced absorption	Jm^{-3}
$\mathbb{P}$	probability	–
R	resolution matrix	–
$\mathfrak{R}$	universal gas constant	$\mathrm{kgm}^2\mathrm{s}^{-2}\mathrm{K}^{-1}\mathrm{mol}^{-1}$
$\mathscr{R}$	Radon transform	–
S	absorption line-strength	$\mathrm{mol\ m}^{-1}$
T	temperature	K
Tr	transmission factor	–
V	volume	m^3
W	weighting matrix	–
$W^\sharp$	Tikhonov regularized inverse	–
$\mathscr{W}$	mapping function	–
Z	objective functions of informative smoothness prior minimization	–

Lower-case Latin letters		Unit
a	penalty term parameter	–
b	band-limitation of transform algorithms	–
$\vec{b}$	SART basis functions	–
$\tilde{b}$	smoothness parameter of informative prior	–

c	volume concentration	ppmv
$\tilde{c}$	velocity of light	ms^{-1}
$\vec{c}$	discretized path-averaged concentrations	ppmv
e	image residual	specific
f	image function	specific
$\vec{f}$	discretized image function	specific
$\vec{g}$	expansion coefficients of SART	–
h	Planck's constant	Js
k_B	Boltzmann constant	J/K
$\vec{k}$	wave vector	–
l	absorption path length	m
m	mass	kg
$\vec{n}$	noise vector	ppmv
p	pressure	$\mathrm{Pa} = \mathrm{kgm}^{-1}\mathrm{s}^{-2}$
$p^\sharp$	number of projections	–
$q^\sharp$	measure for number of beams per projection	–
r	distance between two pixels (normalized)	–
r_{fan}	radius of fan-beam arrangement	m
s	collisional broadening exponent	–
t	time	s
u, v	Cartesian coordinates in Fourier space (spatial)	m^{-1}
w	coefficients of weighting matrix W	–
x, y	Cartesian coordinates	m

Upper-case Greek letters		**Unit**
Γ	covariance matrix	–
Λ	correlation length (normalized)	–
Φ	line-shape function	–
Ψ	beam layout	–
Ω	spatial frequency	m^{-1}

Lower-case Greek letters		**Unit**
α	weighting factor of TV prior	–
α_{LW}	regularization parameter for Landweber iteration	–
α_{tune}	angular beam displacement during wavelength tune	$^\circ$
β	TV prior absolute value function smoothing parameter	–
γ	weight of Gibbs prior	–
δ	Dirac function	–
ϵ	pixel edge length (normalized)	–
ε	threshold for ART stop criterion	–
$\vec{\varepsilon}_c$	mean concentrations residual	ppmv
$\vec{\varepsilon}_{c,n}$	noise normalized mean concentrations residual	–
η	expectation value	–
θ	angular position of projection	rad
κ	scaling parameter for TV adaptation	–
λ	wavelength	m

μ	mean value	specific
ν	wavenumber	m^{-1}
ξ, ζ	Cartesian coordinates in Radon space	m
ρ	spectral energy density	Jm^{-3}
σ	standard deviation	specific
ς	step-size parameter in Gauss-Newton algorithm	–
τ	Tikhonov regularization parameter	–
υ	frequency of photon	s^{-1}
ϕ	rotation angle of polygon	$^\circ$
χ	absorber number density	–

Abbreviations

2D	2-Dimensional
ART	Algebraic Reconstruction Technique
CARS	Coherent Anti-Stokes Raman Spectroscopy
CM	Conditional Mean
DAQ	Data Acquisition
DFB	Distributed Feedback laser
ESF	Edge spread function
FTIR	Fourier Transform Infrared Spectrometer
HITRAN	High resolution Transmission *(spectroscopic database)*
HT	Hyperspectral Tomography
LIF	Laser-Induced Fluorescence
LSF	Line Spread Function
MAP	Maximum A Posteriori 2.0
MFC	Mass Flow Controller 2.0
MTF	Modulation Transfer Function
OP-FTIR	Open-Path Fourier Transform Infrared Spectrometer
PSF	Point Spread Function 2.0
rpm	revolutions per minute
SART	Simultaneous Algebraic Reconstruction Technique
SIRT	Simultaneous Iterative Reconstruction Technique
SNR	Signal to Noise Ratio
SVD	Singular Value Decomposition
TDLAS	Tunable Diode Laser Absorption Spectroscopy
TTL	Transistor - Transistor Logic
TV	Total Variation
VCSEL	Vertical Cavity Surface Enhanced Laser

Chapter 1

Introduction

1.1 Motivation

Gas concentration is one of the crucial properties of many physical systems and is often compulsory for understanding technical and natural processes. Many times a thorough comprehension can only be gained if gas concentration is known also in its spatial distribution and temporal conduct. Optical measurement techniques offer diverse possibilities for non-intrusive detection of concentrations, like *Laser induced fluorescence* (LIF), Raman spectroscopy or absorption spectroscopy, to name a few examples. However, in their primal form, none of them can deliver reliable absolute values for concentration and its spatial distribution at the same time – not to speak of temporal resolution [1]. Regarding the above named examples, the following can be said: Whereas LIF allows for a high spatial resolution, quantitative measurements are demanding or even infeasible. Raman spectroscopy is a relatively insensitive method for point-wise detection of gas concentrations that requires calibration. Absorption spectroscopy includes disparate techniques for absolute concentration measurements, among them a sophisticated variant called *Tunable diode laser absorption spectroscopy* (TDLAS) which does not require calibration [2–10]. As a line-of-sight method, spatial resolution can be achieved by means of tomographic techniques.

While in some applications (foremost in the medical field) state-of-the-art tomographic systems are highly developed and adapted to their specific purpose, deployment for technical or environmental purposes is still somewhat limited. This is due to the often demanding boundary conditions that need to be fulfilled: usually the amount of usable measurement paths is confined in some way, either because accessibility is restrained or because instrumentation expenditure needs to be diminished. This problem is closely linked to the issue of temporal resolution: while common tomographic scanners deliver high spatial resolution, capturing one picture may take several minutes because of the sequential movement of measurement components for beam path multiplication [11].

Reducing the number of measurement paths (either for gaining speed or for accessibility or cost reasons) leads to a severe loss of information, which normally renders impossible the use of standard transform-based tomographic computation methods. In principle, low-data tomographic reconstruction always means solving an ill-posed problem [12]. Most of the times, there are fewer beam paths than unknown values in a sensible discretization, leading to an infinite set of solutions. In addition to that, the arrangement of the beams often leads to badly conditioned systems, that means finding the solution is very sensitive to noise. For this reason, as much as possible additional information and physical

previous knowledge about the measurement system should be utilized in order to restrict the solution space. Adequate algorithms along with a sensible setup of the instrument components have to be found for each specific application in order to compensate for reduced measurement data. As several parameters have an influence on the design, there cannot be a general approach for all systems. The choice of setup and algorithm depend e.g. on the size and accessibility of the measurement object, the desired spatial and temporal resolution and the possible instrumentation effort. It also has to be accounted for physical knowledge about the system and whether it can be used to a certain extent. Last but not least, requirements arise from spectroscopy: The gases that shall be detected and the ranges of their concentrations have to be considered as well as temperature and pressure boundary conditions. In general, an instrument concept developed for a specific purpose cannot directly be transferred to other applications. Therefore, this work focuses on the development of a fast TDLAS-based instrument for tomographic concentration field measurements for an application in soil science. Through this example insights into concepts and principles of performance of low-data tomography systems can be gained also for other systems.

The developed instrument needs to fulfil especially demanding requirements, since it is designated for field measurements in Arctic areas. The objective of environmental scientists is to better model the global warming process by including greenhouse gas emission from thawing permafrost soil in their simulations [13–20]. Although it is well-known that climate gases like H_2O, CH_4 or CO_2 are emitted from melting permafrost, the absolute quantities are still unknown [21–23]. Furthermore, for a better physical understanding of the processes that lead to gas emanation the relevant soil structures have to be identified [24]. One of the supposed mechanisms is the release of methane due to decomposition of organic material stored in underground reservoirs [14, 20]. As the covering ice-layer is melting, the organic material is exposed to oxygen and can be devoured by aerobic bacteria. The gaseous by-products are assumed to be liberated through cracks in the ground. Such theories can only be investigated with a 2D-map of absolute concentrations of the soil-air boundary layer covering a relatively large area in the square meter range. Geoscientists are often interested in gas flow, which could be achieved with a combination of concentration field measurements and gas velocity measurements. Despite the fact that the latter are beyond the scope of this work, it should be borne in mind that a temporal resolution of at least 1 Hz has to be obtained. Although the good accessibility of the soil gives the designer freedom to arrange the laser-beams into nearly arbitrary positions, the optomechanical setup of such a field device has to be kept as simple as possible for transportation and alignment in the field. Robustness against a harsh environment is a basic prerequisite. Along with the development of the instrumentation, appropriate algorithms for the tomographic reconstructions have to be found. Here, information about soil structure sizes, locations and shapes may come in handy since it could be included as physical knowledge into the reconstruction process. There is no patent remedy for finding a good combination of reconstruction and instrument setup, the strategy of design is rather iterative and heuristic. Aptness of algorithms depends on the laser beam setup, which again should be adapted as far as possible to the characteristic requirements of tomographic reconstruction methods.

Plenty of interdependencies exist between tomographic instrument, reconstruction tech-

nique and measurement object, so there is no universal solution for low-data absorption tomography. However, typical problems and characteristics arising from lack of information when reconstructing 2D-concentration fields may become evident in this work. It may lead to a principle understanding for low-data tomography, especially in the field of tomographic algorithms, thus making transfer to other systems from engineering and science easier.

1.2 Structure of the thesis

In the following chapter, a short introduction into the principles of TLDAS and a limited selection of tomographic reconstruction techniques is given. In the latter case, only those techniques were included that are either fundamental for comprehension or promising regarding the application as there is a vast amount of algorithms. Chapter 3 presents the evolution and performance of the instrument itself: First the design process is briefly sketched to clarify the advantages of the chosen setup in comparison to other solutions. It is self-evident that the optimal instrumentation may be outperformed by other setups in other measurement situations. Afterwards, the instrument setup and spectroscopic performance for measuring path-averaged concentrations is elaborated. While reading this work, it has to be kept in mind that designing the tomographic instrument was an iterative process because laser-beam setup and the performance of the algorithms are closely intertwined. The arrangement of the beams was initially adjustable at will, since the soil area can be accessed from all edges. Conceptual laser beam setups were assessed regarding both practical issues and their aptness for tomographic reconstructions. At this point, first tomographic reconstructions of simulated experiments were realized to find out whether a setup was any good, not knowing whether the used algorithm was best suited for the problem. Selecting the exact beam layout was then a process of trial and error. Even though there are approaches of optimizing the beam layout for more simple cases, there is not yet a viable method for finding the best solution for an application with so many degrees of freedom. Furthermore it has to be doubted whether there actually is an unsurpassed solution for all measurement situations, as the achieved quality of reconstruction may depend on the measurement object itself. The heuristic process of the instrument conception and construction seems therefore justifiable. Documenting all the design steps and preliminary solutions is beyond the scope of this work. Instead, principles of finding a good concept are explained, sometimes already implying experiences that were made with simulated tomographic reconstructions.
Another scope of the work is to give an overview over the performance and characteristics of certain tomographic reconstruction techniques. The selection of algorithms might be incomplete, but it is sensible: There is a very wide range of tomographic inversion principles, but not all of them are promising or adequate for the application and most algorithms are excluded in the first place. The most auspicious techniques were implemented, in some cases adapted to the specific use of absorption spectroscopy or modified for performance improvement and evaluated and compared by means of simulated experiments (chapter 4). Owing to the incomplete information of low-data tomography, there is no guarantee that arbitrary concentration fields can be reconstructed, so the strategy was to assess reconstructions of a wide diversity of realistic and relevant simulated concentra-

tion fields. Parameters like structure shape, size, number and "contrast" in concentration are varied towards increasing complexity and aspects of reconstruction quality and spatial resolution are discussed.
Eventually, an experimental validation of the instrument was carried out (chapter 5). For this purpose, effectually known concentration fields were generated by laminar jet flows with known gas mixture and shape. The dynamic range of the instrument is presented, i.e. dependency of reconstruction quality on structure concentrations, sizes and measurement rate. While the dynamic range is mainly determined by spectroscopic issues, the influence of measurement object complexity is owed to limitations of tomography. Like in the case of simulated experiments, measurements with increasing structure complexity (regarding size, number of elements and arrangement) were carried out. Finally, the developed instrument and its tomographic performance is compared to existing devices. In the last chapter, a conclusion and outlook are given.

Chapter 2

Fundamentals

Understanding the designed instrument and the carried out simulated and real experiments premises some fundamental knowledge of absorption spectroscopy and tomography. A short overview of the former is given in chapter 2.1. Chapter 2.2 includes some principle considerations about tomography and presents some selected tomographic reconstruction techniques.

2.1 Absorption spectroscopy

Absorption spectroscopy techniques are based on the principle of induced absorption. For a thorough understanding of the physical processes that are used for absorption spectroscopy, the latter is explained in chapter 2.1.1. Furthermore, mechanisms of absorption line broadening are discussed in chapter 2.1.2 If not denoted otherwise, all information is taken from [1]. Although there are plenty of absorption spectroscopy methods, this work focusses on the variant *tunable diode laser absorption spectroscopy* (TDLAS). With this technique, absolute concentrations can be measured without any calibration or reference-gas. Therefore it was chosen as the appropriate method from the very beginning. The fundamentals of TDLAS are explained in chapter 2.1.3.

2.1.1 Induced absorption

One of the substantial insights of quantum physics is that atoms and molecules have discrete, so-called *quantised* energy levels [25, 26]. Molecules can absorb photons if the energy of the photon equals the difference between two energy levels of the molecule. This is given if the following equation is fulfilled:

$$h \cdot \nu = E_2 - E_1 \tag{2.1}$$

The left hand side corresponds to the energy of the photon, where h is Planck's constant, ν is the frequency of the photon and E_1 and E_2 are the lower and higher energy levels of the molecule. The corresponding processes is called *induced absorption* and takes place with a certain probability per temporal unit:

$$\frac{\mathrm{d}}{\mathrm{d}t}\mathcal{P}_{12} = B_{12}\rho(\nu) \tag{2.2}$$

The constant B_{12} is the so-called *Einstein coefficient of induced absorption* and $\rho(\nu)$ is the spectral energy density, which is a measure for the number of photons with the energy $E = h\nu$ per volume. Because of the discrete energy levels of the molecules, energy differences and therefore frequencies at which a molecule can absorb photons are also discrete. These frequencies are molecule-specific and are called *absorption lines*. Absorption spectroscopy makes use of the weakening of incident light by induced absorption at an absorption line that can be related to a specific molecule. In reality these lines are not entirely discrete but broadened by several mechanisms that are described in the following chapter.

2.1.2 Line broadening mechanisms

The ideally mono-chromatic absorption lines are in reality broadened by several physical effects. They contribute to the overall broadening with different orders of magnitude, depending on boundary conditions like pressure, temperature and concentrations of the absorbing and of interfering species. The first mechanism is the *natural line broadening*, which is due to the decreasing intensity of the stimulating wave. It leads to a Lorentzian absorption profile instead of a sharp transition. However, natural linewidth is very small compared to the other effects and is therefore neglected.
Another broadening mechanism is *Doppler broadening*, which dominates at low pressures. It is caused by the thermal motion of absorbing molecules which is described by a Maxwell-Boltzmann distribution of velocities. The observed absorption frequency of a molecule moving at speed $\vec{v}_M$ is given by

$$\nu_a = \nu_0 + \vec{k} \cdot \vec{v}_M \tag{2.3}$$

where ν_0 is the absorption frequency of a resting molecule and $\vec{k}$ is the wave vector. It can be shown that the frequency shift leads to a Gaussian shaped line broadening with the full half-width

$$\delta\nu_D = \frac{\nu_0}{\tilde{c}}\sqrt{\frac{2k_B T \ln 2}{m}} \tag{2.4}$$

with the velocity of light $\tilde{c}$, the Boltzmann constant k_B, temperature T and molecule mass m.
A further broadening mechanism is the *collisional broadening*, which is often also called pressure broadening. The energy levels of two molecules shift if they approach each other because their electron configurations are influenced mutually, depending on the distance between the molecules [25]. This results in a Lorentz-shaped broadening function with full half-width [27]

$$\delta\nu_C = \delta\nu_{0C}\left(\frac{p}{p_0}\right)\left(\frac{T_0}{T}\right)^s = \delta\nu_C^0 p\left(\frac{T_0}{T}\right)^s \tag{2.5}$$

Equation 2.5 is an empirical expression, where p is the pressure, T is the temperature and the zero subscripts denote the respective magnitudes' standard values. The half-width

at a pressure of 1 atm, $\delta\nu_{0C}$, can be combined with the standard pressure to $\delta\nu_C^0$. The exponent s is often chosen as s =0.5. The collisional broadening can be split into a self-broadening and a foreign gas broadening part:

$$\delta\nu_C = \left(\delta\nu^0_{C_{self}} \cdot p_{self} + \delta\nu^0_{C_{foreign}} \cdot p_{foreign}\right)\left(\frac{T_0}{T}\right)^s \tag{2.6}$$

where p_{self} is the partial pressure of the absorbing gas and $p_{foreign}$ is the partial pressure of interfering gas species.
Depending on the boundary conditions, other mechanisms of absorption line broadening may occur [1]. The overall shape of the broadened absorption line results from a convolution of the contributing broadening mechanisms. In many situations it suffices to consider Doppler- and collisional broadening. The convolution of their Gaussian and Lorentz profiles is called Voigt profile [28] g_V:

$$g_V(\nu - \hat{\nu}) \equiv g_D \otimes g_C = \int_{-\infty}^{\infty} g_D(\nu - \nu', \delta\nu_D) \cdot g_C(\nu' - \hat{\nu}, \delta\nu_C)\mathrm{d}\nu' \tag{2.7}$$

where $\hat{\nu}$ is the center frequency where the absorption line is located, g_D is the Gauss profile of the Doppler broadening and g_C is the Lorentz profile of collisional broadening. The integral in equation 2.7 cannot be solved analytically, but many approaches to approximate it numerically exist [28–35]. Its half-width is roughly given by [27]

$$\delta\nu_V \cong 0\ 5346 \cdot \delta\nu_C + \sqrt{0\ 2166 \cdot \delta\nu_C^2 + \delta\nu_D^2} \tag{2.8}$$

2.1.3 Tunable Diode Laser Absorption Spectroscopy

Tunable Diode Laser Absorption Spectroscopy (TDLAS) is based on the Lambert-Beer law, which gives a relation between the intensities of the incident light I_0 entering an absorbing medium and the light I detected after passing an absorbing medium along a path of length l [27, 36]

$$I(\chi, \lambda) = I_0(\lambda) \cdot \exp\Big\{ - S(T) \cdot \Phi(\lambda - \lambda_0) \cdot \chi \cdot l\Big\} \tag{2.9}$$

$S(T)$ denotes the temperature-dependent line-strength, $\Phi(\lambda - \lambda_0)$ is a normalized lineshape function centred at wavelength λ_0 and χ is the absorber number density of the gas. The latter is the fraction of the amount of substance of the absorbing gas to the overall amount of substance of the gas, $\chi = \frac{\chi_{absorber}}{\chi_{total}}$ and is often also called mole fraction. An even more accurate description of the measurement of I accounts for temporally varying broadband transmission losses $Tr(t)$ and broadband background radiation E and is given by the extended Lambert-Beer law:

$$I(\chi, \lambda) = I_0(\lambda) \cdot Tr(\lambda) \cdot \exp\Big\{ - S(T) \cdot \Phi(\lambda - \lambda_0) \cdot \chi \cdot l\Big\} + E \tag{2.10}$$

Because of the normalization $\int_{-\infty}^{\infty} \Phi(\lambda - \lambda_0)\mathrm{d}\lambda = 1$, equation 2.10 can be rearranged to

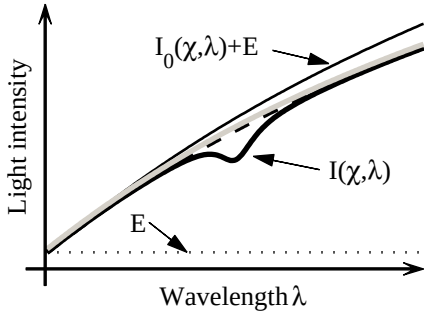

Figure 2.1 Incident and detected light intensities for a TDLAS measurement. Broadband background emission is depicted as a dotted line. It is superimposed to the incident light intensity I_0 which increases with the wavelength λ as a side-effect of laser modulation. The grey line depicts the intensity after superposition of E and with transmission losses, $I_0 \cdot Tr(\lambda) + E$. After passing the absorbing medium, the intensity $I(\chi, \lambda)$ is detected. The dashed line shows the fitted polynomial.

$$\chi = -\frac{1}{S(T) \cdot l} \cdot \int_{-\infty}^{\infty} \ln\left(\frac{I(\chi,\lambda) - E}{I_0(\lambda) \cdot Tr(\lambda)}\right) \mathrm{d}\lambda \tag{2.11}$$

The variant of TDLAS that is applied in the group [3, 7, 37] is based on the detection of the integral on the right sight of equation 2.11 for calculating χ. The wavelength of a diode laser is repetitively tuned across the broadened absorption line by modulating the diode current, thus receiving a temporally changing wavelength. The tuning range depends on the laser type and modulation frequency. With distributed feedback (DFB) lasers, up to about 2 cm^{-1} can be covered, while vertical cavity surface enhanced lasers (VCSELS) allow for wavelength scans of around 30 cm^{-1} [6].
The temporal spectral behaviour $\frac{\mathrm{d}\lambda}{\mathrm{d}t}$ of the laser is characterized for a fixed operation point that is determined by laser temperature,wavelength tuning rate and signal generation hardware, so the time-base can be transformed into a wavelength base. Equation 2.11 can be derived from the time-dependent sizes by integration by substitution [38]

$$\int_{-\infty}^{\infty} \ln\left(\frac{I(\chi,\lambda) - E}{I_0(\lambda) \cdot Tr(\lambda)}\right) \mathrm{d}\lambda = \int_{-\infty}^{\infty} \ln\left(\frac{I(\chi,t) - E}{I_0(t) \cdot Tr(t)}\right) \cdot \frac{\mathrm{d}\lambda}{\mathrm{d}t} \mathrm{d}t \tag{2.12}$$

For calculating the absorber number density χ from equation 2.11, besides known temperature-dependent line-strength $S(T)$ and absorption path length l, the integral (corresponding to the area beneath the broadened absorption line) on the right-hand side is required. All unknown parameters that appear in the integral can be found by the following procedure: First, the measured intensity $I(\chi, \lambda)$ at a wavelength where no absorption takes place is used to fit a polynomial that describes $I_0(\chi, \lambda) \cdot Tr(t) + E$. Figure 2.1 schematically illustrates the light intensities that are relevant for TDLAS. The dotted line describes the broadband background emission E that causes the incident light to be offset to $I_0(\chi, \lambda) + E$, which is marked by the slim black line. If transmission losses occur, intensity takes the form $I_0(\chi, \lambda) \cdot Tr(\lambda) + E$, which is depicted by the gray line. This

line evidently gets very close to the measured intensity $I(\chi, \lambda)$ at wavelengths that are far away from the absorption line centre wavelength. For this reason, the strategy of fitting a polynomial base-line (depicted as a dashed line) is justified. The background emission E can be easily determined by the light intensity that is measured each time the laser does not emit light, which should occur once for every wave-length tune. The modulation current of the laser has to be adjusted so that at a small fraction of the tuning period it lies beneath the laser threshold, so that no emission of light takes place during that part of the wavelength-tune.
Instead of directly evaluating the area beneath the measured absorption line by numerical integration, first a Voigt profile is fit to the optical density of the absorption line, which is given by

$$OD_e = -\ln\left(\frac{I(\chi,\lambda) - E}{I_0(\chi,\lambda)\cdot Tr(\lambda)}\right) \tag{2.13}$$

The fit process takes place with a Levenberg-Marquardt algorithm. Afterwards, the area is extracted by integrating the fitted optical density. During the fitting process, Doppler- and collisional broadening are calculated iteratively with the current concentration, thus permitting only physically sensible combinations of absorber number density, pressure, temperature and the two broadening values.
With known pressure p and temperature T, the volume concentration c is calculated by using the ideal gas law [39]:

$$c = \chi \cdot \frac{\mathfrak{R}T}{N_A \cdot p} = \frac{V_{absorber}}{V_{total}} \tag{2.14}$$

where $\mathfrak{R}$ is the universal gas constant, $\mathfrak{R} = 8.314\ \frac{J}{mol\cdot K}$ and N_A is the Avogadro constant. The volume concentration is the fraction of absorbing gas volume of the overall gas volume and is usually expressed in the unit volume parts per million ([ppmv]).

2.2 Tomography

Giving a complete overview of tomography is impossible, since the term is used for numerous techniques that can be very disparate. The definition of "tomography" is somewhat imprecise. Literally it signifies the imaging of a slice, as it originates from the Greek words *tomos* (slice) and *graphein* (draw) [40]. In this work, tomography is confined to the imaging of slices of an object by gaining information from multiple outside positions, like it is defined in [41]. Both the image and the information can have various physical meanings, for example tissue density, capacitance, concentrations e.g. for the former and absorption, voltages or intensity of light emission for the latter. The picture function of the slice $f(x, y)$ describes the spatial distribution of any kind of physical properties. In the following, the mathematical description of data collection from outside positions is given, and if not denoted otherwise, the literature source is [41]. It is concentrated on situations where the process of collecting data is based on detection of line integrals of the picture function $f(x, y)$ at various positions. This is called *hard-field tomography*. A

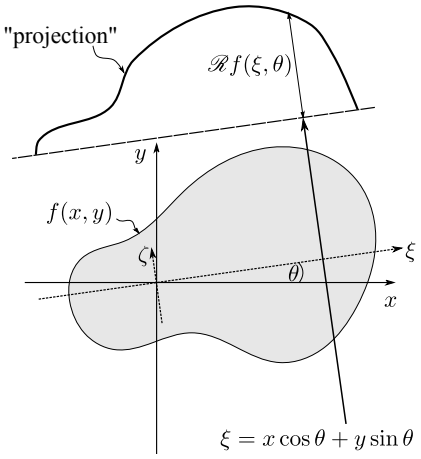

Figure 2.2 Schematic illustration of an object's picture function $f(x, y)$ and its Radon transform and projection at an angle θ

measurement at one position is only influenced by a small, known fraction of $f(x, y)$ (usually along a line). Other problems of tomography, e.g. *electrical impedance tomography* (EIT) [42–45] or *electromagnetic induction tomography* (EMT) [46], are more complicated because each measurement is influenced by the whole field $f(x, y)$. These are summed up under the term *soft-field tomography*. Explanation of soft-field tomography would lead too far since it has no physical meaning for the application.
The data collection process for hard-field tomography is illustrated for the 2D-case in figure 2.2. Each measurement takes place at a certain angle θ and distance to origin ξ. The line equation of the measurement is described by $\xi = x\cos\theta + y\sin\theta$. The line integrals at each position (ξ, θ) are described by the *Radon transform*:

$$\mathscr{R}f(\xi,\theta) = \int_{-\infty}^{\infty}\int_{-\infty}^{\infty} f(x,y)\delta(x\cos\theta + y\sin\theta - \xi)\mathrm{d}x\mathrm{d}y \tag{2.15}$$

where δ is the delta function. For practical reasons, a set of line integrals is often called *projection*. In figure 2.2 such a projection is depicted at a fixed angle for a configuration of parallel beams. Another possibility would be to unite beams into a projection that have a common point of intersection and vary in angles. Such projections form a fan-shaped beam layout and are therefore called fan-beam projections. The definition of the term "projection" can be quite arbitrary and makes sense mostly in practical applications.
If $\mathscr{R}f(\xi, \theta)$ is known completely in its continuous form, the Radon transform can be inverted and has a unique solution (view [47]). However, generally no complete representation of $\mathscr{R}f(\xi, \theta)$ is available, but discrete sets of data are measured. The reconstruction of the unknown field $f(x, y)$ from discrete data sets is not unique any more. There are numerous techniques for finding an estimate $\tilde{f}(x, y)$ of the exact solution $f(x, y)$. Explaining all of them is not sensible since they are all intended for different purposes and some can be excluded in the first place. However, a selection of promising algorithms is elaborated in the following chapters. First, the most straight-forward methods of discrete inversion of the Radon transform are presented, the so-called transform-based methods.

In chapter 2.2.2, very common algorithms based on iterative regularization are introduced. Finally, some examples of statistical inversion methods are presented (section 2.2.3).

2.2.1 Transform-based algorithms

All transform-based algorithms are derived from some kind of approximate inversion of the Radon transform. Very common algorithms are the so-called *backprojection* algorithms, that make use of the close relationship between Radon transform and Fourier transform. This relationship is described by the *Fourier slice theorem*, which states that the (one-dimensional) Fourier transform of a parallel projection of $f(x, y)$ at a fixed angle θ equals a slice of the two-dimensional Fourier transform $F(u, v)$ of $f(x, y)$ itself. The slice is described by a line through the origin of (u, v) at the angle θ. In the following it is briefly explained how the Fourier slice theorem works.

The (ξ, ζ) coordinate system depicted in figure 2.2 can be derived from the (x, y) coordinate system by the following linear transformation:

$$\begin{pmatrix} \xi \\ \zeta \end{pmatrix} = \begin{pmatrix} \cos\theta & \sin\theta \\ -\sin\theta & \cos\theta \end{pmatrix} \cdot \begin{pmatrix} x \\ y \end{pmatrix} \tag{2.16}$$

The Radon transform at a constant position ξ in the (ξ, ζ) coordinate system is given by:

$$\mathscr{R}f(\theta, \xi) = \int_{-\infty}^{\infty} f(\xi, \zeta)\mathrm{d}\zeta = \mathscr{R}f_\theta(\xi) \tag{2.17}$$

The Radon transform is written as $\mathscr{R}f_\theta(\xi)$ if we consider a fixed angle θ, uniting all path-integrals of a parallel-beam constellation into a projection. The Fourier transform of this projection is given by

$$RF_\theta(\Omega) = \mathcal{F}\{\mathscr{R}f_\theta(\xi)\} = \int_{-\infty}^{\infty} \mathscr{R}f_\theta(\xi)e^{-i\Omega\xi}\mathrm{d}\xi \tag{2.18}$$

which equals

$$RF_\theta(\Omega) = \int_{-\infty}^{\infty} \left[\int_{-\infty}^{\infty} f(\xi, \zeta)\mathrm{d}\zeta \right] e^{-i\Omega\xi}\mathrm{d}\xi \tag{2.19}$$

With equation 2.16, the coordinates can be transformed into the (x, y) coordinate system:

$$RF_\theta(\Omega) = \int_{-\infty}^{\infty} \int_{-\infty}^{\infty} f(x, y)e^{-i\Omega(x\cos\theta + y\sin\theta)}\mathrm{d}x\mathrm{d}y \tag{2.20}$$

The two-dimensional Fourier transform of $f(x, y)$ is denoted by:

$$F(u, v) = \mathcal{F}\{f(x, y)\} = \int_{-\infty}^{\infty} \int_{-\infty}^{\infty} f(x, y)e^{-i(ux+vy)}\mathrm{d}x\mathrm{d}y \tag{2.21}$$

The right-hand side of equation 2.20 can be interpreted as the two-dimensional Fourier transform of $f(x, y)$ at the spatial frequencies $u = \Omega \cos\theta, v = \Omega \sin\theta$:

$$RF_\theta(\Omega) = F(\Omega \cos\theta, \Omega \sin\theta) \tag{2.22}$$

The illustrative description of equation 2.22 is: if you have a projection at a fixed angle θ, its Fourier transform corresponds to the 2D-Fourier transform values of the image along the line that is given by

$$\begin{pmatrix} u \\ v \end{pmatrix} = \begin{pmatrix} \cos\theta \\ \sin\theta \end{pmatrix} \cdot \Omega \tag{2.23}$$

The general approach of transform-based algorithms is the following: First, the discrete Fourier transforms of the projections are calculated. By this means an incompletely sampled function $F(u, v)$ is received. Its sampling points are radially distributed in the (u, v)-space (view figure 2.3). An inverse Fourier transform of $F(u, v)$ finally leads to the unknown function $f(x, y)$. Generally, interpolation between the radially sampled values of $F(u, v)$ has to take place before numerical inversion. Again, there are different methods of reconstruction in the transform-based sector, like direct backprojection, linograms, rho-filtered layergrams or filtered backprojection (FBP), to name a few [40, 41, 47]. Since none of them is appropriate for limited data tomography, detailed information about the respective techniques should be taken from literature.
So why are transform-based algorithms not appropriate for limited data tomography? The answer is: too many beams are required to receive a decent reconstructed image. From figure 2.3 it becomes evident that not the entire frequency space can be sampled, but only discrete points. Depending on the instrument geometry, the maximum detectable frequency is determined by the number of projections and the number of samples per projection. Consider an image described by $f(x, y)$ that is essentially b-band-limited according to Natterer [48] , that means $\mathcal{F}\{f(x, y)\} = F(\Omega)$ is negligible for $|\Omega| > b$. If details of down to frequency b shall be reliably detected, the Shannon-theorem has to be fulfilled, which states that the signal has to be sampled with twice the maximum occurring frequency. This is fulfilled for the parallel-beam set-up with $p^\sharp$ regularly spaced projections and $2q^\sharp + 1$ regularly spaced samples per projection [48] if

$$\begin{aligned} p^\sharp &> b \\ q^\sharp &> \frac{b}{\pi} \end{aligned} \tag{2.24}$$

Another very common alignment is the so-called fan-beam layout. Here, a projection is given by a set of line integrals with a common start point and regularly spaced angles. The start-points are arranged regularly in a circle with radius r_{fan} around the measurement object. The Nyquist theorem is fulfilled [48] if

$$\begin{aligned} p^\sharp &> 2b \\ q^\sharp &> \frac{b r_{fan}}{2} \end{aligned} \tag{2.25}$$

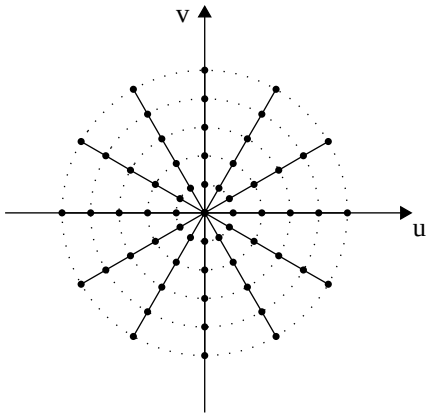

Figure 2.3 Position of the sampled projection data in (u, v) coordinate system according to [41]

It is obvious that for reasonable spatial frequencies the amount of measurement paths rises very quickly. A practical example is given in chapter 4.

2.2.2 Algebraic reconstruction techniques

The term *algebraic reconstruction techniques* (ART) unites several iterative algorithms that are based on the assumption that the concentration field can be described as a discrete array of unknowns [41]. Herman et al. [49] describe the discrete tomography problem as follows: An unknown function $f(x, y)$ that has the range of a discrete set shall be determined for a continuous or discrete domain. In the continuous case, this is done by means of weighted integrals over subspaces of its domain, whereas in the discrete case, weighted sums over subsets of its domain are used. The latter is applied for the ART algorithms. They have in common that the modelled measurement process, the so-called *forward model*, is described by a linear system of equations due to the discretization of the range and domain of $f(x, y)$. This system of equations is iteratively solved. In contrast to transform-based techniques, there need not be numerous equidistant or equiangular beams, but less beams can be positioned in an arbitrary way. There are manifold ART algorithms and only a confined selection of methods is presented in the following for giving a representative overview.

2.2.2.1 ART (Kaczmarz method)

The classical ART algorithm is defined as an application of the Kaczmarz method [50] to Radon's integral equation [48], for both the fully discrete case (where the domain of $f(x, y)$ is discrete) and the semi-discrete case (where the domain of $f(x, y)$ is continuous [48]). It is therefore often called the *Kaczmarz method*. In this work it is focussed onto the fully discrete case. The observation model is built according to [41]. The domain is divided into N square pixels that are assumed to have uniform unknown values f_j. The M measurements c_i are now weighted ray-sums instead of ray-integrals, allowing to model

the experiment as

$$\sum_{j=1}^{N} w_{ij} f_j = c_i, \qquad i = 1 \dots M \tag{2.26}$$

The weights are determined by the fractional contribution of the jth pixel value to the ith measurement. The linear system of equations 2.26 can also be expressed by $W \cdot \vec{f} = \vec{c}$ and is solved by the iterative Kaczmarz method [50]. Explaining the principles of this method would lead too far, therefore only the calculation rule is given. First, an initial guess $\vec{\tilde{f}}^{(0)}$ is made, which is usually a zero vector. Sometimes the average value of $\vec{c}$ is taken as a start-point. Then the current vector is iteratively improved. One iteration consists of M repetitions of the following calculation:

$$\vec{\tilde{f}}^{(i)} = \vec{\tilde{f}}^{(i-1)} - \frac{\vec{\tilde{f}}^{(i-1)} \cdot \vec{w}_i - c_i}{\vec{w}_i \cdot \vec{w}_i} \vec{w}_i \tag{2.27}$$

where $\vec{w}_i = [w_{i1} \dots w_{iN}]$. A better solution $\vec{\tilde{f}}^{(i)}$ is produced for each of the M beam paths in this single update. The whole process is then repeated for k iterations. The algorithm converges to the correct solution if a unique solution exists [51], which is normally not given in tomography because the systems of equations are usually rank-deficient. It has to be expected that in some cases there are solutions that fulfil the systems of equations but do not have any physical meaning or that do not correspond to the real concentration field.

2.2.2.2 SIRT

The SIRT algorithm (Simultaneous Iterative Reconstructive Technique) [41] is a technique that is very similar to the classical ART algorithm. The forward model is the same and therefore the identical linear system of equations is solved. The classical ART algorithm successively computes M improved values of the unknown vector $\vec{\tilde{f}}$ for each iteration, updating the value of $\vec{\tilde{f}}$ after each contribution of a single ray, that means after each i^{th} sub-step in the k^{th} iteration. In contrast to this, SIRT does not update $\vec{\tilde{f}}$ during one iteration, but stores all $\Delta\tilde{f}_j^{(i)} = \tilde{f}_j^{(i)} - \tilde{f}_j^{(i-1)}$ and then calculates the average change for each pixel. The calculation rule for the iteration $(k+1)$ is hence:

$$\tilde{f}_j^{(k+1)} = \tilde{f}_j^{(k)} + \frac{\sum_i \left[w_{ij} \dfrac{c_i - \vec{w}_i^T \vec{\tilde{f}}^{(k)}}{\sum_{j=1}^{N} w_{ij}} \right]}{\sum_i w_{ij}} \tag{2.28}$$

In general, SIRT converges slower than the Kaczmarz technique, but it leads to better reconstructions of $f(x, y)$ [41].

2.2.2.3 SART

The *Simultaneous Algebraic Reconstruction Technique* (SART) [41] is based on a more accurate forward model than ART and SIRT. The domain of $f(x, y)$ is not discretized into pixels any more. Instead, it is assumed that the continuous unknown image function $f(x, y)$ can be approximated by a superposition of basis functions:

$$f(x, y) \approx \hat{f}(x, y) \equiv \sum_{j=1}^{N} g_j b_j(x, y) \tag{2.29}$$

with the expansion coefficients g_j and the basis functions $b_j(x, y)$. The SART algorithm presented by Kak [41] uses bilinear basis functions, i.e. pyramid-shaped elements. Now, the observation model takes a different form than for ART and SIRT and delivers a distinct linear system of equations. Taking the Radon transform of $f(x, y)$ is approximated by

$$c_i = \mathscr{R}_i f(x, y) \approx \mathscr{R}_i \hat{f}(x, y) = \sum_{j=1}^{N} g_j \mathscr{R}_i b_j(x, y) = \sum_{j=1}^{N} g_j a_{ij} \tag{2.30}$$

Here, a_{ij} are the line integrals of $b_j(x, y)$ along the i^{th} path. They are approximated by a finite sum of the approximated Radon transform that is sampled at equidistant points. For solving equation 2.30, the algorithms described in chapter 2.2.2.1 or chapter 2.2.2.2 can be used. Kak et al. [41] recommend the simultaneous iteration like it is used for SIRT.

2.2.2.4 Landweber algorithm

Here, the forward model takes again the form of a linear systems of equations that is given by equation 2.26. Terzija et al. [52] suggested an enhanced Landweber method for solving this system of equations which is briefly presented. In contrast to other algebraic techniques, the initial guess is not a zero vector or a vector with the measured mean values. Instead, the inversion of the linear system of equations is approximated by $\vec{\tilde{f}}^{(0)} = W^T \cdot \vec{c}$. The translated weighting matrix W^T serves as an approximate inverse. The unknown vector $\vec{\tilde{f}}$ is then iteratively updated by

$$\vec{\tilde{f}}^{(k+1)} = \vec{\tilde{f}}^{(k)} + \alpha_{LW} W^T (\vec{c} - W \cdot \vec{\tilde{f}}^{(k)}) \tag{2.31}$$

where α_{LW} is an regularization parameter that according to [53] should be picked such that $0 < \alpha_{LW} < 2(\|W^T W\|_2)^{-1}$. The influence of the choice of the regularization parameter on the reconstruction quality is discussed in chapter 4.2.2.

2.2.3 Statistical inversion

A completely different way of looking at the inversion of the observation model is provided by methods that are counted to statistical inversion. It is not intended to solve a system of equations directly, but the probabilities of the set of infinite solutions are considered. Assessing which solutions are more probable than others presumes physical knowledge about the measured object. To illustrate this in a more comprehensible way, an example

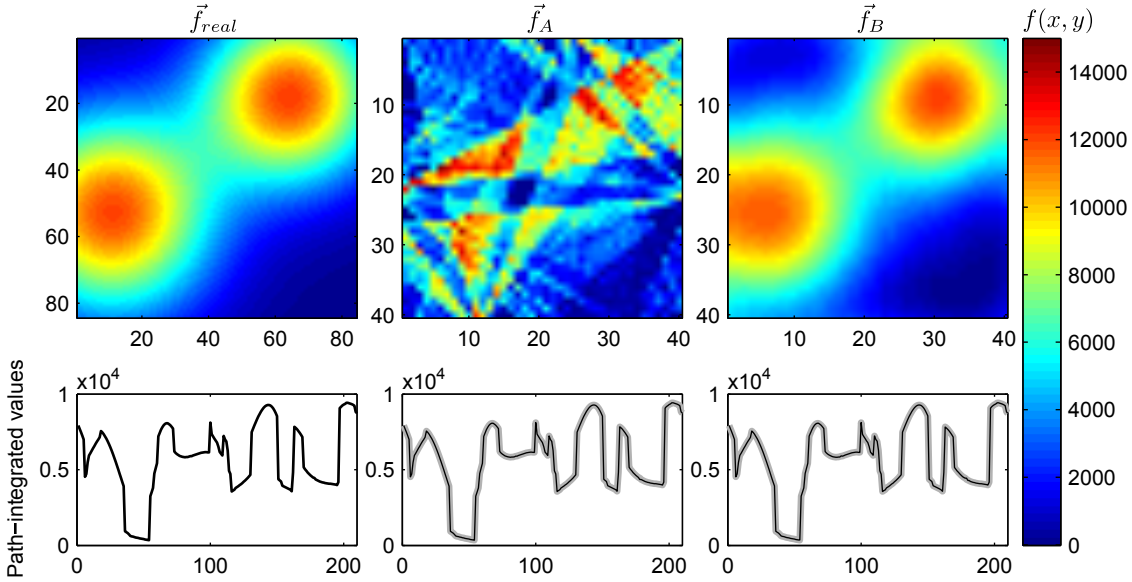

Figure 2.4 Correct field $\vec{f}_{real}$ and two solutions that fulfil the forward model

for solving $\vec{c}_{real} = W \cdot \vec{f}_{real}$ is presented in figure 2.4. To the left, the vector $\vec{f}_{real}$ is depicted in a reshaped form so that it represents an image. The path-integral values, here given by discrete sums $\vec{c}_{real}$ are plotted beneath the image. The two solutions $\vec{f}_A$ and $\vec{f}_B$ both fulfil the linear system of equations $W \cdot \vec{f} = \vec{c}$, as they both lead to path-integrals that are nearly identical to the real ones. They are two solutions from the infinite set of solutions that solve the observation model. However, they are not equally valuable. Whereas solution A cannot be interpreted in a physical way and has no practical meaning, solution B is probably a valuable solution because it coincides with prior knowledge about structure sizes and smoothness.
The strategy is now to give physically sensible solutions a higher probability by taking knowledge about the measurement object into account. Different algorithms are used for this, depending on the type of the physical assumption, which will be presented in the successive chapters. They are all based on Bayes' law [54, 55] which describes the conditional probabilities of two events A and B:

$$\mathbb{P}(B|A) = \frac{\mathbb{P}(A|B) \cdot \mathbb{P}(B)}{\mathbb{P}(A)} \tag{2.32}$$

The *posterior density* $\mathbb{P}(B|A)$ expresses how likely event B occurs having accounted for event A. Vice versa, the *likelihood density* $\mathbb{P}(A|B)$ is defined. The prior density $\mathbb{P}(B)$ gives the probability of event B without any regard to A. Likewise the total probability $\mathbb{P}(A)$ denotes the probability of event A without considering event B.
The tomographic measurement process can be modelled as such a statistical process: the probability to receive a solution $\vec{f}$ under the condition that the path-integrated values $\vec{c}$ were measured is expressed by Bayes' theorem. The general equation 2.32 is transferred to the measurement process, given the discrete measurement $\vec{c}$ and a discretized field of

unknowns $\vec{f}$:

$$\mathbb{P}(\vec{f} \mid \vec{c}) = \frac{\mathbb{P}(\vec{c} \mid \vec{f})\mathbb{P}(\vec{f})}{\mathbb{P}(\vec{c})} \propto \mathbb{P}(\vec{c} \mid \vec{f})\mathbb{P}(\vec{f}) \tag{2.33}$$

Now the likelihood density $\mathbb{P}(\vec{c} \mid \vec{f})$ is interpreted as the probability of measuring $\vec{c}$ if $\vec{f}$ is given. In an ideal case, the likelihood density would be 1, but as in real experiments the measurements $\vec{c}$ are corrupted by noise, the latter can be taken into account with the likelihood density. Physical assumptions about the measurement object can be included in the prior density $\mathbb{P}(\vec{f})$. The total probability of a measurement $\mathbb{P}(\vec{c})$ is generally unknown. However, the strategy is to find the "most probable" solution. Therefore the absolute values of probability are not of interest. It is sufficient to know the relative distribution of probability, so it is made use of the proportionality of equation 2.33.
Bayesian estimation in contrast to the algebraic techniques does not deliver a single solution, it produces a posterior distribution that can be interpreted as how likely one solution is compared to others. As mentioned above, logically the best solution is the most probable one. But how is the most probable solution determined? Several estimators for the most likely solution exist that are elucidated in Kaipio et al. [56]. A very common estimate which will be used in this work for finding the correct solution is the *maximum a posteriori* (MAP) estimate. It determines the maximum value of the posterior distribution:

$$\vec{f}_{MAP} = \arg\max_{\vec{f}\in\mathbb{R}^n} \mathbb{P}\Big(\vec{f} \mid \vec{c}\Big) \tag{2.34}$$

Drawbacks of the maximum a posteriori estimate are that the maximizer can be non-unique or that no maximizer exists. Finding $\vec{f}_{MAP}$ is an optimization problem.
Another way to find the most probable solution is to determine the expectation value of the posterior density, which is done by the conditional mean (CM) of the unknown function:

$$\vec{f}_{CM} = \mathcal{E}\Big\{\vec{f} \mid \vec{c}\Big\} = \int_{\mathbb{R}^n} \vec{f} \cdot \mathbb{P}\Big(\vec{f} \mid \vec{c}\Big)\mathrm{d}\vec{f} \tag{2.35}$$

For the determination of $\vec{f}_{CM}$, an integration problem has to be solved. There are situations where one of the estimators performs better than the other and vice versa. Examples for such situations are presented in [56]. At the same place, there are also *interval estimates* introduced, which describe in what interval the unknown values of $\vec{f}$ lie with a certain probability.
The modelling of noise is valid for various priors, therefore it is described in the following. It is assumed that noise is normally distributed with zero mean and covariance Γ_n:

$$n \sim \mathcal{N}(0, \Gamma_n) \tag{2.36}$$

Thus, the likelihood density takes the form

$$\mathbb{P}(\vec{c} \mid \vec{f}) \propto \exp\left(-\frac{1}{2}\Big(\vec{c} - \mathscr{W}\Big(\vec{f}\Big)\Big)^T \Gamma_n^{-1}\Big(\vec{c} - \mathscr{W}\Big(\vec{f}\Big)\Big)\right). \tag{2.37}$$

where $\mathscr{W}\left(\vec{f}\right)$ is the mapping of the unknown function $\vec{f}$ to the measured path-integrals. In the linear case, this function is given by $\mathscr{W}\left(\vec{f}\right) = W \cdot \vec{f}$. It is useful for a more convenient notation and for the formulation of the optimization problem for finding the MAP estimate to compute the Cholesky decomposition [57] of the inverted covariance matrix Γ_n^{-1}:

$$\Gamma_n^{-1} = L_n^T L_n \tag{2.38}$$

Therefore, the inverse of the matrix Γ_n is decomposed into a lower triangular matrix L_n and its transpose L_n^T. With the Cholesky decomposition, the exponent of equation 2.37 can be simplified.

$$\begin{aligned} & \left(\vec{c} - \mathscr{W}\left(\vec{f}\right)\right)^T \underbrace{\Gamma_n^{-1}}_{L_n^T L_n} \left(\vec{c} - \mathscr{W}\left(\vec{f}\right)\right) \\ = & \left(L_n\left(\vec{c} - \mathscr{W}\left(\vec{f}\right)\right)\right)^T \left(L_n\left(\vec{c} - \mathscr{W}\left(\vec{f}\right)\right)\right) \\ = & \left\| L_n\left(\vec{c} - \mathscr{W}\left(\vec{f}\right)\right)\right\|^2 \end{aligned} \tag{2.39}$$

Thus the likelihood density is written as follows:

$$\mathbb{P}(\vec{c} \mid \vec{f}) \propto \exp\left\{ - \left\| L_n\left(\vec{c} - \mathscr{W}\left(\vec{f}\right)\right)\right\|^2 \right\} \tag{2.40}$$

In the following chapters, different methods of setting the prior density are presented.

2.2.3.1 Tikhonov regularisation

If not denoted otherwise, the information in this chapter is taken from Daun [58]. Assume that the observation model is given by a linear system of equations $\vec{c} = W \cdot \vec{f}$. Tikhonov regularization makes use of a *Gibbs prior* which is based on the presumption that the distribution of $f(x, y)$ is smooth due to diffusion processes. The prior density fulfils

$$\mathbb{P}_{Gibbs}(\vec{f}) \propto \exp\{-\gamma(U(\vec{f}))\} \tag{2.41}$$

where $U(\vec{f})$ is an energy function and γ is a factor that determines the weight of the prior. It is here expressed by the Tikhonov smoothing matrix $U(\vec{f}) = \left\|\mathcal{L}\vec{f}\right\|_2^2$, where $\mathcal{L}$ is an discrete Laplacian operator:

$$\mathcal{L}_{ij} = \begin{cases} 1 & \text{if } i = j \\ -1/G_i & \text{if } j \text{ neighbours } i \\ 0 & \text{otherwise} \end{cases} \tag{2.42}$$

where G_i is the number of neighbouring elements of the i^{th} element. Thus, the prior density is

$$\mathbb{P}_{Gibbs} = \exp\{-\gamma \cdot \frac{1}{2}\vec{f}^T\mathcal{L}^T\mathcal{L} \cdot \vec{f}\} \tag{2.43}$$

With the noise model from equation 2.37 and $\Gamma_n = \sigma^2\mathbf{I}$ the posterior density is calculated by

$$\begin{aligned}\mathbb{P}(\vec{f} \mid \vec{c}) &\propto \exp\{-\frac{\sigma^2}{2}\left\|\vec{c} - W \cdot \vec{f}\right\|^2 - \frac{\gamma}{2} \cdot \vec{f}^T\mathcal{L}^T\mathcal{L}\vec{f}\} \\ &\propto \exp\{-\left\|\vec{c} - W \cdot \vec{f}\right\|^2 - \tau^2\vec{f}^T\mathcal{L}^T\mathcal{L}\vec{f}\}\end{aligned} \tag{2.44}$$

The regularization parameter can be expressed by $\tau^2 = \gamma/\sigma^2$. It is evident that the solutions depend on the choice of τ as it determines the influence of the smoothness prior. Some strategies to do so are presented in Daun et al. [59].

2.2.3.2 An informative smoothness prior

Like for Tikhonov regularization, it is presumed that the unknown function $f(x, y)$ is smooth over its domain due to diffusion processes. The prior density is modelled as a multivariate normal distribution with expectation value η_f and covariance Γ_f:

$$\vec{f} \sim \mathcal{N}(\eta_f, \Gamma_f) \tag{2.45}$$

Its number of degrees of freedom equals the amount of unknown values of the discretized field. The prior density is expressed as [60]

$$\mathbb{P}_{smooth}(\vec{f}) \propto \exp\Big(-\frac{1}{2}(\vec{f} - \eta_f)^T\Gamma_f^{-1}(\vec{f} - \eta_f)\Big) \tag{2.46}$$

With the noise modelled by equation 2.37, the posterior density results in

$$\mathbb{P}(\vec{f} \mid \vec{c}) \propto \exp\Big(-\frac{1}{2}(\vec{f} - \eta_f)^T\Gamma_f^{-1}(\vec{f} - \eta_f) - \frac{1}{2}(\vec{c} - \mathscr{W}(\vec{f}))^T\Gamma_n^{-1}(\vec{c} - \mathscr{W}(\vec{f})\Big) \tag{2.47}$$

The covariance matrix Γ_f has two physical meanings: On the one hand, it contains on its diagonal the variances $var(f_i)$ of the unknown values $\vec{f}$. Those have to be chosen such that all realistic values of the unknown vector are sufficiently probable. An demonstrative example is given for a problem with only one unknown value f in figure 2.5. During a measurement, the expectation value η_f is estimated but it needs not be the correct solution. The maximum prior probability is centred at η_f, but a range of other values is also probable. By determining the variance of $\mathbb{P}(f)$, it is adjusted how probable values deviating from the expectation value are.
Furthermore, Γ_f contains the covariances between the unknown values on its off-diagonal

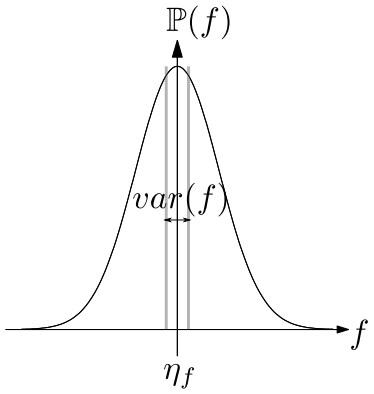

Figure 2.5 Prior density for a one-dimensional unknown function f

elements. The covariances are a direct measure for smoothness as they decide on how strong two unknown values are correlated.
The informative smoothness prior makes use of known structure sizes in the measurement field for adjusting the covariances [61]. It is assumed that the farther two pixels of $\vec{f}$ are located from each other, the less they are correlated. An exponential relationship between the distance between two pixels r and the respective covariance is set up:

$$\Gamma_{f,i} = var(f_i) \cdot \exp\left\{ -\frac{r^2}{2b^2} \right\} \tag{2.48}$$

At a distance of $r = 0$, $\Gamma_{f,i}$ takes the value $var(f_i)$ (view figure 2.6), as the covariance of the pixel value with itself is the pixel's variance. The parameter b determines how strong pixels with a certain distance correlate. It can be sensibly chosen if the size of the structures is known. For a more convenient treatment of the structure size information, the *correlation length* Λ is introduced. It is defined as the distance where the covariance between two pixels amounts 1% of $var(f_i)$ (view figure 2.6). In practice, Λ is set to the a priori known structure size. The correlation length has the value

$$\Lambda = \sqrt{2 \cdot \ln(100)} \cdot b \tag{2.49}$$

The pixel-wise implementation of the covariance matrix is carried out as follows:

$$\Gamma_f(i,j) = var(f_i) \exp\left\{ -\frac{\|r_i - r_j\|_2^2}{\Lambda^2} \cdot \ln 100 \right\} \tag{2.50}$$

with the spatial coordinates $r_i, r_j \in \mathbb{R}^{2,2}$ of the ith and jth discretized element.

The maximum a posteriori estimate of the posterior density (2.47) thus is expressed by

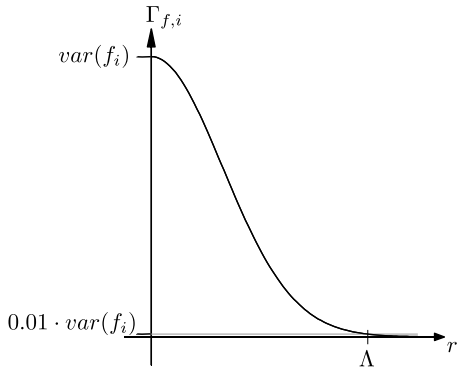

Figure 2.6 Schematic illustration of the covariance depending on the distance r between two pixels. The distance where the covariance drops to 1% of the single pixel variance is called correlation length Λ, and serves as a structural prior.

$$\begin{aligned}\vec{f}_{MAP} &= \arg\max_{\vec{f}}\{-(\vec{f}-\eta_f)^T\Gamma_f^{-1}(\vec{f}-\eta_f) - (\vec{c}-\mathscr{W}(\vec{f}))^T\Gamma_n^{-1}(\vec{c}-\mathscr{W}(\vec{f}))\} \\ &= \arg\min_{\vec{f}}\{(\vec{f}-\eta_f)^T\Gamma_f^{-1}(\vec{f}-\eta_f) + (\vec{c}-\mathscr{W}(\vec{f}))^T\Gamma_n^{-1}(\vec{c}-\mathscr{W}(\vec{f}))\}\end{aligned} \tag{2.51}$$

With the Cholesky-decomposition $\Gamma_f^{-1} = L_f^T L_f$, analogous to equation 2.39, the MAP estimate can be written in a simple form as:

$$\vec{f}_{MAP} = \arg\min_{\vec{f}}\{\left\|L_n(\vec{c}-\mathscr{W}(\vec{f}))\right\|^2 + \left\|L_f(\vec{f}-\eta_f)\right\|^2\} \tag{2.52}$$

This objective function is minimized in a further step. Details about the application-specific implementation are given in chapter 4.

2.2.3.3 Total variation prior

The total variation prior should be used if $f(x, y)$ is expected to have larger contiguous areas with very homogeneous values and gradients are only expected at very few locations [61,62]. Often such images give an impression of "blocky" structures [56], which will be explained in the following.
If the total variation prior is included into the Bayes esimation, solutions with small total variation are favoured. The total variation of a function $f(x, y)$ is defined by

$$TV(f) = \int_\Omega |\nabla f(x,y)|\mathrm{d}x\mathrm{d}y \tag{2.53}$$

For an illustrative understanding of the physical meaning of total variation, a simple example is given. In figure 2.7, three images with identical energy are depicted, that means the sum of all pixel values is equal for each of them (equal pixel colors mean equal pixel values). Nevertheless, they have different total variations. In the discretized case,

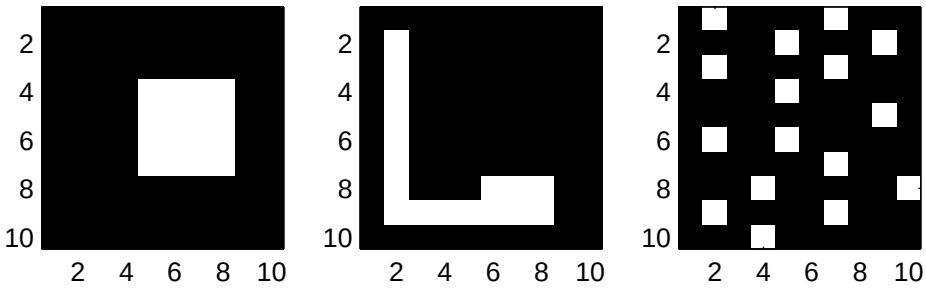

Figure 2.7 Three images with equal energy content but different total variations. If the black pixels are interpreted as zero and the white pixels as one, the figures have the following total variations: 10 (left), 14 (center) and 14.5 (right).

the total variation (TV) is obtained by

$$TV(\vec{f}) = \sum_{i}^{n}(\frac{1}{2}\sum_{j\in G}\epsilon_{ji}\,\|f_j - f_i\|) \tag{2.54}$$

where ϵ_{ji} is the length of the shared edge of the jth neighbour of the ith pixel. The pixel index i runs from 1 to the total amount of pixels N, whereas the neighbour index j runs from 1 to the amount of neighbours G that pixel i has. In the case of a square pixel discretization, pixels in the center have four direct neighbours (diagonal neighbours are omitted), whereas pixels in the corners and at the edges have only two or one neighbours, respectively.
In the practical example, the values of the white pixels are set to one and those of the black pixels are set to zero. The edge lengths are uniform with value 1 since the pixels are quadratic. Thus, the total variation for the left image is 10, for the centre image 14, and for the right image 14.5. If solutions with lower total variation are allocated with a higher probability, images are favoured that show small variation within larger areas and that have gradients at a minimum overall edge length.
The prior density using total variation is defined by

$$\mathbb{P}_{TV}(\vec{f}) \propto \exp\{-\alpha TV(\vec{f})\} \tag{2.55}$$

The parameter α determines the weight that is put onto the prior. The discrete implementation is an approximation that, analogue to equation 2.54 is given by

$$\mathbb{P}_{TV}(\vec{f}) \propto \exp\left\{-\alpha\left(\sum_i \underbrace{\left|\frac{df}{dx}\right|_i}_{(|f_{i+1}-f_i|+|f_i-f_{i-1}|)} + \underbrace{\left|\frac{df}{dy}\right|_i}_{(|f_{i+\sqrt{N}}-f_i|+|f_i-f_{i-\sqrt{N}}|)}\right)\right\} \tag{2.56}$$

The gradients are again approximated by differences between the neighbouring pixels. For a square image with N square pixels (an example is shown in figure 2.8), each pixel i in the center has four neighbours: one in the West $(i-1)$, one in the East $(i+1)$, one in the North $(i-\sqrt{N})$ and one in the South $(i-\sqrt{N})$.

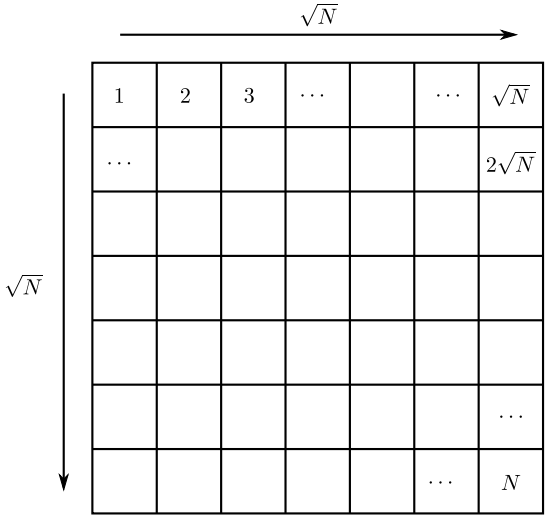

Figure 2.8 Exemplary square discretization into N pixels

For edge or corner pixels, the respective differences are omitted.
For a more handy formulation of the TV prior, the matrix D is defined where each difference operation is represented by a single row, so that

$$\mathbb{P}_{TV}(\vec{f}) \propto \exp\left\{ -\alpha \left\| D\vec{f} \right\| \right\} \tag{2.57}$$

Hence,

$$D = \begin{array}{c} \begin{array}{cccccccccccccc} & & & i-\sqrt{n} & & & & i-1 & i & i+1 & & & i+\sqrt{n} & & \end{array} \\ \begin{pmatrix} \cdots & \cdots & \cdots & \cdots & \cdots & \cdots & \cdots & \cdots & \cdots & \cdots & \cdots & \cdots & \cdots & \cdots \\ 0 & \cdots & 0 & 0 & \cdots & 0 & -1 & 1 & 0 & \cdots & 0 & 0 & \cdots & 0 \\ 0 & 0 & 0 & 0 & \cdots & -1 & 1 & \cdots & 0 & 0 & 0 & 0 & \cdots & 0 \\ 0 & \cdots & 0 & 0 & \cdots & 0 & -1 & 0 & \cdots & 0 & 1 & 0 & \cdots & 0 \\ 0 & \cdots & -1 & 0 & \cdots & 0 & 1 & 0 & \cdots & 0 & 0 & \cdots & \cdots & 0 \\ \cdots & \cdots & \cdots & \cdots & \cdots & \cdots & \cdots & \cdots & \cdots & \cdots & \cdots & \cdots & \cdots & \cdots \end{pmatrix} \end{array} \in \mathbb{R}^{G \times N} \tag{2.58}$$

As every difference of the discrete prior is positioned in a single row, D has G rows, where G is the overall number of neighbours. For a quadratic image with n pixels it can easily be calculated that $G = 4(N - \sqrt{N})$. The rows depicted in (2.58) are an example of an inner pixel, requiring four rows for all its neighbours, while corner or edge pixels need only two or three rows, respectively.
Before the term for posterior density is written down, some practical issues arising form implementation have to be explained. The objective function is minimized with a Gauss-Newton algorithm, which requires the first and second derivatives of the objective function. Unfortunately, the absolute value functions are not differentiable around zero and are therefore approximated by

$$|f_{i+1} - f_i| \approx \sqrt{(f_{i+1} - f_i)^2 + \beta} \qquad = \sqrt{(D_k\vec{f})^2 + \beta} \tag{2.59}$$

$$\widetilde{TV}(\vec{f}) := \sum_{k}^{G} \sqrt{(D_k\vec{f})^2 + \beta} \tag{2.60}$$

A small value of β is added such that the absolute value functions are continuously differentiable around zero. Hence, the posterior density can be expressed with (2.59) as

$$\begin{aligned}\mathbb{P}(\vec{f} \mid \vec{c}) &\propto \mathbb{P}(\vec{c} \mid \vec{f})\mathbb{P}_{TV}(\vec{f}) \\ &\propto \exp\left\{ -\frac{1}{2}\left\| L_n(\vec{c} - W(\vec{f})) \right\|^2 - \alpha \cdot \widetilde{TV}(\vec{f}) \right\}\end{aligned} \tag{2.61}$$

The maximum a posteriori estimate is then given by

$$\vec{f}_{MAP} = \arg\min_{\vec{f}} \left\{ \frac{1}{2}\left\| L_n(\vec{c} - \mathscr{W}(\vec{f})) \right\|^2 + \alpha \cdot \widetilde{TV}(\vec{f}) \right\} \tag{2.62}$$

The influence of the total variation prior can be adjusted with the parameter α from the deregularized problem ($\alpha = 0$) to a solution where the measurement is neglected due to large α values. The choice of α and β is based on experience. Further details about the implementation are illustrated in chapter 4.

Chapter 3

Tomographic Instrument

The design of a tomographic instrument always has to be an application-specific one. It depends on several boundary conditions: First of all, there is always a trade-off between spatial resolution or efficiency of reconstruction and instrumentation effort. As it has been elucidated in chapter 2.2.1, spatial resolution depends on the number of beam paths. In practice, this number is usually limited, either because of accessibility of the measurement object or because of transportability or simply cost. Depending on the measurement object, it has to be decided which spatial resolution is necessary to gain any knowledge about the system. Then it needs to be made sure that the required spatial resolution can be achieved with an acceptable instrumentation effort. Another issue is temporal resolution. While in the permafrost application, image rates of a few Hz are strived for, the time-scales in combustion systems are in the order of μs. This can severely limit the method of measurement as it is shown more detailed in chapter 3.1. Furthermore, boundary conditions like the size of the measurement field, the expected temperature distribution, expected concentration of the measured species and interference with other species play a role. Obviously, the system that shall be examined has to be known to a certain degree already before the experiment is designed. Tomographic systems for environmental or technical purposes are not really flexible regarding measurement objects, as the design has to be adapted to the measurement object for each purpose. Nevertheless, insights that are gained with one instrument can be useful with regard to successive design of experiments for other applications.
The presented instrument was designed for an application in soil physics that was described in detail in chapter 1. The spatially resolved emission of climate gases from thawing permafrost soil shall be monitored. For this purpose, a tomographic TDLAS measurement of areas in the scale of square meters shall take place. The desired image rates are in the range of a few Hertz. Besides the absolute quantification of concentrations, the aim is to identify structures that emit climate gases. The desired spatial resolution should be around 10 cm.
Experiments are intended to take place in Arctic regions, so a field instrument is necessary that is robust, easily transportable and that needs no complicated adjustment in the field. In this chapter, the design process of such an instrument is demonstrated: Chapter 3.1 deals with the choice of the basic concept. The set-up of optical and mechanical components and the process of data acquisition are illustrated in chapter 3.2. Processing and evaluation of measured signals are described in chapter 3.3. In chapter 3.4 it is examined how good path-integrated TDLAS measurements that are the basis for tomographic reconstructions can take place with the designed instrument.

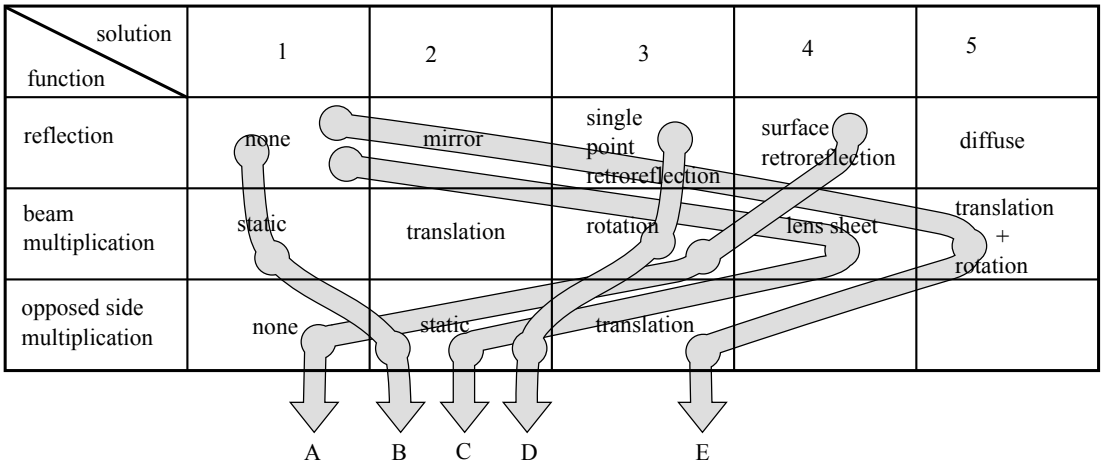

Figure 3.1 Exemplary morphological box for finding a general opto-mechanical concept of the tomographic field instrument

3.1 Conceptual design

For the above described field instrument, several boundary conditions have to be fulfilled. First, the transportability and robustness of the instrument has to be made sure since it is intended for application in Arctic regions. Effort for adjustment in the field shall be minimized. Areas of at least 0.5 m × 0.5 m have to be covered. Spatial resolution should be at least around 10 cm, so that relevant soil structures can be resolved. For future flux measurements that can be gained if concentration measurements are combined with gas velocity measurements, the image rate should at least amount 1 Hz. It is assumed that pressure and temperature are constant all over the measurement area, such that path-averaged concentrations can be detected with TDLAS without large errors. The measurement object, that means the soil area, is quite easily accessible. However instrumentation will be limited due to transportability and cost reasons. A disadvantage in comparison to other measurement objects is that absorption takes place everywhere in the surroundings. In technical systems like for example flames, it is often known that in a certain area around the measurement object no absorbing gas exists. This allows for complete coverage of the object with a single fan-beam, if only the emitting side is moved far enough away from the object. A further drawback of the soil application is that the measurement object itself cannot be moved, which is often a strategy for multiplying measurement paths.
Finding a concept that is fit to these boundary conditions can be realized by means of a so-called *morphological box*, like it is presented by [63]. Here, principle solutions for each product function are combined systematically. The resulting combinations are then assessed regarding their aptness for the application.
In figure 3.1 an extract of product functions and principle solutions for the tomographic instrument is presented for giving a rough impression of the process. The first product function was here abbreviated by “reflection”. It describes how the laser beam is directed onto the detector. This can for example be done directly like in solution 1, so there is no reflection of the laser beam at all. Other possibilities are to deflect the beam with a

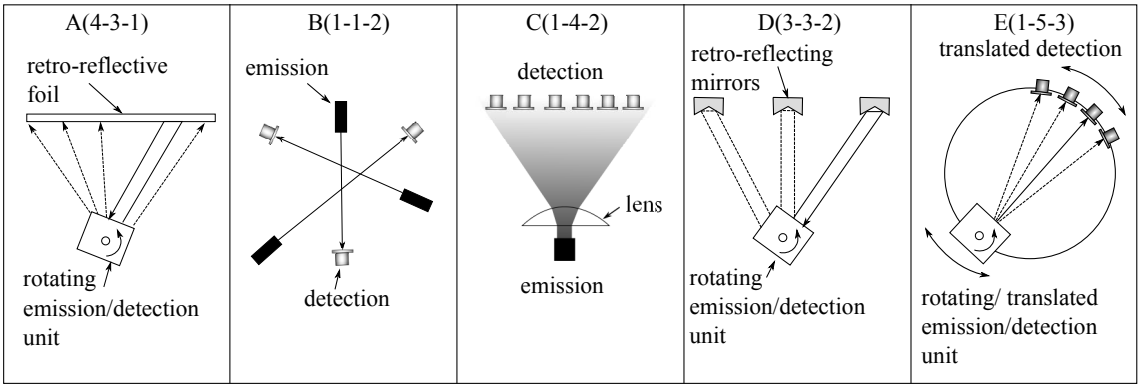

Figure 3.2 Some examples for concepts

mirror (solution 2) or to retro-reflect the beam in some way. The latter can be realized for example by a corner-cube mirror, so the retro-reflection takes place in only a single point (solution 3) or by a retro-reflecting surface (solution 4) given e.g. for retro-reflecting foils. The laser beam can also be reflected diffusely by an arbitrary surface (solution 5).
The second product function that is contemplated is here shortly called "beam multiplication". There are several options how the number of beams can be increased from one to more paths. The first solution, here called "static", is to use many static sources of emission. A rise in beam paths is identical to a rise in instrumentation effort here. The number of beam paths may also be multiplied if the incoming beam is widened with a lens, so that a lens sheet is positioned over the measurement object (solution 4). All other solutions presented in figure 3.1 are based on sequential beam multiplication by some kind of movement of the emitting source.
The third product function, here denoted by "opposed side multiplication" determines how the components that are opposed to the emitting side are multiplied. These components may either serve as reflecting elements or as detectors. One way is to use a surface element instead of many single-point elements (solution 1). Like for the emitting side, it is also possible to use several static single-point objects (solution 2). Another option would be to multiply the points of detection or reflection by a translation of the opposed side element (solution 3).
Not all principle partial solutions are compatible with each other. During the conception process the sensible combinations have to be collected. A small selection of principle solutions is represented by the letters A-E. Their conceptual design is depicted in figure 3.2. For concept A, emission and detection of light take place on the same side of the measurement area. Multiple beam paths are created by rotating the emitting element. At the opposite side of the measurement area, the light is retro-reflected by a cheap foil strip along a continuous surface. Such foils are usually used for traffic or security purposes. Concept B consists of several static pairs of emitting and detection elements. Another possibility is to form a laser sheet by a lens and to detect the light with an detector array on the opposed side (concept C). Like for case A, the emission and detection are located on the same side and the beam is rotated across the field for concept D. Retro-reflection is realized here by corner-cube mirrors, so the reflection takes place at only a few points instead of at a continuous area. Concept E consists of opposed emitting and detecting sides that are translated along a circular path in a certain angular range. At each point,

	Object size	Cost	Speed	Signal quality	Tomographic arrangement	Transport	Alignment
A	++	++	∘	−	∘	++	++
B	+	−−	++	++	∘	−−	−−
C	−−	−	++	++	−	−	−
D	++	−	∘	+	−	−	++
E	∘	−	−−	++	++	−−	∘

Table 3.1 Evaluation of the concept solutions

the beam is rotated such that it moves along the opposite detector array. This is the typical concept for medical applications.
Solutions have to be assessed regarding various criteria. Some representative characteristics are the size of the object that can possibly be measured, the instrument cost, measurement speed, the expected laser signal quality, the transportability and alignment properties. Furthermore, some concepts allow for more convenient arrangement of the beam paths from a tomographic point of view. With numerically simulated experiments, different beam arrangements were tested. In this work, only the results are presented.
An evaluation of the principle concepts is given in table 3.1. It is essential that the measurement object can be imaged completely. Concepts that do not fulfil this requirement are directly excluded. Solutions A and D allow for very large measurement objects. Because retro-reflection makes adjustment mostly unnecessary, large distances between the opposite sides are feasible. A similar situation is given for solution B, but here the maximum distance is bounded by alignment of the detectors, which may become impossible if distances are very large. With concept E, medium-sized objects can be examined. The dimensions are determined by the mechanical device for translation, which could be a rail or similar. Concept C allows for experiments with only very small measurement objects. The coverage of the measurement area is determined by the lens size and thus very limited. Therefore, concept C was excluded right from the beginning.
If the aspect of cost is considered, concept A is the cheapest solution. The retro-reflecting foil strips are very cheap. All other instruments are more expensive because more mirrors, detectors or even laser light sources are necessary.
Regarding measurement speed it has to be said that the fastest concepts are those where the imaging rate of the complete area equals the tuning rate of the laser. This is the case only for static systems like those described by concept B and C. A slower imaging rate is achieved with systems where the laser beam is rotated, like it happens with concepts A and D. The exact duration of one measurement of course depends on whether rotation takes place continuously or step-wise and how fast it is rotated in general. Even longer measurement times are necessary if the beam is not only rotated but also translated, which is the case for solution E. Here the time for rotation is multiplied by the number of positions where the emitting side is translated to. Such systems are known from medical applications like CT scanners or similar [11]. Here the imaging time may be in the order of several minutes. These time-scales are completely inappropriate for the soil physics experiment, for this reason concept E has to be excluded also.
Concerning signal quality of the detected light, mono-static systems like in concepts B,C

and E are expected to work best, because no losses are expected at reflecting elements and incoming intensity is not spread over a light sheet. Moreover, there are few surfaces that can lead to so-called "fringes". The latter are optical disturbances caused by interferences between multiply reflected beams. In contrast to this, systems where the laser beam is reflected by mirrors (e.g. concept D) will show small losses in intensity due to imperfect reflectivity. Additionally, it is more likely that parallel surfaces occur that lead to fringes. Concept A, which is based on foil retro-reflection, shows the lowest reflectivity and therefore the weakest light signal in comparison to the other partial solutions. Moreover, during continuous rotation of the laser beam, reflectivity may alter because the beam moves on the foil which does not have homogeneous reflective properties. Generally TDLAS does not require constant light intensities, but if reflectivity changes too much it can be problematic to evaluate correct concentrations. This effect is explained in detail in chapter 3.4.
A further criterion is here called "tomographic arrangement". This was introduced because some beam set-ups are more convenient for tomographic reconstructions than others. Generally, fan-beam arrangements offer less freedom to position the measurement paths than systems where beams can be arranged arbitrarily. Since beams in a fan-beam that are angularly very close to each other deliver very similar information, increasing the number of beams to a vast extent does not yield the same information that would be achieved if those beams could be positioned arbitrarily. However, economic considerations also play a role. Even though theoretically concept B gives the designer a lot of opportunities to arrange the beams such that projections are sampled from many angles, in practice cost is limiting the amount of paths severely. In this case, arrangements based on concept B are mediocre regarding aptness for tomography. In principle, fan-beam arrangements with static rotation points like concept A, C and D are more unfavourable. However concepts A and C offer very many beams in one fan, so that many more measurement paths are available than for case B. This may outweigh the drawback of fan-beam arrangement of systems A and C in contrast to B. Of all the presented concepts, case E provides the most suitable arrangement of beams regarding tomographic reconstructions. Complete projections can be taken from a large set of positions on the circular rail, so that Radon space can be sampled very thoroughly.
When selecting the best concept, not all criteria have the same weight. For example, the possible measurement object size and measurement speed are premises that are essential. The suitability of tomographic arrangement of some concepts may be very good, but if cost exceeds the budget they have to be neglected. For this reason, concept A was chosen for the described application in permafrost science. Note that for other applications, different concepts might be the best choice.
In a further step, the chosen concept was elaborated and components were selected. First of all, the method of rotating the laser beam had to be determined. This is often done by deflecting the beam with a mirror. Examples are galvanometric scanners, piezoelectric scanners and many more [64]. Even solutions without mirrors as deflecting elements exist, like for example acousto-optic scanners. A polygonal scanner was chosen because it offers wide scanning angles at very high speed. It is continuously rotated by a stepper motor. The latter was selected because of its holding torque and because it can run to pre-set positions very accurately. In practice, after a measurement the beam may be steered

back to its initial position and rest there until the next measurement is started. This is especially helpful because no absolute position of the beams are recorded, only relative ones. The beam has to be set to a starting angle for every measurement. Further details about the positioning of the laser beam are given in chapter 3.2.1.
A retro-reflective micro-prismatic foil that is originally designed for safety light barriers is used because it showed the best reflectivity for larger distances [65].
Tomographic reconstructions with only one fan-beam are not possible, as has been tested with simulated experiments. According to Natterer [48], with one fan-beam frequencies that have spatial periods twice larger than the measurement field can be resolved by one fan-beam projection, as can easily be calculated with equation 2.25. Instead, several fan-beams have to be combined. Again, cost plays a major role. When determining the number of fan-beams, a compromise between material as well as data acquisition effort and possible quality of the tomographic reconstructions has to be found. Each unit requires a laser light source, a stepper motor and polygon mirror for scanning, some more optic elements described in chapter 3.2.1, a detector and data acquisition channels for recording the TDLAS signal and the beam position. Additionally, effort for data processing, evaluation and storage increases with the number of scanning units. As a compromise, a set-up with four scanning units was designed. The choice of the set-up was preceded by preliminary numerical studies, where arrangements with four scanning units delivered satisfying results. The advantage of limiting the number of fan-beams to four is that only one laser is required. Laser light is split up with a beam splitter. Incoming light intensities are still decent afterwards for many beam angles. This aspect is discussed in more detail in chapter 3.4. Furthermore, high-speed data acquisition boards are necessary, which is illustrated in chapter 3.2.2. The required boards each have two DAQ channels. If four scanners are used, only two of them are necessary.
The elaboration of the final concept is presented in chapter 3.2.

3.2 Instrument setup

This chapter deals with the technical elaboration of the conceptual instrument. The exact optomechanical set-up is presented in chapter 3.2.1. It is explained how the laser beam is scanned by the polygonal mirror and how emission and detection of the laser light take place in one scanning unit. Furthermore, the positioning of the scanning units around the measurement field is discussed. A description of the used hardware and the data-acquisition process is given in chapter 3.2.2.

3.2.1 Optomechanical setup

The four scanning units are positioned at the edges of a square measurement field, each scanning the laser beam over an angular range of 144°. Along the rest of the edges that is not blocked by the scanning units, a 0.8 m × 0.8 m frame is positioned that is covered with adhesive retro-reflective foil. A principle image of the instrument is shown in figure 3.3. The light emitted by a fibre-coupled diode laser is split into four parts with a fibre beam-splitter that leads equal intensities of light to each of the four scanning units. The latter are positioned irregularly around the field. The exact positioning was

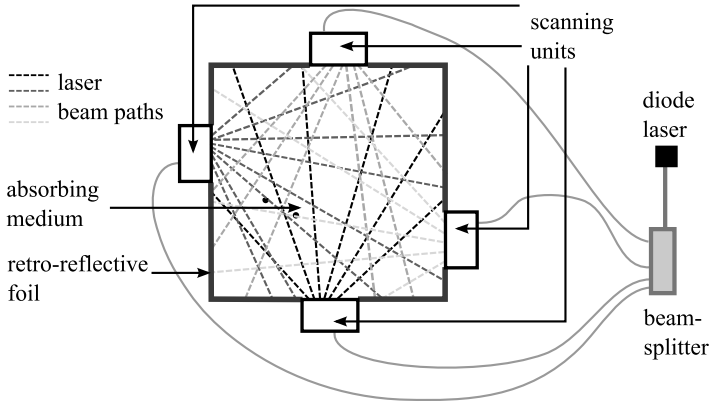

Figure 3.3 Arrangement of the four scanning units around the field and schematic drawing of the laser beam paths

a heuristic process, that is, different solutions were guessed and analysed regarding their tomographic suitability with virtual experiments. In the literature, other methods of optimizing the beam layout are found. Terzija [52] assess heuristically found set-ups by their distribution over Radon space. That means, the coordinates ξ and θ of all beams are collected and then the angles θ are plotted against the linear variable ξ. The geometric definitions of those variables can be looked up in figure 2.2. For a complete sampling of the measurement object, Radon space would have to be filled completely with data points. Terzija suggest that the more the beam data points are spread in Radon space, the closer the arrangement is to complete sampling. A practical example is shown in figure 3.4. Here, the ξ and θ values of two different beam arrangements are plotted in Radon space. If the beams are arranged arbitrarily in the measurement field, they may have all kinds of angles and distances to the center, leading to widely spread data points in Radon space. Fan-beam set-ups are always somewhat limited in their beam-arrangement and therefore lead to more restricted distributions in Radon space. Note that the shown examples have the same amount of measurement paths. The presented fan-beam set-up depicts the final solution that was used for virtual experiments and real measurements.
A systematic approach of optimizing the beam layout is given by Twynstra et al. [66]. It is valid at first instance if the concentration field is reconstructed with Tikhonov regularization. Beam arrangements are assessed by means of mathematical properties of the

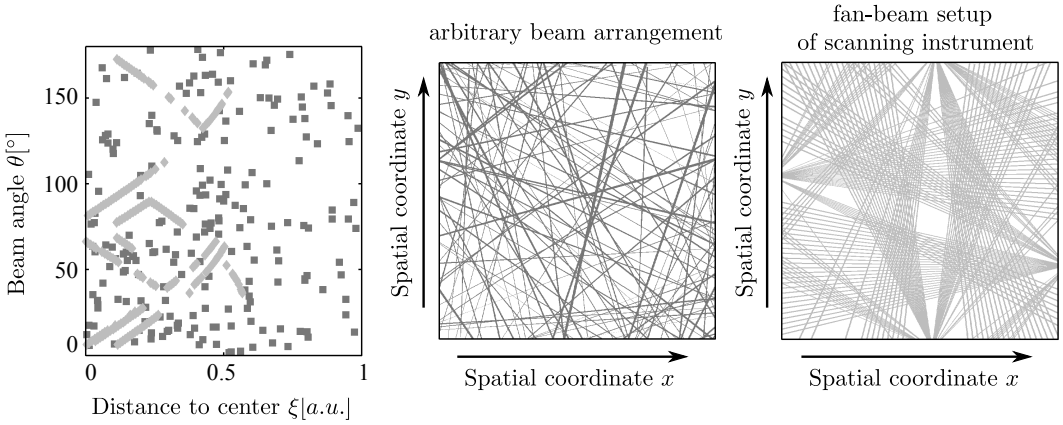

Figure 3.4 Two beam arrangements (one with arbitrary beam positions and one with fan-beam set-up) and their representation in Radon space. In both cases, the same amount of beams is used.

so-called *resolution matrix*, which is derived from the regularized inverse $W^\sharp$ of Tikhonov algorithm. An explicit solution $\hat{f}$ of the regularized term $\left\|W \cdot \vec{f}\right\|^2 + \left\|\mathcal{L}\vec{f}\right\|^2$ is given by

$$\hat{f} = (W^T W + \tau^2 \mathcal{L}^T \mathcal{L})^{-1} \cdot W^T \cdot \vec{c} \tag{3.1}$$

The regularized inverse $W^\sharp$ is thus expressed by

$$W^\sharp = (W^T W + \tau^2 \mathcal{L}^T \mathcal{L})^{-1} \cdot W^T \tag{3.2}$$

such that $\vec{f_\tau} = W^\sharp \cdot \vec{c}$. In reality the measurement vector $\vec{c}$ is corrupted by noise, so that $\vec{c}_{meas.} = \vec{c} + \vec{n}$, where $\vec{c}_{meas.}$ are the measured concentrations and $\vec{n}$ is an additive noise vector. The reconstructed concentrations therefore take the form

$$\vec{f_\tau} = W^\sharp \cdot (W \cdot \vec{f} + \vec{n}) = \underbrace{W^\sharp W \cdot \vec{f}}_{R} + W^\sharp \cdot \vec{n} \tag{3.3}$$

where $R = W^\sharp W$ is called *resolution matrix*. Note that this matrix only depends on the layout of the beams. The reconstruction error $\delta\vec{f}$ is then calculated by

$$\delta\vec{f} = \vec{f_\tau} - \vec{f} = \underbrace{(R - \mathbf{I}) \cdot \vec{f}}_{regularization\ error} + \underbrace{W^\sharp \cdot \vec{n}}_{perturbation\ error} \tag{3.4}$$

It is split into a part that results from measurement noise, the perturbation error, and the regularization error. According to Twynstra et al. [66] the latter dominates in rank-deficient cases. In an ideal experiment, the resolution matrix would equal the identity matrix, setting regularization error to zero. However, this is impossible for rank-deficient systems. The strategy is now to find a beam-arrangement Ψ that minimizes the Frobenius distance between R and the identity matrix. The optimal beam-layout Ψ^* is then given by

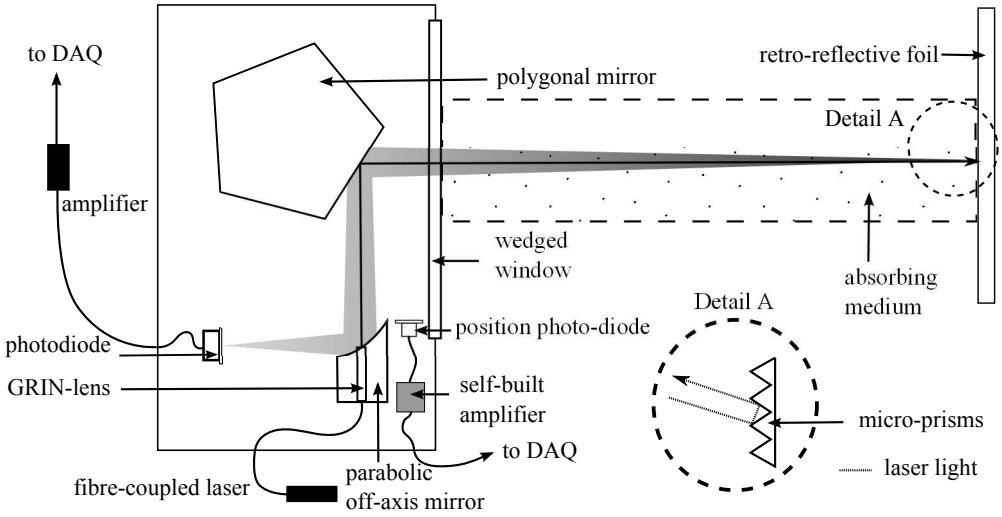

Figure 3.5 Schematic drawing of one spectrometer scanning unit

$$\Psi^* = \arg\min_{\Psi}[\|R(\Psi) - \mathbf{I}\|_F^2] \tag{3.5}$$

For the developed instrument, there are four free parameters for arranging the beam-layout, which are the lateral positions of the scanner units along the edges of the field. Optimization of Ψ was implemented but ran into local minima, as the results depended completely on the starting points. The resulting beam configurations that were detained from the local minima of the objective function led to much worse results in virtual experiments than the heuristically determined layout. Therefore the latter was preferred as a final solution. It is possible however that an even improved configuration can be received if a global minimum of the objective function is found.
For a thorough understanding of the beam propagation, a scanning unit and its laser beam are schematically illustrated for a fixed polygon position in figure 3.5. To the left, the scanning unit is depicted which can be flushed with non-absorbing gas either from a gas bottle or a dry cartridge. By this means it can be made sure that no absorption takes place outside of the measurement field. All fibre and cable bushings are realized with sealed connectors. Light from a fibre-coupled DFB laser is collimated by a GRIN-lens (gradient index lens) which has only 1 mm diameter and is positioned in a hole that is drilled into the center of an off-axis parabolic mirror. The beam is directed onto a polygonal mirror, then leaves the scanning unit through a window and enters the absorbing medium. The window is wedged to avoid multiple reflections that can lead to interferences and can deteriorate the absorption signal. After passing the absorbing medium, the light is retro-reflected by the foil. Detail A illustrates the retro-reflection mechanism of the foil. Under a protective PTFE layer, micro-prisms are engraved into a substrate that deflect the incoming beam into the original direction. As it was shown in [65],the foil reflects up to 60% of the incident light and shows good performance even for small angles of light incidence. The reflective properties alter along the lateral position on the foil strip. In principle, TDLAS does not depend on constant light intensities, so no constant reflectivity is required. The effects that appear when the beam moves on the foil during

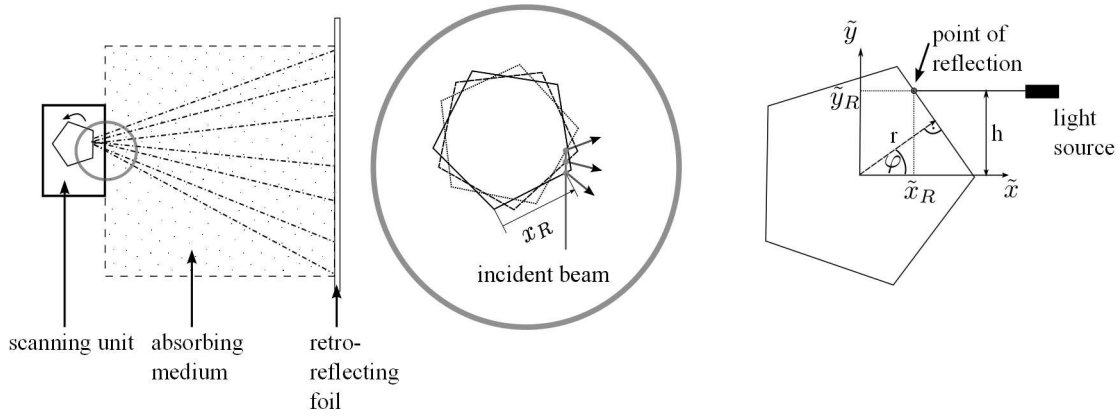

Figure 3.6 Left: Propagation of the laser beam during polygon rotation, right: movement of the reflecting point on the facet

one wavelength-tuning of the laser are described in chapter 3.4. After reflection, the light passes the absorbing medium again and re-enters the scanning unit. It propagates from the window to the polygonal mirror and is guided to the parabolic off-axis mirror. Due to imperfect collimation and diffraction effects caused by the micro-prisms, the laser beam is broadened so that part of the light falls next to the GRIN-lens onto the reflecting part of the off-axis mirror. The latter focusses the light onto a photo-diode that produces a photo-current that is proportional to intensity. The photo current is amplified by a high-end, very low-noise trans-impedance amplifier outside the scanning unit. The outgoing voltage signal is acquired by the data acquisition system that is presented in detail in chapter 3.2.2.
A second photo-diode is placed next to the off-axis parabolic mirror. Its purpose is to set the laser beam to a starting-position once before measuring. A beam at the very edge of the fan is used for this: when the detected light intensity is at its maximum, the beam is situated at the starting position. During the measurement, the relative position of the stepper motor is recorded, which can be read in detail in chapter 3.2.2. As long as the motor voltage is not turned off, the position is known and the starting angle does not have to be found by the photo-diode. A small and simple, self-constructed trans-impedance amplifier for transforming photo-currents to voltages was positioned inside the scanning unit. A more detailed description can be found in appendix A.1.
When the polygon rotates, the laser beam is moved angularly across the measurement field (view fig. 3.6). A rotation of the polygon by the angle φ causes a beam angle change by 2φ. Therefore, for a complete cycle the beam moves by 720° that are evenly distributed throughout the facets. The chosen polygon has five facets, so the overall scanning angle of the fan amounts 144°. During rotation, the point of reflection moves, which can be seen in the center part of fig. 3.6. The reflecting point moves along a line and the distance x_R to the facet edge changes. If a coordinate system is laid into the center of the rotating

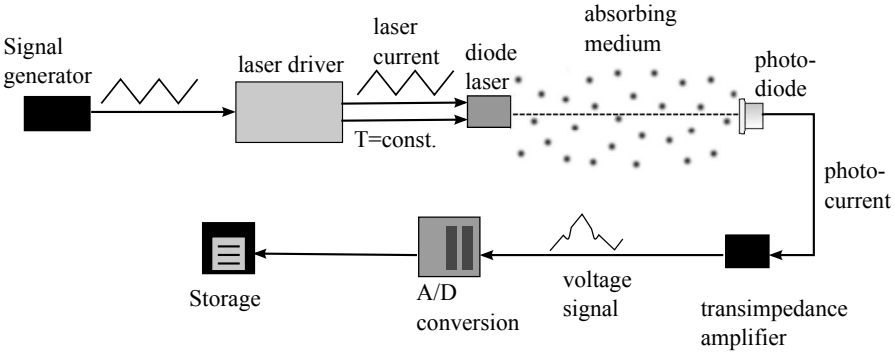

Figure 3.7 Single channel signal generation and acquisition

polygon, the coordinates of the point of reflection $(\tilde{x}_R, \tilde{y}_R)$ can be expressed as

$$\tilde{x}_R = r \cdot \cos\varphi - (h - r \cdot \sin\varphi) \cdot \tan\varphi \tag{3.6}$$

$$\tilde{y}_R = h \tag{3.7}$$

where r is the radius of the inner circle of the polygon, φ is the polygon rotation angle and h is the translated distance of the light source from the rotation center (view fig. 3.6, right part). When modelling the beam propagation for virtual and real experiments, a simplified version of the beam propagation is assumed due to calculation time issues. The beams are modelled to rotate around a fixed point, which leads to small deviations of the beam positions in the model. The error on the start position of the beam may amount up to 6.5% of the measurement field side length. Further explications regarding this topic can be found in appendix B.

3.2.2 Hardware and Data Acquisition

For tomographic reconstructions, for each measurement path the mean concentration and the beam propagation in the measurement field are required. The path average concentrations are delivered by TDLAS measurements, that demand knowledge of wavelength-dependent optical density, temperature, pressure and absorption path length. The former is gained by detecting the intensity of the laser light after it passes the absorbing medium. Details can be read in chapter 2.1.3. The absorption path length can be geometrically derived if the propagation of the beam is known, which is also needed for the tomographic reconstruction. In practice the angular position of the beam is measured and during post-processing the geometrical assignments of length and propagation take place.
This chapter deals with the acquisition of the required signals and the necessary hardware. First of all it is focussed onto the measurement of the mean path concentrations. The principle progress of signals for TDLAS evaluation is depicted for a single measurement channel in figure 3.7. A signal generator delivers a periodically tuned voltage to a laser driver, in our case a symmetric sawtooth profile. The laser driver controls the constant temperature of the diode laser for a rough determination of the wavelength and provides

a laser current that is proportional to the signal generator voltage. By modulating the laser current, its wavelength and, as a side-effect, its light intensity are periodically tuned. The temporally tuned laser light crosses the measurement medium, where it is partially absorbed. Moreover, broadband transmission losses and background emission of light may take place. The remaining light falls onto photo-diode at the opposite side of the measurement path. In the photo-diode, a photo-current that is proportional to incident light is produced. A voltage that is proportional to the photo-current is created by a trans-impedance amplifier (view appendix A.1). Since high gains of more than 10^2 V/A are usual when measuring diode laser photo-currents, an excellent noise suppression is necessary. For this reason, high-end amplifiers manufactured by FEMTO were used. The voltage is digitized by an A/D-converter and stored on a PC hard-drive.
Each wavelength tune should be sampled around 500 times on the rising branch, so a complete symmetric sawtooth should contain 1000 samples. The wavelength tuning frequency amounted more than 5 kHZ and is planned to be raised in future experiments to more than 10 kHz. Therefore, two high-speed PXI sampling boards were selected that acquired 10 MS/s on two channels, each. Such a very fast DAQ rate requires advanced techniques of data storing. The high speed DAQ boards are situated in a separate rack and it has to be made sure that the measurement data can be read out and stored in time without data loss. This was realized by a self-implemented LabView software based on queues which enable continuous data storage at the given sampling rate. The pressure and position signals were acquired at 129 kS/s with a shared PCI board and temperature was sampled with 100S/s with another PCI board to avoid influence of the pressure and position voltages on the very low thermo-voltage.
Furthermore, a new method of acquiring the transmitted intensity had to be developed. Usually, each wavelength-scan measurement is triggered by the signal generator, so that the start point of the sawtooth is known. However during the required continuous measurement of the light intensity, missed triggers impeded the common approach. Alternatively all channels could be triggered once in the beginning, and then the start-points of the wavelength scan could be determined by a mapping of the time-base to wave-length space. Unfortunately, very small inaccuracies of the time-base lead to large shifts of the determined wavelength-scan starting points. This is why another method of data acquisition had to be introduced. The continuous measurement of all signal channels was triggered once in the beginning. For a very accurate determination of the wavelength-tune start point, a short pulse was superimposed onto the detected voltage signal by a simple electrical circuit. It was created by a pulse generator such that the pulse occurred at the same time as the falling edge of the signal generator trigger. By this means it is made sure that the pulse does not interfere with the absorption signal on the rising branch of the wavelength-tune. Each laser tuning scan can thus be separated reliably by pulse detection during post-processing.
Pressure and temperature are assumed to be uniform over the field, as is justified in soil science applications. They were recorded with a barometric capacitive sensor and a thermocouple at the edge of the measurement field.
The relative position of the laser beam is recorded by means of a TTL signal that is sent by the stepper motor 1000 times per revolution. Counter DAQ boards offer a useful opportunity to count either the falling or rising edges of the TTL signal. However, the

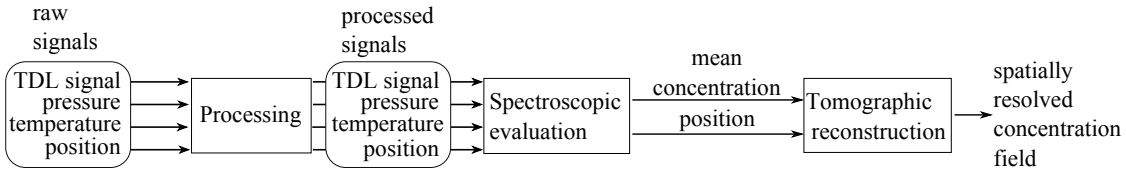

Figure 3.8 Schematic depiction of the data progress for tomographic TDLAS measurements

given board provided no time-base so that no temporal assignment of the counts was possible. Therefore, the analogue voltage of the TTL signal was detected and position was calculated by a software counter during post-processing (view chapter 3.3).

3.3 Processing and Evaluation

The recorded raw signals cannot be used directly for the tomographic reconstruction of the concentration field but have to go through several steps of processing and evaluation first. As temperature and pressure in the measurement area are constant for the soil physics application, it is possible to evaluate path mean concentrations first and in combination with known beam propagation the tomographic reconstruction follows. The process of data processing and evaluation is schematically illustrated in figure 3.8. First, the raw data needs to be processed to a form that can be evaluated by the spectroscopic software. At each measurement point, the voltage of a single wavelength-tune and the according pressure sensor voltage, temperature signal and position are required separately. Afterwards, the mean concentrations at each position are calculated by a spectroscopic in-house LabView software. The information about the beam positions and the average concentrations serve as an input for the tomographic reconstruction, which finally delivers a 2D concentration image.
The principle method of processing is depicted in figure 3.9. The voltage of the detected light has to be split such that each wavelength tune is separated from its predecessors and successors. Therefore, the signal is cut where the pulse on the falling branch of the sawtooth is superimposed. The according time-stamp of the wavelength-tune is assigned at each measured point to make allocation of the other signals possible. The pressure sensor voltage is converted to a pressure value by a linear function. Edge detection of the TTL-signal is necessary for determination of the relative beam position. Therefore, a software implemented edge counter is used, and the increasing counts are converted to an angular position. Afterwards an allocation of the absorption signal, the angular beam position, temperature and pressure at the related position takes place from the different time bases. In a separate processing step, measurement points where no reflection takes place can be discarded. If the maximum voltage of the absorption signal falls below a certain threshold, the measurement points can be deleted. If desired, phase-averaging over a specified number of field scans can be carried out subsequently.
The spectroscopic evaluation is in principle elucidated in chapter 3.4, where measurements of a uniform H_2O concentration field with the scanning instrument are presented. Tomographic reconstructions of virtual and real experiments are shown in chapters 4 and 5, respectively.

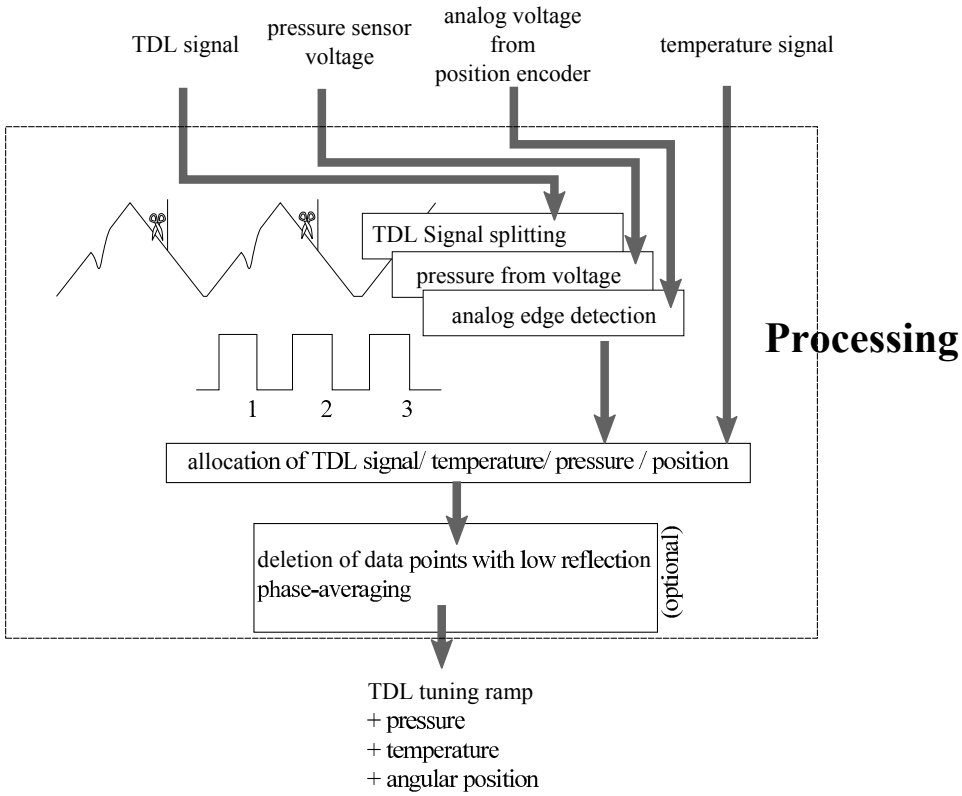

Figure 3.9 Schematic overview of the processing procedure

3.4 TDLAS path-averaged validation measurements

The strategy for tomographic reconstruction of concentration fields with homogeneous temperature and pressure distribution is to measure first the path averaged concentrations and then to reconstruct the concentration image. Therefore, it has to be made sure that absolute concentration measurements are possible with the presented instrument. In the following chapter, it is examined how the scanning movement of the beam in combination with reflecting foil influences the performance of the TDLAS measurement of the average beam concentration. Therefore, a measurement of a uniform H_2O- distribution was realized and compared to a reference measurement. The latter took place with a static instrument with 700 mm absorption path length that is illustrated in figure 3.10. The laser light is collimated by a fibre-coupled collimator and directed straight onto an opposed photo-diode. Its photo-current is amplified to a voltage by an trans-impedance amplifier, which is then recorded similar to the scanning channels. All TDLAS signals were evaluated with a LabView spectrometer software developed in the group.
A DFB laser emitting at 1370 nm was tuned over the 211←110 absorption line of H_2O at 7299.43 cm^{-1} [2, 10] with 5039.8 Hz, whereas the wavelength tuning range amounted approximately 1 cm^{-1}.
As it was expected, different maximum intensities of the TDLAS signal were observed, depending on the angular position of the beam because of different incident angles onto the foil. Figure 3.11 shows various voltages of differently located beams that were recorded

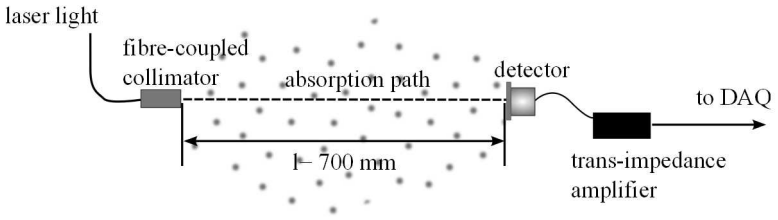

Figure 3.10 Schematic setup of the spectrometer used for the reference measurement of the H_2O-concentration

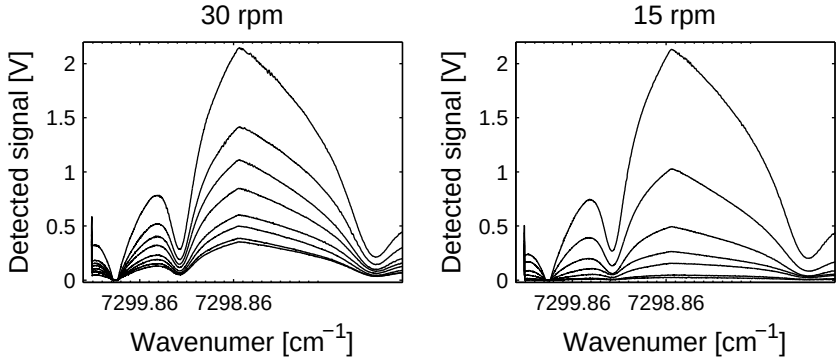

Figure 3.11 Wavelength tunes recorded at two polygon rotation speeds are depicted. Depending on the beam position, the voltage of the detected transmitted light signals varied.

at two rotation speeds of the polygon. A large range of signal intensities is witnessed, which can lead to a limitation of digitization efficiency because the amplification of the photo-diode current is constant. The rotation speed of the polygon does not influence the absolute range of intensities. The limiting factor of rotation speed is the distortion of the sawtooth-profile up-ramp that appears if the beam moves too much along the foil during one wavelength-tune. Some typical TDLAS signals measured with a laser tuning rate of 5039.8 Hz at different polygon rotation rates are presented in figure 3.12. Field measurement rates from 1.25 Hz up to 20 Hz were realized by polygon rotation speeds between 15 rpm and 240 rpm as well as a static measurement. Up to 2.5 Hz, the reflectivity changes that occur during one wavelength-tune are tolerable. If the field measurement rate amounts 5 Hz, first measurement points appear where the wavelength-tune is distorted in a way that no sensible base-line can be fit any more, for example for the two examples on the right. This effect reinforces if the polygon rotates even faster. Evidently the maximum rotation speed depends on the laser tuning rate and the measurement field size. This can be explained if a more systematic view of the problem is taken. The up-ramp of the laser tune is increasingly distorted if the beam moves too far on the foil during one wavelength-tune and therefore reflectivity oscillates to strong. The distance the beam moves on the foil during one tune depends on the laser tuning rate, the polygon rotation speed and the distance of the foil from the center of rotation. Assume that the laser beam moves around a fixed point by the angle α_{tune} during one wavelength-tune. Figure 3.13 schematically illustrates the according beam movement. During the wave-

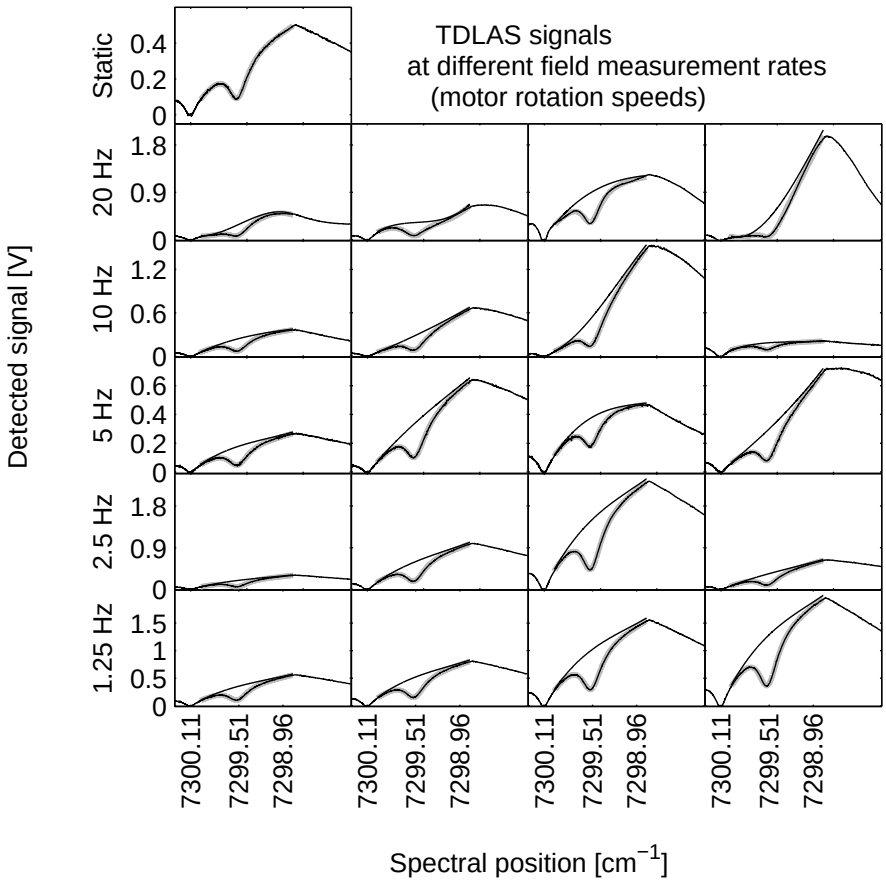

Figure 3.12 Examples of TDLAS signals detected during scanner movement with different motor rotation speeds. Field measurement rates were varied from 1.25 Hz to 20 Hz while the laser tuning rate amounted 5039.8 Hz. The top plot shows a static measurement with the scanning instrument for comparison.

length tune, the beam moves from point B to point C on the foil. If $\overline{AB} \approx \overline{AC}$, then the covered distance of the beam is $\overline{BC} \approx 2 \cdot \overline{AB} \cdot \sin(\alpha_{tune}/2)$. With a rising distance $\overline{BC}$, the up-ramps of the sawtooth-signal are distorted more and more. Consequently, the faster the polygon is rotated, the more often a critical value $\overline{BC}_{max}$,which denotes the largest tolerable beam movement, is exceeded. This critical value $\overline{BC}_{max}$ can be derived by the maximum acceptable field measurement rate of 2.5 Hz at 5039.8 Hz for the 0.8 m

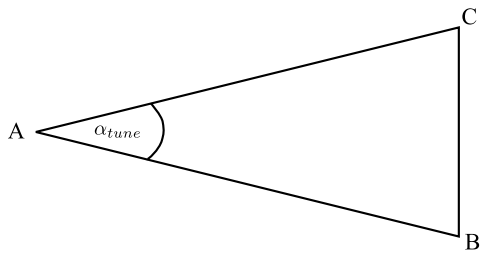

Figure 3.13 Schematic depiction of the beam movement during one wavelength-scan

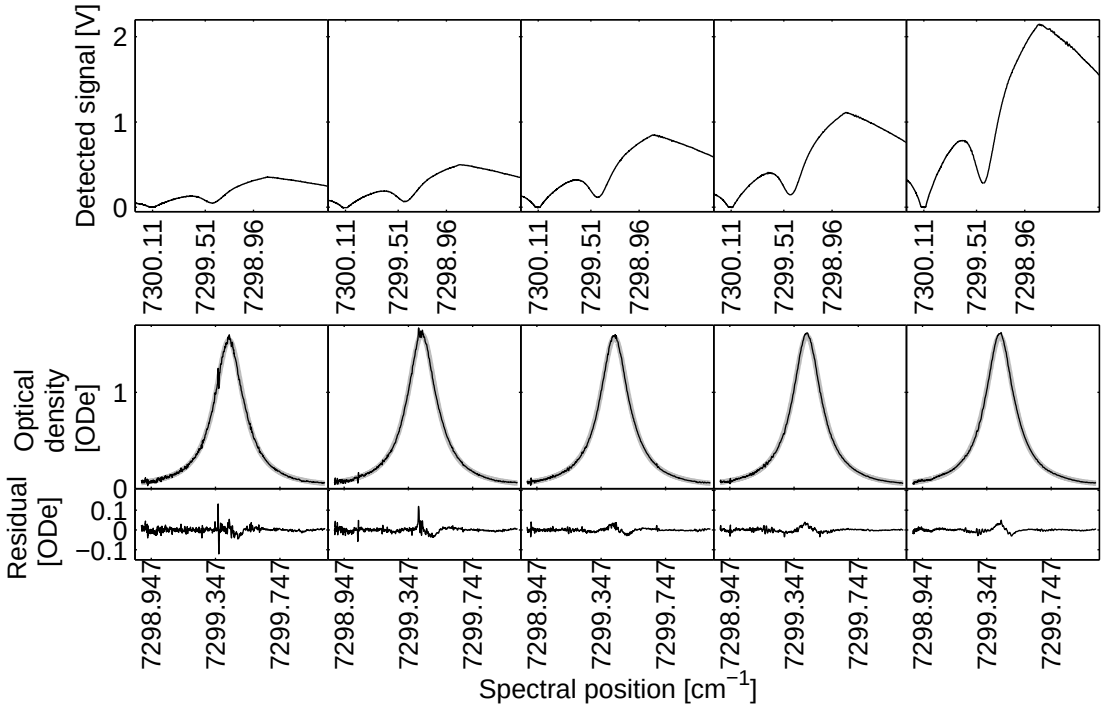

Figure 3.14 Exemplary signals for different reflectivity of the micro-prismatic foil. On top, the detected wavelength tune is shown. Beneath are the fitted (grey) and measured (black) optical densities derived from the acquired signal. At the bottom, the residuals between measured and fitted optical densities are plotted.

$\times$ 0.8 m measurement area. During one wavelength tune, the beam is rotated by about 0.0114°. The longest distance between the point of rotation and the foil appears at a diagonal beam and amounts approximately 1.22 m. The maximum possible covered distance is calculated to $\overline{BC}_{max} \approx$0.25 mm. With this number, rotation speed, laser tuning rate and measurement field size can be attuned to each other for different applications. The micro-prisms have a size in the order of magnitude of 50 mum, so that during one wavelength tune about five prisms are crossed.
Measurements of the uniform H_2O-concentration field were carried out at polygon rotation speeds of 15 rpm and 30 rpm, leading to 1.25 Hz and 2.5 Hz field measurement rate, respectively. As already shown in figure 3.11, the absolute intensity of the detected light alters with the position of the beam. This effects the quality of the spectroscopic concentration evaluation. Some examples of wavelength-tunes with different intensities and their respective measured and fit optical densities are demonstrated in figure 3.14 Furthermore, the residual between the measured and fit optical density is shown. Polygon rotation speed amounted 15 rpm. As a quick reminder: the optical density is defined by $OD_e = -\ln\left(\frac{I(n,\lambda)-E}{I_0(n,\lambda)\cdot Tr(\lambda)}\right)$, where I is the detected intensity of light, I_0 is the intensity of the incident light, E is the broadband background radiation and $Tr(\lambda)$ are transmission losses. Measurements with very similar absorption path lengths were selected so that for better comparison the optical densities are nearly equal. All signals are corrupted by noise that is caused by parasitic electromagnetic radiation from the stepper motors that

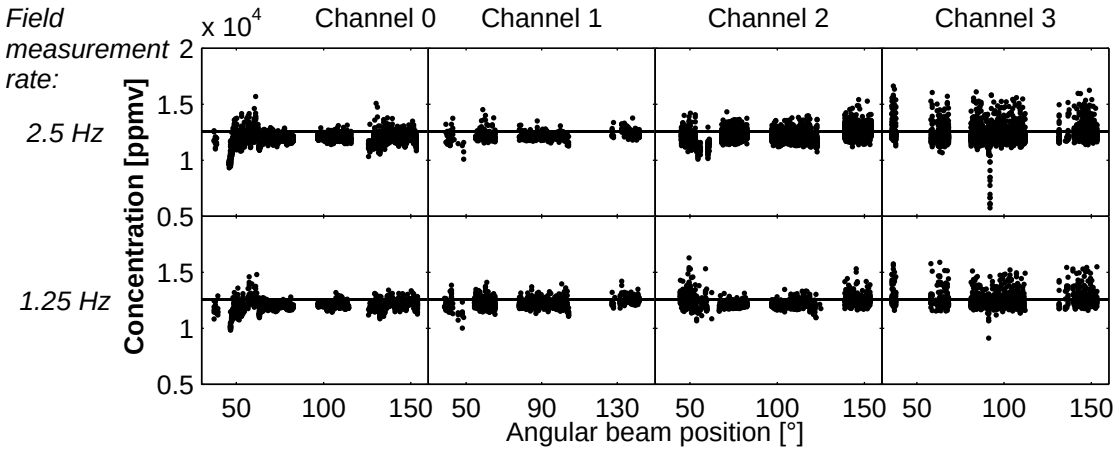

Figure 3.15 H_2O - concentrations measured at two different rotation speeds for all four laser scanners. The solid line shows the concentration measured with the reference channel (12548 ppmv).

interferes with the photo-current from the detector. As the irradiation takes place before signal amplification, the ratio between the photo-current and the electric noise is of very high importance since noise is amplified by the same amount as the signal. Therefore, irradiation has to be kept as low as possible in the first place by good electromagnetic shielding. This was realized with a grounded steel tube that was positioned around the detector, but there is still room for improvement. At low light intensities, the electric noise dominates the residual between measured and fit optical density. At higher light intensities, the influence of electric noise sinks and discrepancies between the approximated Voigt function and the real line-shape gain more weight.

The H_2O-concentrations measured at 15 rpm and 30 rpm polygon rotation speed are plotted over the angular beam position in figure 3.15 for all four scanning channels. The concentration that was measured with the reference channel amounted 12548 ppmv and is plotted as a solid line for comparison. The mean concentrations while scanning amounted 12034 ppmv for 2.5 Hz field measurement rate and 12099 ppmv for 1.25 Hz field measurement rate, which corresponds to systematic underestimations of 4.1% and 3.6%, respectively. Standard deviations while scanning with 30 rpm lay between 389.4 ppmv and 752 ppmv for the different channels, which equals 3.1% and accordingly 6% of the absolute mean concentrations measured at each channel. The large value of 752 ppmv standard deviation is due to some outliers that appear at a fixed angular position at channel 3. Here, multiple reflections at an opposed window led to large errors in the concentration evaluation. Measurements at this angle should be discarded in real applications. If the regarding false measurements are neglected, the standard deviation amounts 559 ppmv. Accordingly, the standard deviations while measuring with 1.25 Hz field measurement rate lay between 379.1 ppmv and 684.7 ppmv, corresponding to 3% and 5.5% of the absolute concentrations. Again, the high value of 5.5% is due to multiple reflection at the same beam path as at the previous experiment. If the false measurements (where reflections take place) are neglected, the standard deviation of channel 3 amounts 432 ppmv, according to 3.5% of the absolute concentration.

Signal quality is not equally good at all beam positions. A spectroscopic signal to noise is

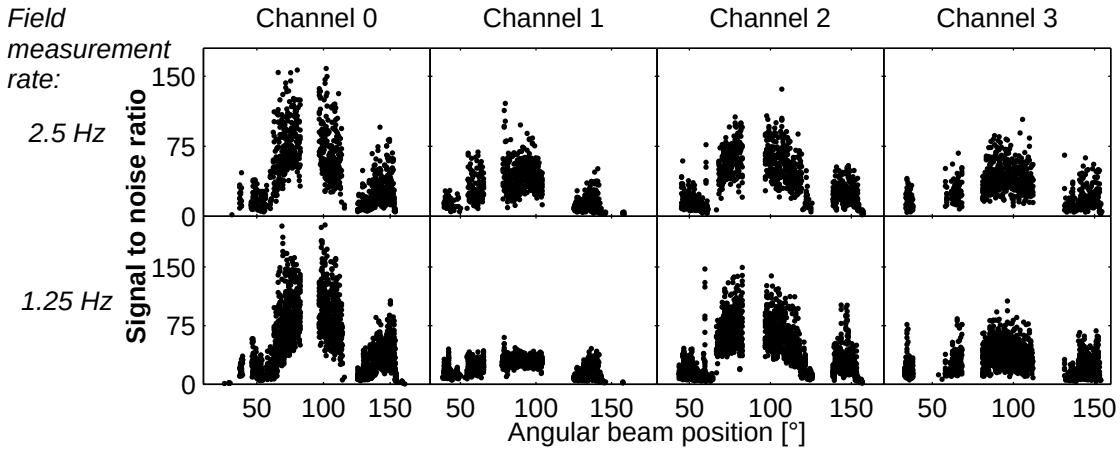

Figure 3.16 SNR of all channels at two different rotation speeds

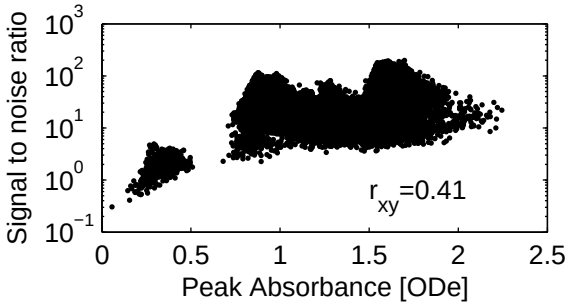

Figure 3.17 SNR depending on the peak absorbance

defined by the relationship between maximum optical density and the standard deviation of the residual between fit and measured optical density:

$$SNR = \frac{OD_{e,max}}{\sigma_{residual}} \tag{3.8}$$

This signal to noise is plotted for the above described experiments in figure 3.16. Not only is a strong dependence of the signal to noise on the position observed, but also large variances of SNR at a fixed position. Possible reasons may on the one hand be the variation in absorption length. For large absorption lengths, at constant concentration the optical densities are larger and with equal noise-dominated residuals higher signal to noise is achieved. On the other hand, the intensity of the reflected light alters and therefore do the residuals, as it was shown in figure 3.14. In figure 3.17, the signal to noise ratio of an exemplary measurement is plotted against the respective peak optical densities. A general trend of increasing SNR with increasing optical density can be seen. However the correlation coefficient between both sizes is only around 0.4, which confirms that strength of optical density is not the only influence on SNR.
A measure for the absolute light intensity is the maximum detected voltage of the wavelength-tune. If the signal to noise ratio of an exemplary experiment is compared

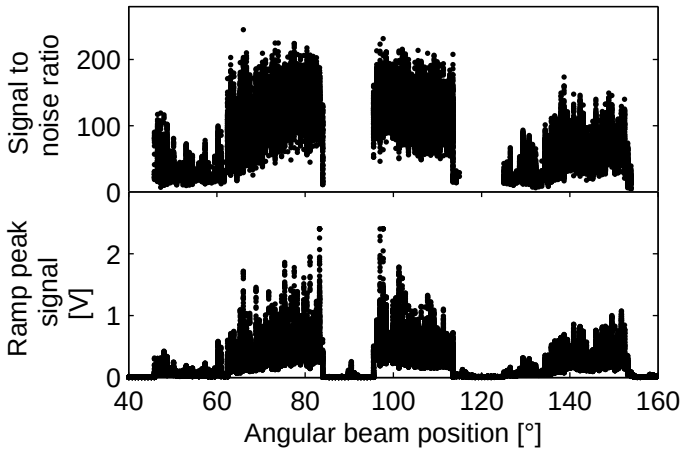

Figure 3.18 SNR and maximum wavelength-tune voltage depending on the laser beam position. This is an example for a polygon rotation speed of 30 rpm measured with channel 0.

to the respective peak voltages (view 3.18), it is obvious that there is some connection between them. In [65] it has been shown that light reflection of the foil alters with the relative position of the beam as well as with the angle of light incidence. For small angles, reflectivity decreases more and more. The observed variance in peak voltages of the reflected light are due to the different angles of light incidence onto the foil and to small vertical displacements of the beam between successive measurements. This can be seen more clearly in figure 3.19, where the maximum detected voltages and SNR values of all channels are plotted against the angle of light incidence onto the foil. The retro-reflective foil is suited best for a perpendicular incidence of the laser beam. If the beam is tilted, less

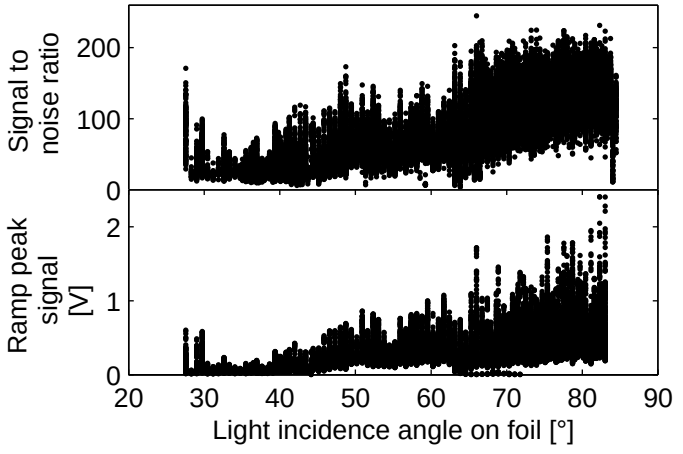

Figure 3.19 SNR and maximum detected wavelength-tune voltage depending on the light incidence angle on the foil

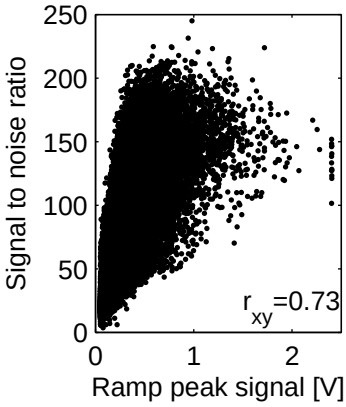

Figure 3.20 Correlation between SNR and maximum detected wavelength-tune voltage

light is reflected. The light incidence angle was defined such that it is always smaller than 90°, that is, it may be situated right or left from the perpendicular beam, as this makes no difference to the reflection. Here the relationship between SNR and detected light intensity gets very obvious. In figure 3.20, it can be seen that SNR generally increases with rising voltage of the detected wavelength-tune. There is a significant correlation between them, as the correlation coefficient amounts more than 0.7, so the suggestion of interdependency seems sensible.

In conclusion, a TDLAS instrument consisting of four scanner units and retro-reflective foil was chosen as the most suitable concept for the application in permafrost research. Four polygonal mirrors scan laser beams over a large proportion of an $0.8\times0.8\text{m}^2$ area. Approximately 78% of the measurement field are covered by laser beams. For high-speed sampling of the fast laser tuning rate of more than 5 kHz, a DAQ software was developed that is based on queues for fast continuous data reading and storage. In addition to that, a method for accurately detecting the start point of the wavelength tune was developed since the LabView timebase proved to be too inaccurate for simple continuous measurements and triggering every wavelength tune was too slow. A short pulse was super-positioned onto the transmitted light signal voltage on the falling branch of the wavelength tune.

An experiment with a homogeneous H_2O field was carried out to assess the spectroscopic performance of the instrument. Imaging rates are limited by the distance the beam moves on the foil during one wavelength tune. With a laser tuning rate of 5039.8 Hz and a field size of 0.8×0.8 m^2, the maximum achieved image rate was 2.5 Hz. If it is scanned faster, due to the varying reflectivity of the foil, the rising branch of the wavelength tune is distorted too heavily for a sensible base-line fit and concentrations show large systematic errors.

Signal to noise depends on the peak absorption as well as on the intensity of the reflected light, which varies due to altering light incidence angle on the foil and vertical position changes between scans. Concentration standard deviations lay between 380 ppmv and 750 ppmv at mean concentrations of around 12000 ppmv. Systematic deviations to a reference measurement amounted around 4%, which is less than the variance of the con-

centration values detected during scanning.

Chapter 4

Tomographic simulations

In classical medical applications, where the amount of collected data is high, the reliability of the tomographic reconstructions can generally be expressed in terms of the smallest detectable image structures or highest frequencies, as has been shown in chapter 2.2.1. From a mathematical point of view, resolution is explicitly given by the number and arrangement of the equidistant or equiangular measurement paths. However, in reality there are a couple of obstacles that produce additional inaccuracies: First of all, there is measurement noise that leads to a certain reconstruction error. A further error source is the discretization of the reconstructed field and the Radon transform itself. Virtual experiments offer a method to assess the influence of these effects: First of all, a discretized image, a so-called *phantom*, is generated. The experiment is simulated by means of a physical model of the measurement process, the *observation model*. The reconstructed picture can then be compared to the original phantom, yielding information about the accuracy of reconstruction. Another reason why such simulations are indispensable is limited data: The determination of cut-off frequencies as shown in chapter 2.2.1 is only valid for transform-based algorithms, that unfortunately require abundant data. The following simple example is given to illustrate the orders of magnitude: Consider the unassuming phantom where $f(x, y)$ is a 2D-Gaussian with a standard deviation of 10% of the measurement field side length, centred at $(x = 0, y = 0)$:

$$f(x,y) = \frac{1}{2\pi\sigma_x\sigma_y} \cdot \exp\Big\{ -\frac{1}{2} \cdot \Big(\frac{x^2}{\sigma_x^2} + \frac{y^2}{\sigma_y^2}\Big)\Big\} \tag{4.1}$$

where σ_x and σ_y are the standard deviations into x- and y-direction. For convenient notation, the dimension of the field is determined to be 1cm×1cm, and accordingly the exemplary standard deviations are $\sigma_x = \sigma_y$ =0.1cm. The Fourier transform of the phantom is then given by (view appendix C):

$$F(u,v) = \mathcal{F}\{f(x,y)\} = \sqrt{2\pi(\sigma_x^2 + \sigma_y^2)} \cdot \exp\Big\{ -\frac{u^2\sigma_x^2 + v^2\sigma_y^2}{2}\Big\} \tag{4.2}$$

Assuming that frequencies smaller than 1% of the maximum frequency are negligible, the largest detectable frequency should be 21.46 cm^{-1} (view appendix C). According to eqs. (2.24) and (2.25), either a parallel-beam arrangement with at least 22 projections and 15 samples per projection or a fan-beam arrangement with at least 43 projections sampled at 23 angles, each, would be necessary. Overall, the amount of beam paths would be at

least 330 beams for parallel sampling and 989 beams for fan-beam sampling. It is self-evident that both arrangements are based on costly instrumentation which is inadequate for the purpose. For this reason, transform-based algorithms were excluded in the first place.
In this chapter, a selection of tomographic algorithms are demonstrated by evaluating the properties of simulated experiment reconstructions. Evidently, no general statements about the ability to reconstruct arbitrary fields can be made, as the applicability of algorithms depends on the phantom itself. This gets very clear in the case of Bayesian estimation, where physical assumptions about the phantom are made, which of course limit the suitability of the algorithm to the specific purpose. The strategy is to examine a large variety of phantoms that seem relevant for the application and getting insights about tendencies and characteristics of the algorithms. Algorithm performance also depends on the measurement path arrangement. The focus is on the final instrument as it was presented in chapter 3, as the documentation of preliminary set-ups is beyond the scope of the work and does not deliver crucial additional information.
First of all, details about the virtual experiment and the observation model are explained (section 4.1). The assessment of algorithms by means of phantom reconstructions is presented in section 4.2. A question that naturally arises is that of spatial resolution. Section 4.3 deals with the definition of this variable and the selected algorithms are compared. Finally, section 4.4 gives an overview of calculation time performance of the different techniques.

4.1 Observation model

At each of the instrument's beam paths, an absorption measurement takes place with TDLAS. The premise is normally that concentration, pressure and temperature remain homogeneous along the line of sight. In the case of spatial inhomogeneities however, the measurement corresponds to taking the Radon transform of the path-varying absorber number density χ:

$$\mathscr{R}\chi_\theta(\xi) = \int_{-\infty}^{\infty} \chi(\xi,\zeta)\mathrm{d}\zeta \tag{4.3}$$

The coordinate system accords with the depiction in figure 2.2. The classical Lambert-Beer law (2.10) is modified to

$$I = I_0 \cdot Tr(\lambda) \cdot \exp\{-\int_0^l \Phi(\lambda-\lambda_0)\cdot S(T)\cdot\chi(\zeta)\mathrm{d}\zeta\} + E \tag{4.4}$$

This is of course only valid if temperature and pressure are constant along the line of sight. The integration limits are set to zero and path length l because elsewhere no absorption takes place and the integral is zero. The measured path-integrals of the absorber number density are expressed by

$$\int_0^l \chi(\zeta)\mathrm{d}\zeta = -\frac{1}{S(T)} \int_{-\infty}^{\infty} \ln \frac{I(\lambda) - E}{I_0(\lambda) \cdot Tr(\lambda)} \mathrm{d}\lambda \tag{4.5}$$

The right hand side of equation 4.5 corresponds to the classical measurement carried out with TDLAS scaled with the path length l. In practice this means, the standard TDLAS evaluation process can be carried out, delivering the path integral of the absorber number density that is afterwards scaled with the corresponding path length. With known temperature T and pressure p, a path-averaged concentration value is determined that is proportional to the line-integral of the absorber number density χ:

$$c = \frac{\Re T}{N_A \cdot p} \cdot \int_0^l \chi(\zeta)\mathrm{d}\zeta \tag{4.6}$$

When modelling this single measurement, the measurement area is divided into N pixels that are assumed to have uniform concentration. The path integral is approximated by a discrete summation:

$$c \approx \frac{\Re T}{p} \cdot \sum_{i=1}^{N} \hat{W}_i \cdot \chi_i \tag{4.7}$$

$$\approx \sum_{i=1}^{N} W_i \cdot f_i \tag{4.8}$$

The weighting factors $\hat{W}_i$ imply the proportional contribution of the ith pixel to the single measurement. For negligible path broadness, the weighting factors are determined by the length of the beam's section inside the ith pixel in relation to the overall length. However, for the presented instrument the broadness of the laser beam is significant, so the weighting factors are calculated by the proportion of the area inside the ith pixel to the overall beam area. If the average concentration shall be expressed in dependency of the unknown concentration values, the equation takes the form of (4.8). Measuring the path averaged concentration c at M different locations, several equations can be combined into a linear system of equations:

$$\vec{c} = W \cdot \vec{f} \tag{4.9}$$

where W_{ij} is the weighting factor of the jth measurement inside the ith pixel. In reality, the measurements are corrupted by noise. This effect should also be modelled when a virtual experiment is set up. Noise is modelled as an additive vector $\vec{n}$, so a simulated measurement can be generated with the following equation:

$$\vec{c}_{sim} = W_{sim} \cdot \vec{f}_{sim} + \vec{n} \tag{4.10}$$

The virtual experiment is completed by reconstruction of the unknown field $\vec{f}$. Therefore, the following expression needs to be solved:

$$\vec{c}_{sim} = W_{rec} \cdot \vec{f}_{rec} + \vec{n} \tag{4.11}$$

The phantom concentration $\vec{f}_{sim}$ and weighting matrix W_{sim} should be higher discretized than the reconstruction weighting matrix W_{rec} and concentration vector $\vec{f}_{rec}$, avoiding so-called *inverse crimes* [56]. Moreover, the number of pixels into one direction of the simulated field should not be an integer multiple of the same size in the reconstruction case.

4.2 Phantom reconstructions

Simulated experiments are used to demonstrate the efficiency of some selected tomographic algorithms. As already described above, transform-based algorithms are disregarded for the low-data system. Algebraic reconstruction techniques are very popular among engineering tomography. For this reason two variants are presented in this work: the basic ART variant (section 4.2.1), sometimes also called the Kaczmarz method, and the Landweber algorithm (section 4.2.2), which is the most recent improvement of ART. The SIRT and SART techniques delivered very similar results to ART, therefore they are not shown in this work. Furthermore, some Bayesian estimation techniques are examined. Tikhonov regularization (section 4.2.3) and the informative smoothness prior (section 4.2.4) presume that the image is somewhat smooth, as it is the case for processes dominated by diffusion. On the other hand, the total variation prior (section 4.2.5) is the adequate choice for "blocky" measurement objects that have steep gradients in only very few locations. It has also been studied to which extent the algorithms work with faulty assumptions, e.g. how good sharp-edged structures can be imaged with smoothness priors and vice versa.
The simplest method of judging the quality of a reconstruction is the visual comparison with the phantom. Very easily it can be controlled whether structure positions, shapes and absolute values are reconstructed correctly and if artefacts appear. The disadvantage is however that these criteria are more or less estimated visually and therefore the assessment of reconstruction quality is subjective. Therefore image quality is often expressed by a single quality number that can be defined in various ways. So-called *picture distance measures* are based on a norm of the image residual. Herman [47] defines the *normalized mean absolute distance measure* which is based on the 1-norm of the image residual:

$$e_{f,1} = \frac{\left\| \vec{f}^{\star}_{sim} - \vec{f}_{rec} \right\|_1}{\left\| \vec{f}^{\star}_{sim} \right\|_1} \tag{4.12}$$

Note that the simulated phantom vector $\vec{f}_{sim}$ has to be down-sampled to $\vec{f}^{\star}_{sim}$, so it has the same size as $\vec{f}_{rec}$. Another picture distance measure is used by Daun [59], which is based on the 2-norm of the image residual:

$$e_{f,2} = \frac{\left\| \vec{f}^{\star}_{sim} - \vec{f}_{rec} \right\|_2}{\left\| \vec{f}^{\star}_{sim} \right\|_2} \tag{4.13}$$

The *normalized root mean square measure* defined by Herman [47] is a slightly different 2-norm-based version:

$$e^*_{f,2} = \frac{\left\| \vec{f}^{\star}_{sim} - \vec{f}_{rec} \right\|_2}{\left\| \vec{f}^{\star}_{sim} - \bar{f}_{sim} \right\|_2} \tag{4.14}$$

This version is normalized in a way that $e^*_{f,2}$ becomes 1 for a uniform reconstruction image with the correct mean value of $\vec{f}$. Obviously, the magnitude of $e^*_{f,2}$ depends on the contrast of the phantom image, so it is focussed onto $e_{f,1}$ and $e_{f,2}$. The disadvantage of expressing reconstruction quality in this manner is that the measures cannot be interpreted easily. First of all, the magnitudes depend on the definition of the measure. Values of $e_{f,1}$ will be larger than $e_{f,2}$ for the same residual image, as $\|x\|_1 \geq \|x\|_p$ with $p > 1$ [67]. In addition to that, $e_{f,2}$ gets large if few outliers appear in the reconstruction. The values of $e_{f,2}$ might therefore sometimes contradict what we think a quite good reconstruction that is corrupted with a high error in a only few pixels. Maybe the most crucial drawback is that with a single quality value, important information about the reconstruction gets lost: It cannot be observed where the error originates from, e.g. whether it is due to artefacts outside the structures of interest or whether absolute values of the structures are not hit or whether simply the position of a structure is shifted by a few pixels. For this reason the visual judgement should be considered in any case.
Similar to the definition of the picture distance measure, a measurement vector error may be defined by

$$e_{c,2} = \frac{\|\vec{c}_{sim} - \vec{c}_{rec}\|_2}{\left\| \vec{f}_{sim} \right\|_2} \tag{4.15}$$

This number is a convenient possibility for controlling whether an algebraic algorithm has converged or not. However, it does not indicate whether the reconstruction is any good or not: Even if the measurement error vector is very small, the found solution may be physically wrong since it could be one of the infinite solutions of the underdetermined problem, or a senseless solution leading to a similar measurement vector due to ill-conditioning of the forward model equation. Note that for Bayesian techniques, $e_{c,2}$ is no measure for convergence due to the regularization. The ideal solution does not yield a zero $e_{c,2}$.
In the following sections, the implementation of the chosen algorithms and reconstructions of virtual experiments are shown. Multiple phantoms were generated by varying structure types, positions, sizes, concentrations, numbers and contrast, so that as many physical situations as possible were covered. All phantoms were discretized with 84×84 pixels and reconstructed into 40×40 pixel images. The noise vector $\vec{n}$ was simulated as white additive noise with 5% magnitude of the path-averaged simulated concentration values. The order of magnitude of noise was determined according to accuracy and precision that are typically achieved when measuring concentrations with TDLAS [2].

4.2.1 ART algorithm

As the Kaczmarz method is apt for linear system of equations only, it can directly be implemented by equation 2.27. A zero vector served as an initial guess $f^{(0)}$. As a stop criterion, the normalized difference between iterations ϵ was used:

$$\epsilon = \frac{\left\| f^{(k+1)} - f^{(k)} \right\|}{\| f^{(k)} \|} \tag{4.16}$$

Iteration was aborted if ϵ fell under 0.01% or if the number of iterations exceeded 50. At each iteration, negative pixel values were set to zero to impede negative concentrations which are physically not sensible. Furthermore, a smoothing by a 3×3 median filter was implemented since otherwise ART converges towards completely senseless solutions of the infinite solution space. It proves to be an algorithm with only very limited applicability for the given instrument. A large variety of virtual experiments with three different phantom types was carried out. Smooth phantoms with Gaussian-shaped structure elements were generated as well as sharp-edged features and bell-shaped structures. Generally, all structures are quite blurred and the maximum concentration is underestimated significantly. Figure 4.1 shows some exemplary reconstructions of smooth and sharp-edged circular structures. Sharp-edged structures are generally reconstructed better, since the absolute structure values are closer to the simulated phantoms, the shapes of the features are less blurred and there are less artefacts in the background. For an enhanced visual impression of the reconstruction quality, the difference between a down-sampled phantom image and the reconstruction is shown in the lower part of figure 4.1. Note that the choice of the down-sampling method has an influence on the difference image, as can easily be seen by comparing the lower three rows. Another way of visually comparing the down-sampled phantom with the reconstruction image is explained in the following. First, the pixels of the phantom are sorted such that the pixels values descend. Then, the values of the sorted phantom pixels and the according values of the reconstruction are plotted as a line. An example for this is shown in figure 4.2 for the phantoms A-F of figure 4.1. In contrast to the visual assessment, the image errors expressed by picture distance measures imply that the reconstructions of the smooth objects were better: Figure 4.3 shows the values of $e_{f,1}$ and $e_{f,2}$ for the three phantom types, depending on the number of features in the phantom. The image errors of the smooth reconstructions are globally smaller than those of the more sharp-edged phantoms. Here it gets very clear that the 1-norm based error is always larger than the 2-norm based error, so the relative values should be considered instead of absolute values. Moreover, the algorithm seems to converge better for the smooth objects since the values of $e_{c,2}$ are closer to zero. Interestingly, there is a correlation of more than 0.9 between the image errors and $e_{c,2}$: obviously, the algorithm is not able to find a solution to the equation $\vec{c} = W \cdot \vec{f}$ at all, leading of course to quite bad results of $\vec{f}_{rec}$. Reconstruction quality of ART deteriorates very quickly if the number of features increases, as can also be seen in figure 4.3 and can be further proved by the simulation results shown in appendix F. If the algorithm is used at all, the number of features should not exceed two, as otherwise strong artefacts appear. Figure 4.4 depicts the phantoms, reconstructions and difference images of some of the critical situations that can occur when using ART: The corresponding line plots can be found in appendix E, figure E.1. Even if

there are less than three features, reconstructions may look disappointing, depending on the position and size, as it can be seen for phantom A. Typical artefacts that appear with increased number of features can be seen for phantom B. Sharp-edged structures that are not circular are totally blurred and strongly underestimate the correct concentration value, as is shown by the square phantom C and rectangular phantom D. Problems also arise if the structures differ in concentration (view phantoms E and F). Concentrations may be reconstructed completely wrong, or structures are not reconstructed at all (view appendix F). It is even possible that the relative heights of the structures are erroneous, like it happens to be in case E: here, the feature with higher phantom concentration has a much lower reconstructed concentration than the other feature, leading to a completely

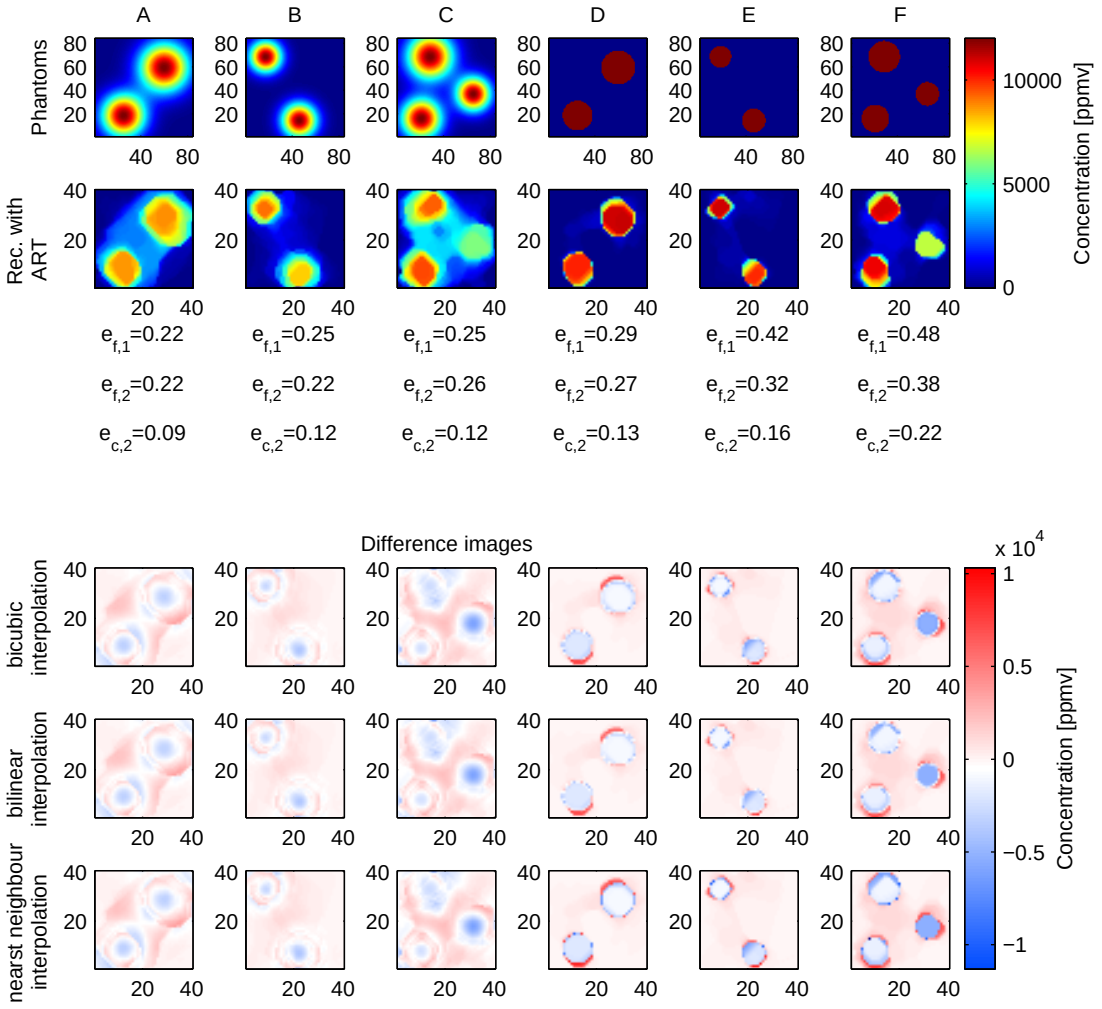

Figure 4.1 Reconstructions of some smooth objects and sharp-edged circular objects with the ART algorithm. In the top row shows the phantom concentration images while the second row shows the reconstructions achieved with ART algorithms. Note that the reconstructions have a discretization of 40×40 pixels, only. The bottom part shows the pixel-wise difference images between a down-sampled phantom concentration and the ART reconstructions. Each row shows the difference images that were generated while using different methods for down-sampling.

wrong impression of the measurement field. With decreasing contrast, the reconstruction of phantoms with ART gets more and more difficult. In appendix F a study is shown where the background concentration is increased step by step, so that contrast is reduced. Shapes get more and more distorted, artefacts in the background increase and in some cases features are completely lost. Altogether the application of Kaczmarz algorithm is not recommendable for the designed instrument.

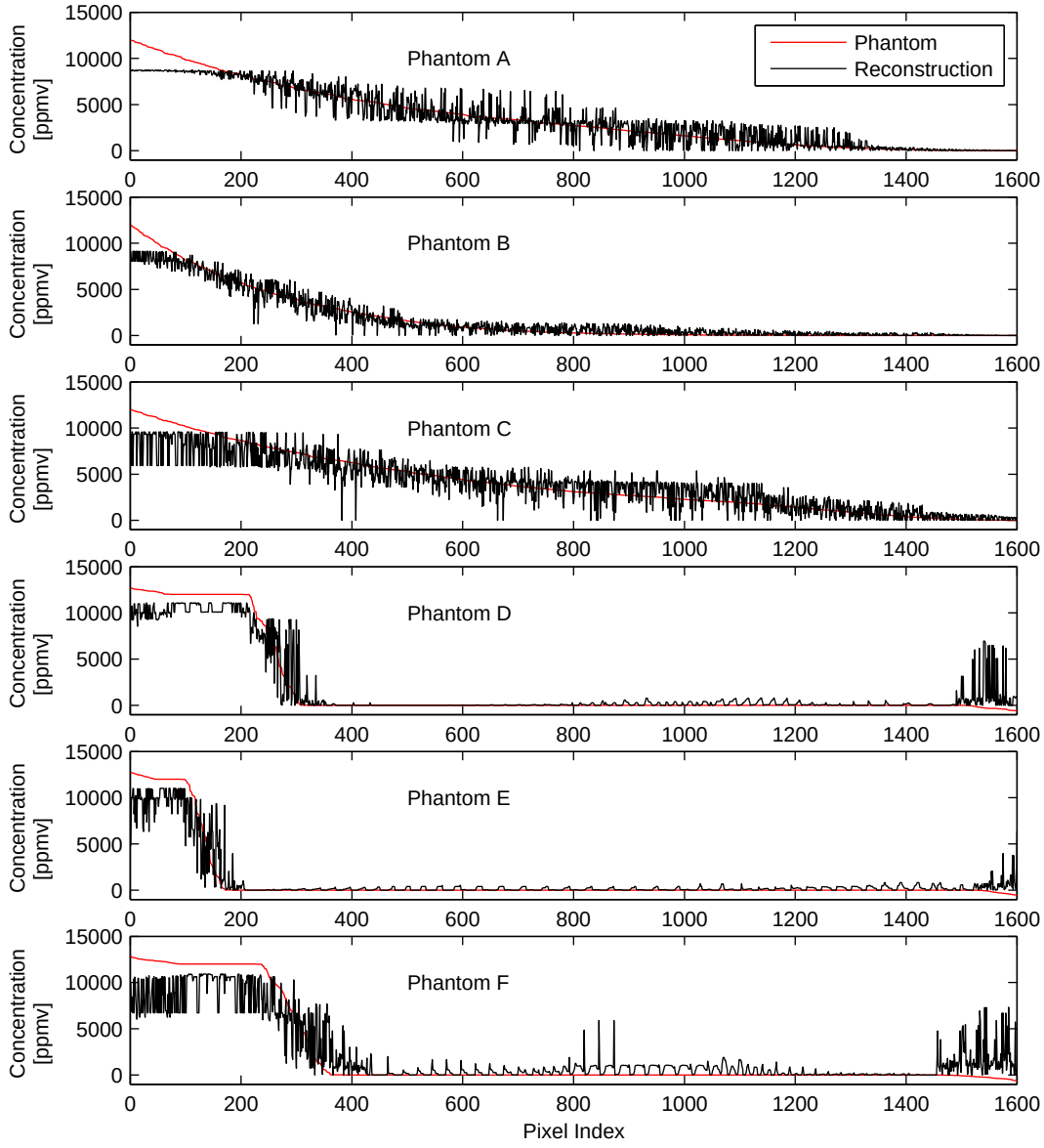

Figure 4.2 Lineplots of the pixel values of phantoms A-F shown in figure 4.1 (red lines) and reconstructions (black lines) with ART algorithm. The phantoms were first down-sampled with a bi-cubic interpolation and then the pixels were sorted such that pixel values descend.

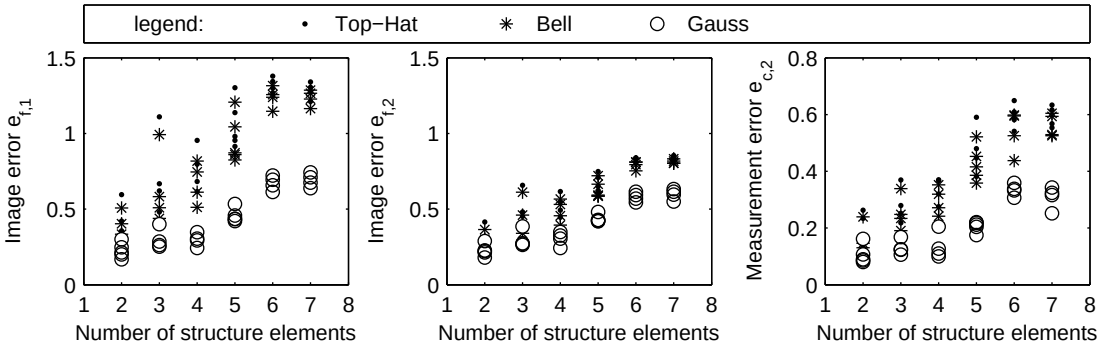

Figure 4.3 Image errors and measurement vector errors for a simulation study with different phantom types and element numbers. Reconstructions were carried out with the ART algorithm.

4.2.2 Landweber algorithm

Landweber algorithm is a method for regularizing linear systems of equations, therefore equation 2.31 could be directly implemented. The stop criterion, non-negativity constraint and median filtering were implemented analogous to ART, like it is described in chapter 4.2.1. The initial guess is computed by $\vec{\tilde{f}}^{(0)} = W^T \cdot \vec{c}$. According to [52] the

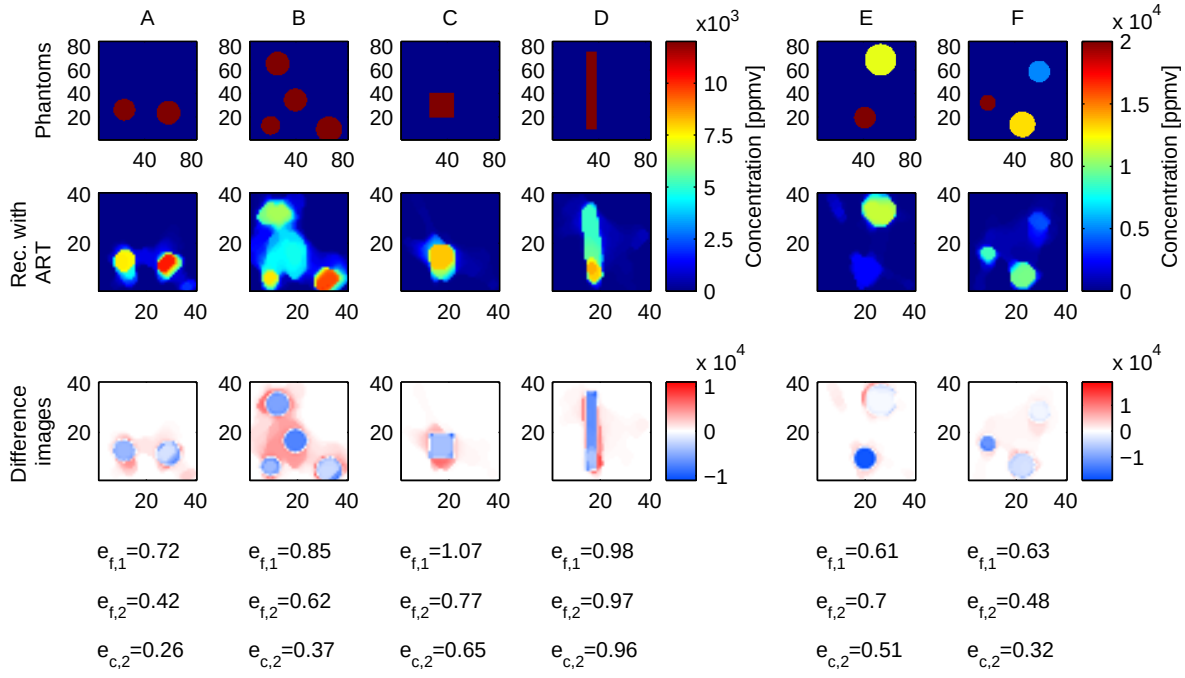

Figure 4.4 ART reconstructions of problematic phantoms. In the top row, the phantoms with a 84×84 pixel discretization are depicted, while the 40×40 pixel reconstructions are plotted in the second row. The difference images (bottom) were calculated by subtracting a down-sampled phantom from the reconstruction. The down-sampling method was bi-cubic.

parameter α_{LW} shall be picked in the range of $0 < \alpha_{LW} < 2(\|W^T W\|_2)^{-1}$. An empirical study was carried out for demonstrating the effect of the choice of the regularisation parameter. A virtual experiment with a top-hat shaped phantom (view figure D.1) was carried out, assuming a beam distribution as shown in figure 3.4. The above described range for choosing α_{LW} in this case was $0 < \alpha_{LW} < 5\,86$. The regularization parameter was varied between $\alpha_{LW} = 10^{-5}$ and $\alpha_{LW} = 10^4$. If the reconstructed images are considered, it becomes obvious that it is not sufficient to specify such a relatively large range like given by Terzija et al. [52], as the quality of reconstruction alters strongly within this range. This becomes even more clear if a one-dimensional comparison of the pixel values is drawn. The discretisation of the phantom was reduced to 40 times 40 pixels, i.e. the reconstruction image size, for enabling a direct comparison of the pixel values of original image and reconstruction. In addition to this, the pixels were sorted such that the pixel values descend for making the line plots clearer. The 1D - comparison of phantom and reconstructions can be seen in figures D.2 and D.3. A more concise recommendation of how to determine α_{LW} is given by Yang et al. [53]. They suggest the parameter fulfil $\alpha_{LW} = 2/\max[eig(W^T \cdot W)]$. In the above described study, that would correspond to $\alpha_{LW} = 5\,86$. In this order of magnitude, the reconstructions look most sensible and show less deviations from the phantom. Therefore, the regularisation parameter was always calculated like recommended by Yang et al. [53].
Although Landweber algorithm is considered an improved variant of the Kaczmarz method, the virtual experiments yielded worse results regarding structure shapes and artefacts. However, the maximum concentration values are closer to the phantom maximum values. Figure 4.5 shows phantoms, reconstructions and difference images of a few examples of the study that is found in appendix F. The difference images were calculated by subtracting a bi-cubically down-sampled phantom image from the reconstruction. The corresponding line-plots can be found in appendix E, figure E.2. Like for Kaczmarz algorithm, sharp-edged circular structures are reconstructed better than the smooth Gaussian structures, which are heavily distorted even for very few, large objects. If the top-hat shaped features are considered, Landweber algorithm seems to prefer solutions with features that have non-uniform concentration but locally have smaller concentration errors, while ART delivered flatter features, accepting larger underestimation of the correct concentration. This conduct is evidently the reason why image errors of both algebraic algorithms behave similarly. Again, problems are caused by increasing the number of structures, by differing feature concentrations (view figure 4.5) and by decreasing the phantom image contrast. Blocky quadratic or rectangular shapes are awry and non-uniform in concentration. In all cases, Landweber algorithm seems to perform worse, even though the image errors are in the same order of magnitude as for the Kaczmarz method, as can be seen exemplary for top-hat phantoms in figure 4.6.

4.2.3 Tikhonov regularization

The maximum a posteriori estimate of the posterior density 2.44 is given by

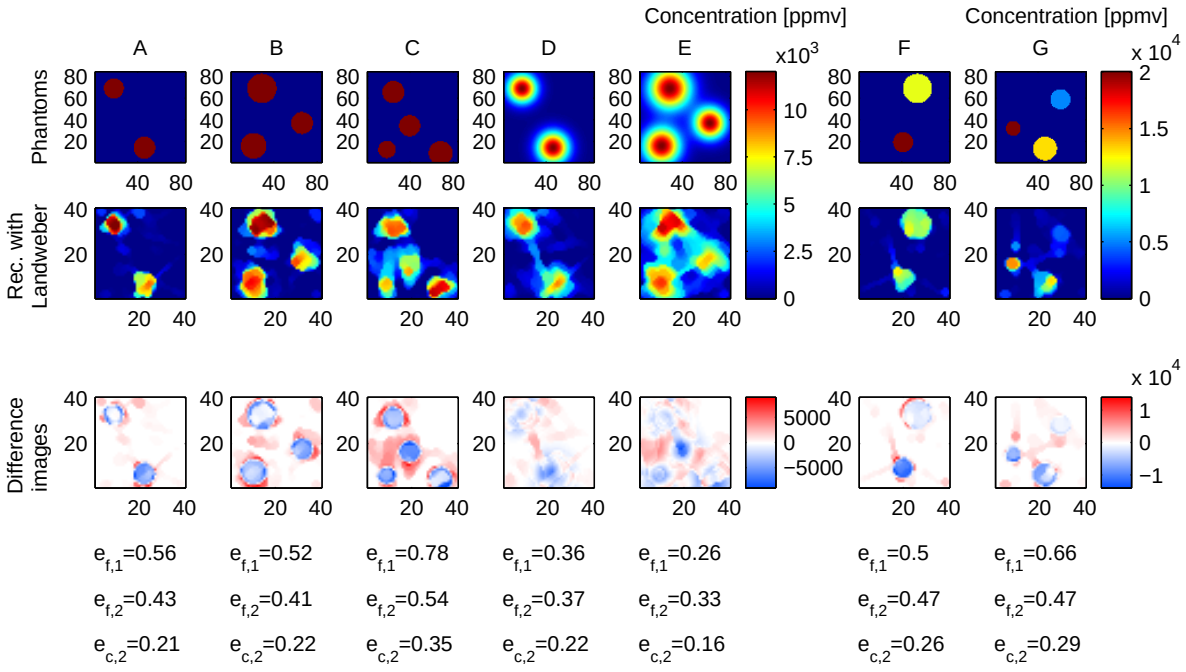

Figure 4.5 Some examples for reconstructions of simulated experiments with Landweber algorithm. The top row shows the 84×84 pixel phantoms, the second row the 40×40 pixel reconstructions and the bottom row the difference images. The latter were generated by down-sampling the phantoms to 40×40 pixels with a bi-cubic interpolation and then subtracting the smaller phantom from the reconstruction.

$$\begin{aligned} \vec{f}_{MAP} &= \arg\min_{\vec{f}}\left(\left\|\vec{c} - W\vec{f}\right\| + \tau^2 \vec{f}^T \mathcal{L}^T \mathcal{L} \vec{f}\right) \\ &= \arg\min_{\vec{f}} \left\| \begin{bmatrix} W \\ \tau\mathcal{L} \end{bmatrix} \cdot \vec{f} - \begin{bmatrix} \vec{c} \\ 0 \end{bmatrix} \right\| \qquad = \vec{f}_\tau \end{aligned} \tag{4.17}$$

Various techniques deal with the right choice of the smoothing parameter τ, e.g. L-curve

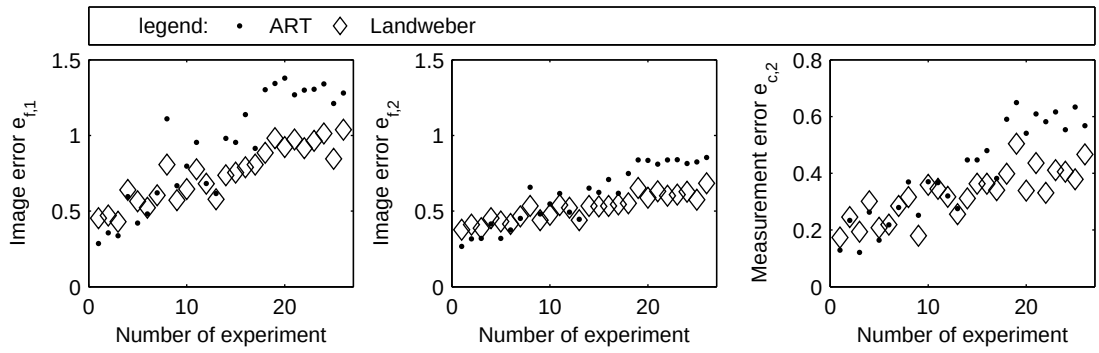

Figure 4.6 Image and measurement errors of top-hat phantoms reconstructed with ART and Landweber algorithm

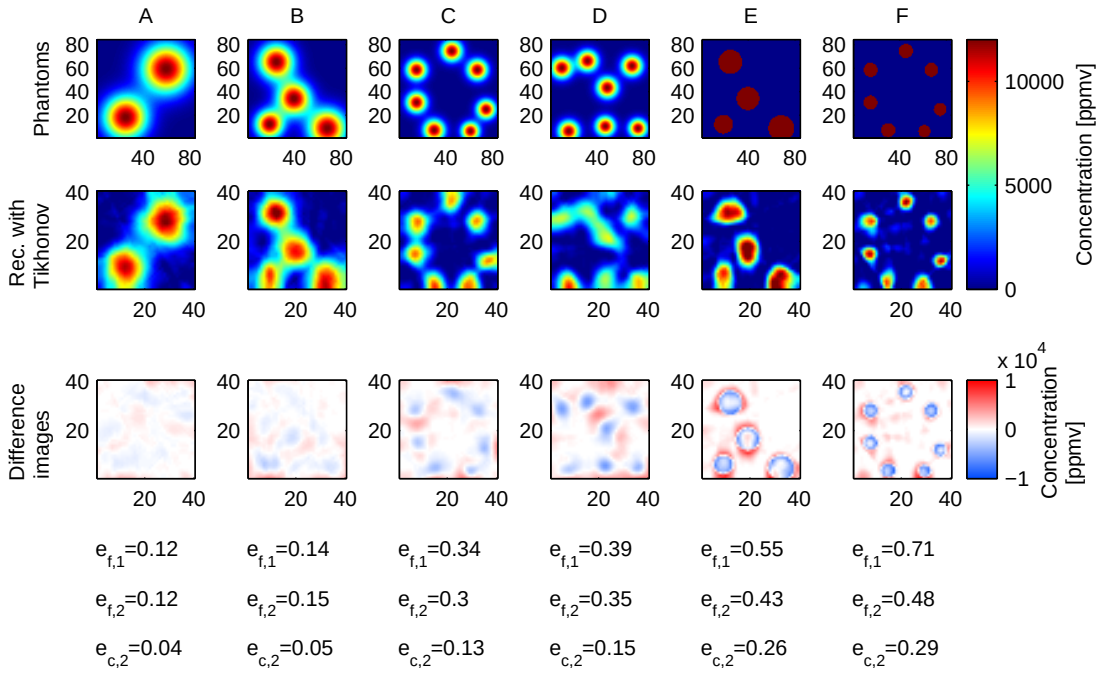

Figure 4.7 Reconstructions of smooth and sharp-edged circular structures with Tikhonov algorithm. The top row shows the 84×84 pixel phantoms, the second row the 40×40 pixel reconstructions and the bottom row the difference images. The latter were generated by down-sampling the phantoms to 40×40 pixels with a bi-cubic interpolation and then subtracting the smaller phantom from the reconstruction.

curvature [58], discrepancy principle or cross-validation, to name a few. Daun et al. [58] suggest for a noise-corrupted system of equations a method using the singular value decomposition (SVD). The SVDs of the weighting matrix W and the augmented matrix $(W \;\; \tau L)^T$ are computed for various orders of magnitude of τ. Then τ is picked such that the singular values of the augmented matrix do not exceed the singular values of the weighting matrix. By this way, it is impeded that too much weight is put onto the Gibbs prior. The recommendable value of τ that was determined with this method was τ <0.1. Heuristic studies however have revealed that a slightly stronger influence of smoothing leads to better results. Therefore τ was set to 0.2 for all studies. Solving equation **??** means minimizing an objective function, which can be done with various algorithms. In this case, a least-squares algorithm with a non-negativity constraint was applied to exclude non-physical negative concentration values. The MATLAB algorithm `lsqnonneg` offers a convenient possibility of implementation. Tikhonov regularization implicitly assumes that the solution is smooth, therefore it is mainly suited for the reconstruction of smooth features. The virtual experiments with Gaussian- or bell-shaped phantoms show that good reconstructions are achieved even for larger numbers of features (view 4.7 for some examples of phantoms, reconstructions and difference images and appendix F for the complete study). The corresponding line plots can be found in appendix E, figure E.3. Absolute concentrations and feature locations are reconstructed adequately and shapes mostly correspond nicely to the correct solution. Moreover, there are hardly any artefacts

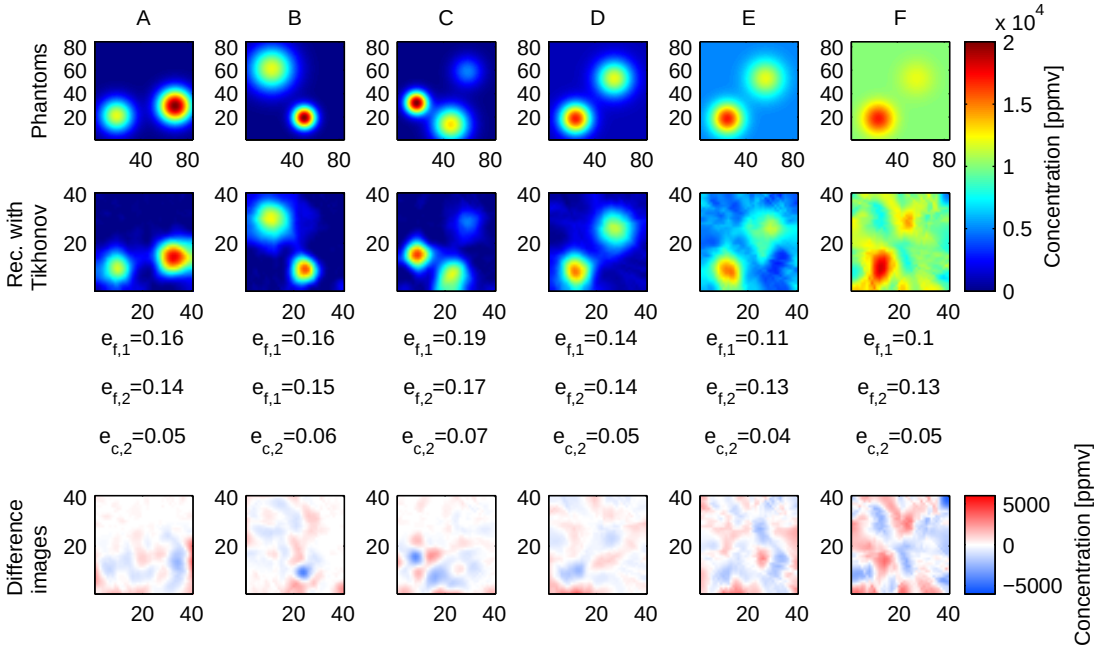

Figure 4.8 Reconstructions of smooth structures with differing concentrations (A–C) and non-zero background concentration (D–E) with the Tikhonov algorithm. The top row shows the 84×84 pixel phantoms, the second row the 40×40 pixel reconstructions and the bottom row the difference images. The latter were generated by down-sampling the phantoms to 40×40 pixels with a bi-cubic interpolation and then subtracting the smaller phantom from the reconstruction. The corresponding line plots can be found in appendix E, figure E.4.

in the image background. Image errors $e_{f,1}$ and $e_{f,2}$ are significantly lower than those achieved with algebraic algorithms. If the number of structures does not exceed four, $e_{f,2}$ is in the range of $e_{f,2}$ <0.1... $e_{f,2}$ <0.2, which is about half of the magnitudes achieved with algebraic techniques. Interestingly, even the values of $e_{c,2}$ lie below those that result from ART techniques, even though there is no exact solution to the over-determined augmented equation system. Typical values of $e_{c,2}$ that result from Tikhonov regularization amount less than 0.1, while ART techniques lead to values about twice higher.

For sharp-edged phantoms, Tikhonov algorithm is expected to be not the perfect choice, since the smoothness assumption is physically wrong in this case. Nevertheless, satisfying reconstructions can be obtained in expedient cases (view some examples in figure 4.7). All features are smoothed and image errors $e_{f,1}$ and $e_{f,2}$ are slightly higher than in the smooth case. In the worst case, absolute concentration values are wrong and artefacts appear, while shape is mainly hit good due to the homogeneous smoothing. Generally, $e_{c,2}$ is much higher than for smooth phantoms, implying that the the smoothness assumption contradicts the correct solution.

In contrast to algebraic reconstruction techniques, absolute values of the phantoms are reconstructed accurately even if features differ remarkably in concentration (view figure 4.8, cases A – C). Diminishing the contrast between background and feature concentrations, artefacts appear in the surroundings (view figure 4.8, cases D – F). However, this effect is not as strong as for ART algorithms. The image and measurement errors are small

even for the low-contrast cases. Surprisingly, Tikhonov regularization even allows for the reconstruction of square and rectangular shapes (view appendix F). The features are smoothed at the edges but absolute concentration values are correct.
All in all, the application of Tikhonov regularization with the designed instrument is considered possible.

4.2.4 Bayesian estimation with informative smoothness prior

The linear problem $\vec{c} = W \cdot \vec{f}$ had to be implemented into the Bayesian smoothness prior framework such that the observation takes the form of $\mathscr{W}(\vec{f}) = W \cdot \vec{f}$. Thus, the posterior density is given by

$$\mathbb{P}(\vec{f} \mid \vec{c}) \propto \exp\Big(-\frac{1}{2}(\vec{f} - \eta_f)^T \Gamma_f^{-1}(\vec{f} - \eta_f) - \frac{1}{2}(\vec{c} - W \cdot \vec{f})^T \Gamma_n^{-1}(\vec{c} - W \cdot \vec{f}) \Big) \tag{4.18}$$

With some conversions, the MAP estimate is expressed by

$$\vec{f}_{MAP} = \arg\min_f \{ \Big\| L_n(\vec{c} - W \cdot \vec{f}) \Big\|^2 + \Big\| L_f(\vec{f} - \eta_f) \Big\|^2 \} \tag{4.19}$$

The objective function was minimized by a self-implemented Gauss-Newton algorithm. It is a method to solve non-linear least squares problems and is based on the iterative minimization of a second order Taylor expansion of the objective function [68]. For convenient notation the objective function is split into its noise term Z_1 and the prior term Z_2:

$$Z(\vec{f}) = \underbrace{\Big\| L_n(\vec{c} - W(\vec{f})) \Big\|^2}_{Z_1} + \underbrace{\Big\| L_f(\vec{f} - \eta_f) \Big\|^2}_{Z_2} - a \cdot \underbrace{\sum_i \ln f_i}_{Z_3} \tag{4.20}$$

Z_3 is a penalty term for impeding negative solutions by making them very improbable, as the overall objective function gets large for negative arguments. Its weight is adjustable by the value a. Iterating the following equation leads to a minimum [68]:

$$\vec{f}^{(k+1)} = \vec{f}^{(k)} - \left(\frac{\partial^2 Z(\vec{f})}{\partial \vec{f}^2} \right)^{-1} \cdot \left(\frac{\partial Z(\vec{f})}{\partial \vec{f}} \right) \tag{4.21}$$

For Gauss-Newton minimization, the first and second order derivatives of the objective function are required. The gradient of the first term Z_1 is given by

$$\begin{aligned} \frac{\partial Z_1}{\partial \vec{f}} &= \frac{\partial}{\partial \vec{f}} \Big((\vec{c} - \mathscr{W}(\vec{f}))^T \cdot \Gamma_n^{-1} \cdot (\vec{c} - \mathscr{W}(\vec{f})) \Big) \\ &= -2(\vec{c} - \mathscr{W}(\vec{f}))^T \cdot \Gamma_n^{-1} \cdot \frac{\partial \mathscr{W}(\vec{f})}{\partial \vec{f}} \end{aligned} \tag{4.22}$$

The Hessian is given by:

$$\frac{\partial^2 Z_1}{\partial \vec{f}^2} = -2\Big(\sum_{i=1}^{m} (c_i - \mathscr{W}_i(\vec{f})) \cdot \Gamma_n^{-1} \cdot \frac{\partial^2 \mathscr{W}(\vec{f})}{\partial \vec{f}^2}\Big) + 2(J^T \cdot \Gamma_n^{-1} \cdot J) \tag{4.23}$$

with the Jacobian $J = \frac{\partial \mathscr{W}(\vec{f})}{\partial \vec{f}}$. In the linear case $\mathscr{W}(\vec{f}) = W \cdot \vec{f}$, the Jacobian is simply $J = W$. Since it does not depend on the actual value of $\vec{f}$, it remains constant throughout the recursions. Consequently, the second derivative is zero: $\frac{\partial^2 \mathscr{W}(\vec{f})}{\partial \vec{f}^2} = 0$. In the linear case, the first and second derivatives of Z_1 are given by

$$\frac{\partial Z_1}{\partial \vec{f}} = -2(\vec{c} - W \cdot \vec{f})^T \cdot \Gamma_n^{-1} \cdot W \tag{4.24}$$

$$\frac{\partial^2 Z_1}{\partial \vec{f}^2} = 2W^T \cdot \Gamma_n^{-1} \cdot W \tag{4.25}$$

Similarly, the first and second derivatives of Z_2 can be calculated:

$$\frac{\partial Z_2}{\partial \vec{f}} = 2(\vec{f} - \eta_f)^T \cdot \Gamma_f^{-1} \tag{4.26}$$

$$\frac{\partial^2 Z_2}{\partial \vec{f}^2} = 2\Gamma_f^{-1} \tag{4.27}$$

The gradient and second derivative of the penalty term Z_3 are given by

$$\frac{\partial Z_3}{\partial \vec{f}} = \frac{\partial}{\partial \vec{f}}\Big(\sum_{i=1}^{N} \ln f_i\Big) = \sum_{i=1}^{n} \frac{1}{f_i} \tag{4.28}$$

$$\frac{\partial^2 Z_3}{\partial \vec{f}^2} = \frac{\partial}{\partial \vec{f}}\Big(\sum_{i=1}^{N} \frac{1}{f_i}\Big) = -\sum_{i=1}^{n} \frac{1}{f_i^2} \tag{4.29}$$

Thus, the iterative Gauss-Newton procedure for optimizing the objective function of the informative smoothness prior is expressed by

$$\begin{aligned} \vec{f}^{(k+1)} = \vec{f}^{(k)} + & \\ & \varsigma \cdot (W^T \cdot \Gamma_n^{-1} \cdot W + \Gamma_f^{-1} - a \cdot \sum_{i=1}^{N} \frac{1}{f_i^2})^{-1} \\ & \cdot ((\vec{c} - W \cdot \vec{f})^T \cdot \Gamma_n^{-1} \cdot W + (\vec{f} - \eta_f) \cdot \Gamma_f^{-1} + a \cdot \sum_{i=1}^{N} \frac{1}{f_i}) \end{aligned} \tag{4.30}$$

The factor 4 is pushed into the step size parameter ς, which is determined at each iteration by a line-search algorithm. The parameter a is scaled accordingly. The informative smoothness prior requires physical knowledge about the structures sizes and expectation values of concentration. Obviously, both values were known when carrying out the virtual experiments. Fortunately, η_f could be varied in quite large ranges in the order of magnitude of physically sensible values without harming reconstruction quality. Another

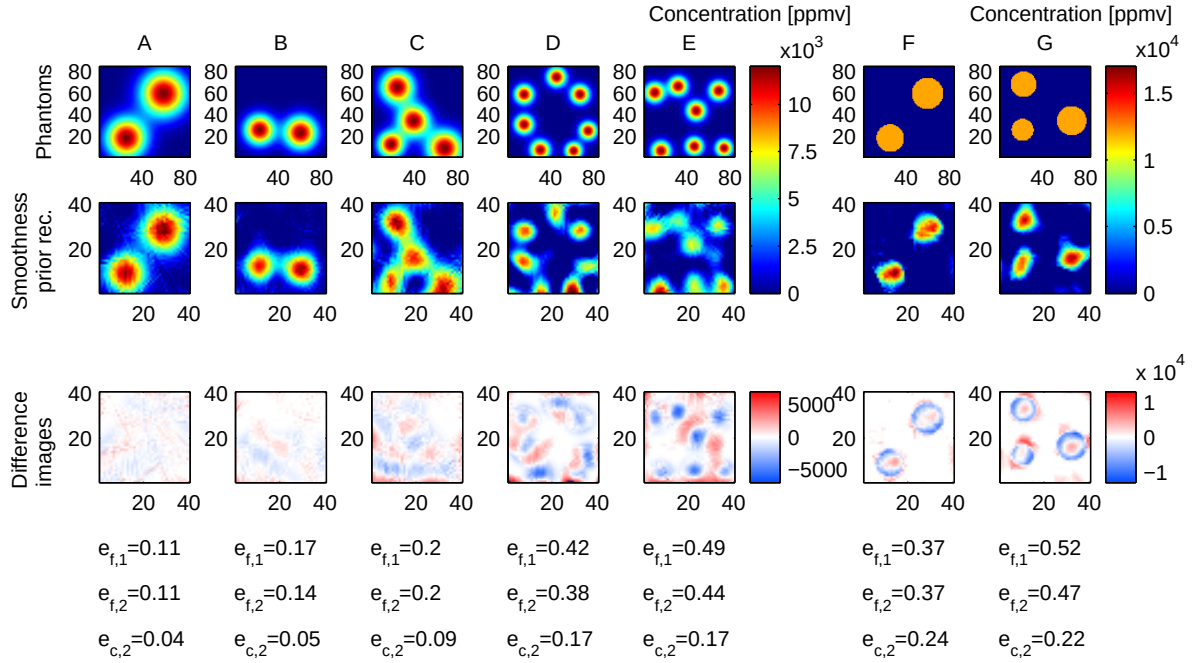

Figure 4.9 Reconstructions of smooth structures (left) and circular sharp-edged structures (right) with the informative smoothness prior. The top row shows the 84×84 pixel phantoms, the second row the 40×40 pixel reconstructions and the bottom row the difference images. The latter were generated by down-sampling the phantoms to 40×40 pixels with a bi-cubic interpolation and then subtracting the smaller phantom from the reconstruction.

parameter that needs to be fixed is the variance of concentrations $\Gamma_f(i,i)$. It has to be made sure that all concentration values that are considered to be realistic have a certain probability. This condition can be expressed by

$$c_{i,max} - \eta_{f,i} = 3 \cdot \sigma_{c,i} \tag{4.31}$$

where $c_{i,max}$ is an upper estimate of possible concentrations and $\sigma_{c,i} = \Gamma_f(i,i)$. Reconstruction quality proved to be insensitive to the choice of $\sigma_{c,i}$ over several orders of magnitude. Like for Tikhonov regularization, the smoothness assumption limits the application of the algorithm to soft-edged features. Very good reconstructions were obtained for Gaussian-shaped phantoms, as can be seen for some examples of phantoms, their reconstructions and difference images in figure 4.9. The corresponding line plots can be found in appendix E, figure E.5. The complete documentation of the virtual experiments can be found in appendix F. Positions and absolute values are correct even for higher numbers of features and deteriorate slightly for phantoms with more than five features. Shapes are reconstructed very good, even if the structures are located closely together or overlap and look still better than the Tikhonov results. Image and measurement errors are only slightly higher compared to Tikhonov regularization.
For top-hat phantoms, a wrong physical smoothness assumption is made about the mea-

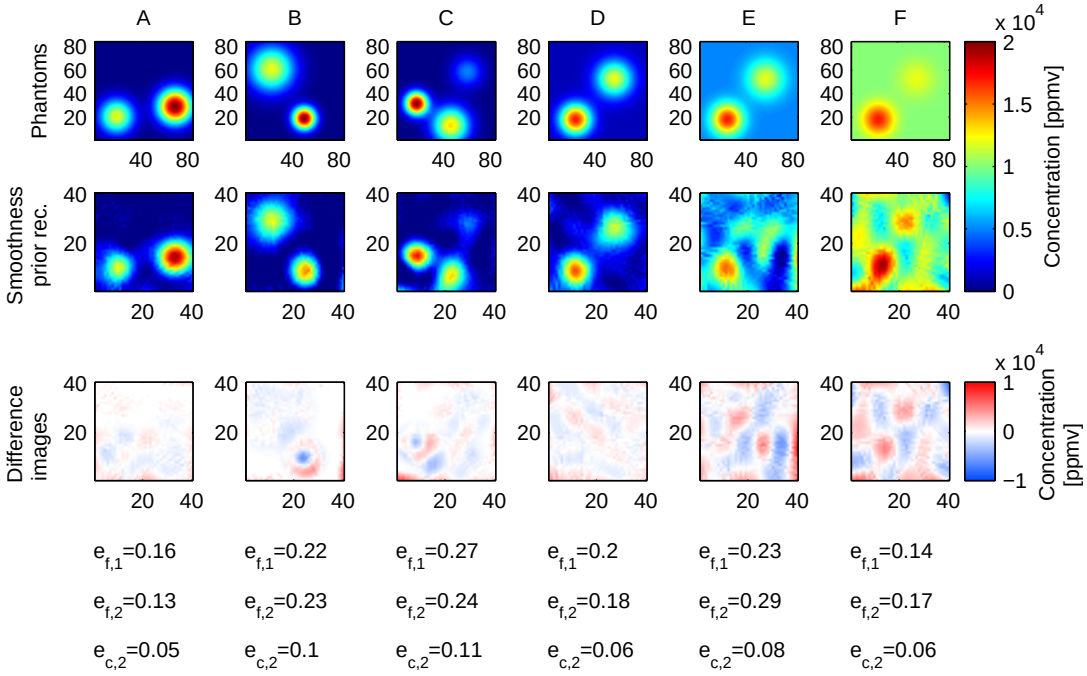

Figure 4.10 Reconstructions of smooth structures with differing concentrations (A – C) and phantoms with non-zero background (D –F) with the informative smoothness prior. The top row shows the 84×84 pixel phantoms, the second row the 40×40 pixel reconstructions and the bottom row the difference images. The latter were generated by down-sampling the phantoms to 40×40 pixels with a bi-cubic interpolation and then subtracting the smaller phantom from the reconstruction.

surement field. Anyway, if only a few structures need to be imaged, the results may look still acceptable. Some examples are given in figure 4.9. Image errors are larger than in the smooth case, absolute concentrations are estimated worse and shapes are slightly distorted and smoothed.

Bell structures have smooth edges, however they are not correctly described by the smoothness prior. The assumption here is that the correlation between two pixels depends exponentially on their distance. In a bell phantom per contra, the correlation of two pixels is very high if they are both situated inside the bell feature or outside the feature, while it is very low if one is located inside and one outside the feature. The region where smoothness in the sense of the informative prior occurs is located only in the sloping edge of the bell function. In the rest of the pixels, the phantom resembles the top-hat case. Therefore, the reconstructed images lead to similar results. They are fully documented in appendix F. The effects of differing feature concentrations and contrast variation are exemplary presented in figure 4.10 (line-plots can be found in appendix E, figure E.6). Differing concentrations can be reconstructed very well, even though images look slightly worse than Tikhonov results for high numbers of features. Image and measurement errors are slightly higher also. The same can be said about the contrast variation results: all reconstruction quality measures are slightly worse than for Tikhonov algorithm, but significantly better than for ART techniques.

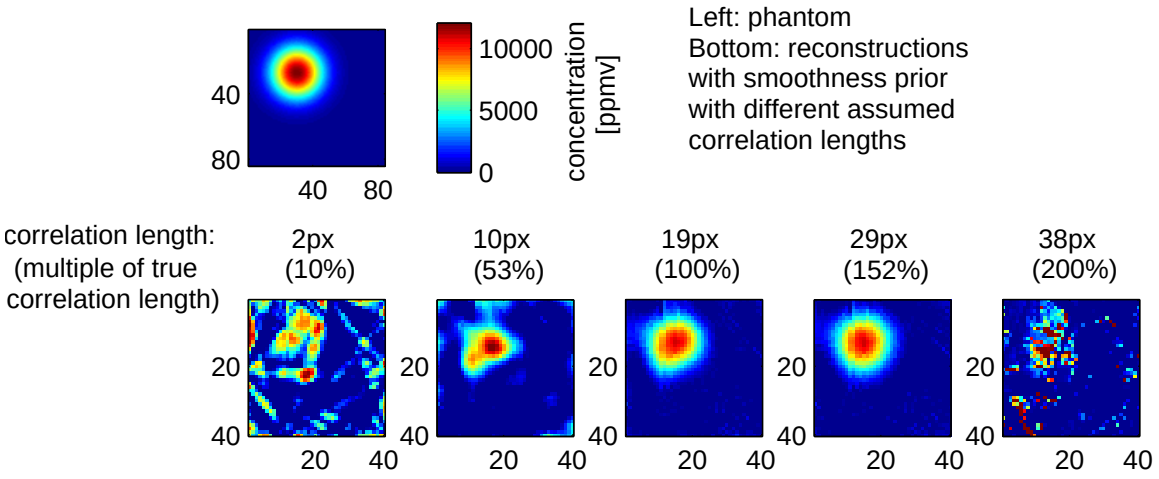

Figure 4.11 Reconstruction of a Gauss-shaped structure with the informative smoothness prior. The correlation length was assumed to have different percentages of the correct length.

In practical applications, the correlation length Λ can only be estimated. Therefore the sensitivity of reconstruction quality on this parameter was also examined. The results are depicted in figure 4.11. In the parameter-study Λ took values between 10% and 200% of the correct correlation length. If Λ amounts only a few pixels, there is hardly any correlation at all and the problem resembles the unregularized case. This equals to not making any physical assumptions at all, enabling an infinite set of solutions. For this reason, the regarding reconstructions look completely erroneous. As soon as there is a significant correlation between the pixels, results improve: Due to the role of the measurements, the algorithm tries to assemble the correct solution by several smaller structures. Even if the image may look slightly awry, structure location and absolute values are estimated correctly. Over-estimation of Λ does not impair the reconstructions as long as not all $\Gamma_{i,j}$ are equal: Even for an over-estimation of more than 50% the reconstructed image is adequate, which is due to the influence of measurement beams crossing outside the Gauss feature. What happens if all $\Gamma_{i,j}$ resemble each other too closely can be seen in the case with $\Lambda = 38px$: like in the unregularized case, no relevant information about the correlation between two pixels exists any more, since all "distances" are treated almost equally. Like it was expected, the reconstruction is useless in such a case.
In practice wrong estimation of Λ is unproblematic as long as real correlation information exists, especially if the characteristic structure sizes are over-estimated. A limitation is of course the discretization: it has to be made sure that correlation lengths are determined in a way that Λ is larger than a few pixels but significantly smaller than the field discretization.
So far, only situations were considered where structure dimensions were radially uniform. In reality there might occur situations where the correlation length actually depends on the direction in the field. Some examples are depicted in figure 4.12. Consider the two inhomogeneous Gaussian phantoms: When using the classical informative smoothness prior, their shapes are squashed in a way that correlation length gets close to uniform.

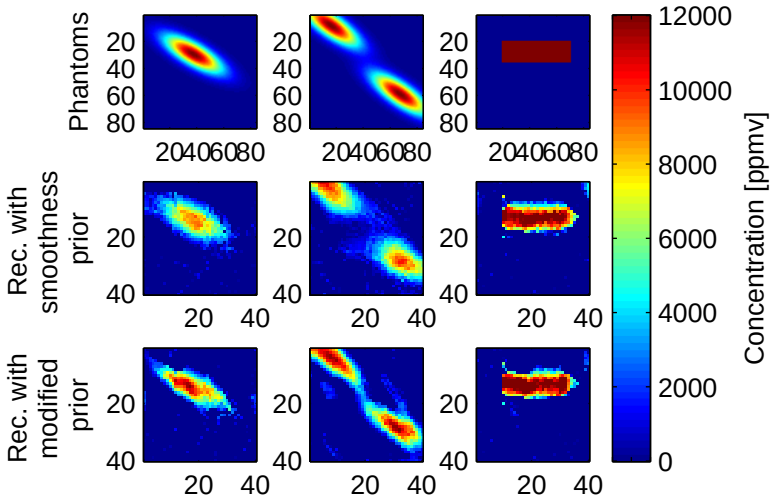

Figure 4.12 Reconstruction of objects with anisotropic correlation length. In the center row, the normal informative smoothness prior results are presented. In the bottom row, the results achieved with a modified, anisotropic smoothness prior are presented.

Although the results do not look bad, still better results can be achieved when a modified informative smoothness prior is implemented.
To clarify this prior, a different view on the correlation length is taken. In the classical version, the correlation length between a fixed pixel i and all other pixels j is described by a scaled discrete two-dimensional Gaussian function with equal standard deviations σ_x and σ_y centred at pixel i. For simplification, the continuous case is considered here. In practice, the discrete coordinates $(x, y)_j$ of each pixel are used. The ith row of the covariance matrix Γ_f is given by

$$\Gamma_i(x, y) = var(\vec{f}) \cdot \exp\left\{ -\frac{1}{2}\left[\frac{(x-\mu_x)^2 + (y-\mu_y)^2}{\sigma^2}\right]\right\} \tag{4.32}$$

where μ_x and μ_y denote the x- and y-location of the ith pixel. Figure 4.13 shows schematically the magnitude of Γ_i for a pixel i in the centre of the image (left). The height of the Gaussian is scaled in a way that the covariance at $\Gamma(i, i)$ has the magnitude of concentration value variance. The bold line shows values of x and y that have a magnitude of 1% of $var(\vec{f})$, so the distance to the pixel i is given by Λ. The modified informative smoothness prior takes into account the anisotropy of covariances between pixels j and i. On the right side of figure 4.13, a schematic example of Γ_i^{mod} is given for a pixel i in the centre of the image. Again, the magnitude is such that $\Gamma(i, i) = var(\vec{f})$, but standard deviations are unequal. Now the x and y values that lead to magnitudes of 1% concentration value variance describe an ellipse instead of a circle. This ellipse is characterized completely by the length of the semi-major axis Λ_1 and the semi-minor axis Λ_2 and the major axis angle γ. In the Matlab-implementation, the values of $\Gamma_f(i, j)$ were calculated by creating a discrete anisotropic 2D-Gaussian for each pixel i and filling the rows of Γ_f with the respective reshaped values. This prior enables us to control two different correlation lengths

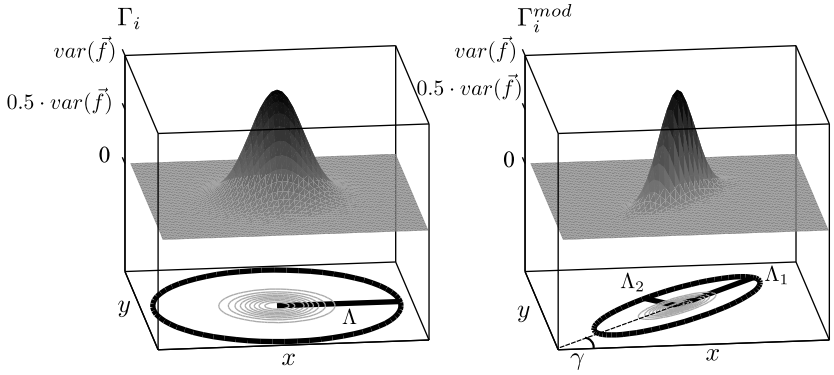

Figure 4.13 Covariance matrix of pixel i for the classical informative smoothness prior (left) and the modified, anisotropic version (right)

and their direction.
Reconstructions that are achieved with the modified prior lead to even better shapes and more accurate absolute concentration values (view figure 4.12). Even the rectangular structure that has completely inhomogeneous correlation length can be imaged with both versions of the prior. Unfortunately, this cannot be turned into a general statement about blocky structures. As can be seen in figure 4.14, such sharp-edged features are mostly not reconstructed very well with the smoothness prior, as is actually expected for a smoothness assumption. The corresponding line plots of figure 4.14 can be found in appendix E, figure E.7. The informative smoothness prior is a good choice for the reconstruction of smooth concentration fields, especially because smoothness can be influenced directly by physical knowledge about the structure sizes and no parameter has to be heuristically determined. The presented variant improves results if structures have inhomogeneous extent in space, which is likely to occur in environmental applications. Blocky circular structures may also be reconstructed if there are only few features in the measurement area.

4.2.5 Bayesian estimation with total variation prior

As for the implementation of the smoothness prior, the general observation model is adapted to the linear case, so that $\mathscr{W}(\vec{f}) = W \cdot \vec{f}$. The posterior density that is given by equation 2.61 now takes the form

$$\mathbb{P}(\vec{f} \mid \vec{c}) \propto \exp\left\{ -\frac{1}{2}\left\| L_n(\vec{c} - W \cdot \vec{f}) \right\|^2 - \alpha \cdot \widetilde{TV}(\vec{f}) \right\} \tag{4.33}$$

The MAP estimate is found by minimizing the objective function O:

$$\vec{f}_{MAP} = \arg\min_f \left\{ \underbrace{\frac{1}{2}\left\| L_n(\vec{c} - W \cdot \vec{f}) \right\|^2 + \alpha \cdot \widetilde{TV}(\vec{f})}_{O} \right\} \tag{4.34}$$

The global minimum may be a vector $\vec{f}$ that takes negative values. To prohibit such un-

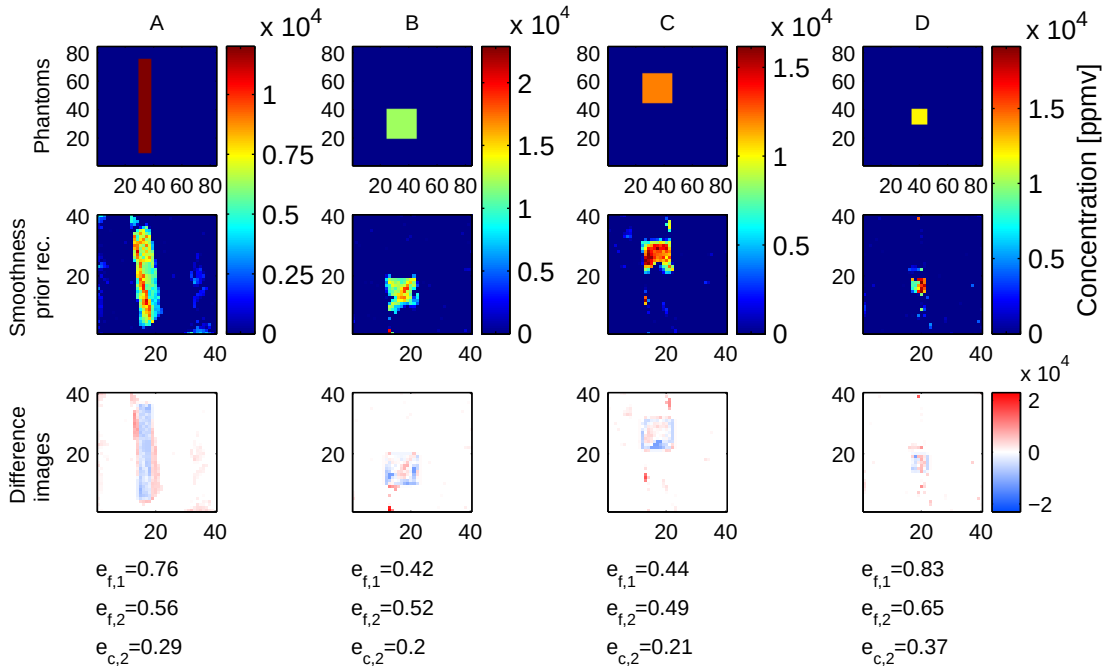

Figure 4.14 Reconstruction of rectangular and quadratic objects with the informative smoothness prior. The top row shows the 84×84 pixel phantoms, the second row the 40×40 pixel reconstructions and the bottom row the difference images. The latter were generated by down-sampling the phantoms to 40×40 pixels with a bi-cubic interpolation and then subtracting the smaller phantom from the reconstruction.

physical solutions, a penalty term is added, like it was done for the informative smoothness prior, such that the objective function takes large values close to zero:

$$O^* = \underbrace{\frac{1}{2}\left\| L_n(\vec{c} - W \cdot \vec{f}) \right\|^2}_{O_1} + \underbrace{\alpha |D\vec{f}|}_{O_2} - a \cdot \underbrace{\sum_i \ln f_i}_{O_3} \tag{4.35}$$

where a is a factor for adjusting the influence of the penalty. Again, minimization was carried out with a self-implemented Gauss-Newton algorithm. Therefore the objective function was split into three terms O_1, O_2 and O_3. The term O_1 is half of the term Z_1 introduced in section 4.2.4 by equation 4.20, therefore derivations of the gradient and Hesse matrix are not repeated. Term O_2 describes the total variation prior part of the objective function. The gradient of O_2 is a vector that is calculated by

$$\begin{aligned}\frac{\partial O_2(i)}{\partial \vec{f}} &= \frac{\partial}{\partial \vec{f}}\left(\sum_{r=1}^{m}\sqrt{(\sum_{j=1}^{n} D_{rj}f_j)^2+\beta}\right)\\ &= \sum_{r=1}^{m}\left(D_{ri}\cdot[(\sum_{j=1}^{n} D_{rj}f_j)^2+\beta]^{-\frac{1}{2}})\cdot(\sum_{j=1}^{n} D_{rj}f_j)\right)\\ &= \sum_{r=1}^{m}[D_{ri}\left((D_R\cdot\vec{f})^2+\beta\right)^{-\frac{1}{2}}\cdot\left(D_R\cdot\vec{f}\right)]\end{aligned} \tag{4.36}$$

The element (q,i) of the Hessian matrix is then derived by

$$\begin{aligned}\frac{\partial^2 O_2(q,i)}{\partial \vec{f}^2} &= \frac{\partial}{\partial f_q}\left(\sum_{r=1}^{m}\left[D_{ri}\cdot\left((\sum_{j=1}^{n} D_{rj}f_j)^2+\beta\right)^{-\frac{1}{2}}\left(\sum_{j=1}^{n} D_{rj}\cdot f_j\right)\right]\right)\\ &= \sum_{r=1}^{m}\Bigg[-\frac{1}{2}D_{rm}\left(\left(\sum_{j=1}^{n} D_{rj}f_j\right)^2+\beta\right)^{-\frac{3}{2}}\cdot 2\left(\sum_{j=1}^{n} D_{rj}f_j\right)\cdot D_{rq}\cdot\left(\sum_{j=1}^{n} D_{rj}f_j\right)\\ &\qquad + D_{rm}\left(\left(\sum_{j=1}^{n} D_{rj}f_j\right)^2+\beta\right)^{-\frac{1}{2}}\cdot D_{rq}\Bigg]\\ \Rightarrow \frac{\partial^2 O_2(q,i)}{\partial \vec{f}^2} &= \sum_{r=1}^{m}\left[D_{ri}D_{rq}\left\{\left((D_R\vec{f})^2+\beta\right)^{-\frac{1}{2}}-\left((D_R\vec{f})^2+\beta\right)^{-\frac{3}{2}}\cdot(D_R\vec{f})^2\right\}\right]\end{aligned} \tag{4.37}$$

The gradient and second derivative of the penalty term O_3 are given by

$$\frac{\partial O_3}{\partial \vec{f}} = \frac{\partial}{\partial \vec{f}}\left(\sum_{i=1}^{n}\ln f_i\right) = \sum_{i=1}^{n}\frac{1}{f_i} \tag{4.38}$$

$$\frac{\partial^2 O_3}{\partial \vec{f}^2} = \frac{\partial}{\partial \vec{f}}\left(\sum_{i=1}^{n}\frac{1}{f_i}\right) = -\sum_{i=1}^{n}\frac{1}{f_i^2} \tag{4.39}$$

In the following, some aspects of the choice of parameters are discussed. Up to now, there is no physical interpretation of the exact value of α, which necessitates a heuristic determination of the parameter. It clearly influences how much weight is put on the blockiness assumption in relation to the fulfilment of the measurement equations. If α gets very low, the objective function resembles the unregularized problem. For large values of α, too much weight is put onto the prior and the measurement is neglected in favour of blocky solutions. With concentration expectation values in the order of magnitude of a few percent, best results were achieved with $\alpha = 10^{-4}$. To keep the influence of the prior constantly strong for other ranges of $\vec{f}$, α has to be adapted. This can be made clear when taking a look at the objective function O again. Suggesting that noise is proportional to $\vec{f}$, the first term of O remains in the same order of magnitude if $\vec{f}$ is changed. Therefore, when the concentration range is changed, the second term should also stay in the same range so that the relation between the two terms stays constant. With the heuristically

determined value of α, a scaling for other concentration ranges can be carried out very easily. Consider two concentration vectors that are scaled by a factor κ:

$$\vec{f_2} = \kappa \cdot \vec{f_1} \tag{4.40}$$

Keeping the second term of the objective function constant, the following must be fulfilled:

$$\begin{aligned} \alpha_1 \cdot |D \cdot \vec{f_1}| &\stackrel{!}{=} \alpha_2 \cdot |D \cdot \vec{f_2}| \\ \alpha_1 \cdot |D \cdot \vec{f_1}| &= \alpha \cdot |D \cdot \kappa \cdot \vec{f_1}| \\ \alpha_1 \cdot |D \cdot \vec{f_1}| &= \alpha \cdot \kappa \cdot |D \cdot \vec{f_1}| \\ \alpha_2 &= \frac{\alpha_1}{\kappa} \end{aligned} \tag{4.41}$$

Similarly, the magnitude of β can be adjusted, which was determined to $\beta = 10^7$ for the above described case. Recall the following approximation:

$$\alpha \cdot |D\vec{f}| \approx \alpha \sum_k^G \Big(\underbrace{(D_k \cdot \vec{f})^2}_{t_1} + \underbrace{\beta}_{t_2} \Big)^{\frac{1}{2}} \tag{4.42}$$

When changing the orders of magnitude, the two terms t_1 and t_2 should grow or shrink to an equal degree for keeping the influence of β constant. This is fulfilled if the relations between t_1 and t_2 remain constant for two vectors scaled according to equation 4.40 :

$$\begin{aligned} \frac{(D_k \cdot \vec{f_1})^2}{\beta_1} &\stackrel{!}{=} \frac{(D_k \cdot \vec{f_2})^2}{\beta_2} \\ &= \frac{(D_k \cdot \kappa \cdot \vec{f_1})^2}{\beta_2} \\ \Rightarrow \beta_2 &= \kappa^2 \cdot \beta_1 \end{aligned} \tag{4.43}$$

Finally, the penalty term weighting factor a (in the presented case $a = 10^{-4}$) can be adjusted accordingly.
The total variation prior is suited for sharp-edged features and therefore leads to good reconstructions of square or rectangular shapes, as is presented in figure 4.15. The corresponding line plots of figure 4.15 can be found in appendix E, figure E.8. Values of $e_{f,2}$ are partly relatively high (>0.4) due to single outlier pixels. In contrast to this, visual perception is much better, since the shapes and absolute concentrations are properly imaged. The case to the very right illustrates that there may occur situations where TV prior fails, presumably quality is phantom-dependent. Another interesting aspect is the magnitude of $e_{c,2}$. Generally, Bayesian estimation will not lead to a measurement that corresponds exactly to the real measured data because of the prior. Here the influence of the total variation prior was such that blockiness was slightly more important than the exact reproduction of the measurement.
Analogue to the studies presented for the preceding algorithms, virtual experiments were carried out for a large variety of top-hat, Gaussian and bell phantoms. The complete

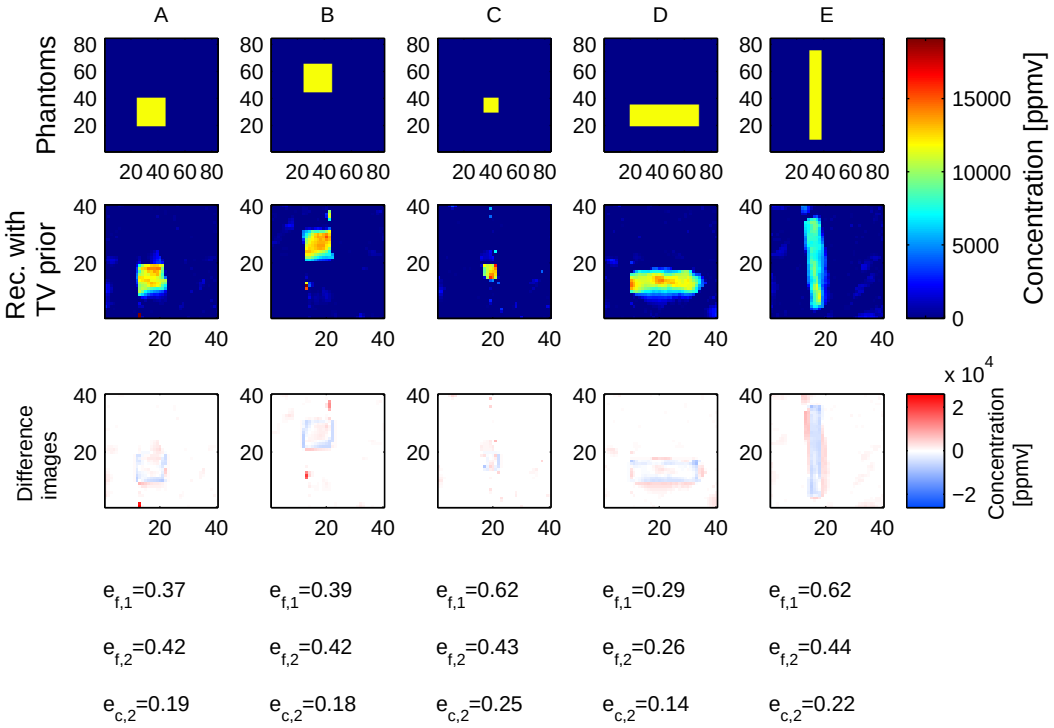

Figure 4.15 Reconstruction of rectangular and square structures with the TV prior. The top row shows the 84×84 pixel phantoms, the second row the 40×40 pixel reconstructions and the bottom row the difference images. The latter were generated by down-sampling the phantoms to 40×40 pixels with a bi-cubic interpolation and then subtracting the smaller phantom from the reconstruction.

study is found in appendix F. Figure 4.16 demonstrates some typical characteristics of TV prior reconstructions. The corresponding line plots can be found in appendix E, figure E.9. Sharp-edged circular objects are reconstructed very well if the number of features does not exceed five. Similar results are achieved for the bell-shaped phantoms, although the edges are more blurred. Despite the smoothness of Gauss function that contradicts the blockiness assumption, good reconstructions can be produced for phantoms with up to four features. Like the other Bayesian estimation techniques, TV prior is able to handle differing feature concentrations as well as decreasing contrast (view figure 4.17, line plots in appendix E,figure E.10). Compared to Tikhonov and smoothness prior, these reconstructions look slightly worse, but significantly better than ART reconstructions.

4.3 Spatial resolution

As it has been demonstrated in the introduction of this chapter, the highest resolvable frequencies of a tomographic set-up can be calculated for an ideal measurement with equally spaced beams. Besides the fact that the measurement paths of the designed instrument are arranged irregularly, in reality spatial resolution is influenced by several sources, for example optical effects, noise, and tomographic algorithms themselves [11].

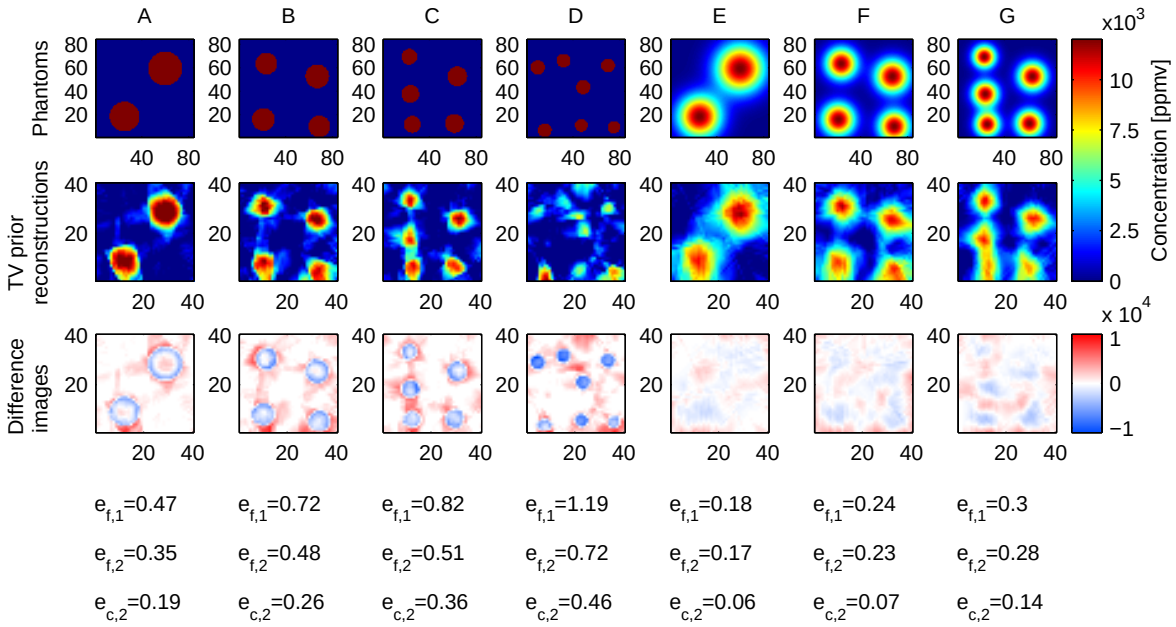

Figure 4.16 Reconstructions of circular shapes with TV prior. Sharp-edged (left) and smooth (right). The top row shows the 84×84 pixel phantoms, the second row the 40×40 pixel reconstructions and the bottom row the difference images. The latter were generated by down-sampling the phantoms to 40×40 pixels with a bi-cubic interpolation and then subtracting the smaller phantom from the reconstruction.

The question of spatial resolution for this reason turns into the determination of the smallest structure that can be resolved with a certain algorithm. It is expected that due to the irregular arrangement of the beams, the critical structure size is not equal at all positions in the field, that is, spatial resolution is non-uniform. Typical measures for describing spatial resolution in imaging are for example the *point spread function* (PSF), the *modulation transfer function* (MTF), the *line spread function* (LSF) or the *edge spread function* (ESF) [11]. PSF and MTF are the impulse response and its 2D-Fourier transform. Even though they could be approximated by reconstructing a phantom with value 1 in only one pixel, the derived information is expected to be worthless since it is assumed that none of the algorithms can deal with such a phantom. Accordingly, the ESF and LSF are the image responses to a sharp edge phantom and a line. Even though the former might be reconstructible with the presented algorithms, it would only allow for statements about this exact phantom because image quality depends on the type of the features like shown in chapter 4.2. Evidently no general statement about spatial resolution is possible, especially it may not be expressed in a single number. In the following, two alternatives are discussed for illustrating the behaviour of the algorithms concerning structure sizes.

The simplest approach is to define spatial resolution as the ability to reconstruct a single structure of a certain size. Of course this ability depends on the location and type of the structure. A study was carried out where for each algorithm, both a top-hat and a Gauss-shaped feature located at 16 different regularly arranged positions were varied in size. It is said that spatial resolution is limited by the smallest reconstructible object

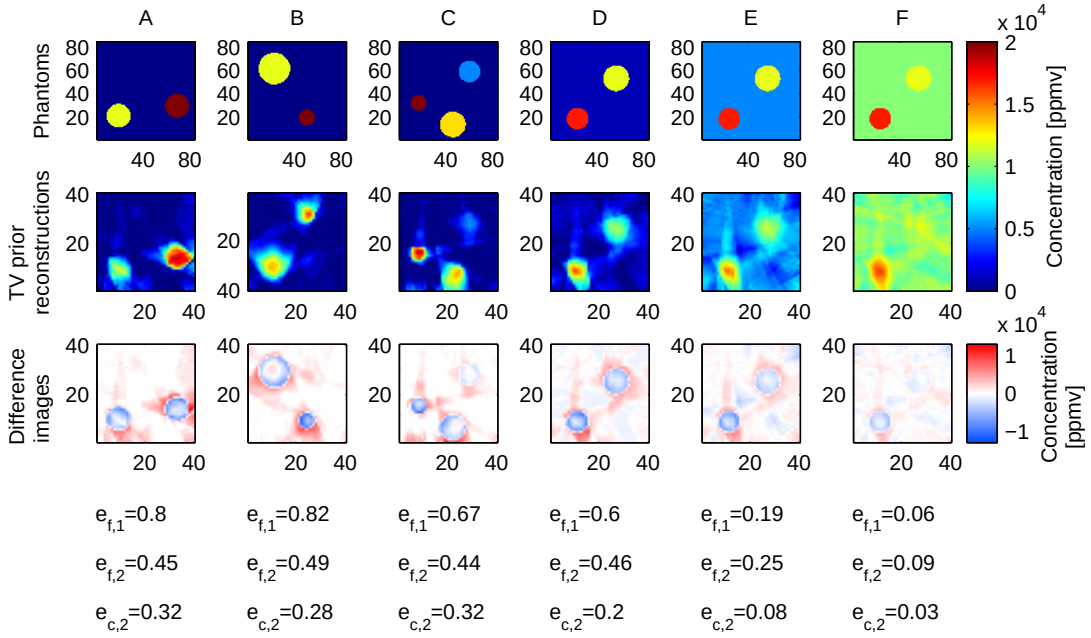

Figure 4.17 Reconstructions of shapes with different concentrations (left) and with non-zero background concentration (right) with TV prior. The top row shows the 84×84 pixel phantoms, the second row the 40×40 pixel reconstructions and the bottom row the difference images. The latter were generated by down-sampling the phantoms to 40×40 pixels with a bi-cubic interpolation and then subtracting the smaller phantom from the reconstruction.

- this leads to the question what "reconstructible" means. Until when is a reconstructed image still acceptable? A quantitative criterion would be limiting the tolerated image errors, but as seen in chapter 4.2 they are not always representative for reconstruction quality. Another way would be to consider the absolute magnitudes of image extreme values. Images that differ in their minimum and maximum concentration values more than a fixed percentage could be discarded, but the choice of this threshold is subjective. Moreover, absolute values may improve if the size of a structure is decreased.

Figure 4.18 shows an example of a Gaussian shaped phantom situated at the edge of the field. Reconstructions with the informative smoothness prior are displayed for structure sizes of the Gaussian feature between 5% and 20% of the field side length. For a structure size of 15% field length, the maximum concentration is underestimated by more than 25%, but decreasing the feature size to a structure size of 10% leads to a quite accurate maximum concentration again. This points out one more difficulty when defining spatial resolution.
Not only the absolute concentration values should be observed, but also the shapes and artefacts. Landweber algorithm is a nice example for situations where extreme values of the concentration may be more or less accurate but image quality is nevertheless inacceptible, as it happens to be for the Gaussian phantom with three features shown in figure 4.5. For this reason, the images were visually assessed, even though this method is subjective. Figure 4.19 depicts the size of the smallest reconstructed structure at 16 different positions for all implemented algorithms while measurement noise was assumed to be 5%. Globally, Tikhonov reconstructions of smooth features yielded the highest spatial resolution. In chapter 4.2 it was illustrated that top-hat structures are harder to reconstruct with Tikhonov regularization due to the non-smoothness. Accordingly it can be seen that spatial resolution is also lower in that case. With smoothness prior, the smallest reconstructible smooth objects are slightly larger. Top-hat features cause difficulties (view chapter 4.2) as the prior is actually not suited for sharp-edged phantoms. Therefore they can only be imaged if they are quite large. TV prior performs even slightly weaker regarding spatial resolution, but astonishingly here both features can be reconstructed equally good since the importance of shape accuracy is not the only criterion when determining the smallest size. Reconstructions with Landweber algorithm commonly look visually worse than in any other case, but as the choice of the smallest tolerated feature resolution is quite complex, spatial resolution is mainly larger than for the Kaczmarz method. At some locations it was not possible to image the phantoms with Landweber at all. The classical ART method yields the lowest spatial resolution. In accordance with the virtual experiments in chapter 4.2, the top-hat phantom results are better than the Gaussian phantom results.
Another influencing factor is the noise level. As has been examined in a study with only 2% measurement noise, spatial resolution generally increases with diminishing noise. One example is shown for Gaussian-shaped objects reconstructed with the informative smoothness prior in 4.20. The grey circular data points show the already presented case with 5% measurement noise. If noise is reduced to 2%, the resolvable structures tend to be smaller, as is indicated by the white squares.
Of course this depiction only gives a very vague impression about spatial resolution. First of all, samples were only taken at 16 positions and it cannot be ruled out that a completely different behaviour occurs if positions are shifted. Additionally, the two chosen, quite theoretical structures do not reveal anything about arbitrary structures that differ from top-hat or Gaussian features. Last but not least, it should be kept in mind that the reconstruction of only one structure is rather simple. In practice, more structures may appear that might even overlap, and so far nothing is known about such a situation. For this reason, another study was carried out with phantoms that show many more smooth structures. Such concentration fields are likely to occur in diffusion-determined systems

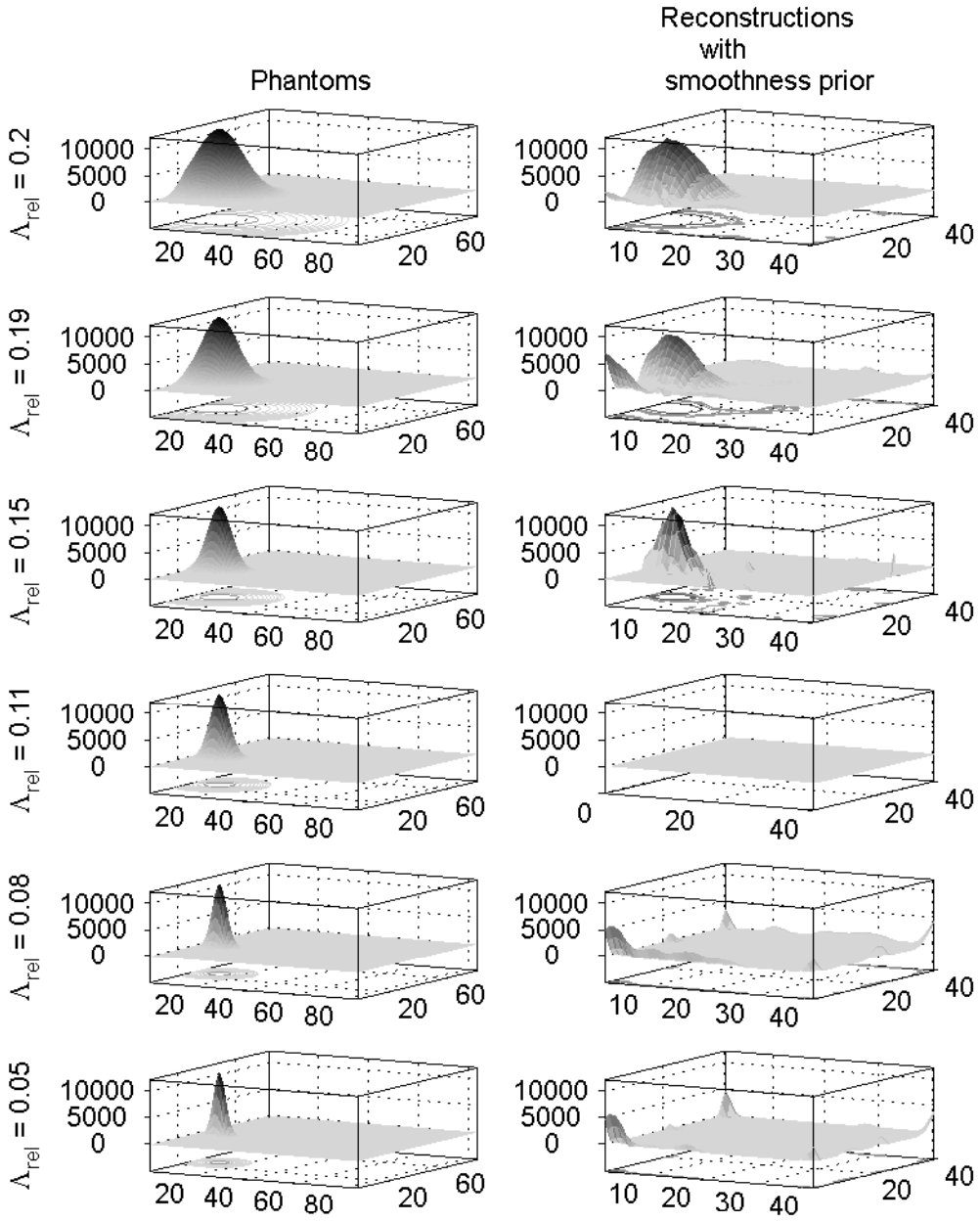

Figure 4.18 Example of determining the spatial resolution of the informative smoothness prior at one feature position: a Gauss-shaped structure is varied in size and reconstructed with the informative smoothness prior.

like the environmental application, but also in combustion processes. The phantoms were generated by drawing random samples from the Gaussian prior density described by the informative smoothness prior. The structure size is directly determined by the choice of Λ. A random sample is the result of a random experiment and thus reveals one of the possible solutions admitted by $\mathbb{P}_{smooth}(\vec{f})$. Naturally, solutions with high $\mathbb{P}_{smooth}(\vec{f})$ are more probable to result as a sample. A random point $\vec{p} \sim \mathcal{N}(0, I)$ in the prior density is chosen, leading to an sample image of $\vec{f}^*$. This sample is determined by

$$\vec{f}^* = L_f^{-1} \cdot \vec{p} + \eta_f \tag{4.44}$$

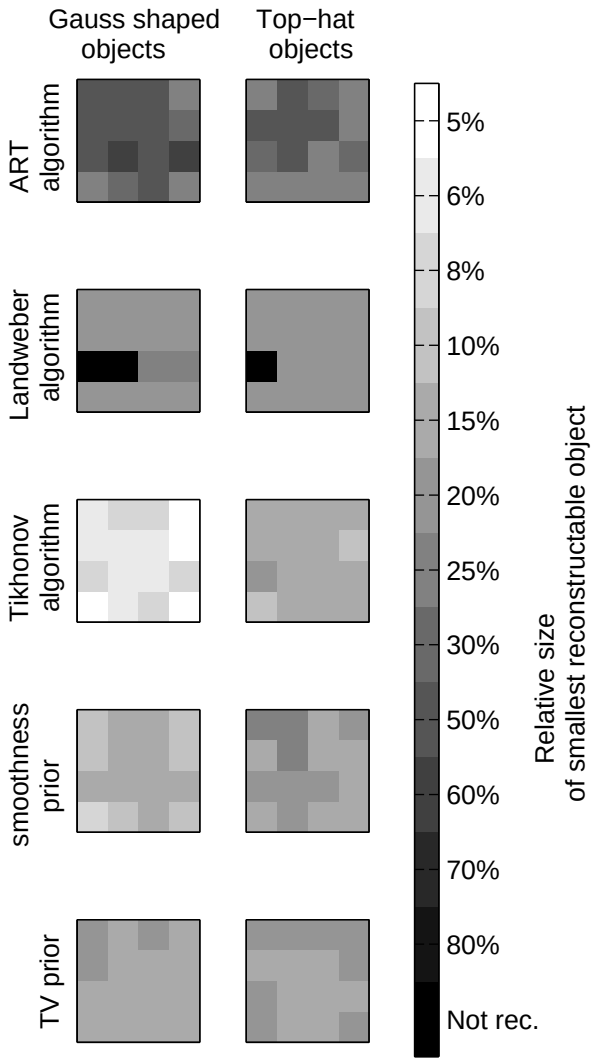

Figure 4.19 Spatial resolution of different algorithms depending on the location in the field and the shape of the structure that shall be reconstructed

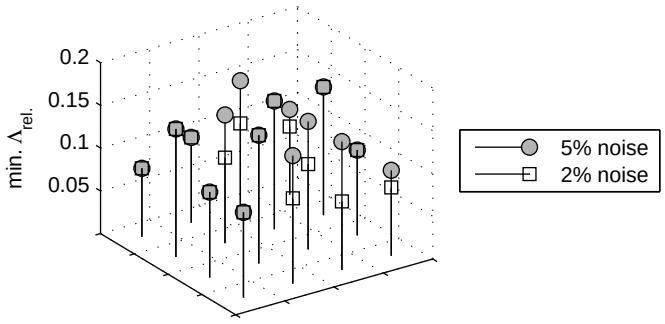

Figure 4.20 Minimum size of Gaussian shaped structures resolvable with the informative smoothness prior for two different noise levels

Structure sizes of the phantoms were varied between Λ_{rel} =0.06 and Λ_{rel}=0.55, where Λ_{rel} denotes the relative structure size to the field edge length. All phantoms were reconstructed with the presented algorithms for three samples at each structure size. An exemplary overview for Λ_{rel} down to 8% field edge length is given in figure 4.21. The only tolerable reconstruction produced by the classical ART algorithm is received for a relative structure size of Λ_{rel} =0.55. Down to structure sizes of Λ_{rel} =0.3, we still get a very rough idea of the concentration field as at least some structures can be recognized. If the structures are further decreased, the reconstructions are more and more blurred, leading to an almost uniform concentration field in the extreme case. It is alarming that measurement errors are not significantly higher than for good reconstructions of other algorithms (view figure 4.22): $c_{e,2}$ is smaller than 0.15 in all cases, so that in real measurements there is no way of detecting an erroneous reconstruction. In those cases, the ART algorithm gets close to one of the infinite solutions that is physically senseless. However, picture errors are large, confirming the visual assessment of the reconstructed images. For both ART and Landweber algorithm, concentrations close to zero appear at the edges of the field, which is certainly also a reason for large image errors.
Even though image errors of Landweber reconstructions are in the same range as for ART, visually the images look poorer because of too strong spatial concentration oscillations. Structures are recognizable down to Λ_{rel} =0.3 and extreme values of concentrations are roughly correct, but the spatial oscillations make results intolerable in all cases. Like for ART algorithm, $e_{c,2}$ is quite small, so that in practice bad reconstructions cannot be distinguished from good ones.
A much better image quality is achieved with Tikhonov regularization, where phantoms are reconstructed nicely down to relative structure sizes of 0.19. For Λ_{rel} =0.15, the rough spatial concentration distribution is still recognizable, even if features are blurred. This can be explained by the smoothness parameter: τ stays constant for all phantoms, as it is more or less inherent to the beams set-up (remember the choice of τ by the SVD of weighting matrices, view chapter 4.2). However, it is a measure for smoothness that in contrast to the informative prior cannot be controlled directly. Smoothness is not equal for all the phantoms, so it is obvious that Tikhonov algorithm does not perform equally

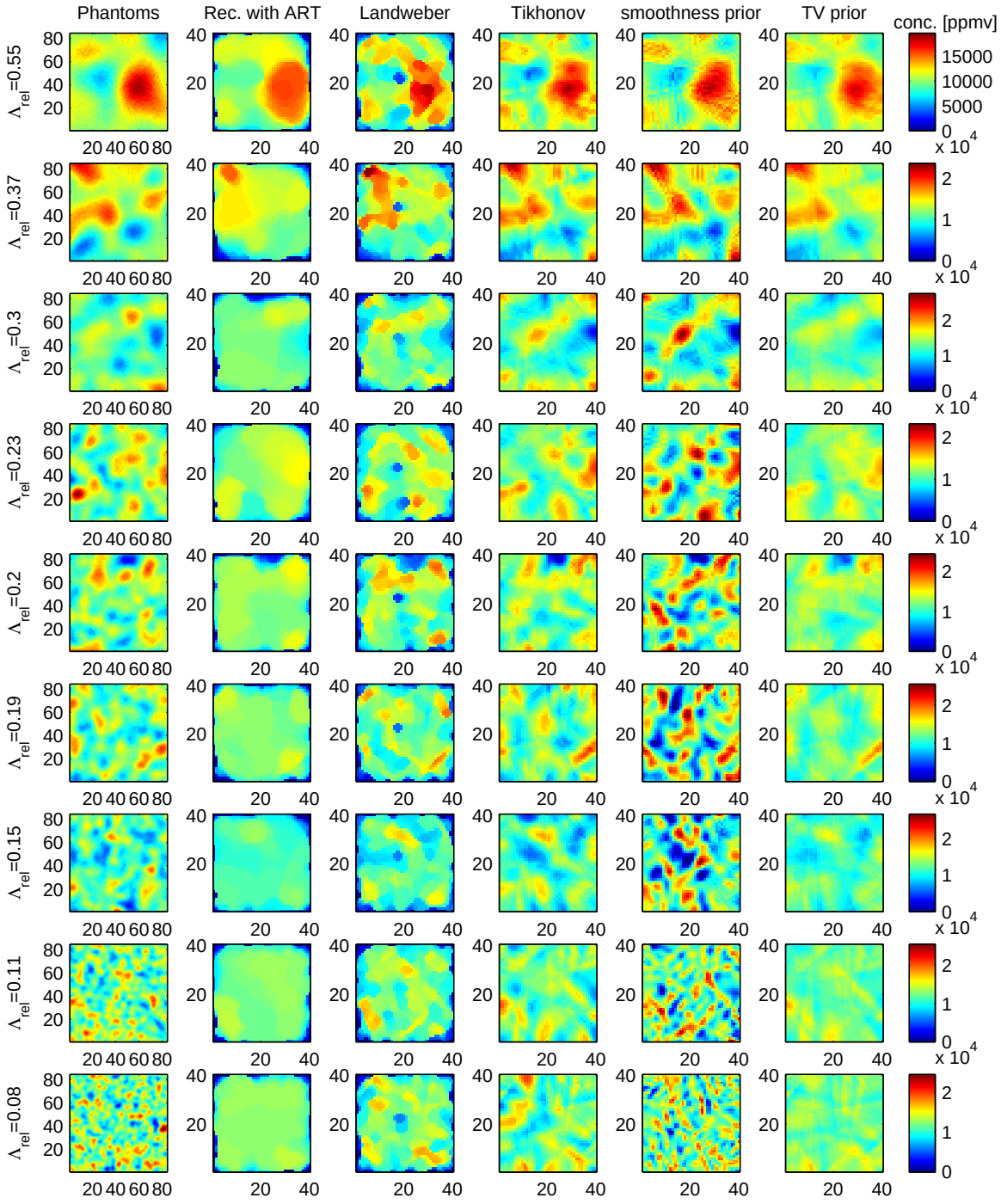

Figure 4.21 Variation of correlation length of drawn samples and reconstruction with 5 algorithms

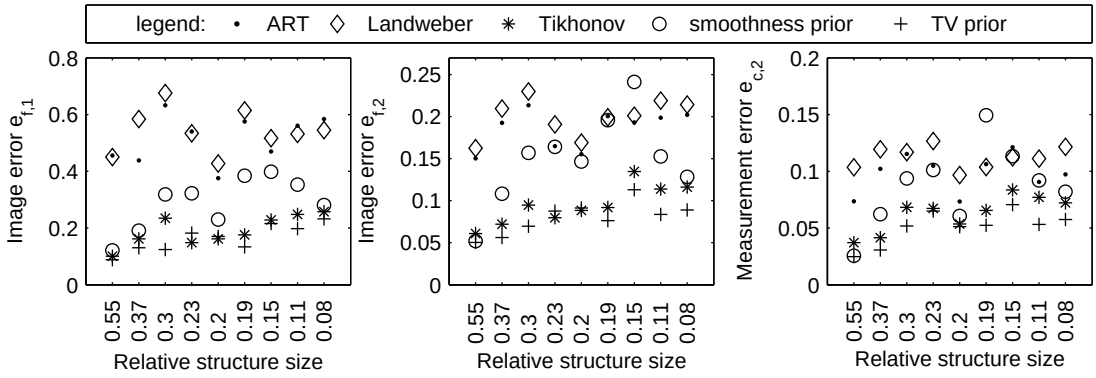

Figure 4.22 Image and measurement errors of the spatial resolution study with random samples

well in all cases. If feature size is decreased such that $\Lambda_{rel} \leq 0.11$, the reconstructions are worthless because they have nothing to do any more with the phantom distributions. The visually interpreted results correspond nicely with the quantitative image errors. For a decreasing feature size, $e_{f,1}$ and $e_{f,2}$ increase, and at the "critical" size of $\Lambda_{rel} \leq 0.15$, $e_{f,2}$ exceeds 0.1 for the first time. Measurement error is small in all cases ($e_{c,2}$<0.1), so the unacceptable cases are plainly close to one of the infinite solutions without any physical meaning.
With the informative smoothness prior, good reconstructions are procured for relative structure sizes down to 19% of the field length, but an increasing overestimation of the absolute concentration values is observed for $\Lambda_{rel} \geq 0.3$, leading to a rise in image and measurement errors. For Λ_{rel} =0.15, the coarse arrangement of structures can still be recognized. For a further reduction of feature sizes, reconstructed absolute concentrations and also structure sizes are accurate due to the nature of the informative smoothness prior, which assigns a high probability to solutions with correct Λ and η_f. Despite the fact that image errors get even smaller, those solutions are completely worthless since the structures are somewhat randomly arranged and have nothing to do with the real situation.
Total variation prior is actually not suited for the smooth random samples, but reconstructions look astonishingly good for $\Lambda_{rel} \geq 0.3$. A further reduction of the structure size leads to smoothing, but acceptable reconstructions can be produced for down to 19% field length. Afterwards, the TV prior tends to find solutions without any physical meaning.

All in all, although the question of spatial resolution cannot be answered comprehensively for the above described reasons, the presented studies give a rough idea of the possibilities that each algorithm offers. Shortly, the algebraic reconstruction techniques have the lowest spatial resolution of the tested algorithms. The Bayesian priors of course behave differently, depending on the phantom type, because the explicit physical assumptions do not describe all phantoms equally well. The smallest objects could be reconstructed with Tikhonov regularization, although smoothing gets stronger for small structures. The informative smoothness prior almost performs equally good for smooth phantoms, at the same time it offers a direct way of controlling smoothness, so that the reconstructions

of larger objects are partly more accurate than with Tikhonov regularization. Spatial resolution of the total variation prior is slightly smaller in the smooth case, but generally the best for sharp-edged phantoms.

4.4 Calculation time

Despite the fact that calculation time depends on the efficiency of the computer, some typical characteristics of the algorithms concerning computation speed can be elucidated. The investigated algorithms can be grouped into simple iterative techniques and techniques that require some sort of minimization. While in the former case, computation speed is inherent to the algorithms themselves, the implementation of the minimization is no specific characteristic of the Bayesian algorithms. For this reason, more general examination is possible for the algebraic reconstruction techniques, whereas for the Bayesian estimation, mainly insights about the implemented versions are gained.
The classical ART technique, or Kaczmarz algorithm, computes M updates of the vector $\vec{f}_{rec}$ at each iteration, M being the number of measurement paths. The computation of one update is a simple matrix equation. Additionally, after each update the image is smoothed by a median filtering operation and negative values are set to zero. The number of iterations can either be controlled by a fixed number of iterations or by a stop criterion. For example, iteration can be interrupted if ϵ falls beneath a certain threshold. The absolute computation effort is determined by the choice of this threshold or the maximum number of iterations.
In contrast to ART, Landweber algorithm requires only one update of the image per iteration, again this is realized by a simple matrix equation. Again, negative values are set to zero and the image is smoothed by a median filter at each iteration. Before the iteration begins, Landweber requires two more calculation operations: The regularization parameter $\alpha_{LW} = 2/\max(eig(W^T W))$ needs to be computed once for unaltered weighting matrices. In practice, the amount of usable beam paths varies, so that α_{LW} has to be computed for every measurement. Furthermore, an initial guess is computed by a simple matrix equation.
In contrast to algebraic algorithms, the calculation time of Bayesian estimation techniques is influenced by the time required for minimization and by preparing calculation steps that are typical for each algorithm. First, the algorithm-specific parts are considered since they do not change with the implementation. For Tikhonov regularization, the discrete Laplace matrix $\mathcal{L}$ is required. For enhanced speed it can be calculated once for a fixed discretization and then be called during reconstruction. For each measurement, the augmented matrices and vectors are created by simple concatenation. For Bayesian estimation with the informative smoothness prior, the covariance matrices of noise Γ_n and concentration Γ_f and their Cholesky factorizations L_n and L_f have to be computed for every measurement. The computation of Γ_n is very fast since it is only a diagonal matrix with the measurement noise vector on its diagonal. In Matlab, a simple command exists for filling this diagonal with the correct vector (`diag`). Building Γ_f is quite intricate: for every pixel all covariances to all other pixels have to be calculated. For an N-discretized image it needs N^2 computation steps. A method to accelerate this process can be used if discretization of the reconstructions remains the same. Then, the matrices Γ_f can be

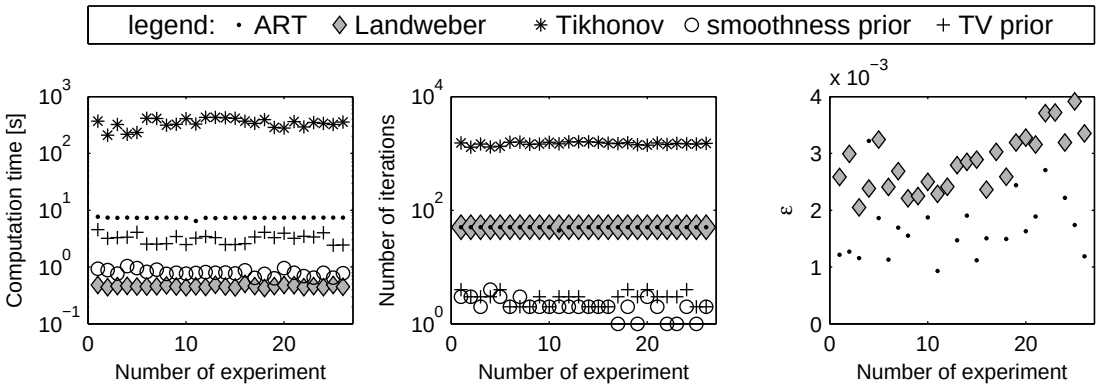

Figure 4.23 Calculation time study with 26 simulated experiments

pre-computed once for all possible values of Λ, and the corresponding covariance matrix can be called from a look-up table during reconstruction.
For TV prior minimization, the discrete neighbourhood matrix D and again Γ_n and L_n are necessary. D is built by a simple assignment of neighbourhood values that takes places N times, where N is the number of pixels. This computational step can be outsourced as well for a fixed discretization.
Another crucial part that requires calculation time during Bayesian estimation is the minimization of the objective function. For non-negative least-squares curve fitting problems in the form of $\min_{\vec{f}} \left\| W \cdot \vec{f} - \vec{c} \right\|_2^2$, Matlab offers the `lsqnonneg`-algorithm which was used for minimization during Tikhonov regularization. The objective functions of smoothness prior and TV prior cannot be minimized with this algorithm. Methods for finding local minima of constrained non-linear multivariate functions that are already implemented in Matlab are for example `fmincon` and `patternsearch`. Unfortunately, none of the algorithms provided by Matlab converged to a solution for the given problems. Therefore, the self-implemented Gauss-Newton technique demonstrated in chapters 4.2.4 and 4.2.5 were used. In both cases, at each iteration, the gradient and Hessian of the objective function habe to be calculated and the step-width is optimized by a line-search algorithm.
To give an impression of the calculation speed as it is achieved with the present implementations, the reconstruction durations and their respective number of iterations of 26 simulated experiments were recorded (view figure 4.23). Of course results depend on the efficiency of the computer. The study was carried out with an Intel Core i7-2700K processor with 3.5 GHz rate, four cores and two threads per core.
Tikhonov regularization requires a multiple of time compared to all other techniques. Values lie between about 200 s and more than 400 s. On the one hand, one optimization step takes longer than one iterative update of algebraic techniques. On the other hand, `lsqnonneg` requires many more iterations than all other techniques (view figure 4.23), that means more than 1000 iterations in comparison to less than ten when other Bayesian techniques are used. For algebraic reconstruction algorithms, the maximum number of iterations was set to 50, and in all but one cases the residual ϵ surpasses the pre-set threshold value of 10^{-3} (view figure 4.23). Even though the number of iterations is almost always equal for the algebraic techniques, calculation time differs strongly: ART takes between

six and eight seconds, thus being the second-slowest algorithm, while Landweber requires only about half a second. The latter is the fastest technique although informative smoothness prior and total variation prior only need less than five iterations because of course the simple matrix equation is solved much faster than a single optimization step. ART of course needs many more calculation steps in one iteration than Landweber, as it is described above.
Although Bayesian techniques need very few iterations, they are a bit slower than Landweber algorithm. Smoothness prior reconstruction takes between 0.6 s and 1 s, while TV needed between 2.4 s and 4.5 s. TV prior is slower than informative smoothness prior mainly for two reasons: In the given implementation, the matrix D is built once for every measurement, which could be outsourced in future implementation. In addition to that, the generation of gradients and Hessian matrices is more complicated for the total variation prior.

Chapter 5

Tomographic measurements

Before the measurement instrument is applied for real measurements in the environment, it has to be made sure that it is able to deliver reliable tomographic reconstructions. It is not sufficient to rely on the results that were achieved in the virtual experiments. Validation should also take place with the measurement of known concentration fields. On this account, experiments were carried out with different circular jets emitting gas of defined composition. By this means, the shapes and concentrations of the features in the field could be controlled. Reconstructions could then be compared with the assumed approximate concentration fields.
The following sections deal with tomographic measurements of three circular laminar jets emitting mixtures of methane in nitrogen. Laminarization was realized with a filling consisting of several layers of glass padding and glass beads that have decreasing diameter in the direction of flow. The emission of defined mixtures of methane and nitrogen was controlled by two mass-flow controllers. The measurements took place in a plane that was 5 mm above the jet exit.
In chapter 5.1, the evaluation of mean concentrations with TDLAS is demonstrated. Aspects of precision and signal to noise ratio are discussed. Afterwards, tomographic reconstructions of the laminar jet experiments are presented. Since the jets emit quite sharp-edged profiles in the measurement plane, the total variation prior is a sensible physical assumption. Therefore all experiments were reconstructed with TV prior. However, in chapter 4 it has been revealed that in some cases Tikhonov regularization and the informative smoothness prior also yield good reconstructions of sharp-edged features, so they have been tested also.
Not only the instrument and the reconstruction algorithms have an influence on image quality, but also the measurement object itself. The suitability of TDLAS is impacted by absorption strength, which may vary strongly in spatially inhomogeneous systems. Chapter 5.2 gives an overview about the effects of unequal absorption strengths during tomographic measurements. Another crucial issue is measurement speed. In chapter 3 it was shown that instrument precision depends on the relation between laser tuning frequency and rotation speed of the polygon scanner. Evidently the reconstructions are therefore affected by speed also, which is examined in section 5.3. The possibilities of tomographic concentration field reconstructions are not unlimited regarding the complexity of the measurement object. For example, in chapter 4 it has been shown that image quality deteriorates for large numbers of objects. Positions of the features are also decisive. The effects occurring when making the concentration field more challenging are elucidated in section 5.4.

Absorption band	Absorption line	Wavenumber
$2\nu_3$	3F2 1 ← 4F1 1	6046.94 cm^{-1}
$2\nu_3$	3F1 1 ← 4F2 1	6046.95 cm^{-1}
$2\nu_3$	3A2 1 ← 4A1 1	6046.96 cm^{-1}

Table 5.1 Wavenumbers of the used absorption lines of CH_4

5.1 Evaluation of mean concentrations

Methane path-averaged concentrations were evaluated by fitting a Voigt function to the superposition of three broadened absorption lines centred at a wavenumber of 6046.95 cm^{-1}. The exact spectral positions, absorption bands and quantum numbers are listed in table 5.1. The line selection was carried out according to [69]. In this absorption band, the rovibronic transitions are split up into three absorption lines that are situated closely together and are therefore united into one Voigt fit [70]. A DFB laser was modulated over a spectral range of about 1 cm^{-1} with a tuning frequency of 5039.8 Hz. For a DFB laser, this frequency is quite high, limiting the spectral range significantly. If tuning rates shall be further increased, other diode lasers like VCSELs (*vertical cavity surface enhanced lasers*) have to be applied. Witzel et al. [6] compare the dynamic tuning ranges of DFB and VCSEL lasers. It was demonstrated that very fast wavelength tuning frequencies of up to 30 kHz can be achieved with VCSELs, while the tuning range still amounts more than eight wavenumbers. Spectroscopic data required for the evaluation, like line strengths and positions or pressure and temperature broadening coefficients, were taken from the HITRAN2012 database [71]. The base-line was fitted with a third order polynomial in all cases.

The performance of the TDLAS fitting varied strongly throughout the measurements due to absorption strength variation and non-uniform signal intensity. As each beam sees a different absorption path, concentrations and path lengths differ. Both parameters impact absorption strength and consequently the quality of mean concentrations and tomographic reconstructions. Since this topic is quite substantial, it is illuminated more detailed in section 5.2. During one field scan, reflectivity fluctuates depending on the position and incidence angle of the laser beam, like it was presented in chapter 3. TDLAS is not reliant on absolute light intensities, therefore reflectivity should not have any influence on the absolute concentration values. However, it affects signal to noise. In the following, some aspects regarding precision and signal to noise of the tomographic TLDAS measurement are clarified.

Consider the measurement carried out with a single laminar jet positioned approximately in the center of the field. Figure 5.1 schematically illustrates the position of the jet and the propagation of the laser beams in the measurement area. Only very few laser beams cross the gas jet and therefore are absorbed significantly, whereas most beams are only absorbed by the amount of methane in the surrounding air, which amounts around 1.7 ppmv [72]. The concentrations and signal to noise ratios measured at each of the four channels are depicted in figure 5.2. It can be seen that concentrations and SNR vary not only during one field scan, but that at fixed positions they have standard deviations that are not negligible. To foreclose the possibility that absolute concentration values are influenced

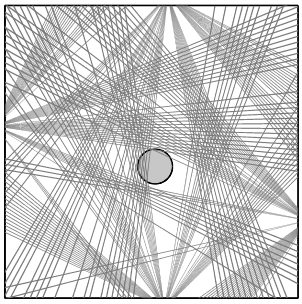

Figure 5.1 Beam arrangement and jet position of an exemplary measurement

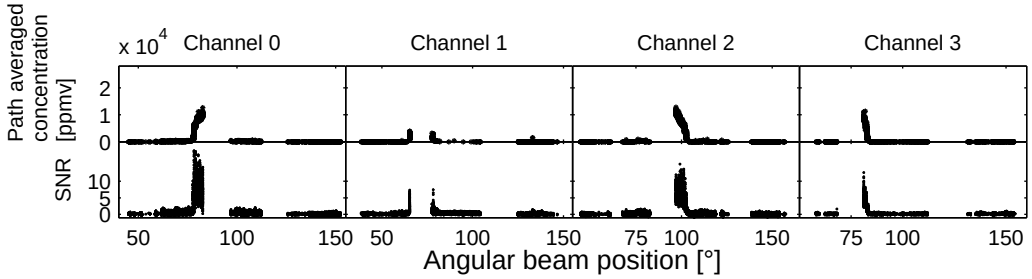

Figure 5.2 Concentration and SNR of an exemplary measurement with one laminar jet

by absolute light intensities in any way, repetitive measurements at a fixed position are observed. In figure 5.3, the mean concentrations for eleven successive measurement realizations of a fixed beam are plotted. Likewise, the maximum detected voltage of the light signal is depicted, which is a direct measure for the intensity of the reflected light. Each of the five polygon facets leads to a slightly different reflectivity, since the beam is vertically displaced to a small degree because of the imperfect alignment of the polygon inside the

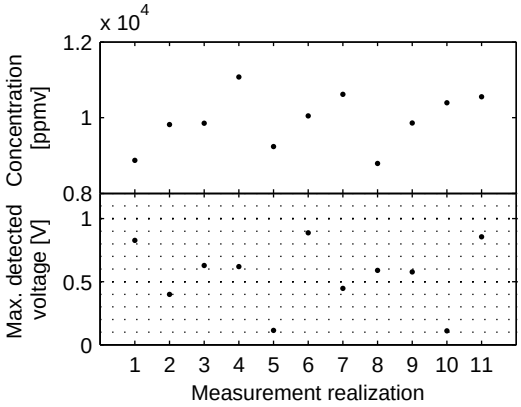

Figure 5.3 Variation of concentration and maximum detected voltage of different realizations of the same measurement

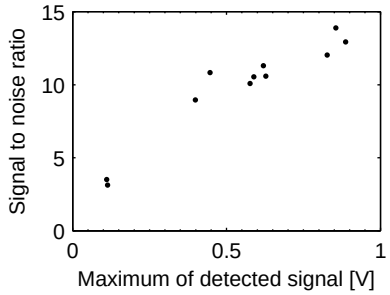

Figure 5.4 SNR depending on the maximum value of the detected wavelength-tune voltage

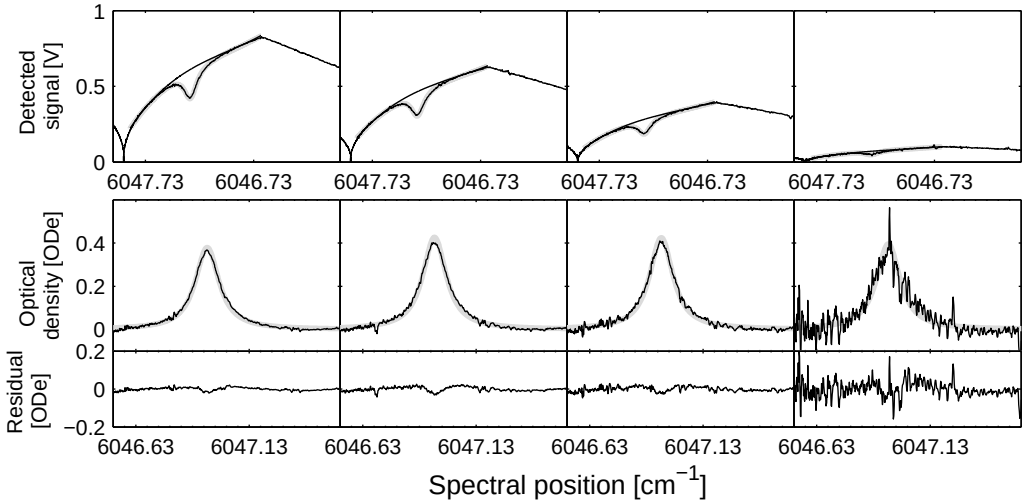

Figure 5.5 Wavelength-tunes, measured and fitted optical densities and residuals of measurements at the same beam position and concentration, for four different realizations

scanner box. It was made sure that there is no correlation between the magnitude of light intensity and the absolute concentrations. The variance in concentration might therefore arise from limited precision or from real concentration fluctuations. The gas mixture was generated by two mass-flow controllers defining the proportional amount of gas that was emitted. If one or both of the MFCs deliver a slightly unsteady flow, concentration deviations occur. For the above presented case, concentration varies by $7\%_{vol}$, a value that might as well originate from the mass-flow controllers. The MFCs were controlled in a range that amounted only between 7 and 12% of their maximum flow.
As far as signal to noise ratio is concerned, the deviations result from the variation of light intensity. As long as the residual between the measured signal and the Voigt fit is dominated by electrical noise, signal to noise ratio depends essentially on the intensity of the reflected light. In figure 5.4, the SNR of the above described measurement at a fixed angle is plotted against the maximum detected voltage of the amplified photo-diode current. The five facets lead to different reflectivity at a fixed angle, and therefore also to varying signal to noise. It is demonstrated in figure 5.5 how residuals and accordingly signal to noise varies if only the light intensity is changed. Four different realizations

of a concentration measurement at a fixed beam are presented. Concentration and and absorption path length stay the same, and so does optical density as it is a direct measure for absorption. All measurements are corrupted with electrical noise. Its absolute magnitude stays the same, therefore TDLAS signals with small voltages are corrupted relatively stronger. The optical density is constant for the shown examples, therefore the SNR, which is defined by $SNR = \frac{OD_{e,max}}{\sigma_{res.}}$, decreases.
This effect is dominated by errors caused by the imperfect absorption line broadening model at high absorptions. Saturation is reached when at some wavelengths all of the light is absorbed. The used software is not capable any more to fit a correct model, so that completely senseless concentration values and signal to noise ratios are computed. If there is no detectable absorption, that means noise is larger than absorption, the fit fails and produces misleading concentration values and signal to noise ratios smaller than one. Issues of signal quality that is determined by absorption strength are further discussed in the following chapter.

5.2 Influence of absorption strength

In tomographic absorption spectroscopy, absorption strength is a complex issue because it is influenced by concentration as well as the length where absorption takes place. Therefore, absorption can vary strongly and it has to be made sure that at least a decent amount of measurement paths can be evaluated. For the jet measurements, absorption takes place almost only where the gas is emitted. Methane concentrations in the air are around 1.7 ppmv and are not detectable with the given set-up. Their influence on the overall absorption can be neglected since errors resulting from imperfect fitting are larger. The actual absorption length in this case results from the size of the jets and the beam propagation through the emitted gas flow. Figure 5.6 depicts the detected voltages, optical densities and fit residuals of four laser beams that intersect differently with the laminar methane flow. The concentration of the absorbing gas is constant for all cases and amounted $10\%_{vol}$, but the relative path length where absorption takes place varies. For many beams, no absorption at all can be detected, either because the beam intersects with the absorbing medium too shortly or not at all. Such a case is presented in the very left plot, where the relative absorption length was zero. The used spectroscopic evaluation software delivers no sensible concentration data in such cases. Nevertheless there is information about these measurement paths: if SNR drops to values smaller than one, it is known that their integrated concentration value is below the detection limit of the system. Mean concentration values can be set to zero, and in case the measurement noise is modelled its value for the corresponding path is set to the detection limit, enabling all solutions smaller than this. Three more examples with rising absorption length are given in figure 5.6. For large absorptions, the Voigt model does not describe the broadening accurately anymore, resulting larger residuals at the center of the line. Hence for beams with large relative absorption paths a decline of signal to noise ratio is observed. An exemplary measurement with two jets emitting a mixture of $10\%_{vol}$ methane in nitrogen is shown in figure 5.7. The above described effect can be seen very plainly for channel 1. Here, one jet is crossed by beams with angular positions between about 80° and 100°. The path integral concentration rises with increasing relative absorption path length and

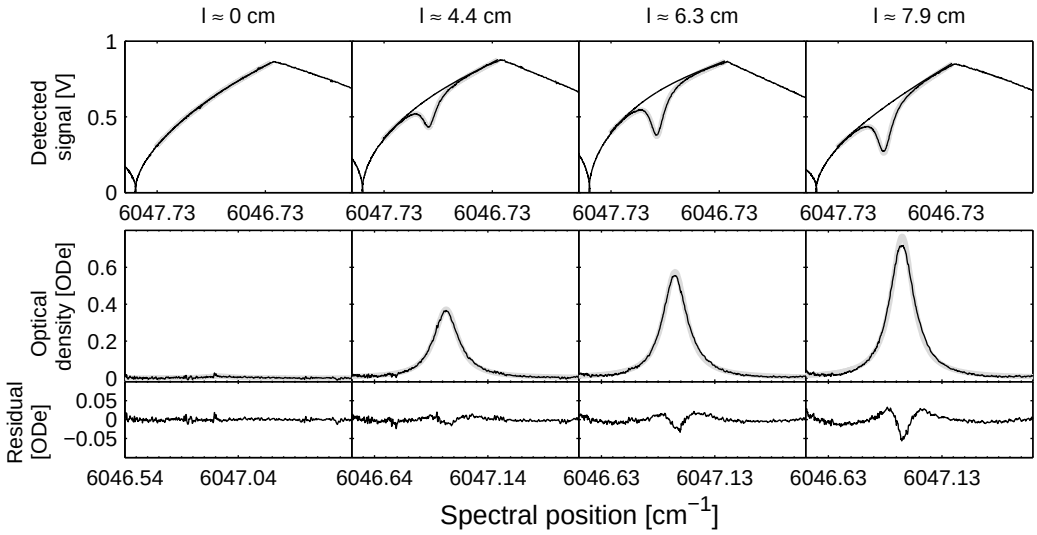

Figure 5.6 Wavelength-tunes, measured and fitted optical densities and residuals of measurements at different absorption lengths

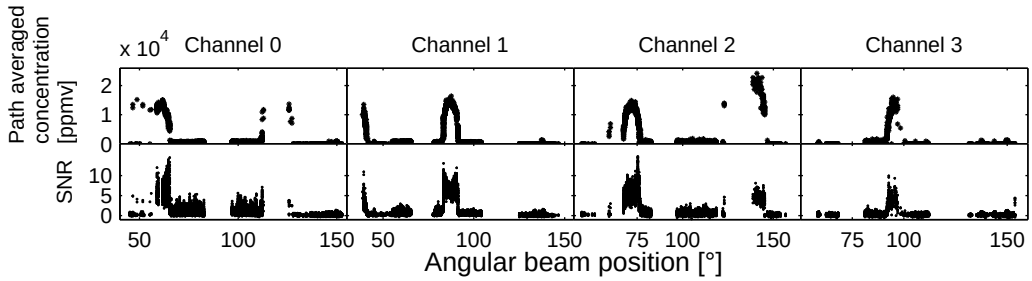

Figure 5.7 Path-averaged CH_4-concentrations and SNR measured while two laminar jets are running. Gas mixture of the jets was $10\%_{vol}$ CH_4 in N_2.

so does the SNR if absorption does not exceed a certain threshold, since electrical and optical noise stay more or less constant and optical density rises. If the absorption path grows further, SNR drops because now it is dominated by the error resulting from the inaccurate Voigt model.
The length of the absorbing path in all cases stays relatively small because of the structure sizes. Absorption could be raised up to saturation by varying the concentration of the methane/nitrogen mixture. Figure 5.8 demonstrates the evaluation of experiments carried out with four different methane concentrations measured at a fixed beam position. The quality of the Voigt fit deteriorates with rising concentration. On the one hand, the Voigt model is not accurate any more for large absorptions. On the other hand, at large absorptions the line is broadened to such an extent that absorption does not get zero throughout the whole spectral tuning rate of the laser, which was only about 1 cm^{-1}. In those cases, like for example at $14\%_{vol}$ methane concentration at the presented path length, the base-line fit is deficient and therefore so is the Voigt fit. The worst case is if saturation occurs, as can be seen in the example with $50\%_{vol}$ methane. The spectrometer

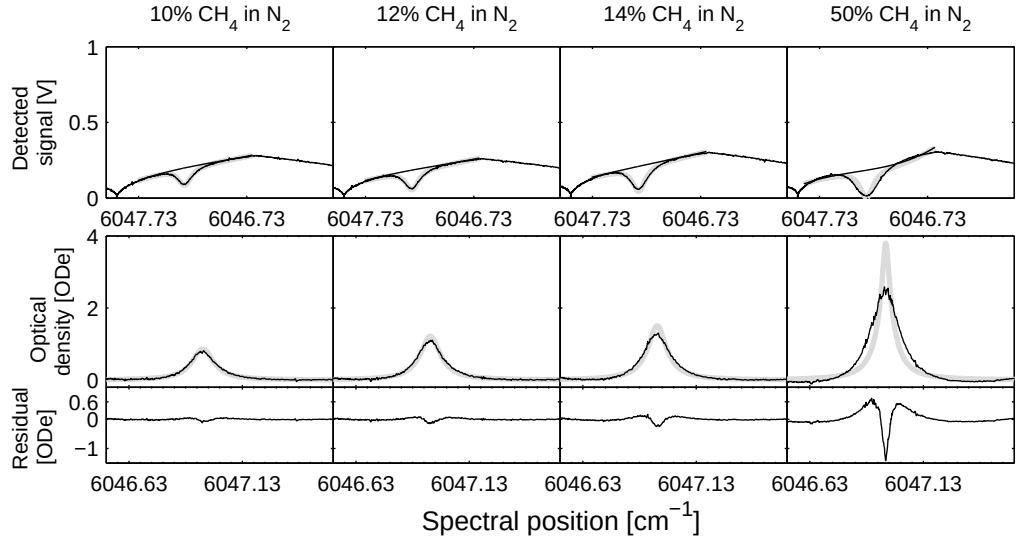

Figure 5.8 Wavelength-tunes, measured and fitted optical densities and residuals of measurements at different concentrations

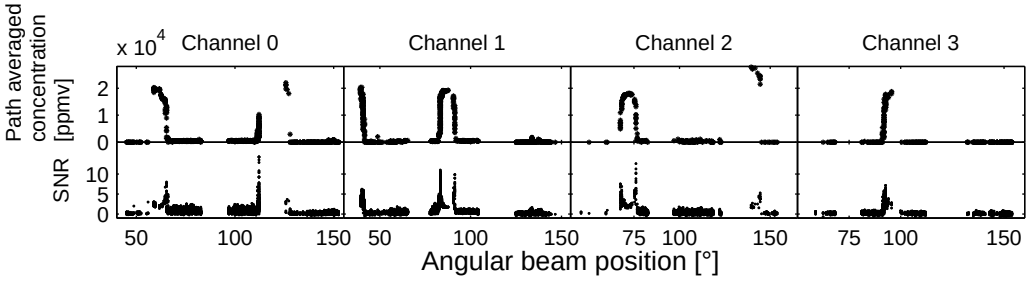

Figure 5.9 Path-averaged CH_4-concentrations and SNR measured while two laminar jets are running. Gas mixture of the jets was $50\%_{vol}$ CH_4 in N_2.

software is not able to compute sensible concentrations any more since it intends to fit a Voigt profile, which does not describe the saturated line any more. Calculated mean concentrations are corrupted with large systematic errors and in some cases no fit is possibe at all.

An example for a measurement where saturation occurs at some measurement paths is given in figure 5.9 Here, the methane concentration amounted $50\%_{vol}$. Many beam paths could not be evaluated at all despite good reflectivity due to saturation. For some beam paths there are large systematic errors in concentrations: If for example channel two is considered, a very sudden drop of SNR is observed for angular positions around 70°, where absorption path lengths increase. Here the situation depicted in figure 5.8 occurs: concentration is underestimated strongly because the fitted line is much too narrow.

The influence and dynamic range of the expected absorption should be considered before real measurements are carried out. It has to be made sure that the expected mean concentrations can be evaluated with the used spectral lines. This insight leads to two conclusions: on the one hand, the rough circumstances of expected concentrations and ab-

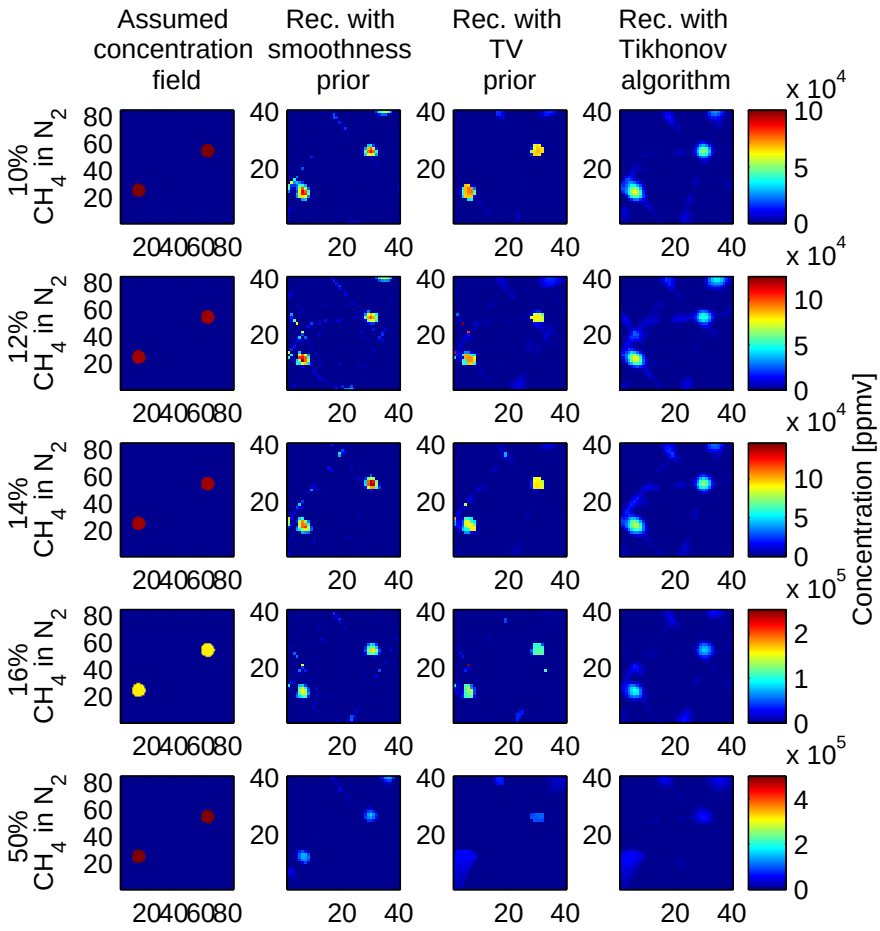

Figure 5.10 Reconstructions of two jets emitting a laminar flow of different concentrations of CH_4 in N_2

sorbing lengths have to be known in the first place. For the application in environmental science, this is certainly the case, but problems may arise in other systems. On the other hand, it has to be acknowledged that for spatial resolution of the reconstructed image not only tomography plays a role, but also absorption spectroscopy, as structure sizes directly impact absorption strength.

To illustrate the impact of absorption strength on tomographic reconstructions, a study was carried out with two jets emitting gas mixtures from $10\%_{vol}$ CH_4 in N_2 up to $50\%_{vol}$ CH_4 in N_2. An overview of the results is given in figure 5.10. Absorption lengths stay the same for all measurements since the jets are not shifted in position, for this reason concentration is the only parameter that influences absorption strength. For tomographic reconstruction, the most promising algorithms were tried out, that means the Bayesian estimation techniques. In the very left column, the estimated expected concentration field is illustrated, which was generated by means of known structure sizes, positions and concentrations. However, the real concentration distribution is unknown. The images of the assumed concentration field are intended to serve as a quick and convenient possibility to

judge the reconstruction image quality. Good reconstructions were achieved in a certain concentration range up to $14\%_{vol}$ methane concentration. Afterwards, concentrations are increasingly underestimated due to systematic errors on the measured mean concentrations.
Even though the informative smoothness prior is not the best choice for reconstructing sharp-edged features, it leads to astonishingly accurate results of absolute concentration and feature positions. At the edges, the structures are smoothed however and artefacts partly appear in a few background pixels. Total variation prior should actually suited best for this measurement object. Reconstructions of those concentration fields that are not corrupted by systematic errors on the mean concentrations have correct structure sizes and positions, but absolute concentrations are underestimated to a small degree. In the background, single outlier pixel appear in some measurements. In contrast to this, Tikhonov algorithm leads to very smoothed features with strongly underestimated concentration, but correct feature positions.
In real practical situations, the correct concentration field is of course unknown. One possibility to find out whether reconstructions are trustworthy is too examine the measurement vectors of the mean concentrations $\vec{c}$. The image is a correct solution to the equation $\vec{c} = W \cdot \vec{f} + \vec{n}$, if the mean concentrations that would be measured with the reconstructed field differs from the real measured mean concentration not more than would be caused by noise. It can be said that reconstructions are inaccurate if mean concentrations derived from the image do not lie within the "allowed" range. The inverse conclusion that correct mean concentrations signify correct concentration fields may normally not be drawn for sets of infinite solution, but as the prior limits the solution space to physically sensible images, solutions that fulfil the observation model equation are much more likely to be correct than in the unregularized case.
Figure 5.11 shows the measured mean concentrations for the experiment with $12\%_{vol}$ CH_4 in nitrogen and the mean concentrations that would be measured with the reconstructions delivered by the informative smoothness prior, TV prior and Tikhonov regularization. At first sight it seems that all tomographic techniques lead to solutions with mean concentration similar to the real measurement. Differences can be observed if the residual between the simulated mean concentrations of the reconstruction $\vec{c}_{rec}$ and the measured mean concentrations $\vec{c}_{real}$ is considered. For a more convenient discussion, this difference is from now on called *mean concentration residual* and abbreviated by $\vec{\varepsilon}_c$:

$$\vec{\varepsilon}_c = \vec{c}_{rec} - \vec{c}_{real} \tag{5.1}$$

Values of $\vec{\varepsilon}_c$ for the three presented reconstructions are presented in the second row of figure 5.11. For all of the tomographic techniques, there are deviations from the real measured values of up to several thousand ppmv. Tikhonov algorithm leads to many more deviations than smoothness or total variation prior. The question is whether noise in the real measurement is that large that the reconstructed mean concentrations can be considered a more accurate measurement or whether the reconstruction is erroneous. In the former case, values of $\vec{\varepsilon}_c$ should not exceed the measured noise vector $\vec{n}$, which is determined by the variance of concentration values measured at repetitive experiments. For simple visualization the *noise normalized residual* $\vec{\varepsilon}_{c,n}$

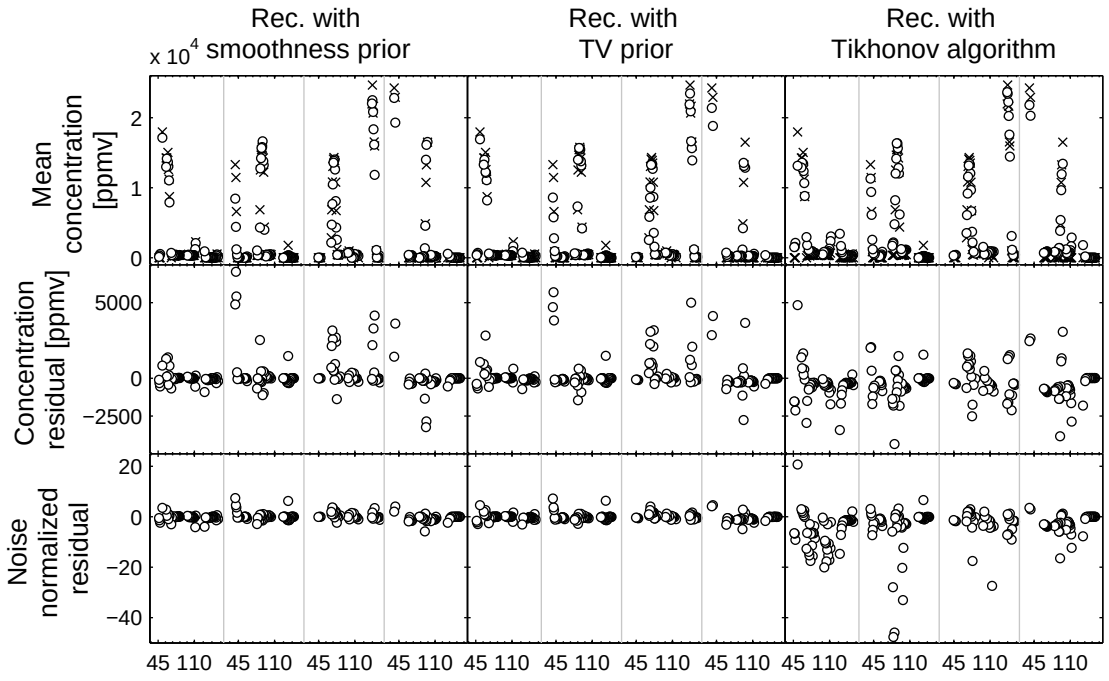

Figure 5.11 Measurement vectors and reconstructed vectors of an exemplary measurement with 12%$_{vol}$ CH_4 in N_2

$$\vec{\varepsilon}_{c,n}(i) = \frac{\vec{\varepsilon}_c(i)}{\vec{n}(i)} \tag{5.2}$$

is plotted in the third row of figure 5.11. Obviously, all of the tomographic techniques deliver solutions that lead to larger mean concentration residuals than could be explained by measurement noise, since all have values of $\vec{\varepsilon}_{c,n}$ larger than one. However, Tikhonov regularization performs significantly worse than the other techniques, as it shows mean concentration residuals that are up to 40 times larger than measurement noise. This coincides well with the image of Tikhonov reconstruction depicted in figure 5.10: undoubtedly, the reconstructed concentration field is erroneous as it does not even fulfil the observation model equation.

All in all, when tomographic measurements are carried out, the expected absorptions should be estimated in the first place to make sure that absorption is larger than the detection limit in sufficient cases and that saturation is avoided. Even if in some measurement paths it comes to saturation, it has to be made absolutely sure that those measurement points are discarded in the spectroscopic evaluation of the mean path concentrations. Once there are systematic errors on the measurement vector $\vec{c}$, completely misleading tomographic reconstructions are produced that cannot be distinguished from good measurements because mean concentration residuals can be within the range of noise.

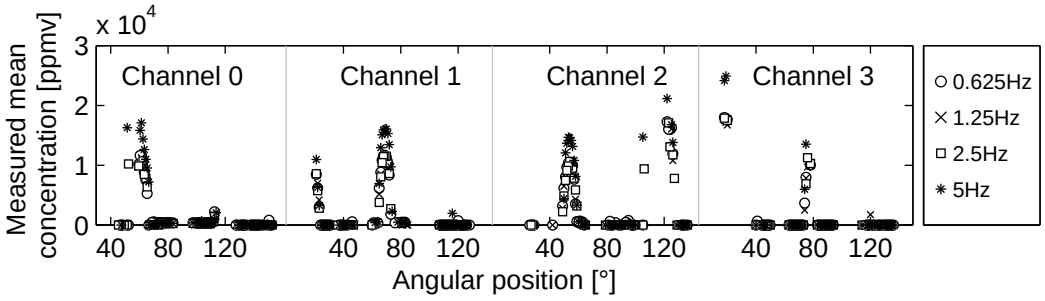

Figure 5.12 Measured mean concentrations at different angular positions of the four scanners, recorded at different field measurement rates

5.3 Influence of field measurement rate

It was already shown in chapter 3 that the field measurement rate of the instrument should not exceed 2.5 Hz for the given laser tuning rate of 5039.8 Hz. In this chapter, it is examined how scanning velocity impacts tomographic measurements. A measurement with two laminar jets emitting a mixture of $10\%_{vol}$ methane in nitrogen was repeated at four different spatial scanning rates. The mean concentrations are plotted in figure 5.12 for all scanning velocities. For field measurement rates up to 2.5 Hz, similar mean concentrations are measured: the variance between experiments at different velocities is not larger than variances of repetitive experiments at constant speed. However, if the scanning rate amounts 5 Hz, much higher concentrations are measured. Like it was presented in figure 3.12, the TDLAS ramps are distorted heavily at this speed, leading to a systematic overestimation of mean concentrations.
Figure 5.13 shows the tomographic reconstructions that are gained at the measurements with different scanning velocities. It has been focussed onto the results gained with smoothness prior and total variation prior since Tikhonov regularization leads to smoothed structures with underestimated maximum concentration as it can be observed in F. Up to a speed of 2.5 Hz field measurement rate, reconstructions look satisfying. There are only few background artefacts in the form of outlier pixels; shapes and positions of the jets are imaged correctly. A smoothing of the edges is observed for the reconstructions with the informative smoothness prior. If total variation prior is applied, concentrations are underestimated because structures are very small, so that TV prior is at the limit of spatial resolution. For repetitive measurements at fixed speed, the reconstructions vary. The variation that is seen between the reconstructions at different speeds is not larger than the variance between repetitive measurements at the same speed. Moreover, results that are gained at 0.625 Hz scanning rate are not significantly better than those at 2.5 Hz. Even tough there are more laser beams in the field, not all of them carry independent information: Beam paths that lie closely together carry very similar information, so that an angular multiplication of beams does not improve tomographic reconstructions.
If the scanning velocity amounts 5 Hz, the reconstructed concentration fields are completely misleading. Not only are some of the feature concentrations underestimated severely, like it is shown for the upper right gas jet in the total variation prior reconstruction. What is even worse is that structures are displayed that in reality do not exist,

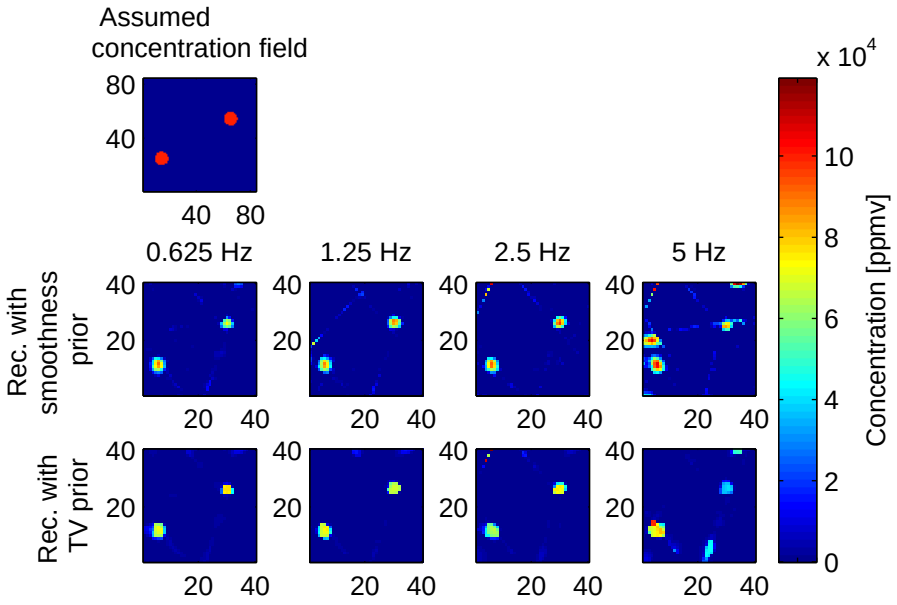

Figure 5.13 Reconstruction of a laminar flow at different field measurement rates

which would be fatal in the permafrost application. In such a case, not only the absolute values of concentration would be quantified erroneously, but also the identification of emitting structures would be wrong. This is especially bad because the measured and reconstructed mean path concentrations give us no hint about the corruptness of the image. Experiments at 0.625 Hz and 5 Hz field measurement rate are displayed in figure 5.14. In

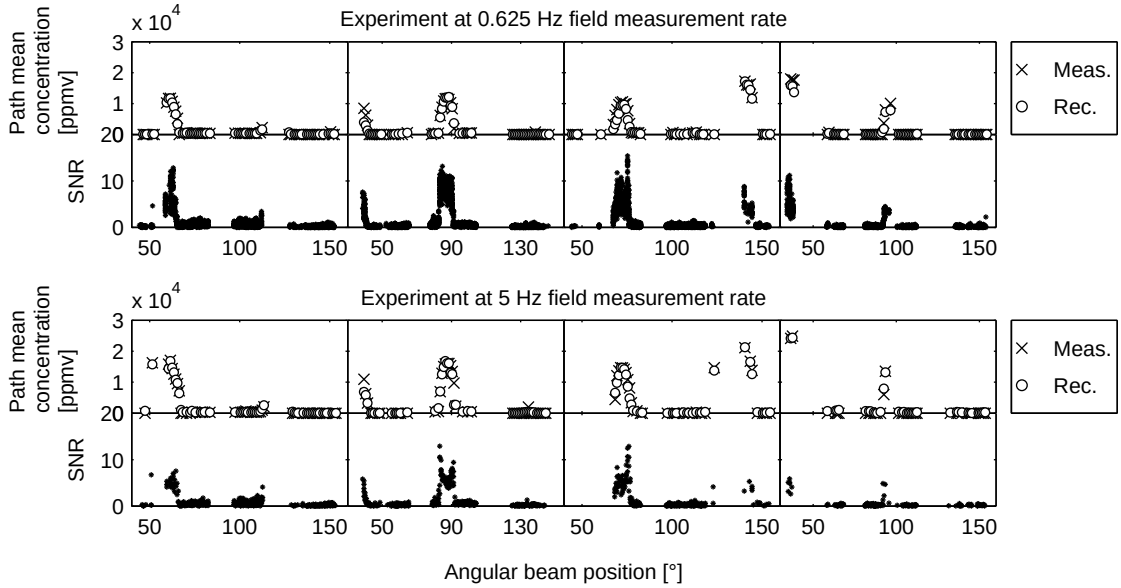

Figure 5.14 Measured path-averaged concentrations and reconstructed vectors (smoothness prior) and SNR for experiments at 0.625 Hz and 5 Hz field measurement rate

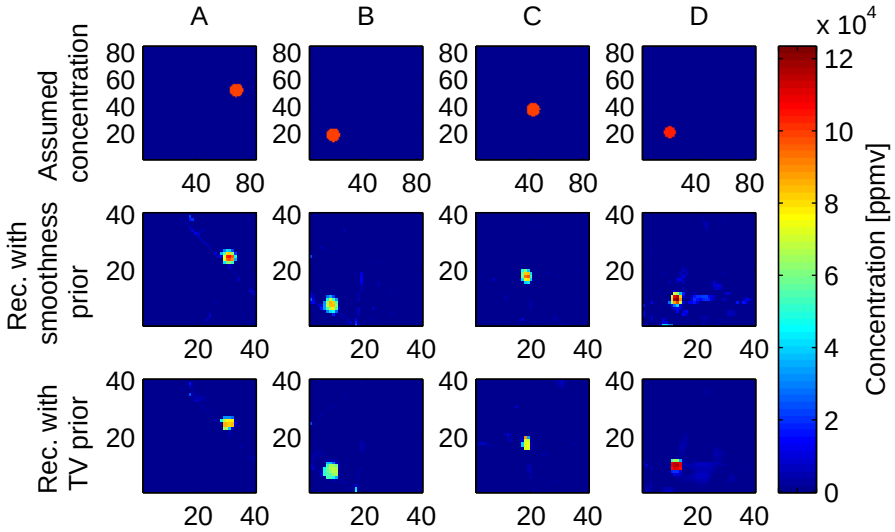

Figure 5.15 Reconstructions of measurements with one laminar jet

both cases, the reconstructed measurement vector coincides well with the real measurement vector. Furthermore, there is no significant difference in the signal to noise range of both experiments.
Bad solutions caused by too fast field scanning rate cannot be distinguished from good solutions during the tomographic reconstruction process. This is why it has to be made sure already during the spectroscopic evaluation that the mean concentrations are accurate: in this case, it has to be monitored that ramp distortion is not too strong. In practice, the rotation speed is fixed for a certain laser tuning rate.

5.4 Influence of measurement object complexity

As seen in chapter 4, parameters like element number, sizes, type, position and concentration contrast have an influence on the ability to reconstruct the measurement field with certain tomographic algorithms. In this chapter, it is examined how measurement objects with increasingly complex combinations of those parameters are reconstructed. In the experiments, a variation of structure numbers, sizes (to a certain degree) and positions was realized.
The simplest case is the reconstruction of only one object. Measurements were carried out for different jet positions and two jet diameters, which amounted 95 mm and 85 mm. Those sizes correspond to Λ_{rel} ≈0.12 and Λ_{rel} ≈0.11, which is on the border of spatial resolution. Fortunately, many measurement paths can be considered almost noise-free, as they are set to zero in the first place, which is generally a good approximation of methane concentration in air (≈1.7 ppmv). This enhances the possible spatial resolution, as has been confirmed with virtual experiments. In all cases, field measurement rate was 1.25 Hz and the emitted gas mixture was 10%$_{vol}$ CH_4 in N_2. “Single” shot results are displayed in figure 5.15 for the informative smoothness prior and total variation prior. For smoothness prior, all reconstructions show very good shapes and positions, and hardly any artefacts

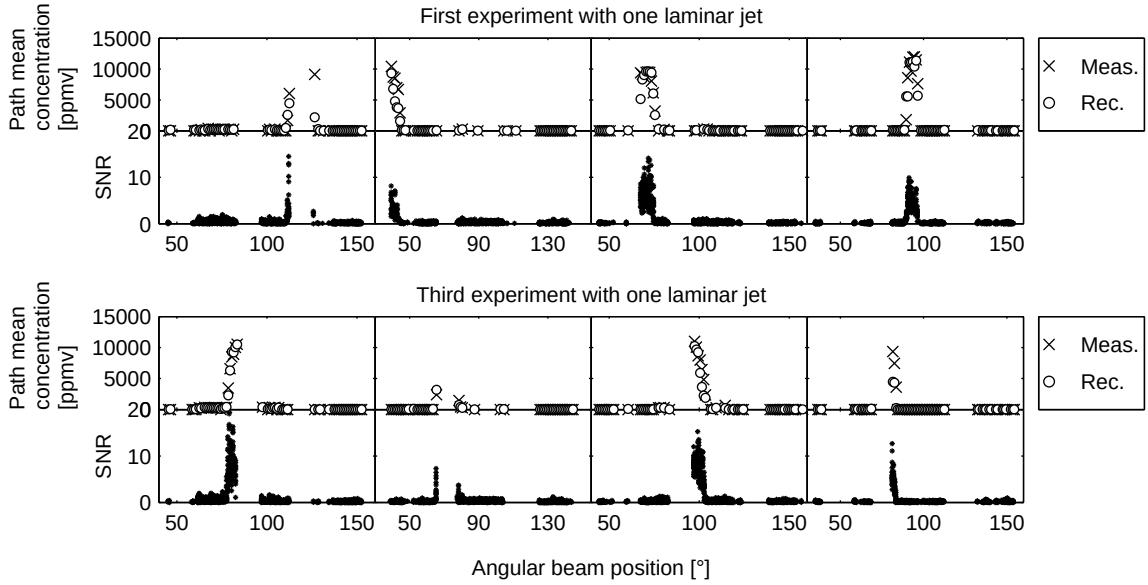

Figure 5.16 Measured and reconstructed (TV) mean concentrations and SNR of two experiments with differently located laminar jet

are visible in the background. Besides the edge smoothing, absolute concentrations are hit accurately in most of the times, with a tendency to underestimation due to blurring. Here it has to be acknowledged that relative structure sizes are very small even for the easier case and the limits of spatial resolution are reached.
For total variation prior, such small structures often already lead to an underestimation of the reconstructed concentrations, but shapes and positions are imaged very well in most cases and hardly any artefacts are visible. However, if the jet is located in a position where hardly any beams cross, total variation prior leads to difficulties. Such a situation is given for measurement C: jet position and beam propagation of this experiment are depicted in figure 5.1. Concentrations are only detected at the edges of the gas jet since there is a hole in the beam arrangement because of missing reflectivity at opposite scanner box windows. The measurement vectors and signal to noise ratios of experiment A and C and the path mean concentrations derived from the TV prior reconstructions are compared in figure 5.16. Even though SNR lies in the same order of magnitude in both cases, it is observed that the amount of non-zero path-averaged concentrations is much lower in case C. Mean concentrations are hit about equally good. In the latter case, the TV prior has more freedom to produce results that lead to reconstructed mean path concentration vectors with similar sloping edge that would lead to different mean concentrations at the missing angles. For this solution, the shape changes to a more rectangular, smaller feature. Here, the smoothness prior has the advantage that it offers more possibilities to control the feature shape and size due to the informative smoothness prior Λ.
The next step towards complexity was taken by increasing the number of jets to two. First, the easier case with two identical jets of 95 mm diameter was examined. The concentration of methane in nitrogen was set to $10\%_{vol}$ in all cases. The experiment was carried out with 1.25 Hz polygon rotation speed. The single-shot reconstructions with informative

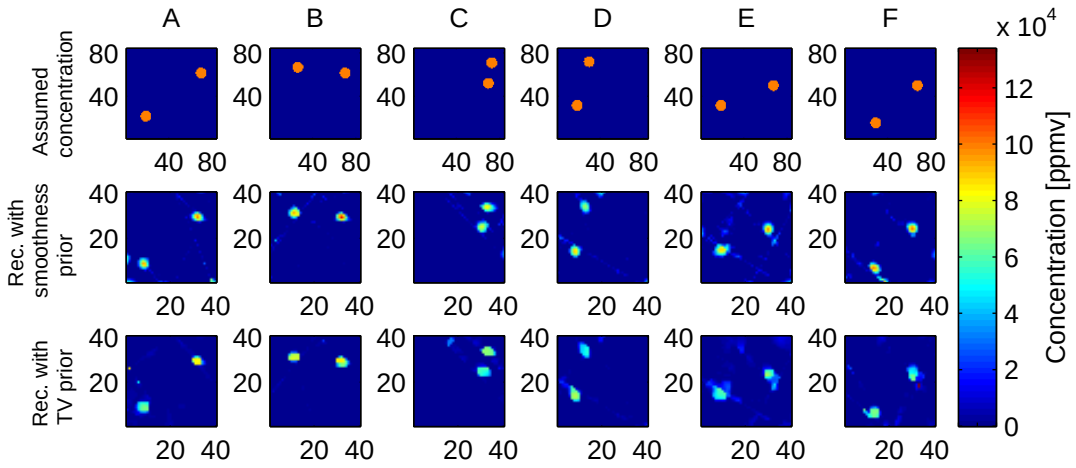

Figure 5.17 Reconstruction of laminar flow from two identical jets with diameter 95 mm

smoothness and total variation prior are shown in figure 5.17. In general, position and sizes are reconstructed very well. Depending on the jet positions, there are some cases where concentration is underestimated. In some images there are more artefacts in the background than in the single-jet experiments.
The measured path mean concentrations and those received from TV prior reconstructions of experiments B and E are depicted in figure 5.18. Experiment B leads to a quite good reconstruction without any background artefacts and good location of jets. Shapes are imaged nicely although there is a slight underestimation of concentration which is

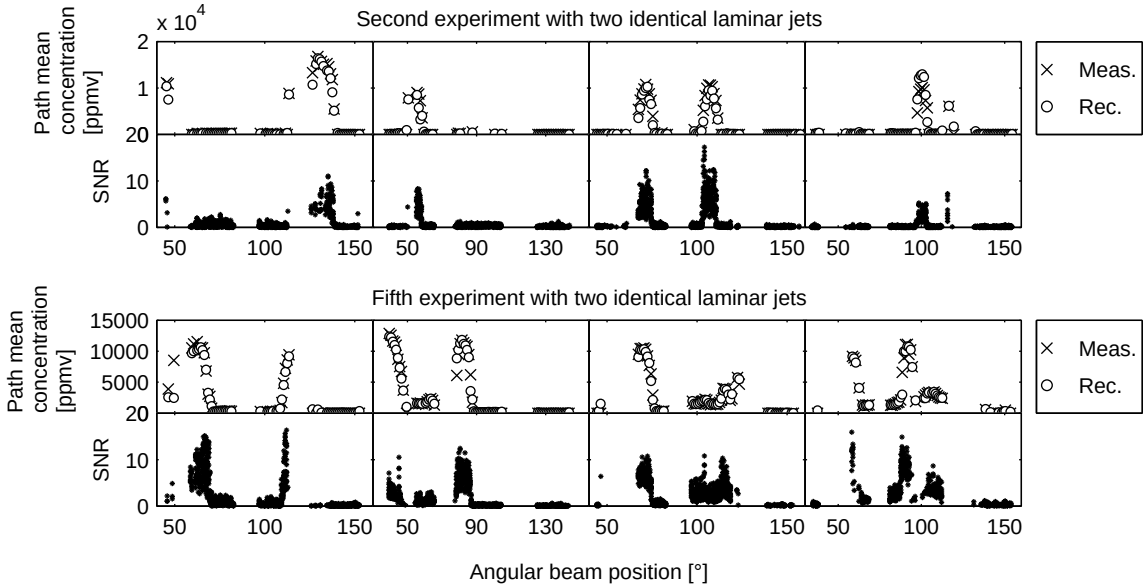

Figure 5.18 Measured and reconstructed (TV) mean concentrations and SNR of two experiments with two identical, differently located laminar jets

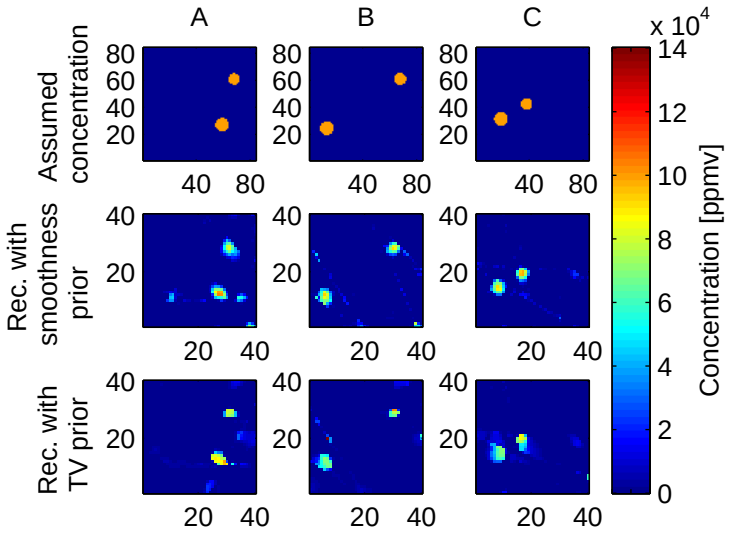

Figure 5.19 Reconstruction of the laminar flow from two jets with diameters 95 mm and 85 mm, respectively

generally observed with TV prior reconstructions of structures of this size. If the jets are positioned like in experiment E, shapes are blurred stronger and artefacts increase. However the artefacts are small and low in concentration. Moreover, absolute concentration values are underestimated more strongly. If the reconstructed mean path concentrations of both experiments are compared to the respective real measurements, both experiments lead to similar results. In both cases, $\epsilon_{c,n}$ is small and SNR range is similar, such that worse reconstructions cannot be distinguished from good ones in a real experiment with unknown concentration field. It has to be kept in mind however that the structure size is very challenging and that in relation the reconstructions for such a difficult phantom look very satisfying.

Even a bit more sophisticated are experiments with a larger jet (diameter 95 mm) and a smaller jet (diameter 85 mm). The assumed concentration fields and images reconstructed with informative smoothness prior and TV prior are demonstrated in figure 5.19. Even if the jets are positioned very closely together, like in experiment C, smoothness and TV prior are able to reconstruct positions and shapes quite good with only a slight underestimation of absolute concentration. Again, sometimes artefacts in the background appear that are small in size and that have much lower concentration than the real objects.

The most difficult experiments that were carried out consisted of three jets emitting a mixture of $10\%_{vol}$ CH_4 in N_2. Two of the jets had a diameter of 95 mm and the smaller jet had 85 mm diameter. Assumed concentration fields and reconstructions with smoothness and total variation prior of single-shot measurements are illustrated in figure 5.20. For two exemplary measurements (E and D) the measured and reconstructed path-averaged concentrations and signal to noise ratios are given in figure 5.21. Here, the reconstruction with smoothness prior is presented. Overall, reconstructions with smoothness prior show correct structure locations and sizes. Mostly, absolute feature concentrations are correct despite the edge blurring effect. However there are measurement object arrangements

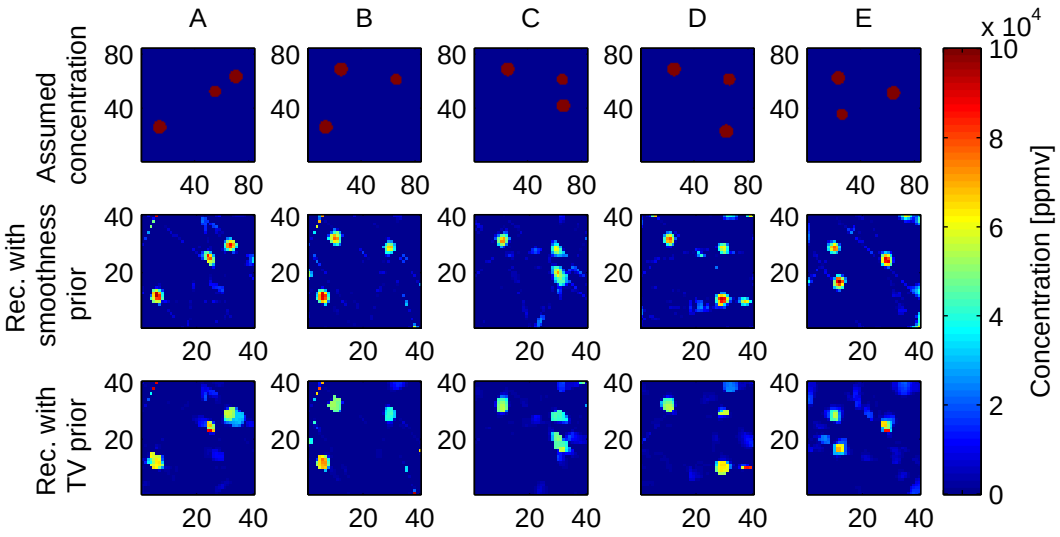

Figure 5.20 Reconstruction of a laminar flow from three jets (two identical jets with diameter 95 mm and one smaller jet with diameter 85 mm)

where concentration is underestimated, for example in experiment C. Artefacts in the background are visible in all reconstructed images. They are in most cases only few outlier pixels or have much lower concentrations than the real objects. Unfortunately, there are exceptions: In some cases, like experiment D, it is possible that artefacts are in a concentration range similar to the real reconstructed objects, so they might be mistaken as really emitting structures. In any case, the noise normalized residuals were low.
Imaging three objects with such small sizes with total variation prior proved to be very dif-

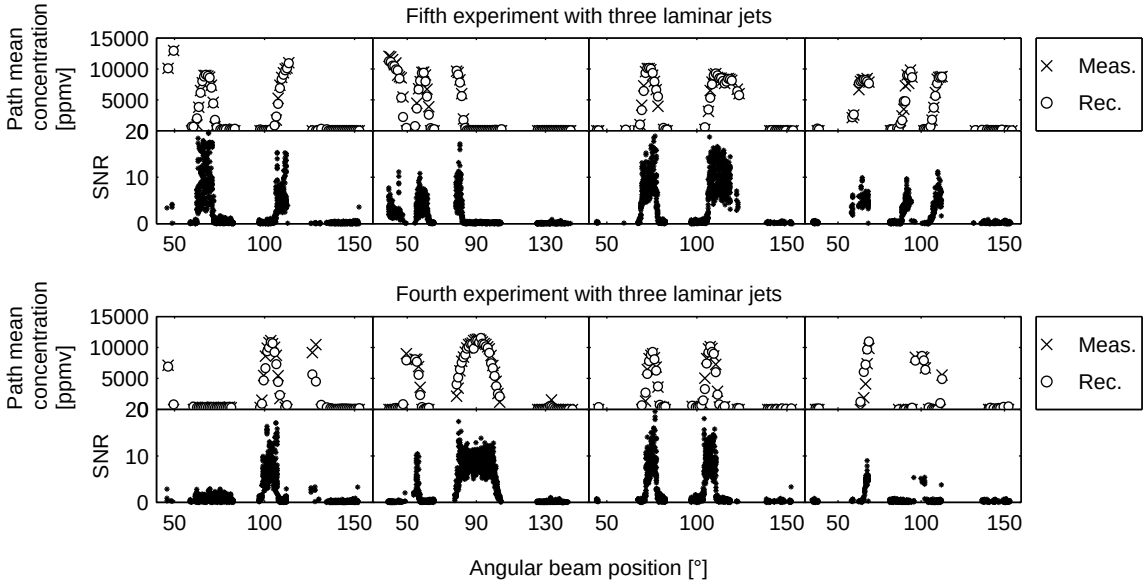

Figure 5.21 Measured and reconstructed mean concentrations and SNR of two experiments with three differently located laminar jets. The used algorithm was the informative smoothness prior.

ficult. Although all structures are recognisable for the presented measurements and their locations are correct, shapes can be distorted (view experiment C) and concentrations are sometimes underestimated strongly (view experiment B). The latter can be especially problematic. Sometimes, artefacts in the background arise (experiment D) that are equal in size and concentration. In practice, it cannot be said for sure which objects really emit gas and which structures are only artefacts.

5.5 Comparison to other instruments

The aim of this chapter is to give an overview about similar tomographic instruments and to examine whether they would be apt for the application in environmental science also. Furthermore, they may be compared to the designed instrument regarding future applications. It is focussed onto sparse-sampling instruments that are based on some variant of absorption spectroscopy.
The intercomparison can take place at several design levels: First, there is the instrument concept that dictates properties like possible measurement object size, image rate, transportability or cost. Then, the spectroscopy type often plays a role as it can have strong influence on the instrument set-up and the possibilities of imaging. At last, the tomographic algorithm can be important as in some cases the whole instrument design is inherent to the algorithm.
Existing sparse-data absorption tomography instruments can be grouped into devices that measure only the 2-dimensional distribution of concentration and such that aim to detect both the temperature- and the concentration field. It is begun with the former case, since temperature is not the crucial issue in the given application.
Tomographic reconstructions of concentration fields were carried out in the former group of Hugh McCann at the University of Manchester [52,73–75]. As a spectroscopic method, direct absorption spectroscopy at two wavelengths is used, where one wavelength is used for a reference measurement because it is hardly absorbed. Not only tomographic reconstructions of simulated fields were presented [52, 73, 75], but also real experiments with generic laboratory measurement objects [74]. In all cases, the design of the experiment is based on a static system where each path needs a laser source and a detector. With numbers of beams that range from 27 to 32, images with a similar pixel discretization are received. As a tomographic technique, an enhanced Landweber algorithm is used [53] and image processing techniques were introduced for enhanced results [73]. The presented reconstructed images show structures that are somewhat larger than those that were measured with the designed instrument, but of course general statements about spatial resolution cannot be made. Those concepts are however not suitable for the application in Arctic regions, as it would be too tedious to align multiple rays in the field. Another drawback is the cost of the system. The disadvantage of the required reference measurement could be easily eliminated by using the same set-up with TDLAS.
Verkruysse et al. [76] have carried out numerical simulations for reconstruction of two-dimensional concentration fields. As a measurement method in practice, they suggest the use of open-path Fourier transform infrared spectroscopy (OP-FTIR). Their virtual experiments were received by a modelled set-up with 40 beams. Even though they received good reconstructions with a so-called grid translation method, that show similar spatial

resolution like the designed instrument, the whole concept seems unrealistic for the permafrost application. Not only does FTIR spectroscopy have much slower measurement rates than TDLAS and require calibration, it is also connected with complicated transport and alignment.
Some other solutions for sparse 2D-tomography aim at the simultaneous reconstruction of temperature and concentration. In principle, this is a question of the choice of the spectroscopic method and the reconstruction algorithm. Their conceptual design is examined regarding suitability in the field application.
Kasyutich [77] presents a spectroscopic method to determine temperature and concentration distribution by measuring absorptions at two different wavelengths. The strategy is to reconstruct the 2D-field of absorption with ART algorithm first. With the known absorption values of the two wavelengths, for each pixel a two-line-thermometry is carried out for reconstructing the temperature field. In a further step, the concentration values at each pixel are calculated by means of the reconstructed absorption and temperature values. The spectroscopic method is not the decisive point here, as it could be easily replaced by TDLAS in the case of constant temperature, thus gaining calibration-free measurements and reducing effort. If it is focussed onto the principle set-up of the instrument, it has to be considered that it was intended for proof-of-concept experiments. Only one laser was used in combination with a scanning mirror that scanned the laser beam over a small angular range. At the opposite side of the field, a detecting unit with a mirror for beam deflection and a photo-detector was located. Both units were situated on carriages that were translated step-wise after each sequential fan-beam scanning along a circular rail with 97 cm diameter. Overall, 11 angular measurements are taken at 5 radial positions. For the permafrost application, this device has several drawbacks. While its temporal resolution may be sufficient for generic experiments, it is much to low for the planned use. No exact imaging duration is given but it is probably in the range of minutes. Furthermore, the scanning angles of the fan-beams are quite small, even though their actual value is unknown. This is no problem for the experiment that Kasyutich carried out, because absorption only took place in a limited area that was totally covered by the laser beams. In contrast to this, absorption takes place almost to the points where the fan-beams originate in the permafrost measurements, so that larger scanning angles are necessary to cover at least part of the measurement area. Reconstructions with a discretization of up to 18×18 pixels received by the classic ART algorithm are presented. Images look quite accurate, and surely reconstruction quality could be even enhanced if for the calculation of the absorption values, more sophisticated inversion techniques were used.
Deguchi et al. [78] demonstrated tomographic TDLAS measurements for the detection of 2D-temperature and concentration distributions of water vapour. The designated use of their instrument is the examination of engine exhausts. They use eight static measurement paths to resolve an area divided into 4×4 pixels, so only a very coarse image of the gas composition in the exhaust is gained. With this discretization, relevant structures in permafrost cannot be resolved. Theoretically, the set-up could allow for higher discretizations. The tomographic implementation of Deguchi et al. limits the amount of possible degrees of freedom, since the applied reconstruction technique minimizes errors between measured and reconstructed path-integrals without any regularization. By this way it is

not recommendable to solve severely under-determined systems of equations.
In the group of Ma, a spectroscopic measurement technique called *hyperspectral tomography* (HT) was developed and is used for 2D imaging of temperature and species concentration [79–83]. The absorbances at various wavelengths are used for multiplying the amount of measurement equations, such that determined or even over-determined sets of equations are solved. The reconstruction technique minimizes temperature- and concentration dependent residuals between measured and simulated path-integral values, while regularization terms for smoothing of the temperature and concentration fields are added. Virtual and real experiments were realized for example with a Hencken burner [81] and in the exhaust of an aero-propulsion engine [83]. In the former case, six beams are arranged in a static setup to image seven different irregularly spaced zones. 100 absorption transitions are taken into account for reconstruction. Imaging rate amounted 200 Hz. Again, the discretization is so low that it impedes reliable detection of emitting permafrost structures. A more recent application of HT is the 2D- measurement of water vapour concentration and temperature in the exhaust of an aero-propulsion engine. The measurement field is subdivided into 14×14 pixels and 30 static laser beams are positioned in a parallel way on two edges. Evaluating the absorption with 50 kHz rate at twelve wavelengths for each beam leads to an over-determined system of equations. Here, discretization is significantly lower than for the designed instrument. Thus, spatial resolution is considered still too low for the planned soil science application. Furthermore, for HT two reference measurements are necessary: one for detecting the intensity without absorption, and one for a time-dependent wavelength reference. Higher spatial resolutions might be achieved if the system of equations was allowed to be under-determined. Instead of a simple regularization method, more sophisticated reconstruction algorithms would have to be used then. Still, the disadvantages of the static set-up remain. The evaluation of absorption at multiple wavelengths is however an interesting perspective if non-homogeneous temperature distributions are expected.
Wang et al. [84] present a 10 Hz tomographic instrument for detecting spatially resolved NH_3 concentrations and gas temperature. As a spectroscopic method, they use TDLAS at two wavelengths. With a classic ART algorithm, the concentration and temperature fields are updated independently in turns, beginning with uniform distributions of the unknown values as initial guesses. The measurement field was scanned with four irregularly positioned fan-beams. Each scanning unit consisted of a single laser on a rotation plate and a large- area detector directly beneath it. On the opposed side of each scanner, a curved gold mirror is situated for retro-reflecting the laser beam. Due to a small tilt of the incoming laser beam, the reflected beam is guided to the slightly lower surface detector. Although the instrument has a higher temporal resolution of 10 Hz, it is not fit for the environmental science application. The size of the retro-reflecting mirrors limits the scanning angle and possible distance from the laser source. Thus, only relatively small areas are covered by the fan-beams, which have an opening angle of 11°. For Wangs application this is no problem since absorption is known to be restricted to a small area of 16×16 cm^2, which can be entirely covered by the beams. They divided the measurement field into 16×16 pixels, which is lower than the established discretization of the developed instrument. Presumably the discretization is limited by the grade of under-determination of the system of equations which should not be to high for the ART algorithm.

Song et al. [85] present numerical and experimental studies of reconstructing gas temperature. They also measure integrated absorptions with TDLAS and reconstruct the spatial distribution of absorption with an ART algorithm on a 30×30 grid. Unfortunately it does not become clear how the temperatures are derived from the absorption values. Moreover, their experimental set-up is only suited for laboratory proof-of-concept measurements. They examine a furnace that is moved sequentially to 97 linear positions and then rotated by 90° for repeating the linear scan. Of course the soil area cannot be moved, an neither does the temporal resolution of such a tedious sequential scan suffice.
All in all, none of the existing instruments could be used for measuring the 2D-concentration field in the soil-air boundary layer of permafrost. Either the measurement fields are to small [77, 84],imaging rates are too low [76, 77, 85], or transportability and cost are inconvenient [52, 73, 76, 78, 83]. In some cases, the spatial resolution is too low for the permafrost application [78, 83, 84]. Surprisingly, the most popular techniques are algebraic reconstruction algorithms, which are mostly represented by the Kaczmarz method. In the group of McCann, Landweber algorithm is used. Ma use regularized minimization of a residual error between measured path-integrals and those that would arise from the current reconstructed image. It has to be made sure the system of equations is determined or over-determined, hence the achieved spatial resolution is considerably lower than for the newly developed instrument. However, the HT technique, or in general multiple-wavelength techniques, may be interesting if temperature is non-uniform, like in combustion research or exhaust gas analysis. Combining such spectroscopic techniques with more powerful tomographic reconstruction methods might be promising for simultaneous detection of temperature and concentrations fields.

Chapter 6

Conclusion and Outlook

The aim of the work was to develop instrumentation for spatially and temporally resolved measurements of concentration fields. Therefore, the spectroscopic method TDLAS, which allows for absolute and calibration-free measurements of path-averaged concentrations, had to be extended to a tomographic system. In technical and scientific applications, typically it has to be dealt with low-data problems because of practical reasons like accessibility, transport effort or cost. In contrast to standard tomographic instruments, a severe lack of information has to be handled. Since the instrument design needs to be adapted to the specific purpose, it was focussed onto an application from soil science.
The developed instrument facilitates imaging of an 0.8×0.8 m^2 area with rates up to 2.5 Hz at a laser tuning rate of 5039.8 Hz. It consists of four scanning units that serve for emission and detection of light that are positioned irregularly on the edges of the measurement field. On the remaining part of the border, an inexpensive, adhesive retro-reflecting foil strip is stuck onto a frame. Large areas of the measurement field are covered, which is indispensable for this application, since absorption can take place everywhere in the area that is surrounded by the instrument.
A completely new method of TDLAS data acquisition was introduced for maintaining the necessary speed when scanning the laser beam continuously. All required signals (transmitted intensity, pressure, temperature, position) are recorded continuously after an initial triggering. The conventional method is a triggered acquisition of each wavelength-tune, which is too slow in this application due to lost triggers and DAQ response time. A simple continuous acquisition is unfortunately not possible due to time-base inaccuracies that accumulate with increasing measurement duration. Therefore, a pulse is super-positioned on the falling branch of the wavelength tune that is detected during post-processing. Thus, an accurate time-base is ensured while at the same time data can be gathered very quickly. Accuracy of TDLAS measurements with the scanning instrument was demonstrated with path-integrated measurements of a uniform water vapour distribution.
By means of virtual experiments, a selection of promising tomographic algorithms was compared regarding their reconstruction abilities. Image quality, spatial resolution and computation time were discussed. It was focussed onto two different algebraic reconstruction techniques and three algorithms that belong to statistical inversion. Both algebraic techniques performed generally poorer than the Bayesian methods. Only very few, large structures can be imaged and partly show large systematic errors on absolute concentrations. Shapes are distorted heavily and strong artefacts in the background appear.
Existing Bayesian algorithms were adapted to the hard-field tomography application and partly modified for enhanced reconstruction results. They require prior physical knowl-

edge about the measurement object. In contrast to the algebraic techniques, they allow for decent reconstructions of several structure elements in the measurement field. Two smoothness priors were implemented as well as a prior that assumes "blocky" structures that show gradients only in very few locations of the measurement area. One of the smoothness priors, the informative smoothness prior, even makes use of the expected structure sizes. With a slightly modified version, even improved reconstructions of anisotropic features are achieved. In numerical studies, both smoothness priors showed good reconstructions of absolute concentrations, structure shapes and sizes and yielded only very few background artefacts. Up to seven features in the measurement could be imaged.
The total variation prior showed good reconstructions of blocky features and is the best choice for rectangular or square measurement objects. The number of features should however not exceed five.
The Bayesian techniques allowed for simultaneous reconstruction of objects with differing concentration and also tolerated decreasing image contrast. Algebraic techniques failed in both cases.
Computation time not only depends on the computer efficiency, but in some cases also on the exact implementation of the algorithms. Bayesian techniques include the minimization of an objective function, and the implementation of the optimization process has a decisive influence on speed. For example, Tikhonov algorithm was the slowest of all techniques because of the vast numbers of iterations ($>10^3$) that the pre-implemented Matlab algorithm `lsqnonneg` needed for finding a minimum. With a self-implemented Gauss-Newton algorithm, the calculation speed of the informative smoothness prior and TV prior was even lower than for the simple iterative Kaczmarz method. The latter is inherently slower than the very fast Landweber algorithm because each iteration needs a single updte for each of the M measurement paths, thus computation effort is around M times higher than for Landweber algorithm.
An experimental study with approximately known concentration fields was presented to validate the tomographic instrument. The concentration distribution was generated by a laminar flow from circular jets. A mixture of methane in nitrogen was defined by two mass-flow controllers. The quality of the measurement of path mean concentration was discussed regarding aspects of light intensity, absorption strength and measurement speed. Tomographic reconstructions of experiments with varying concentrations and measurement speeds were carried out. In addition to that, the number, sizes and positions of the emitting jets were varied. Thereby the structure size, given by the jet diameters, was on the limit of spatial resolution. From the experimental studies a few general insights were gained that are of interest also for other applications.
A crucial issue is absorption strength. The dynamic range of TDLAS is of course not infinite. It is limited towards low absorption by noise and towards high absorption by saturation and broadening of the absorption line. The latter becomes problematic if the line is broadened to such an extent that across the complete wavelength-tune there is absorption, and no polynomial base-line can be fit for determining the intensity before absorption. Whereas measurement paths with low absorption can be included in the reconstruction as measurements with a concentration below detection limit, systematic errors caused by too large absorption are a deathblow to reconstructions. Not only do the reconstructed images look completely misleading, it is not even recognizable any more

that they are erroneous once the false path mean values are used. Hence, it already has to be made sure during the spectroscopic evaluation of the mean concentrations that large systematic errors are avoided and measurements at too high absorptions are discarded.
The same prevails for measurements at too high rotation speed of the laser beam in relation to wavelength tuning rate and measurement field size. It has to be made sure in future applications, that during one wavelength tune the laser beam does not move more than around 0.25 mm along the retro-reflecting foil anywhere in the field.
Best tomographic reconstructions were achieved with the informative smoothness prior and total variation prior, even though the smoothness assumption is not correct in this case. Due to the small feature sizes, Tikhonov smoothed the objects too strongly, so that concentrations were systematically underestimated. Up to three jets were imaged, where a decreasing image quality is observed with rising number of emitting elements. Image quality also depended on the object positions in the measurement field. All in all it can be said that reconstructions with the informative smoothness prior and the TV prior look good, keeping in mind the very small object sizes.
In future, it would be sensible to repeat the presented measurements with even larger objects and some more concentrations. Measurements at higher laser tuning rates could be carried out with *vertical cavity surface enhanced lasers* (VCSELS). Not only do they have a larger tuning rate (up to 30 kHz), but also a broader tuning range of up to 20 cm^{-1}. However, the emitted intensities of VCSELs are very low (in the order of magnitude of few mA compared to about 20 mA for DFB lasers). Experimental studies are necessary to determine SNR at such low incident intensities. Especially critical is the strong magnitude of electromagnetic noise, which certainly will have to be reduced further if VCSELs are applied. Either this can be done with an enhanced electromagnetic shielding, or the stepper motors would have to be replaced by other motors. The latter option requires an alternative concept for absolute position measurement. Regarding future measurements in the Artic, it would also be of interest to realize even larger measurement fields in the order of magnitude of several square meters. It was shown that TDLAS measurements with retro-reflecting foil were successful even at distances of more than 5 m [65], and still larger distances are expected to be possible.
Better tomographic reconstructions are expected if the observation model is further improved. The first step would be to model the beam propagation more accurately by taking into account the movement of the point of reflection on the polygon mirror. Furthermore, a modelling of the model inaccuracies and uncertainties may be included into the noise prior like it is suggested by Lipponen et al. [43].
Successive works may engage in the transfer to other applications like exhaust gas analysis or combustion processes. The adaptation requires modifications in the concept as well as in tomographic algorithms. The main issues here are temporal and spatial resolution and the inhomogeneity of temperature. For combustion research, the necessary time-scales are in the order of magnitude of micro-seconds, which cannot be achieved with the scanning instrument. Also spatial resolution needs to be significantly higher than what is achieved currently. It has to be found out which temporal and spatial resolutions can be accomplished with a justifiable material effort and whether absorption tomography still is beneficial compared to other measurement techniques. A certainly easier case is exhaust gas analysis. Here the structures and time-scales are doubtless larger than in a flame.

Even though the implemented algorithms may serve as a basis for tomography in high-temperature surroundings, they will have to be adapted due to an inhomogeneous distribution of temperature. The basic assumption for measuring path-averaged concentrations is that temperature is constant along the path – which is not necessarily given in combustion and exhaust gas surroundings. Large errors of around 20% can occur when measuring the average concentrations, as has been found out in numerical studies. Therefore the temperature field needs to be reconstructed simultaneously with the temperature field, even if it was not the magnitude of interest. The inverse problem becomes more difficult in this case due to the non-linear dependence of absorption on temperature. It might be promising to use multiple wavelengths absorption to bound the solution space. All in all, the transfer of the developed instrument to other applications requires further considerable effort.

Appendix A

Electrical circuits of constructed data-acquisition hardware

A.1 Trans-impedance amplifier

A very simple trans-impedance amplifier was used for detecting laser-light that falls onto a photo-diode for finding the zero position of the polygon scanner. Figure A.1 shows the electrical circuit of this amplifier. If laser light falls onto the photo-diode, a photo-current I_{photo} is generated. The amplifier consists of a operation amplifier and a resistor. The voltage V_{out} that is generated amounts $V_{out} = -I_{photo} * R$. The operation amplifier was a type LT1097CN8 (Linear Technology) and the resistor had a resistance of 180 Ω.

A.2 Pulse-adding circuit

Adding a pulse to the laser light signal delivered a highly precise and stable time-basis for the TDLAS measurements. This was realized by a simple electrical circuit that is depicted in figure A.2. The photo-current that is generated by the InGaAs photo-diode is amplified by a FEMTO DLPC-2000 trans-impedance amplifier (TIA), which delivers a voltage that is proportional to the photo-current. A voltage pulse from a SRS pulse generator is super-imposed by a very simple circuit. Afterwards, the sumper-imposed voltages are detected by a 16 bit A/D-board (NI PCI 6281).

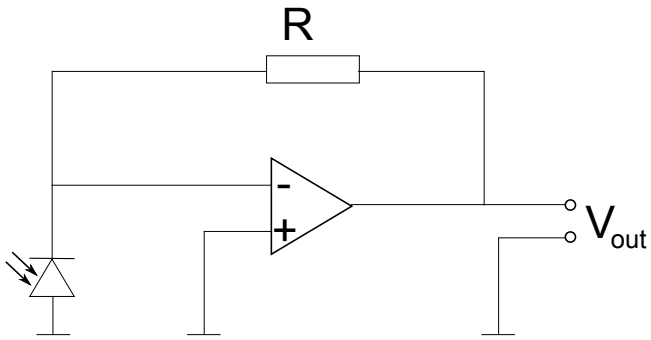

Figure A.1 Electrical circuit of the trans-impedance amplifier that was used for amplifying the current of the position-detection photo-diode

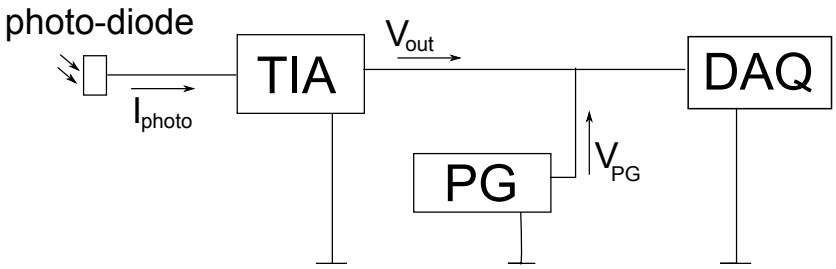

Figure A.2 Electrical circuit for adding the voltage from the pulse generator to the TDLAS signal

Appendix B

Beam position error of simplified model

A simplified model of the beam propagation assumes that the laser beams rotate around a fixed point. In reality, the point of reflection on the polygon alters, as is described in section 3.2.1. A schematic illustration of the measurement field and the beam points of rotation can be seen in figure B.1. The points of rotation that are assumed in the simplified model (P_0 to P_3) are marked by a black dot. In reality, one of the spatial components of the point of rotation alters throughout the polygon rotation. The red dots show the direction of the movement along either of the axes. If the incoming laser beam is oriented horizontally, as is the case with P_0 and P_2, the x-component of the point of reflection varies. In contrary to this, the reflection point's y-component changes during the polygon rotation if the incoming laser beam is parallel to the y-axis, as is the case for P_1 and P_3. Figure B.2 shows the relative position errors of the points of reflection that arise when modelling a fixed point of rotation. As only one coordinate is relevant for

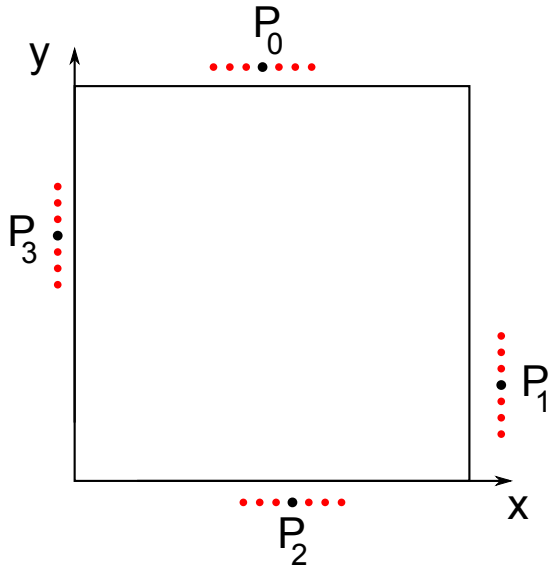

Figure B.1 Schematic depiction of the measurement field (top view). The points of rotation of the laser beams that are included in the simplified model are shown in black (points P_0 to P_3). In reality, the points of reflection on the polygon alter. The red dots illustrate the direction of the movement of the point of rotation.

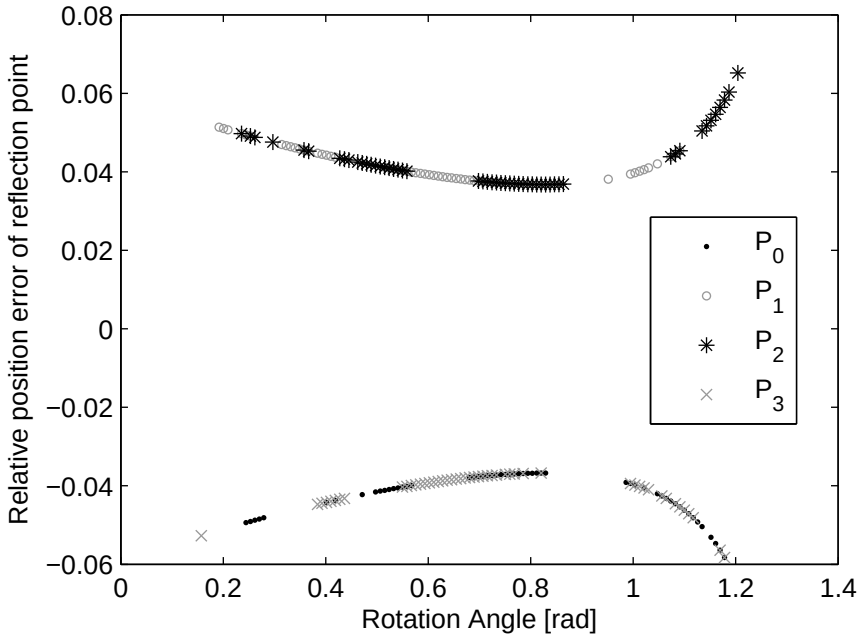

Figure B.2 Relative position errors of the points of reflection of the different scanning units P_0 to P_3.

each scanning unit P_0 to P_3, it is sufficient to express the error by only one number. For evaluating the error, the polygon movement was modelled and a more accurate point of reflection was extracted for each angular position of the polygon. The relative position error is calculated by subtracting the more accurate position from the simplified position and afterwards dividing by the side length of the field. The position errors of the reflection points lie between 3.7% and 6.5%.

Appendix C

Exemplary calculation of required beams for transform based algorithms

Consider a phantom distribution given by a 2D-Gaussian function with standard deviations $\sigma_1 = 0\ 1$ cm and $\sigma_2 = 0\ 1$ cm:

$$f(x_1, x_2) \propto \mathcal{N}(\eta, \sigma^2) \tag{C.1}$$

Its expectation values η_1 and η_2 are set to zero for simplicity, such that the Gaussian is centred at $(x_1 = 0, x_2 = 0)$. Thus, the Gaussian is expressed by

$$f(x_1, x_2) = \frac{1}{2\pi\sigma_1\sigma_2} \cdot \exp\Big\{ -\frac{1}{2} \cdot \Big(\frac{x_1^2}{\sigma_1^2} + \frac{x_2^2}{\sigma_2^2}\Big)\Big\} \tag{C.2}$$

The Fourier transform of $f(x_1, x_2)$ is given by:

$$\begin{aligned} \mathcal{F}\{f(x_1, x_2)\} &= \int_{-\infty}^{\infty}\int_{-\infty}^{\infty} f(x_1, x_2) \exp^{-i(ux_1+vx_2)}\, \mathrm{d}x_1\mathrm{d}x_2 \\ &= \frac{1}{2\pi\sigma_1\sigma_2} \int_{-\infty}^{\infty}\int_{-\infty}^{\infty} \exp\{-\frac{1}{2}[\frac{x_1^2}{\sigma_1^2} + \frac{x_2^2}{\sigma_2^2}] - i(ux_1 + vx_2)\}\mathrm{d}x_1\mathrm{d}x_2 \quad = F(u, v) \end{aligned} \tag{C.3}$$

The mathematical identity [86]

$$\int_{-\infty}^{\infty} \exp(-bx)^2 \exp(iax)dx = \sqrt{\frac{\pi}{b}} \cdot \exp(-\frac{a^2}{4b}) \tag{C.4}$$

can be used to solve the inner integral of equation C.3. Here, $b = 1/2\sigma_1^2$ and $a = -u$, such that

$$\begin{aligned} F(u,v) &= \int_{-\infty}^{\infty} \exp\{-\frac{1}{2}\frac{x_2^2}{\sigma_2^2} - ivx_2\} \cdot \sqrt{\pi \cdot 2\sigma_1^2} \cdot \exp\{-\frac{u^2\sigma_1^2}{2}\} \mathrm{d}x_2 \\ &= \sqrt{2\pi(\sigma_1^2 + \sigma_2^2} \cdot \exp\{-\frac{u^2\sigma_1^2 + v^2\sigma_2^2}{2}\} \end{aligned} \tag{C.5}$$

It is assumed that frequencies that are smaller than 1% of the maximum frequency can be neglected. The maximum frequency occurs at $u = 0, v = 0$. Hence, the frequencies where the Fourier transform still have 1% of the maximum amplitude are given by

$$0\ 01 = \exp\{-\frac{u^2\sigma_1^2 + v^2\sigma_2^2}{2}\} \tag{C.6}$$

If the "limit frequencies" are chosen equally ($u_{lim} = v_{lim}$), the minimum necessary frequency for depicting the 2D-Gaussian is given by

$$u = \frac{\sqrt{\ln 100}}{\sigma} \tag{C.7}$$

Here, $\sigma = \sigma_1 = \sigma_2$. As in the above described example both standard deviations amounted 0.1 cm, the minimum required frequency amounts 21.46 cm^{-1}.

Appendix D

Variation of the regularization parameter for Landweber algorithm

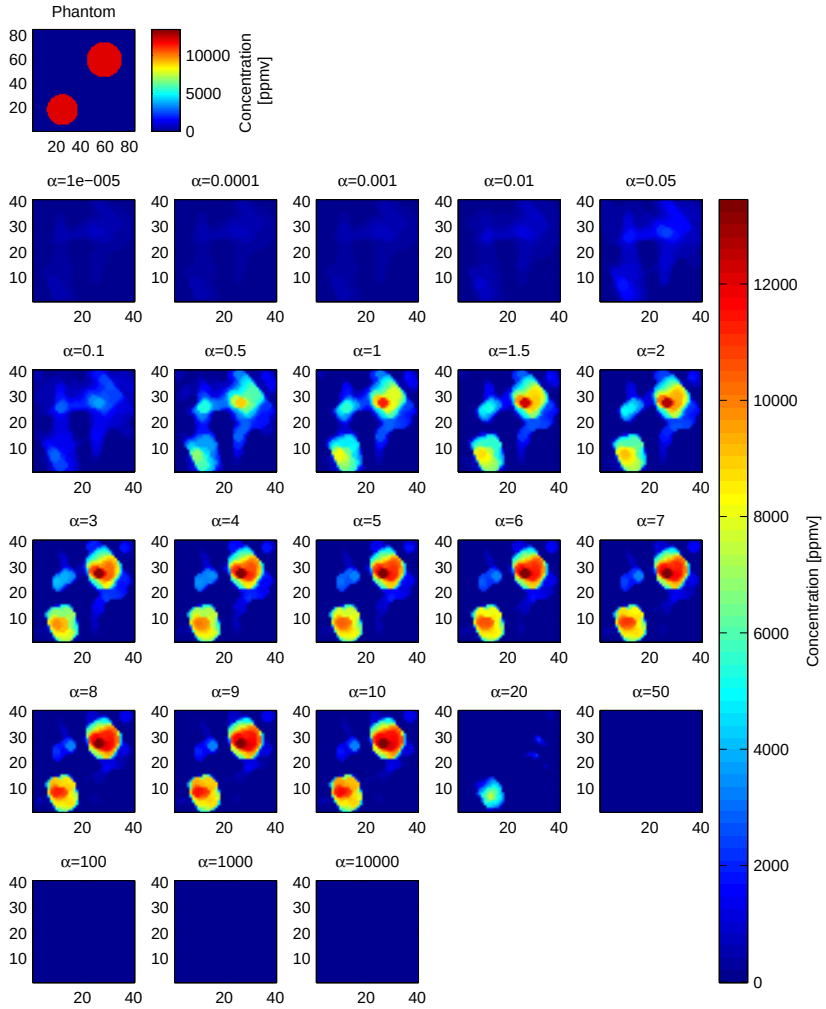

Figure D.1 Virtual experiment with a top-hat phantom and reconstructions carried out with Landweber algorithm with varied regularisation parameter α_{LW}

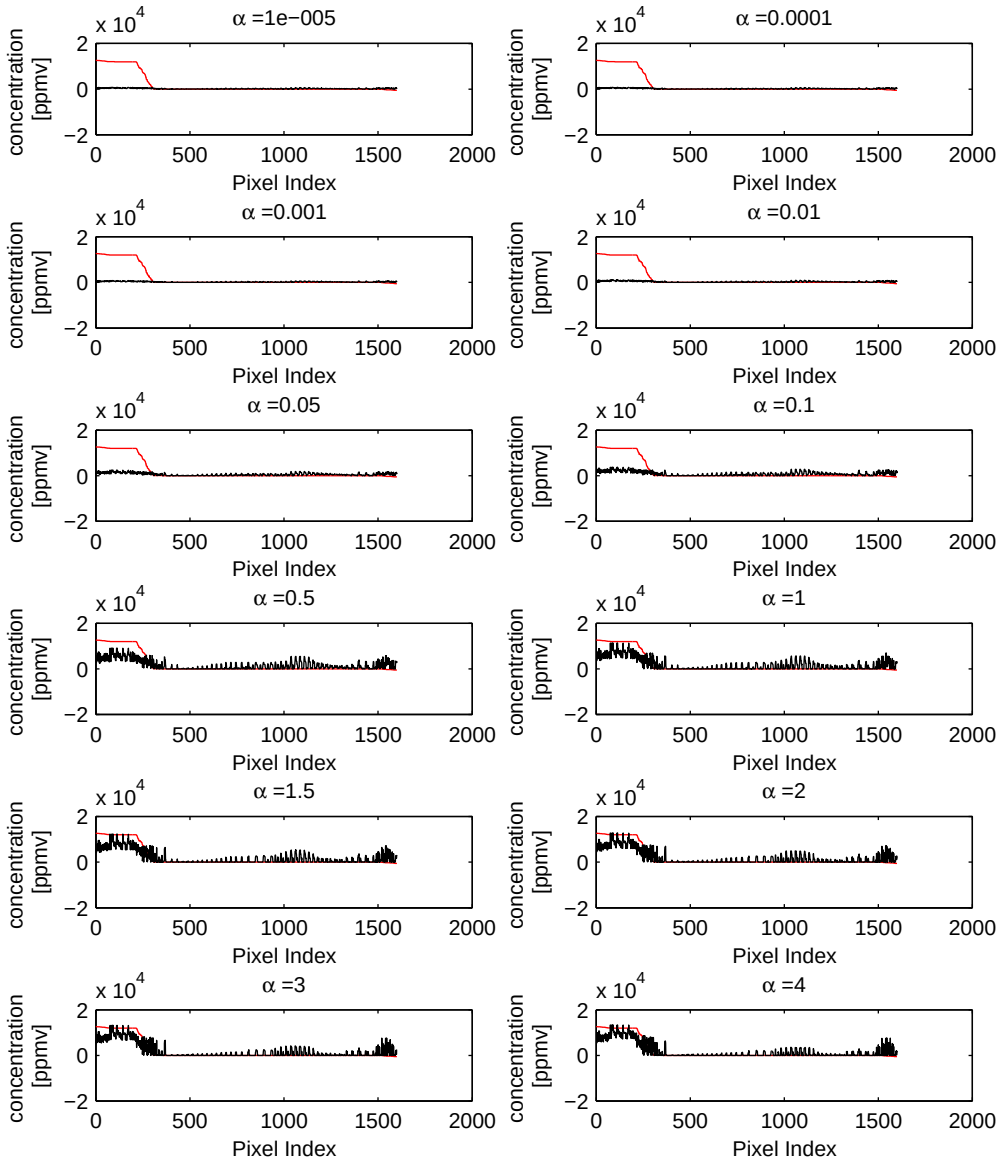

Figure D.2 Parameter variation study of α_{LW} – part I.The discretisation of the phantom had to be reduced to the size of the reconstruction image for comparing the images pixel-wise. The pixels of the phantom were sorted such that their regarding concentrations (i.e. pixel values) decrease. The red lines show the values of the down-sampled phantom image, while the black lines show the corresponding pixel values of the reconstructions with varied regularization parameter.

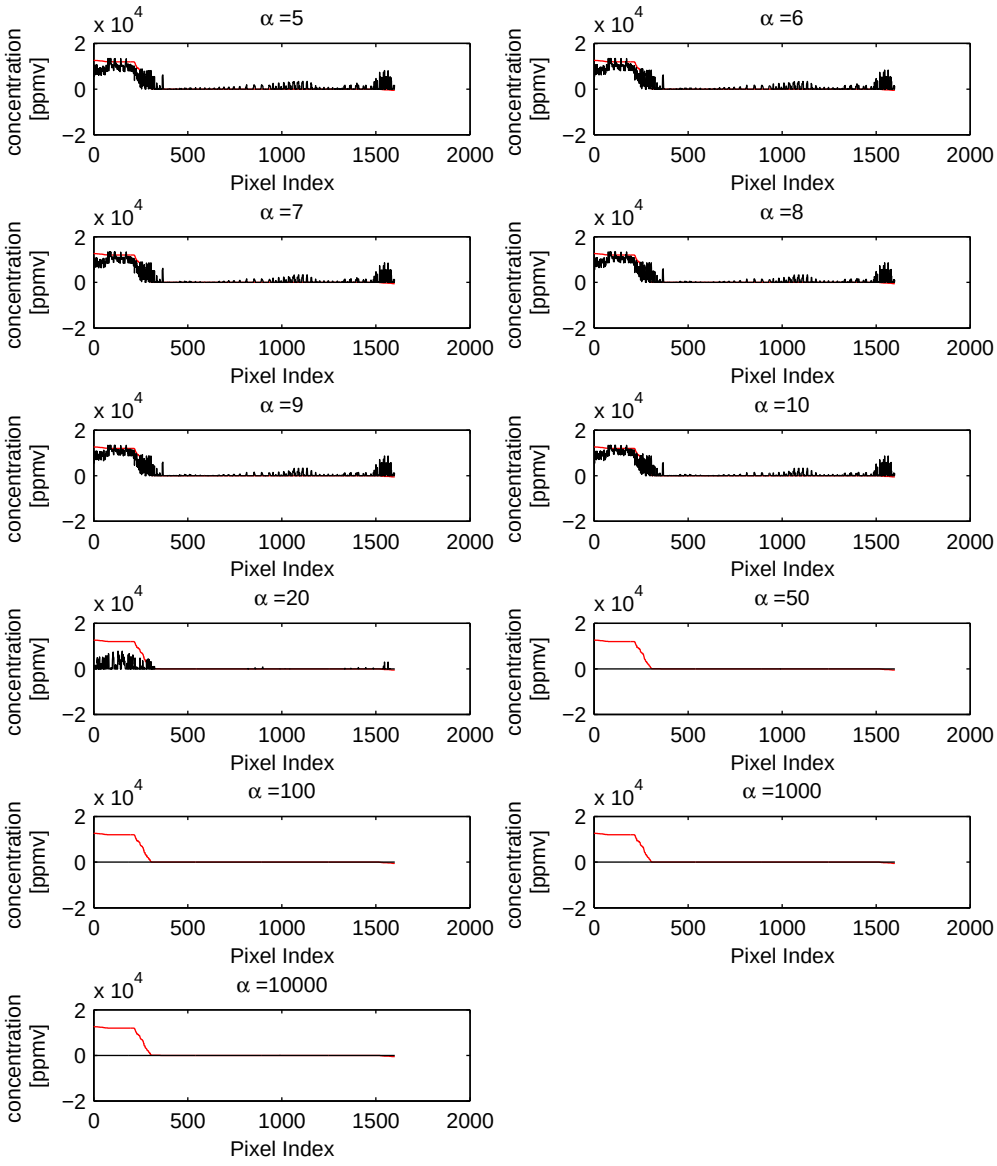

Figure D.3 Parameter variation study of α_{LW} – part II.The discretisation of the phantom had to be reduced to the size of the reconstruction image for comparing the images pixel-wise. The pixels of the phantom were sorted such that their regarding concentrations (i.e. pixel values) decrease. The red lines show the values of the down-sampled phantom image, while the black lines show the corresponding pixel values of the reconstructions with varied regularization parameter.

Appendix E

Virtual experiments: line plots of phantoms and reconstructions

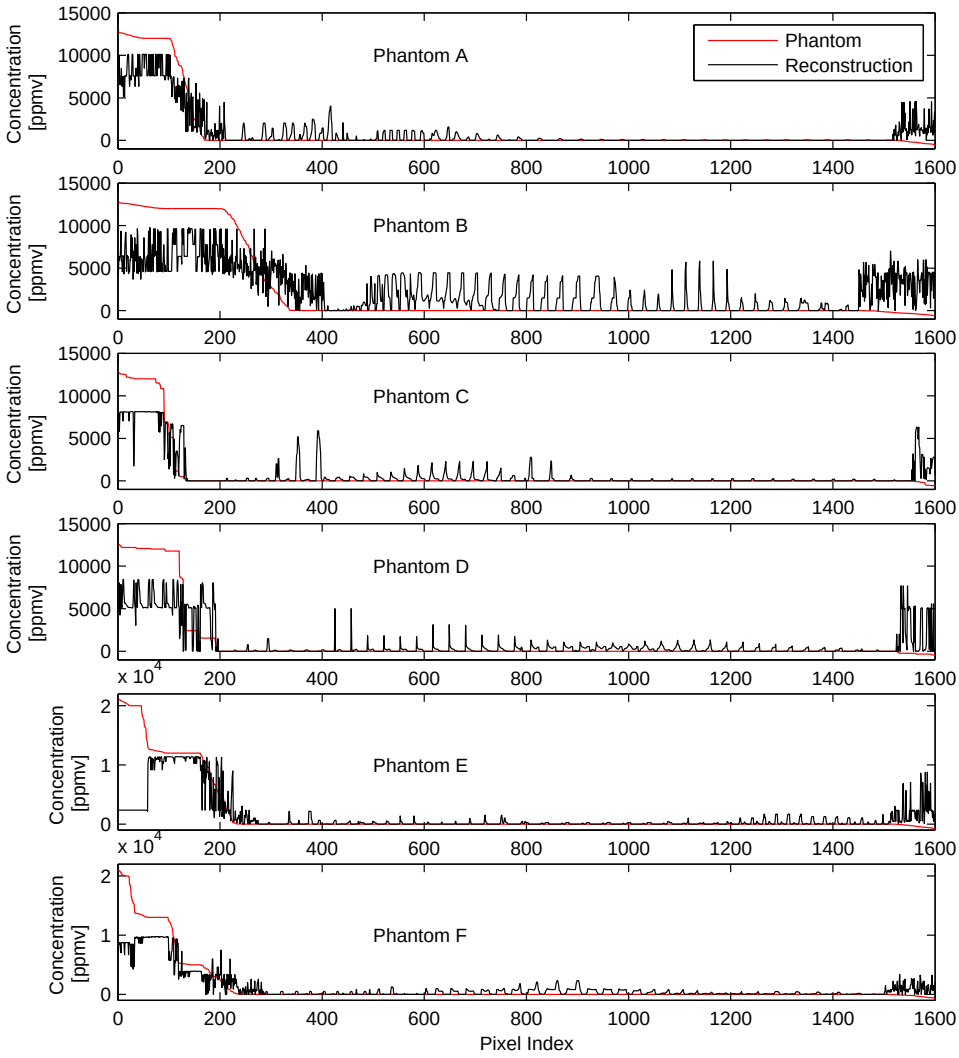

Figure E.1 Lineplots of the phantoms (red) and reconstructions with ART (black) that are shown in figure 4.4. The phantoms were first down-sampled with a bi-cubic interpolation and then the pixels were sorted such that pixel values descend.

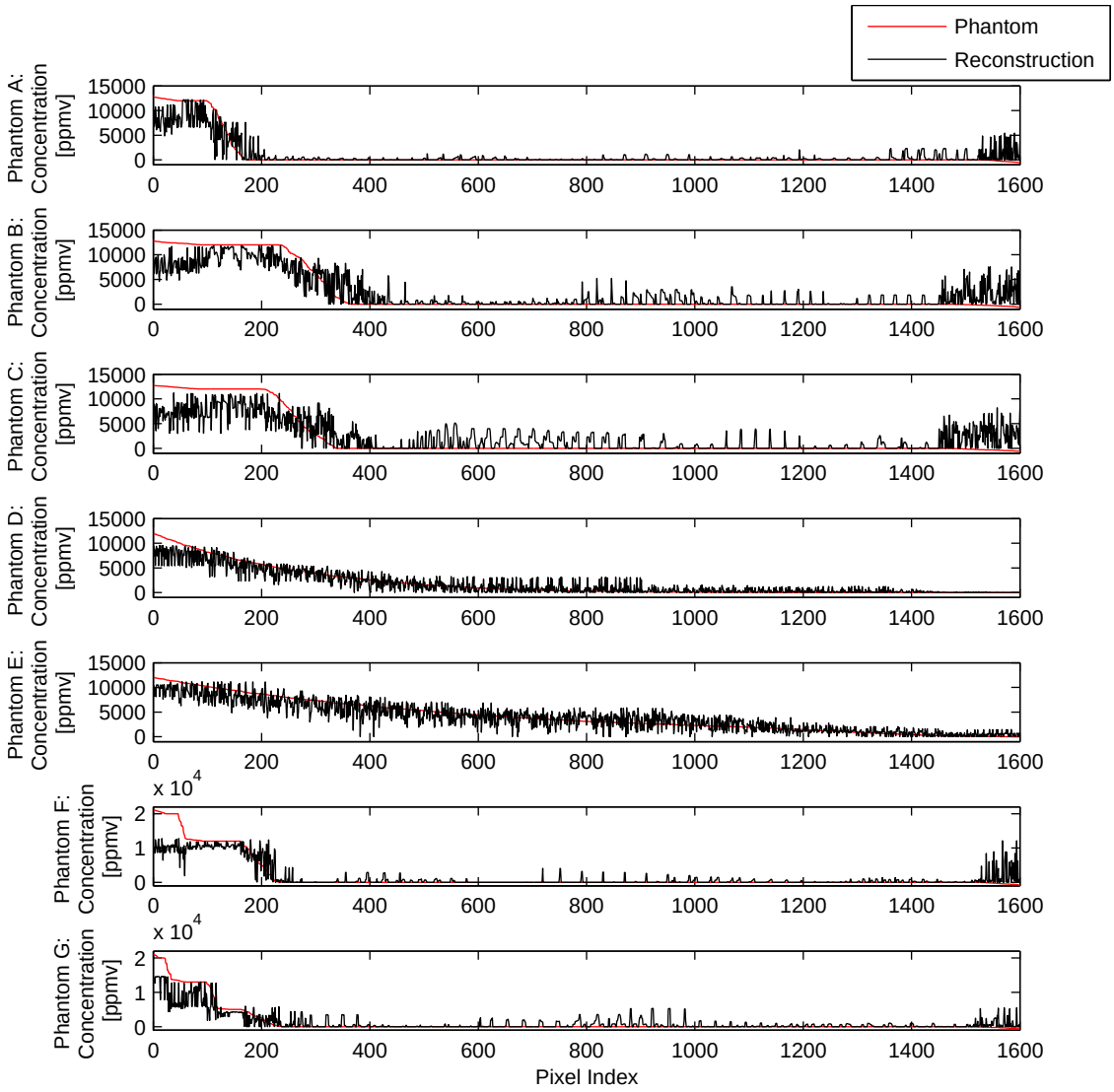

Figure E.2 Lineplots of the phantoms (red) and reconstructions with Landweber algorithm (black) that are shown in figure 4.5. The phantoms were first down-sampled with a bi-cubic interpolation and then the pixels were sorted such that pixel values descend.

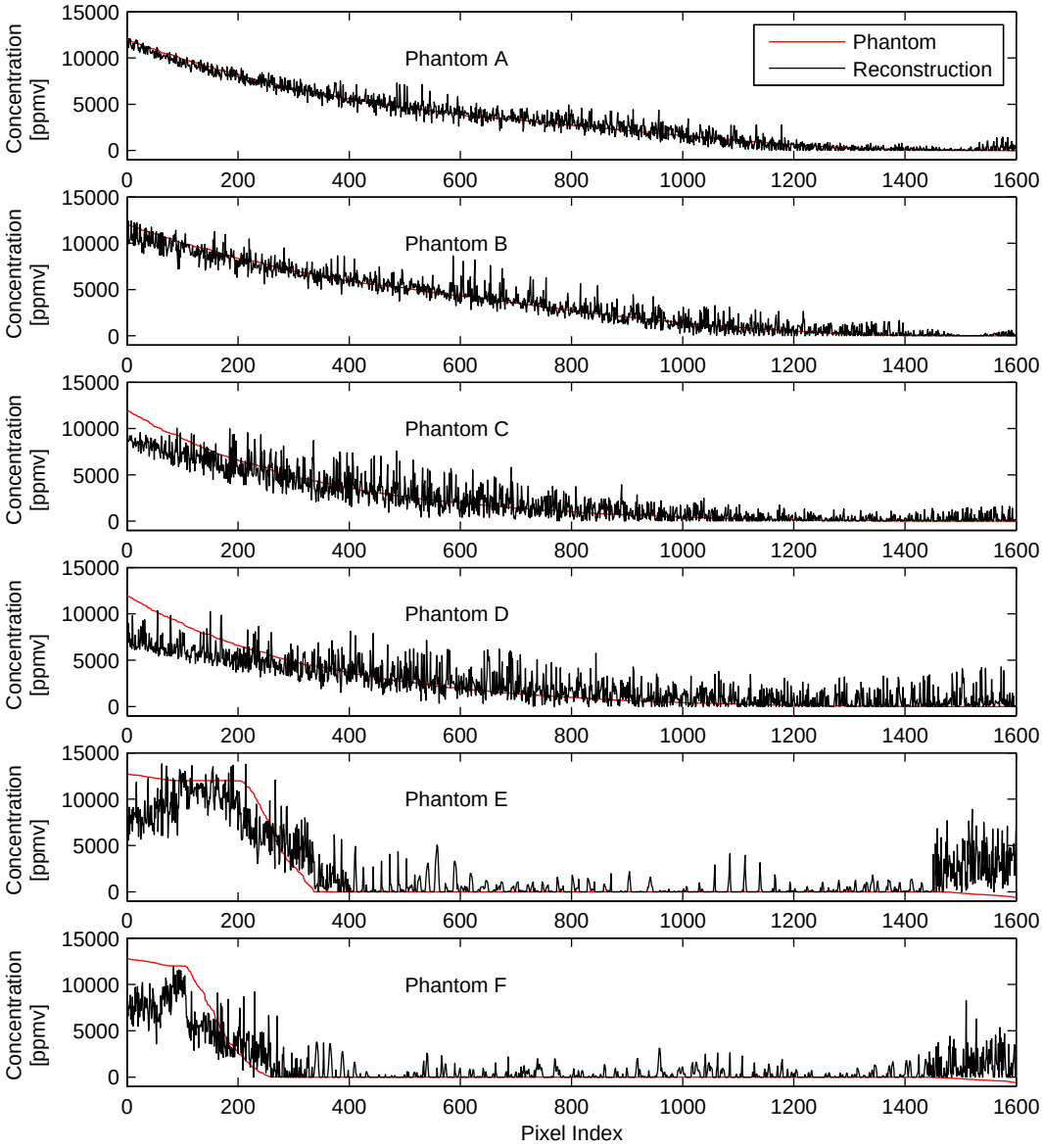

Figure E.3 Lineplots of the phantoms (red) and reconstructions with Tikhonov algorithm (black) that are shown in figure 4.7. The phantoms were first down-sampled with a bi-cubic interpolation and then the pixels were sorted such that pixel values descend.

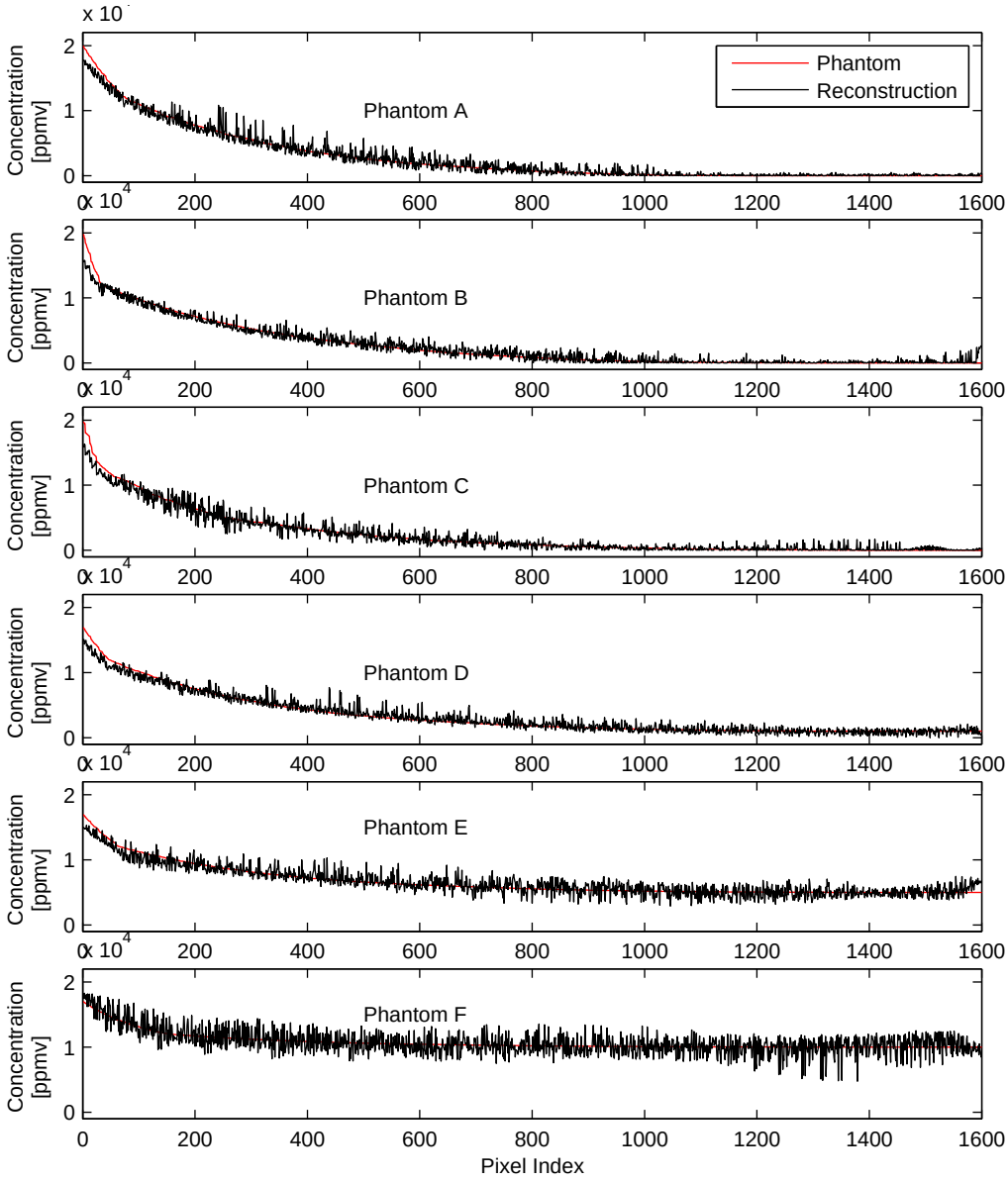

Figure E.4 Lineplots of the phantoms (red) and reconstructions with Tikhonov algorithm (black) that are shown in figure 4.8. The phantoms were first down-sampled with a bi-cubic interpolation and then the pixels were sorted such that pixel values descend.

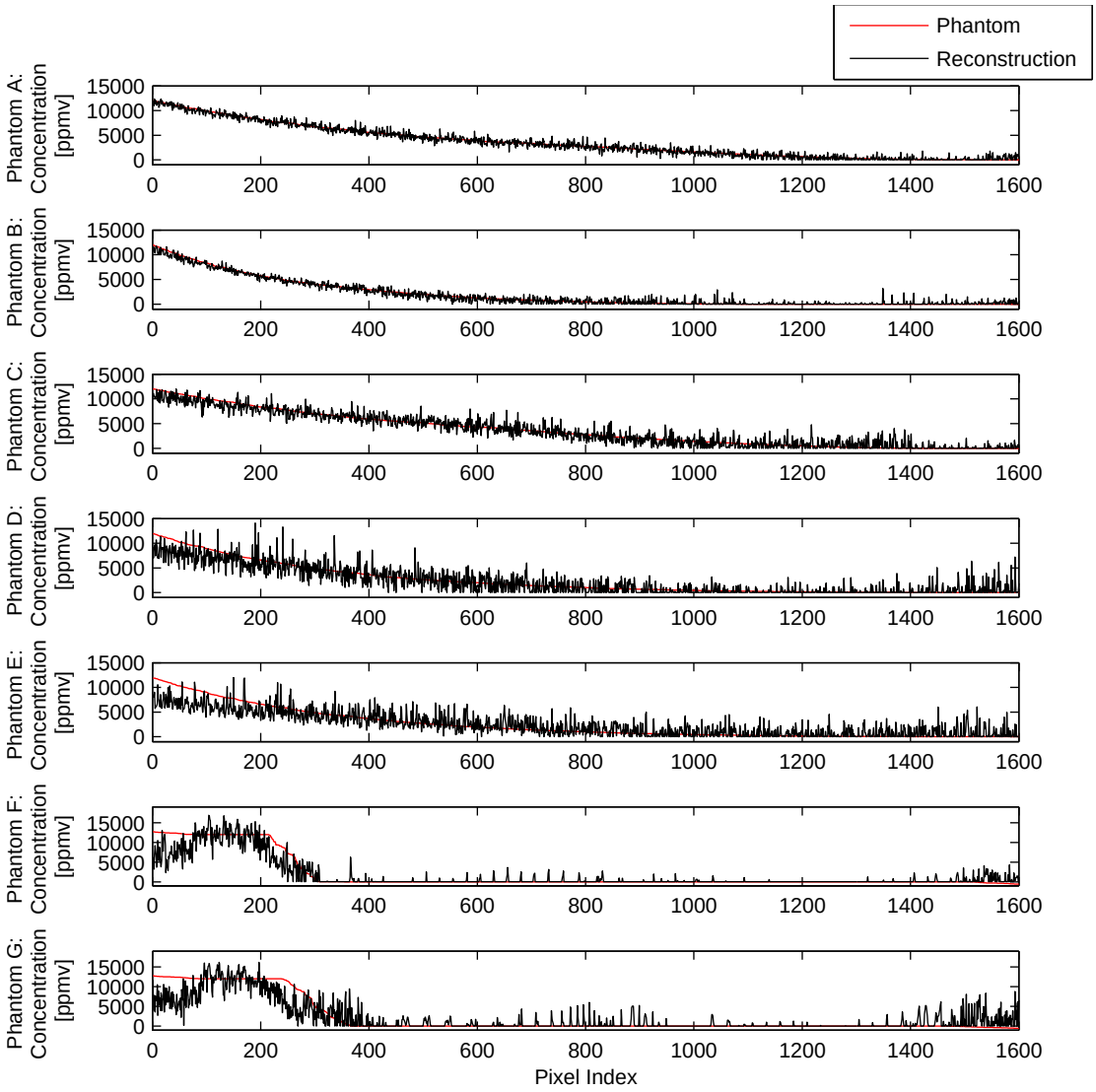

Figure E.5 Lineplots of the phantoms (red) and reconstructions with informative smoothness prior (black) that are shown in figure 4.9. The phantoms were first down-sampled with a bi-cubic interpolation and then the pixels were sorted such that pixel values descend.

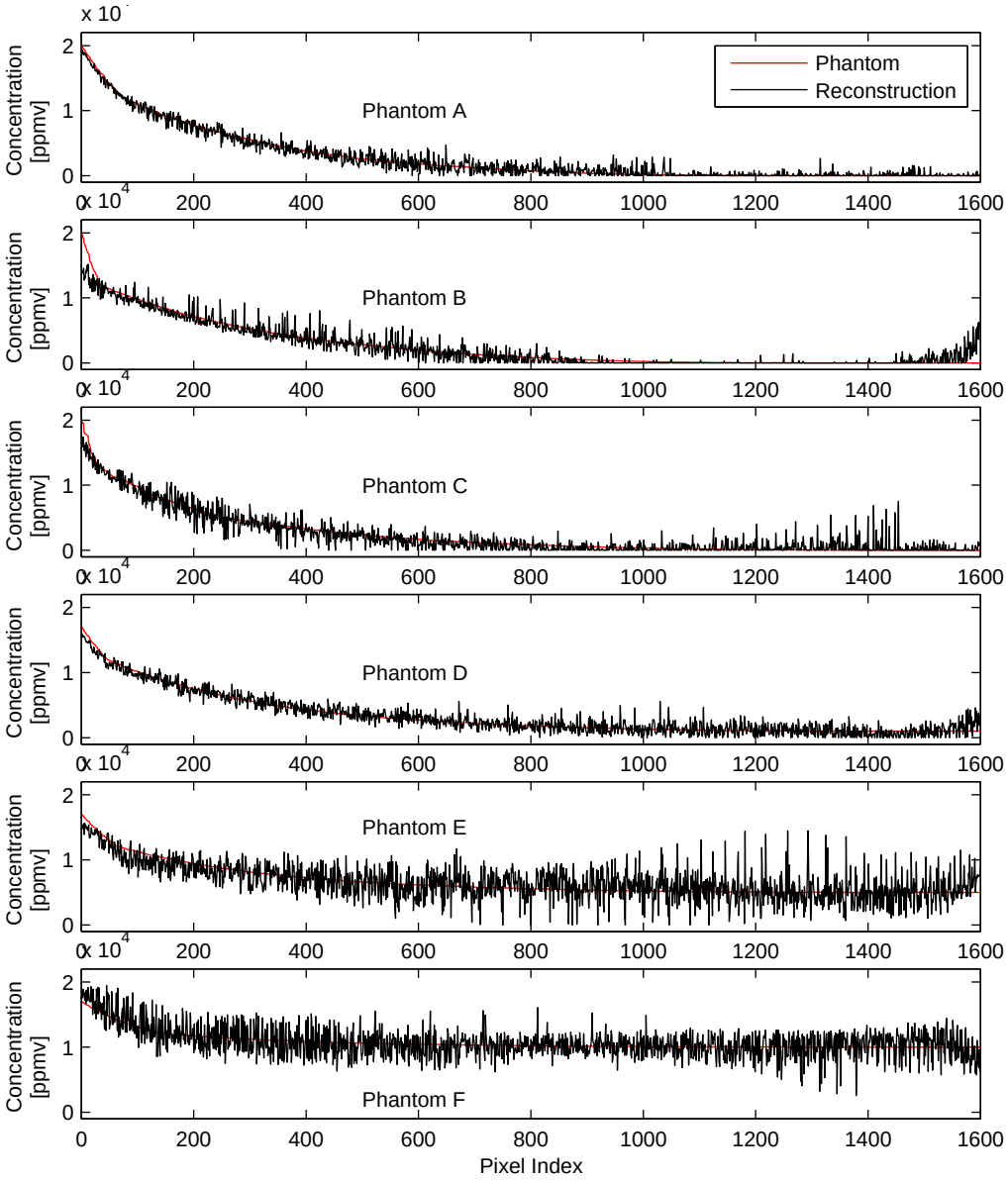

Figure E.6 Lineplots of the phantoms (red) and reconstructions with informative smoothness prior (black) that are shown in figure 4.10. The phantoms were first down-sampled with a bi-cubic interpolation and then the pixels were sorted such that pixel values descend.

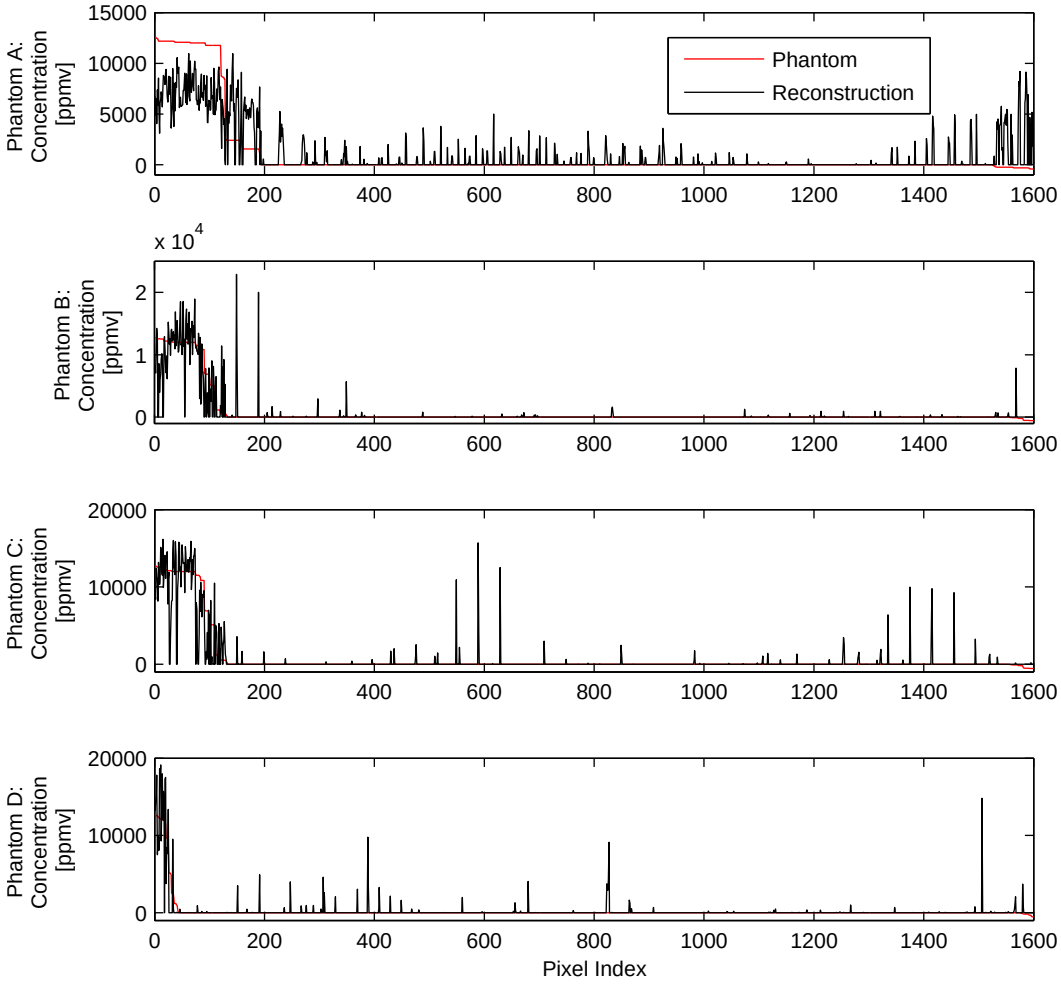

Figure E.7 Lineplots of the phantoms (red) and reconstructions with informative smoothness prior (black) that are shown in figure 4.14. The phantoms were first down-sampled with a bi-cubic interpolation and then the pixels were sorted such that pixel values descend.

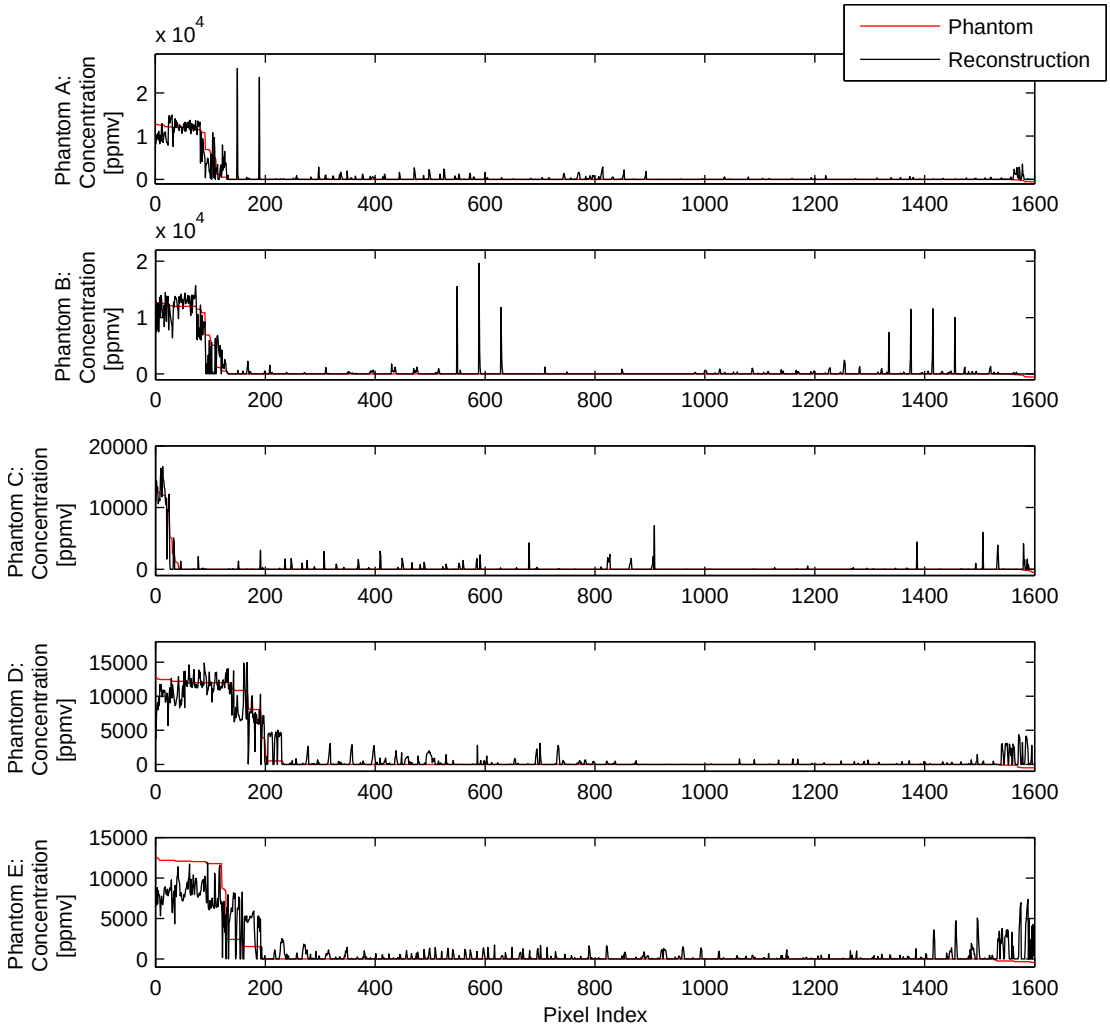

Figure E.8 Lineplots of the phantoms (red) and reconstructions with TV prior (black) that are shown in figure 4.15. The phantoms were first down-sampled with a bi-cubic interpolation and then the pixels were sorted such that pixel values descend.

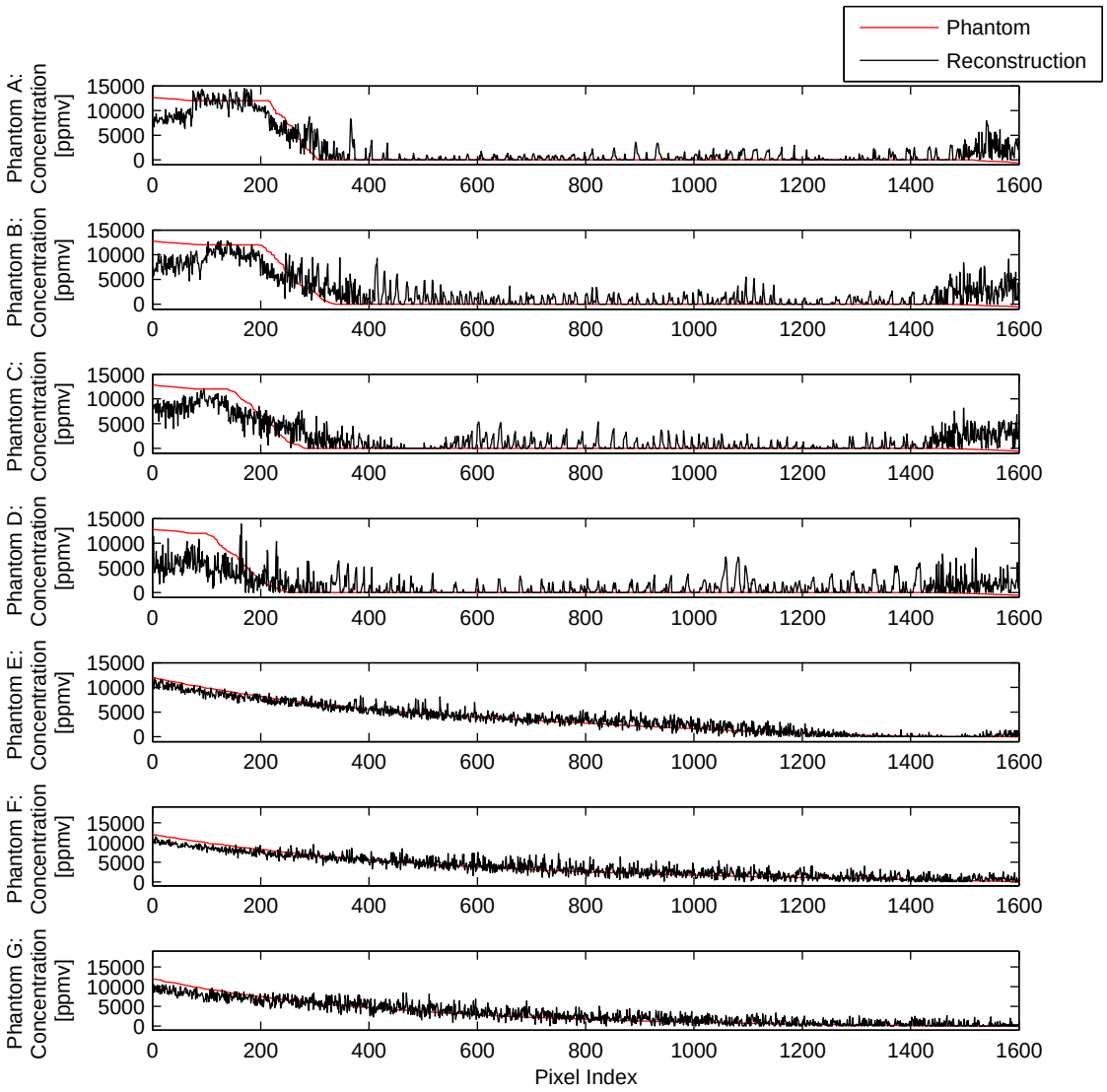

Figure E.9 Lineplots of the phantoms (red) and reconstructions with TV prior (black) that are shown in figure 4.16. The phantoms were first down-sampled with a bi-cubic interpolation and then the pixels were sorted such that pixel values descend.

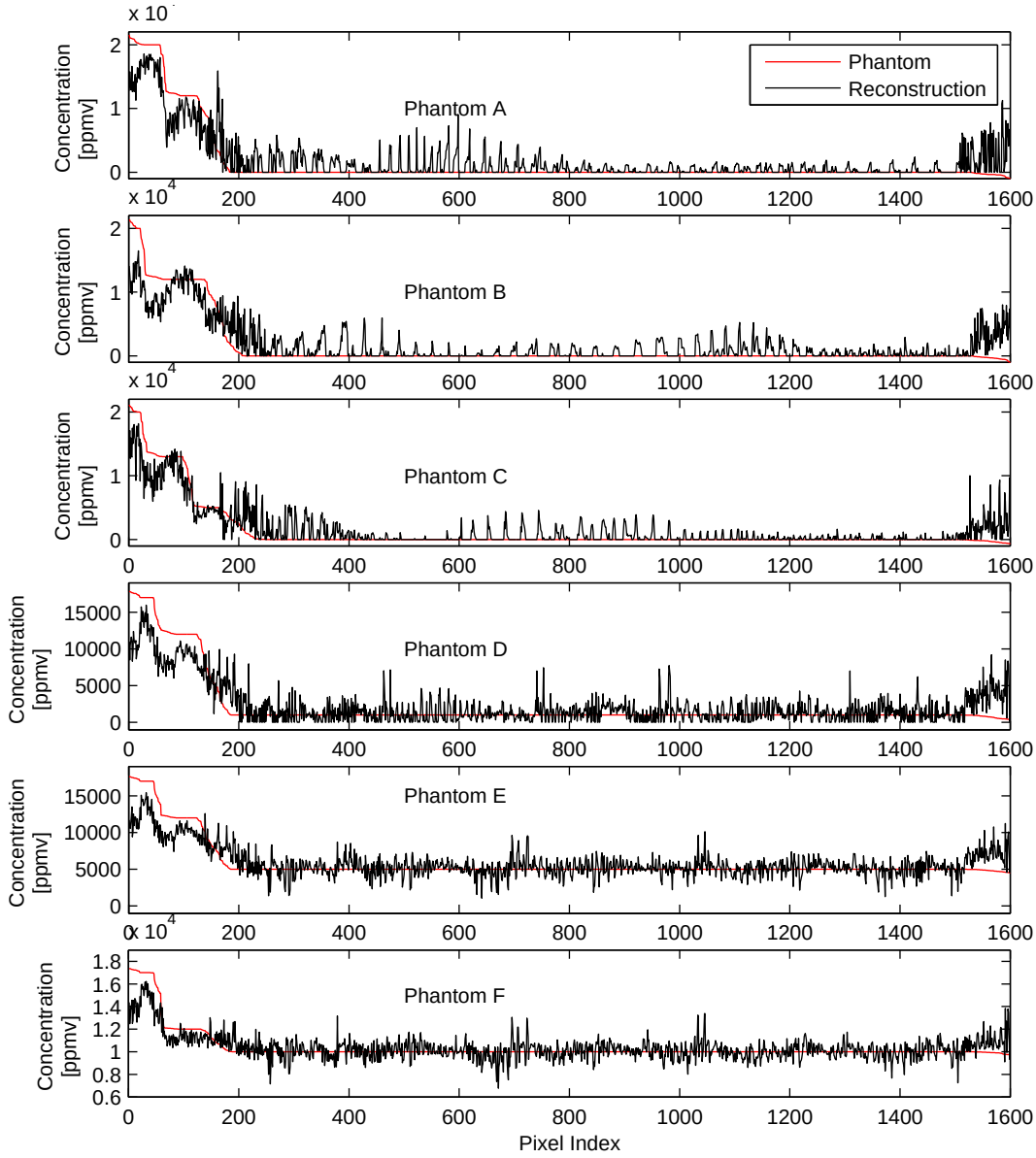

Figure E.10 Lineplots of the phantoms (red) and reconstructions with TV prior (black) that are shown in figure 4.17. The phantoms were first down-sampled with a bi-cubic interpolation and then the pixels were sorted such that pixel values descend.

Appendix F

Virtual experiment studies

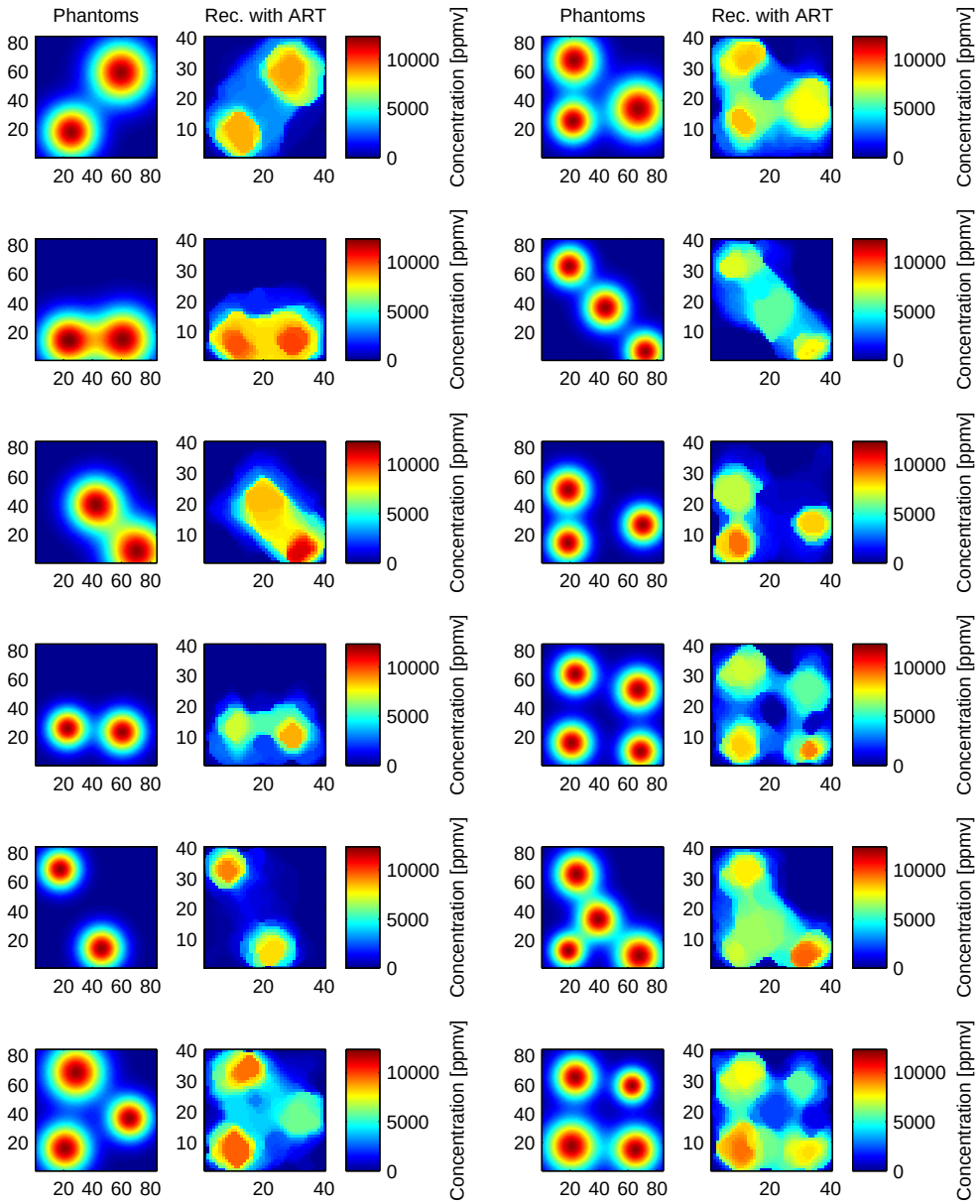

Figure F.1 Virtual experiment study: Reconstructions with ART algorithm – part I

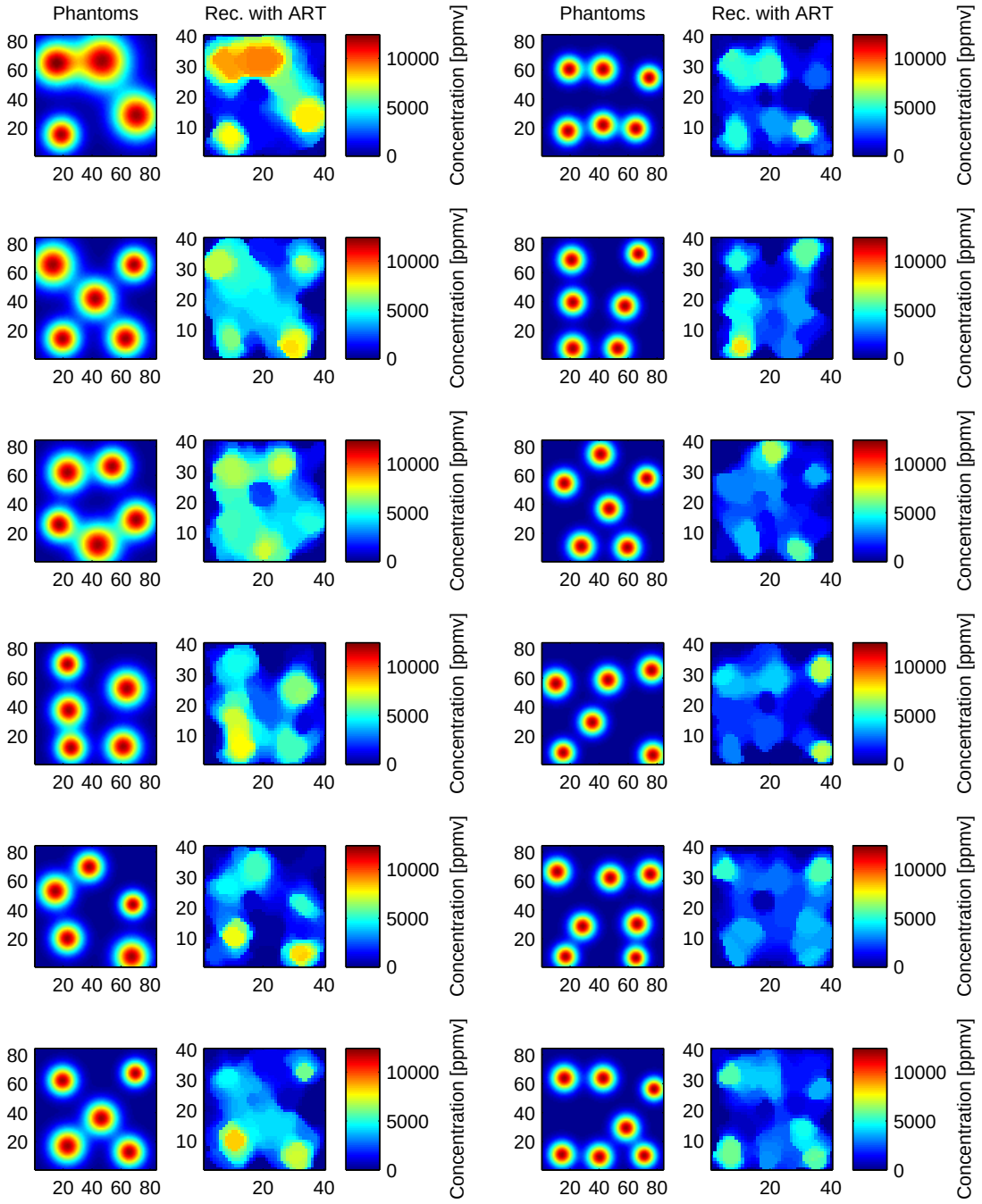

Figure F.2 Virtual experiment study: Reconstructions with ART algorithm – part II

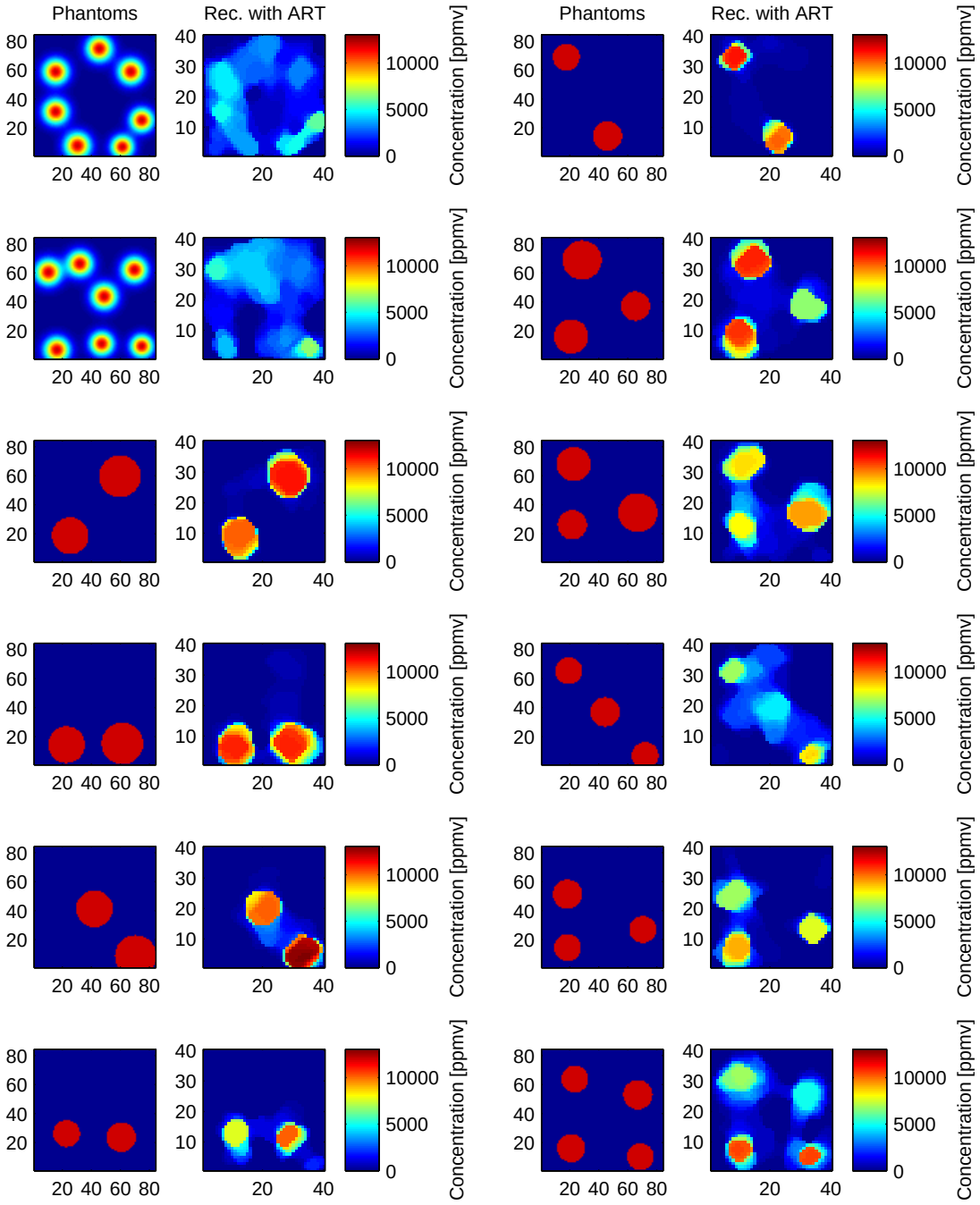

Figure F.3 Virtual experiment study: Reconstructions with ART algorithm – part III

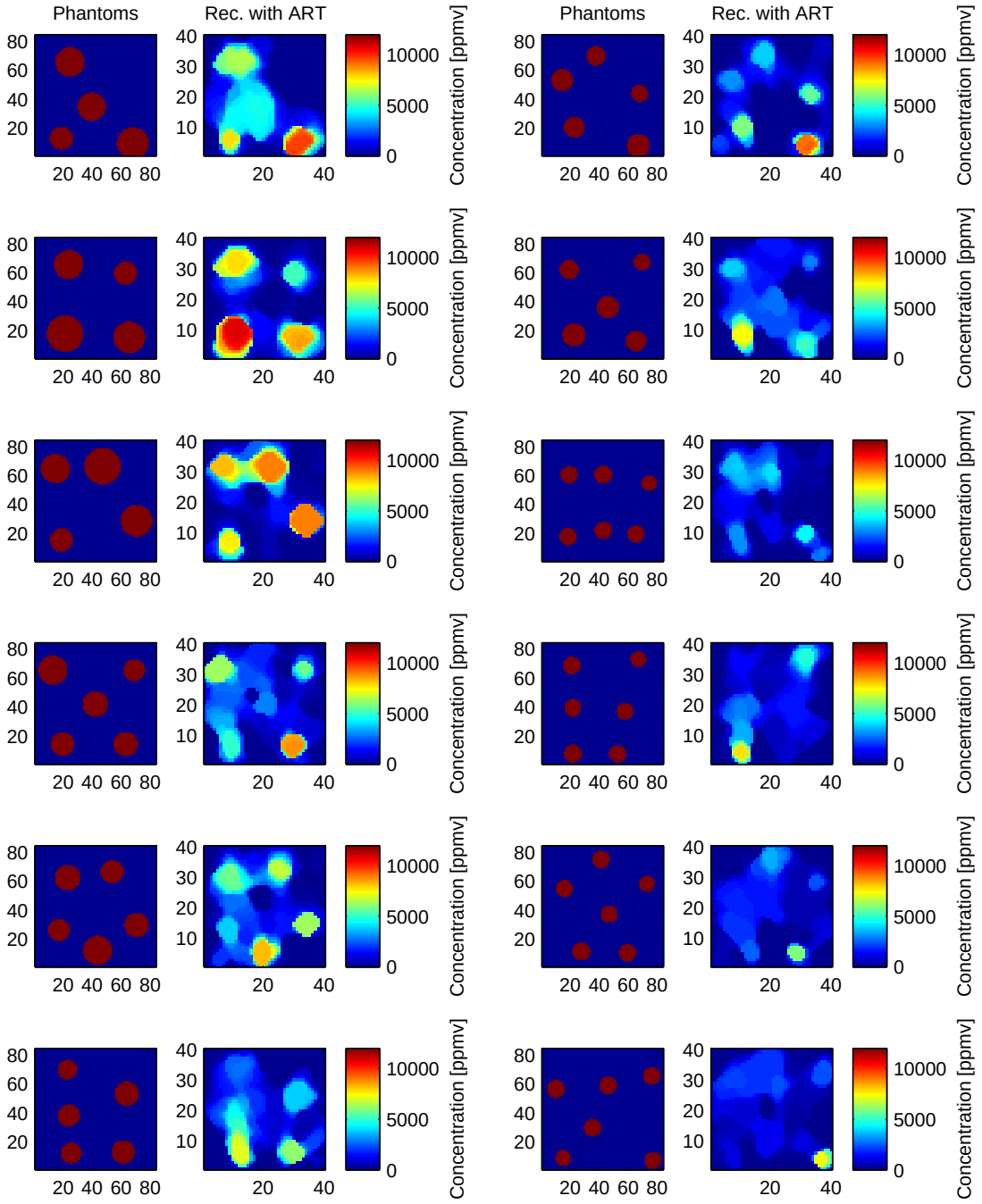

Figure F.4 Virtual experiment study: Reconstructions with ART algorithm – part IV

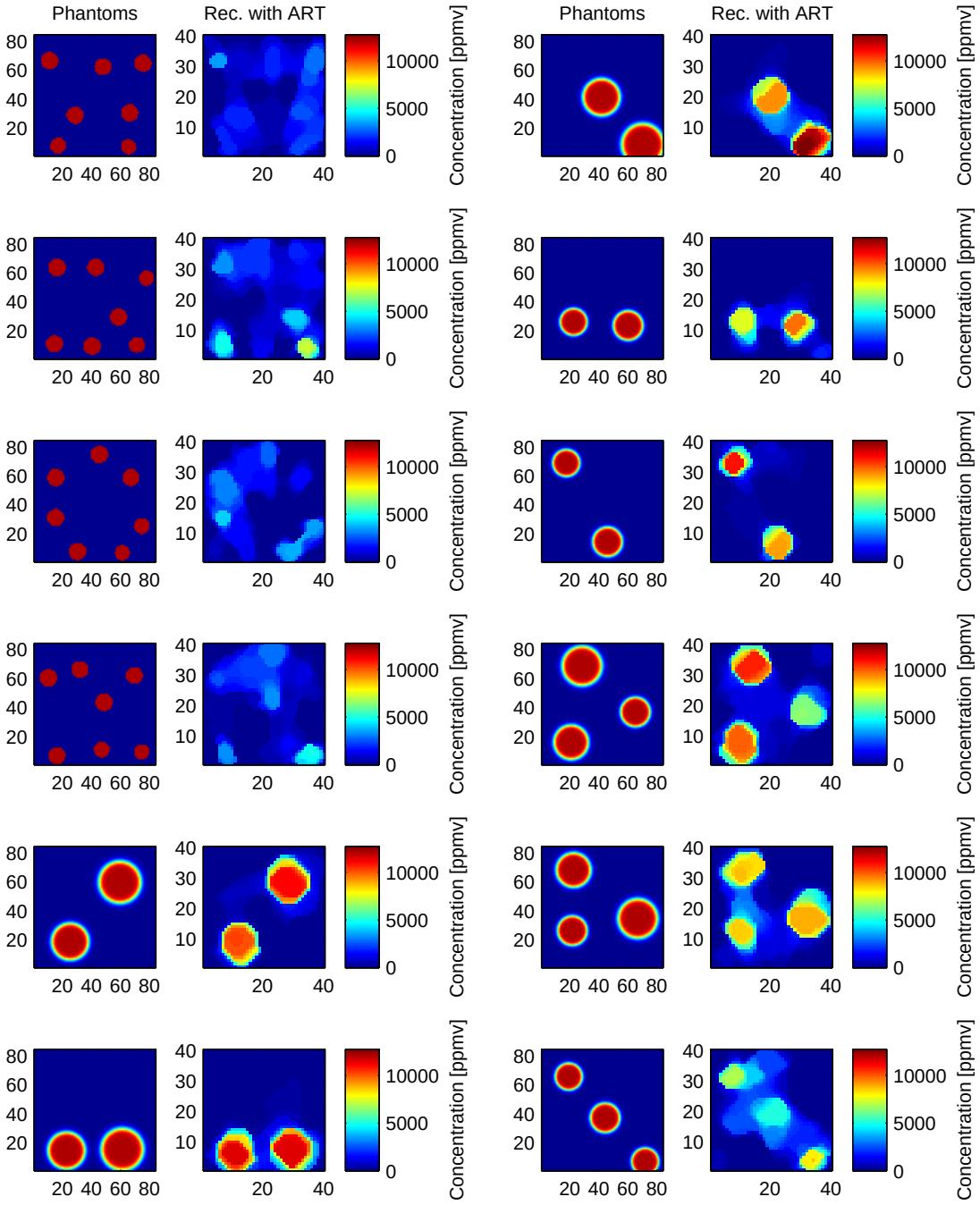

Figure F.5 Virtual experiment study: Reconstructions with ART algorithm – part V

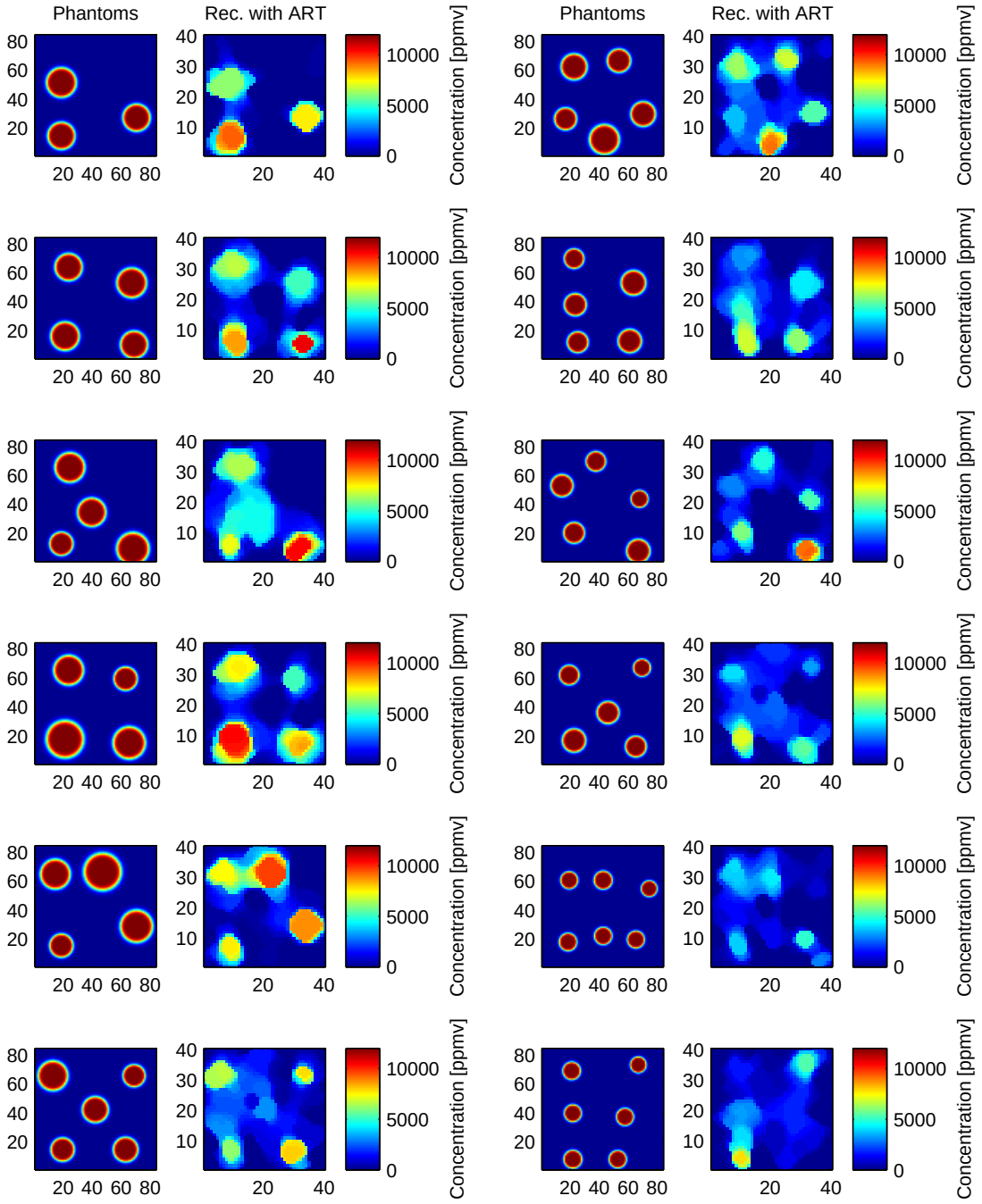

Figure F.6 Virtual experiment study: Reconstructions with ART algorithm – part VI

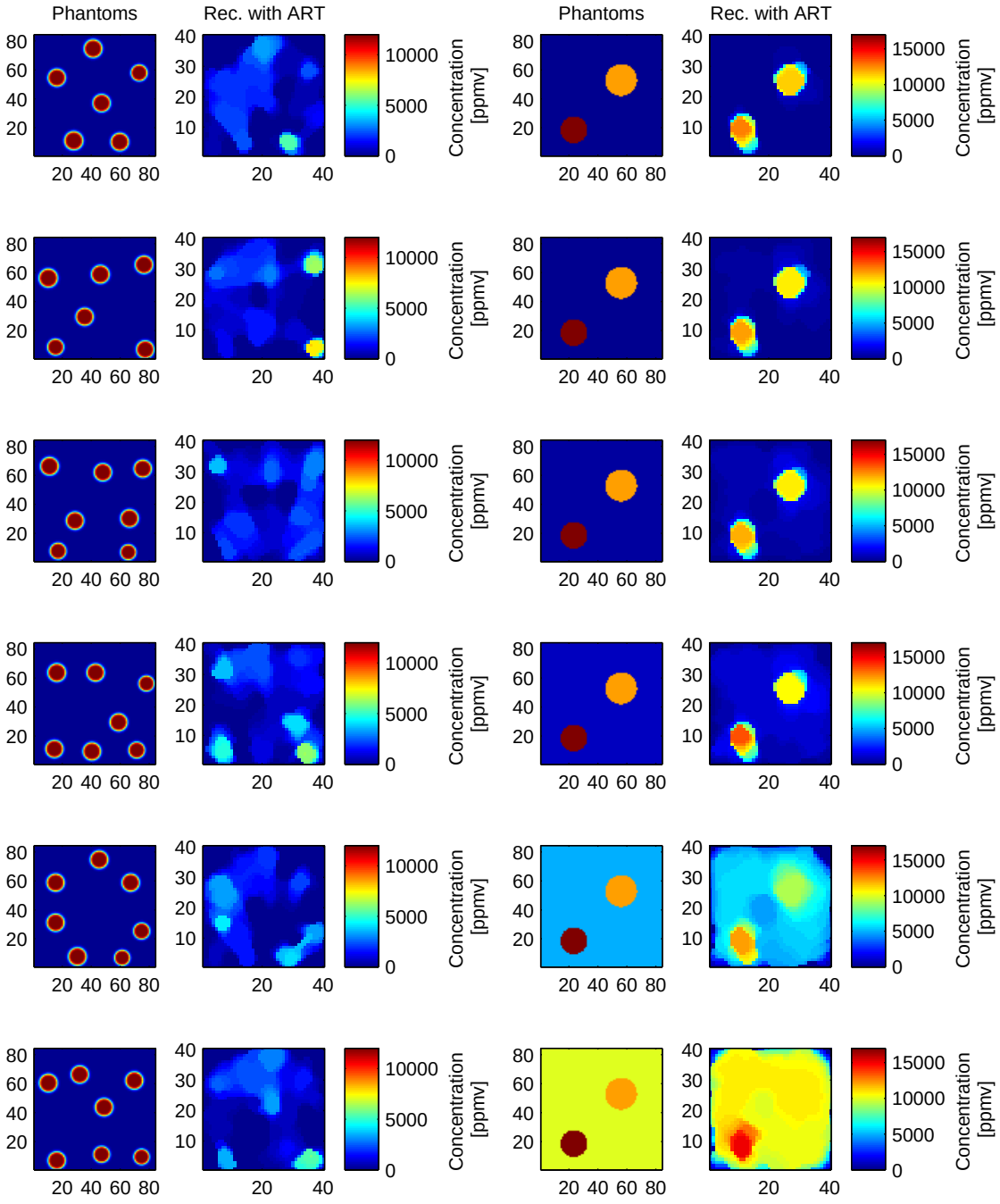

Figure F.7 Virtual experiment study: Reconstructions with ART algorithm – part VII

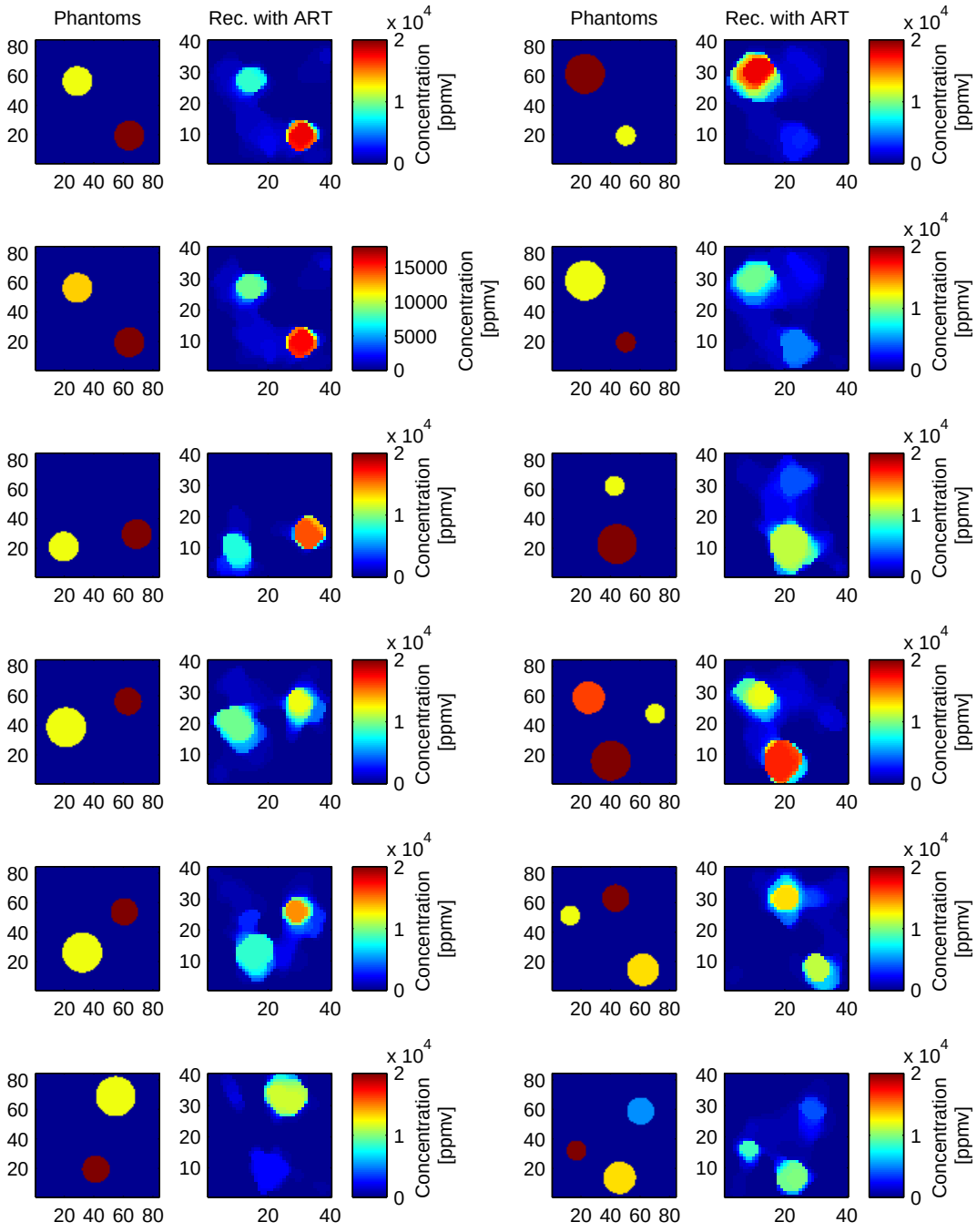

Figure F.8 Virtual experiment study: Reconstructions with ART algorithm – part VIII

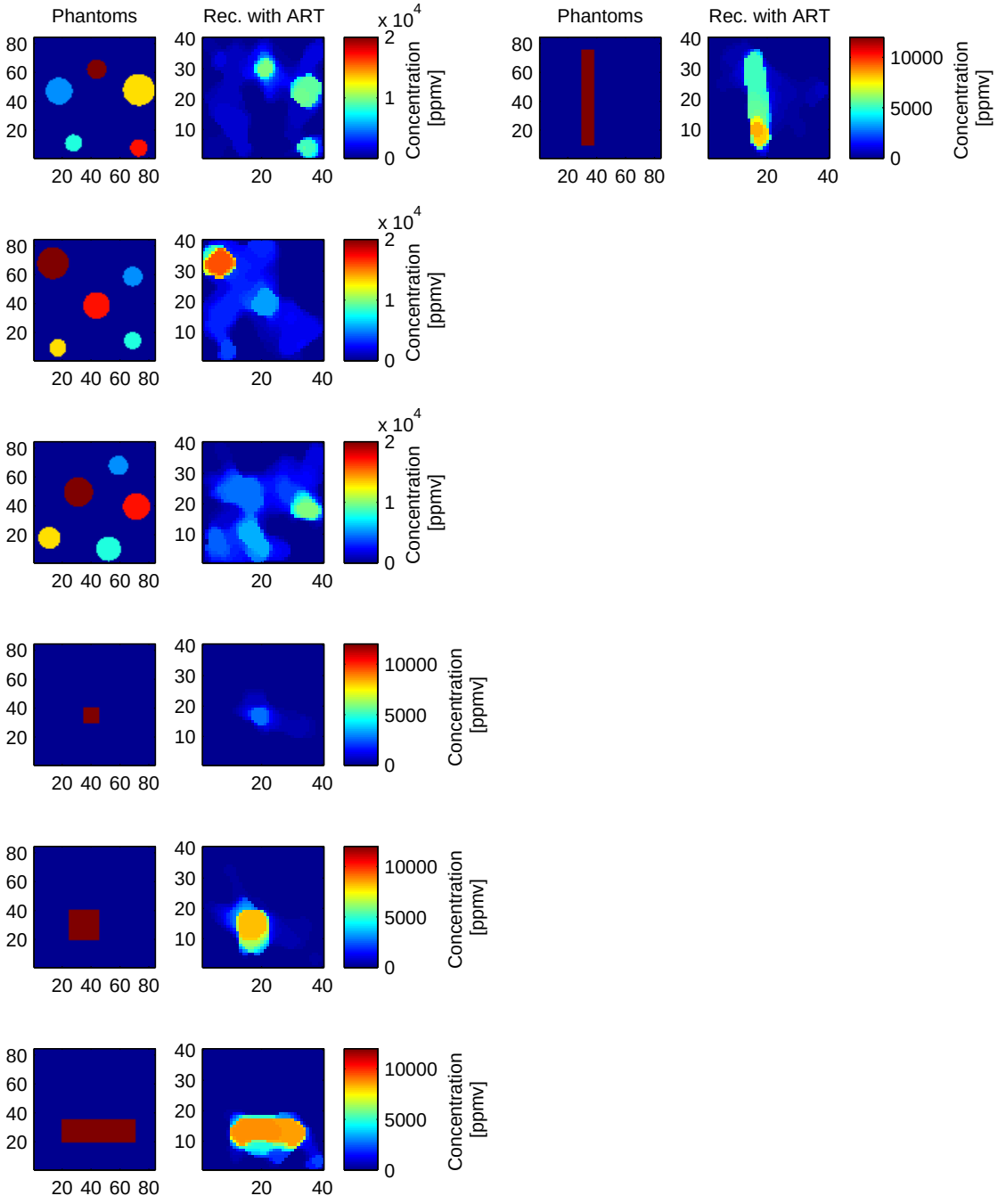

Figure F.9 Virtual experiment study: Reconstructions with ART algorithm – part IX

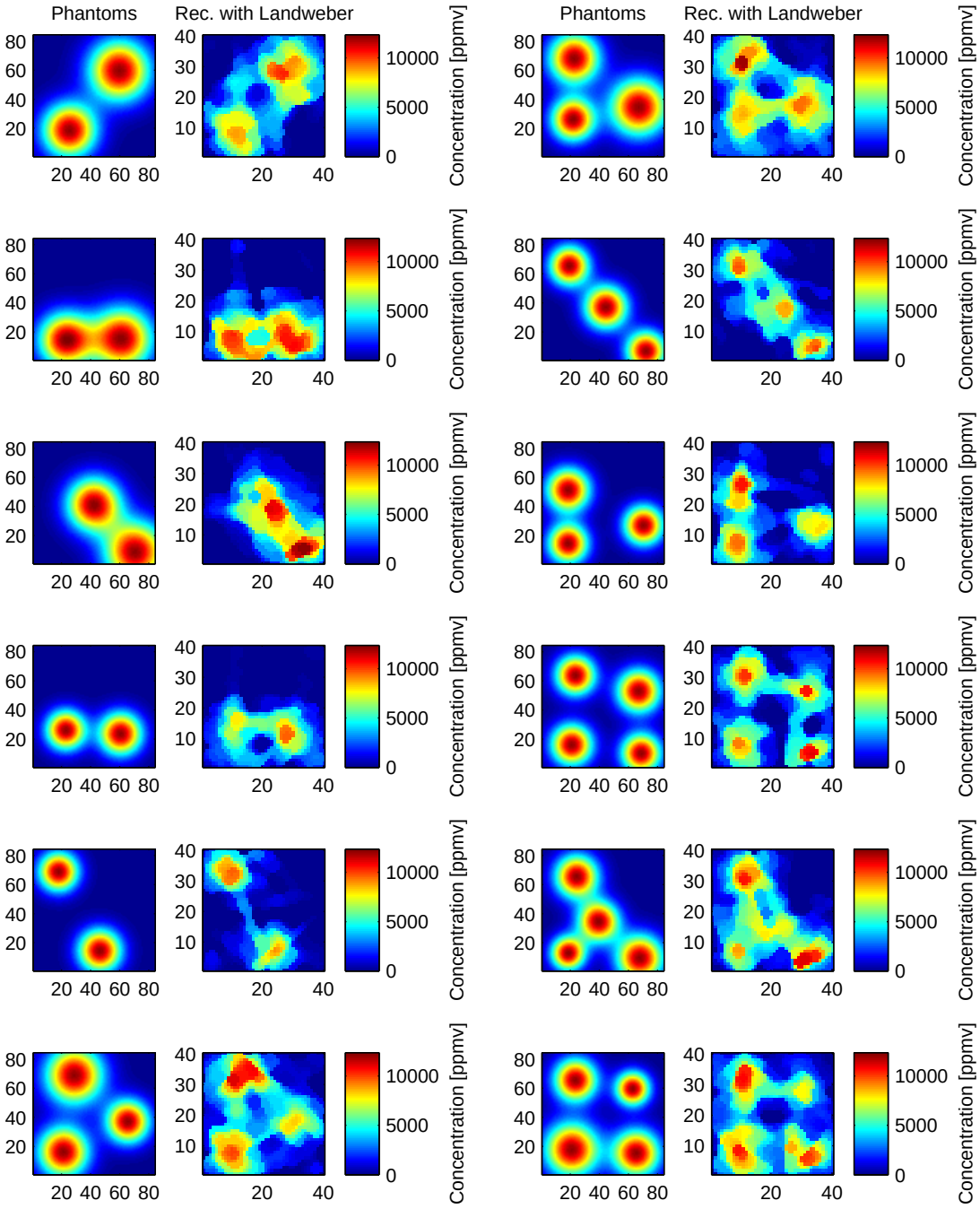

Figure F.10 Virtual experiment study: Reconstructions with Landweber algorithm – Part I

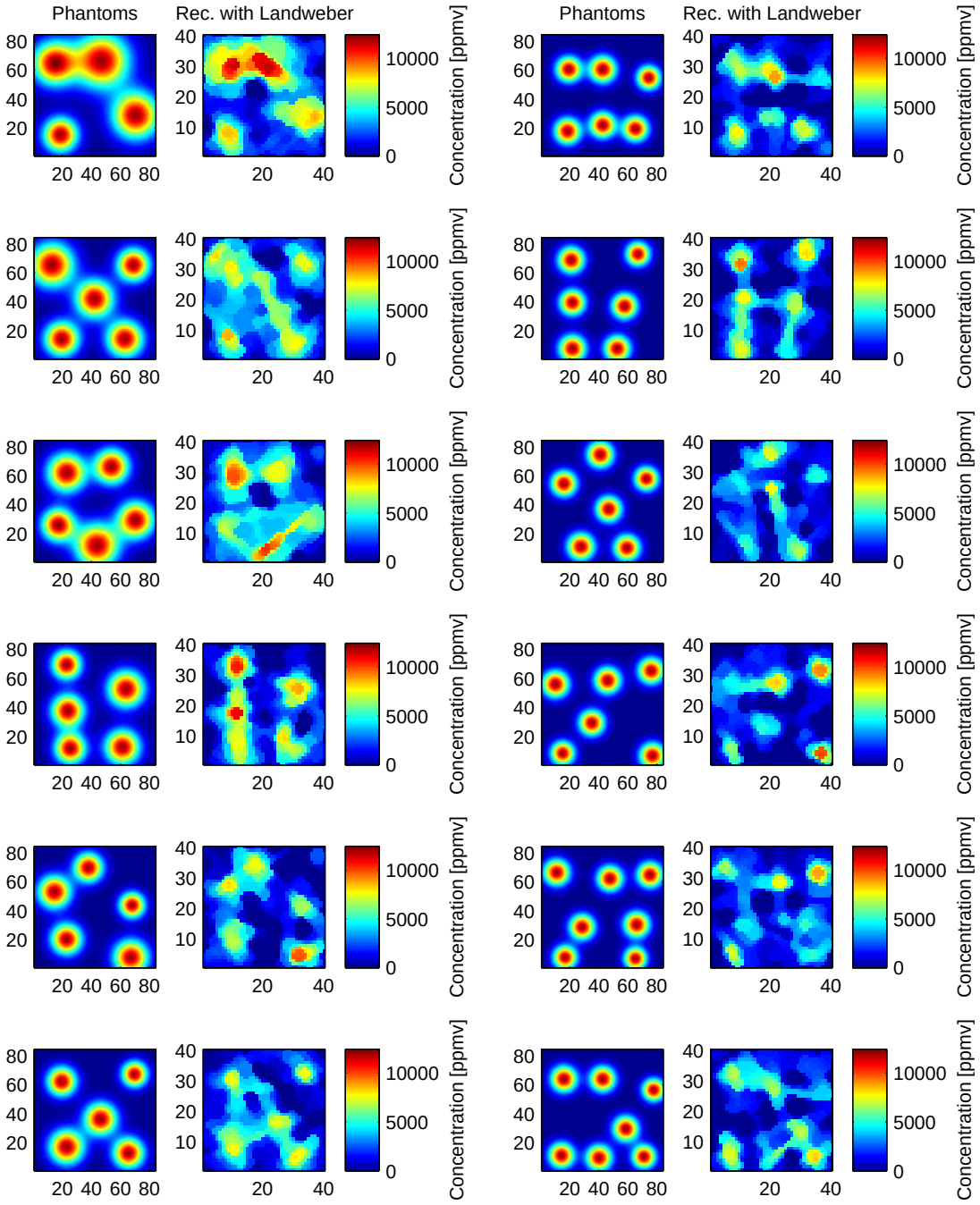

Figure F.11 Virtual experiment study: Reconstructions with Landweber algorithm – Part II

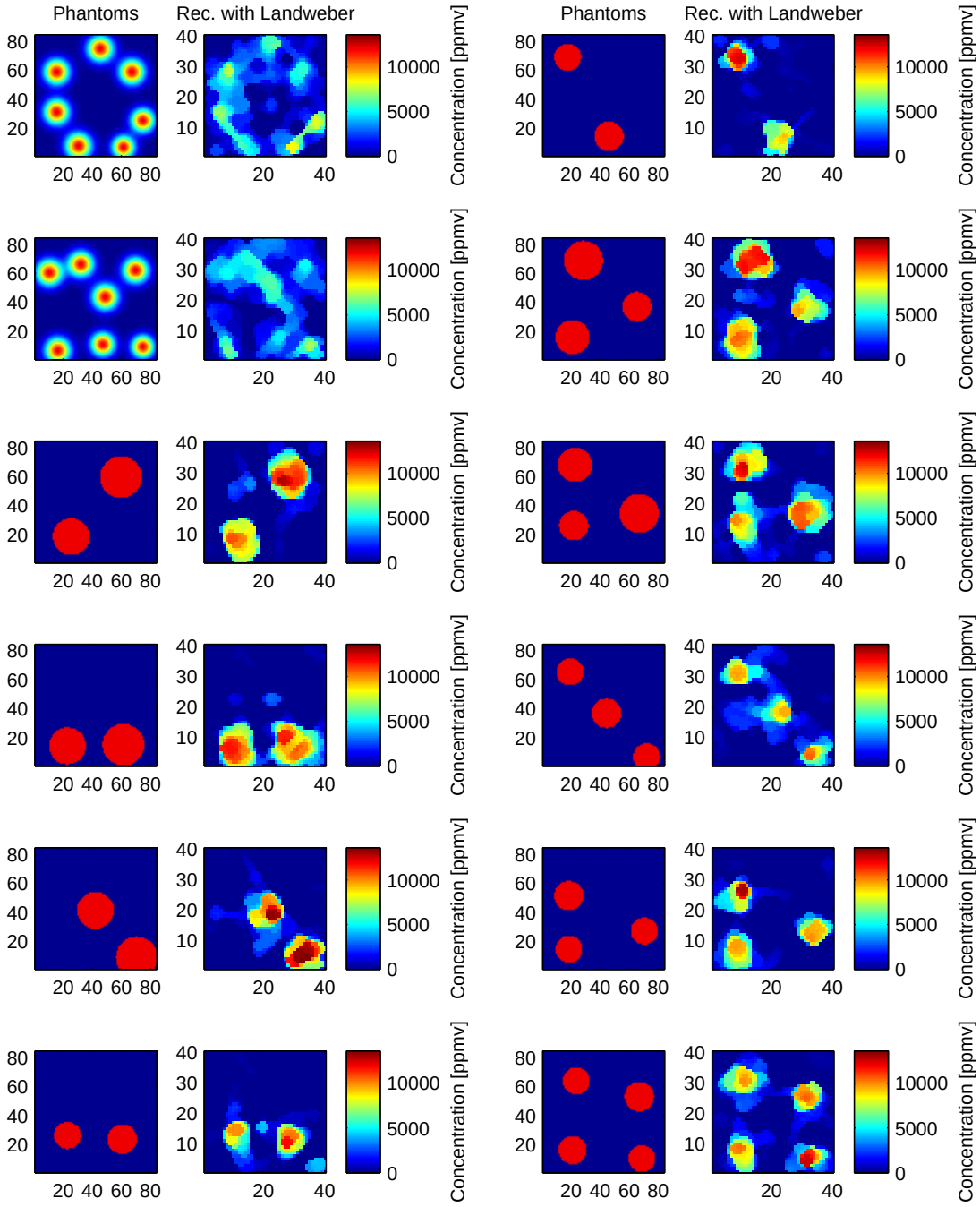

Figure F.12 Virtual experiment study: Reconstructions with Landweber algorithm – Part III

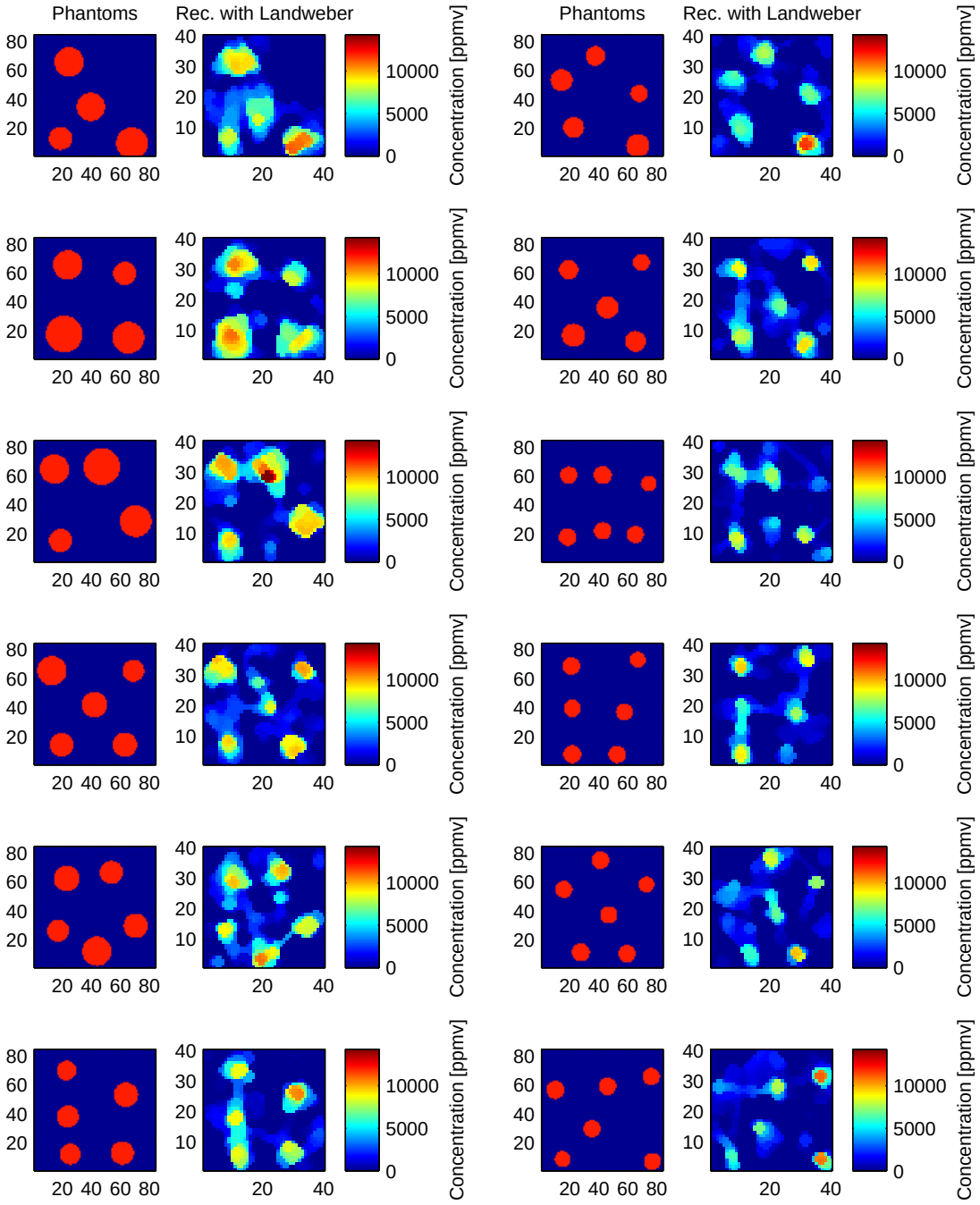

Figure F.13 Virtual experiment study: Reconstructions with Landweber algorithm – Part IV

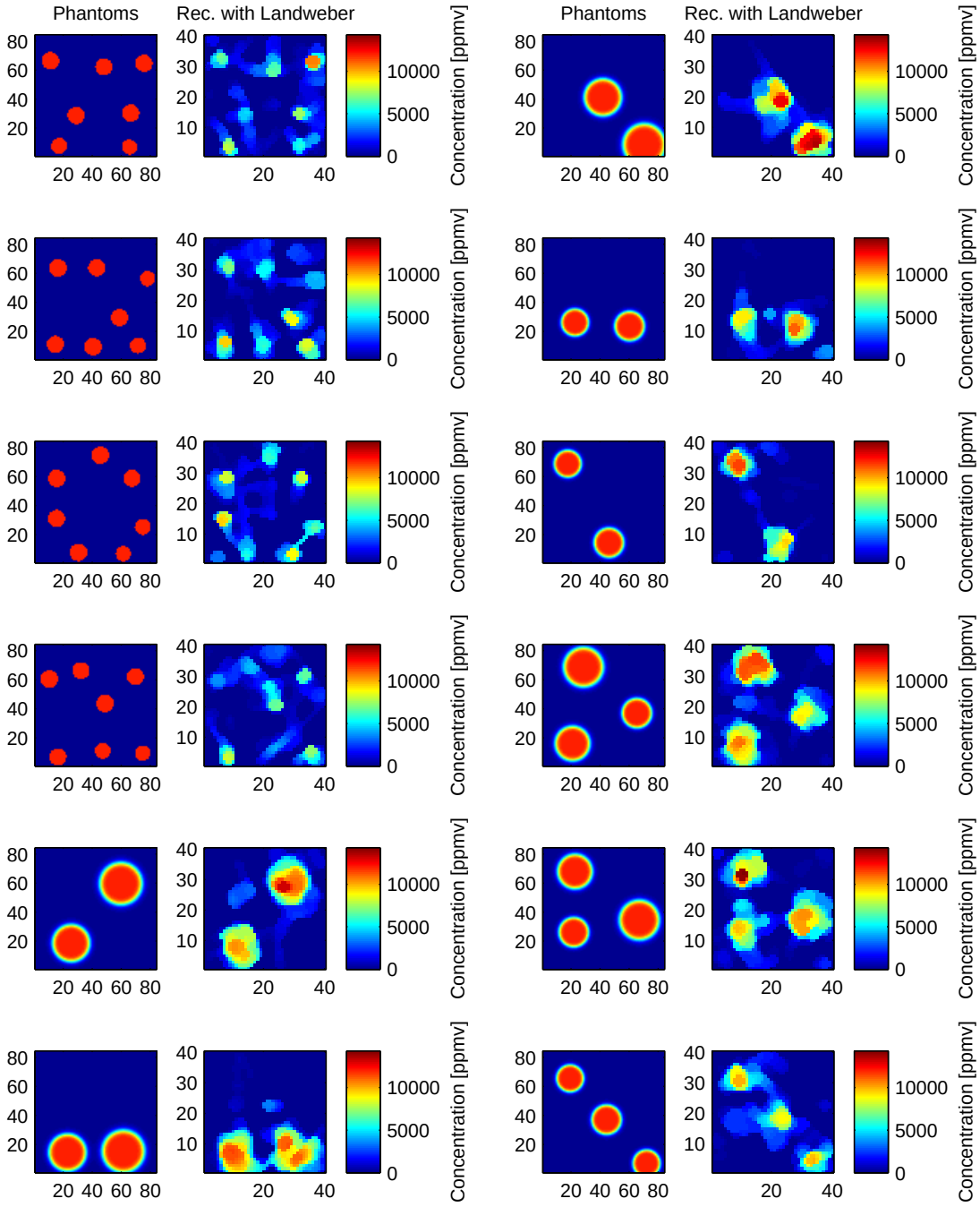

Figure F.14 Virtual experiment study: Reconstructions with Landweber algorithm – Part V

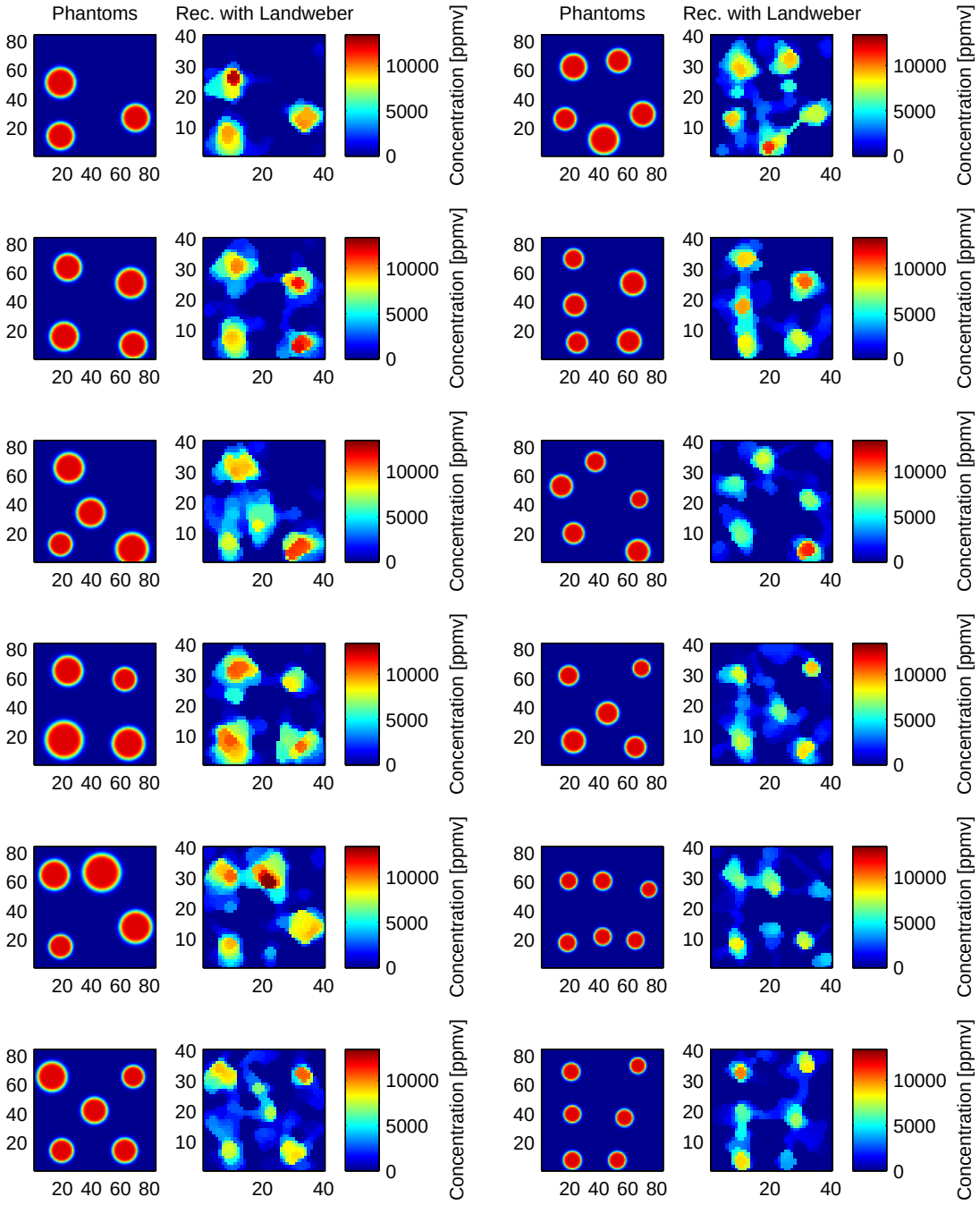

Figure F.15 Virtual experiment study: Reconstructions with Landweber algorithm – Part VI

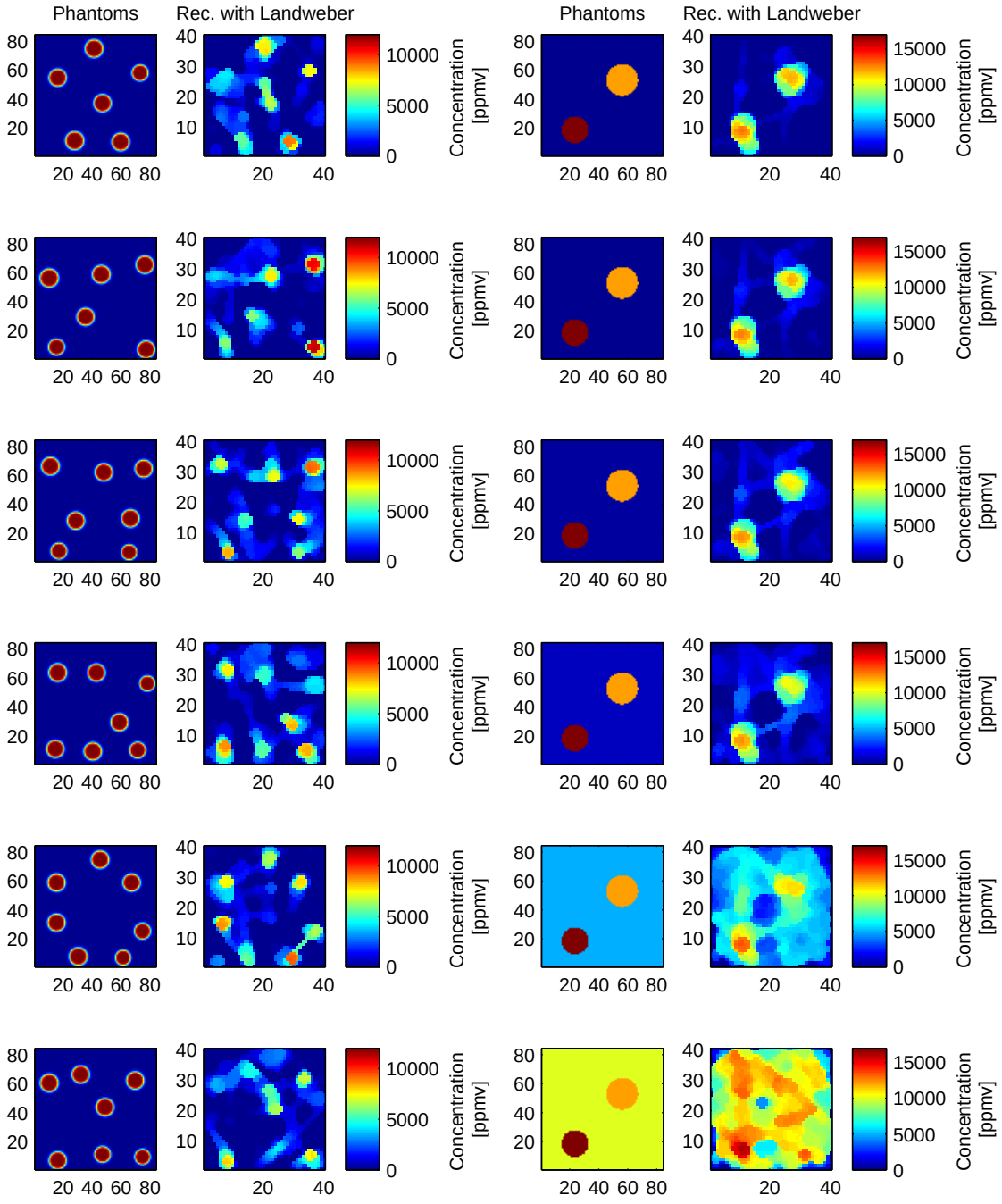

Figure F.16 Virtual experiment study: Reconstructions with Landweber algorithm – Part VII

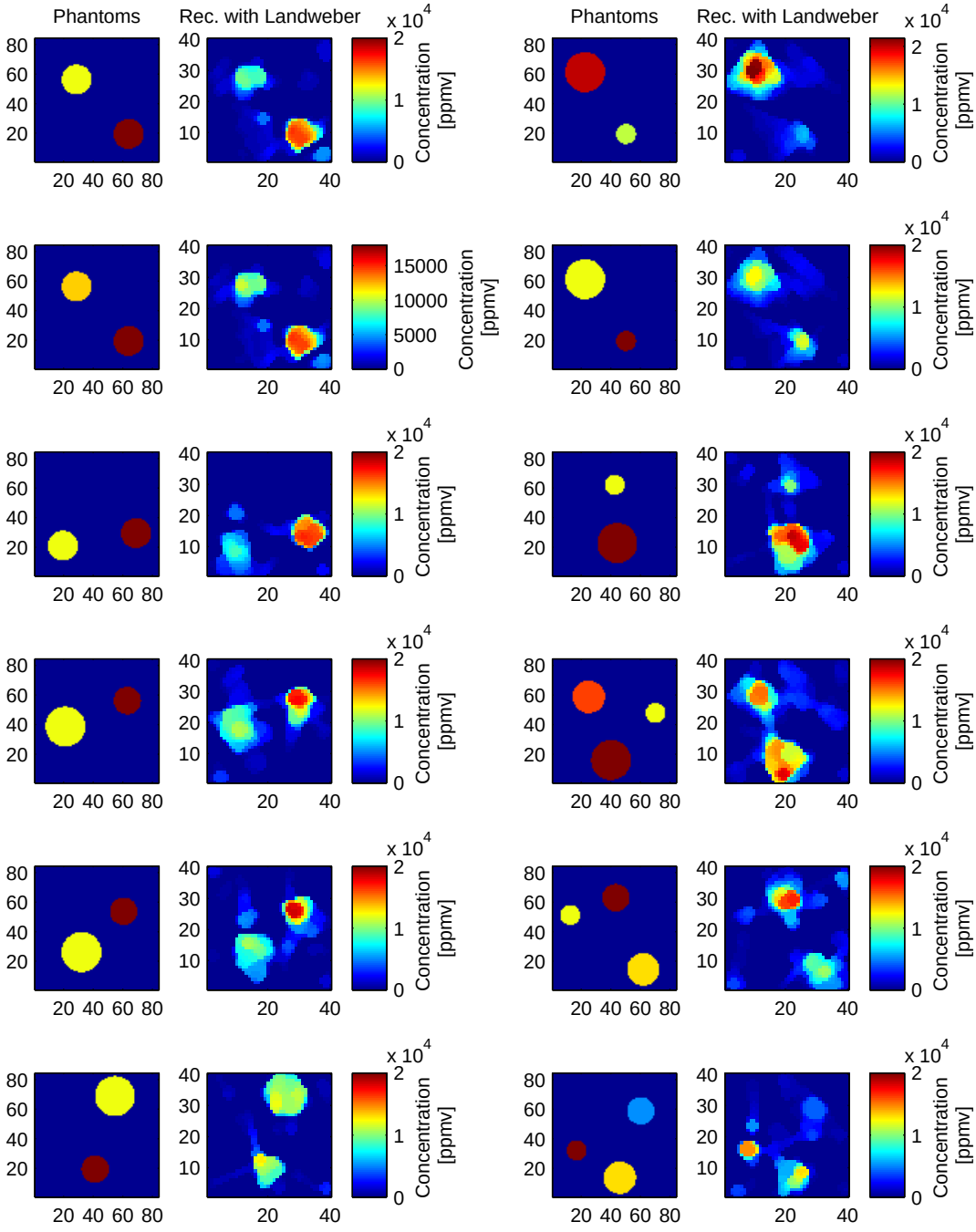

Figure F.17 Virtual experiment study: Reconstructions with Landweber algorithm – Part VIII

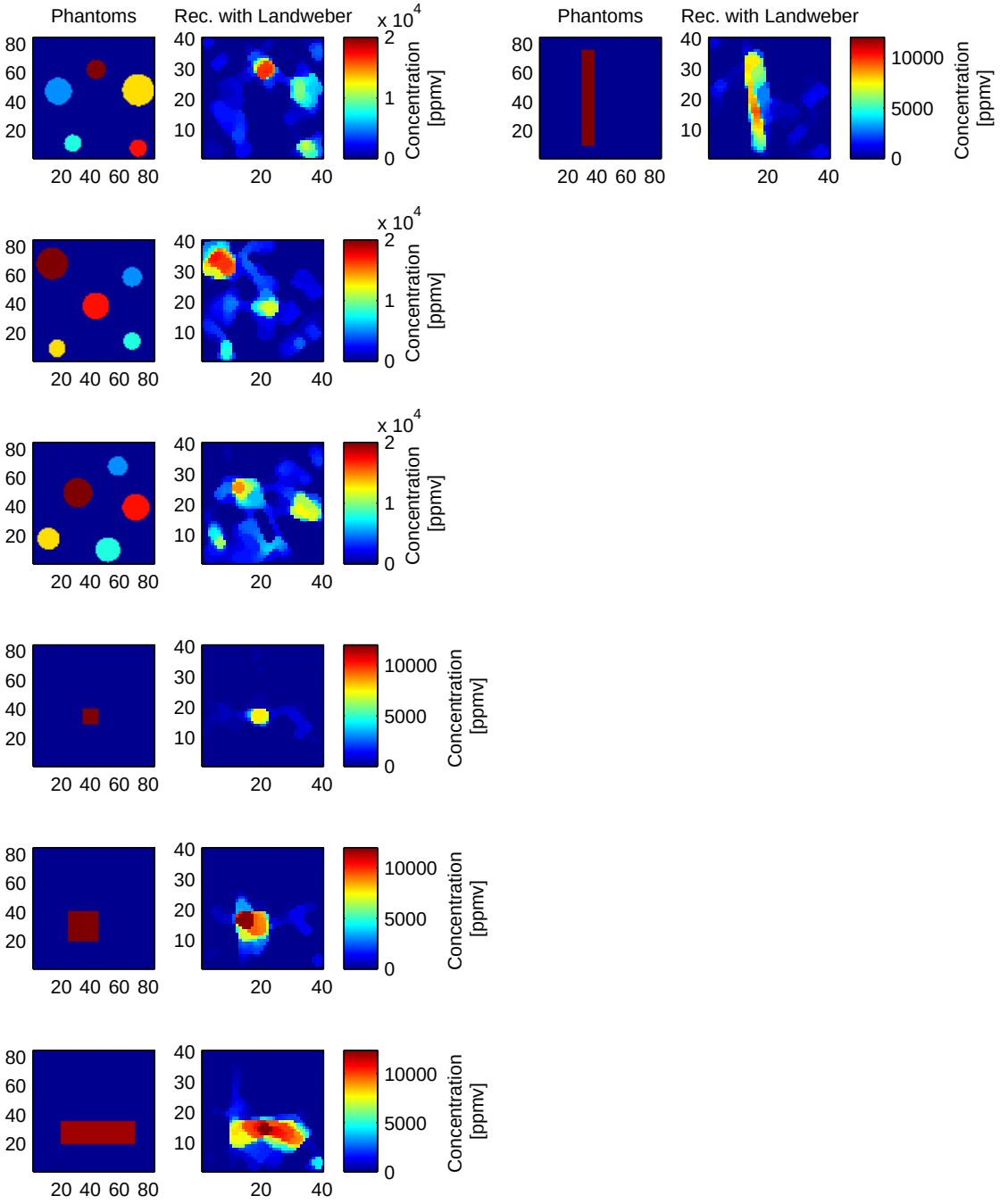

Figure F.18 Virtual experiment study: Reconstructions with Landweber algorithm – Part IX

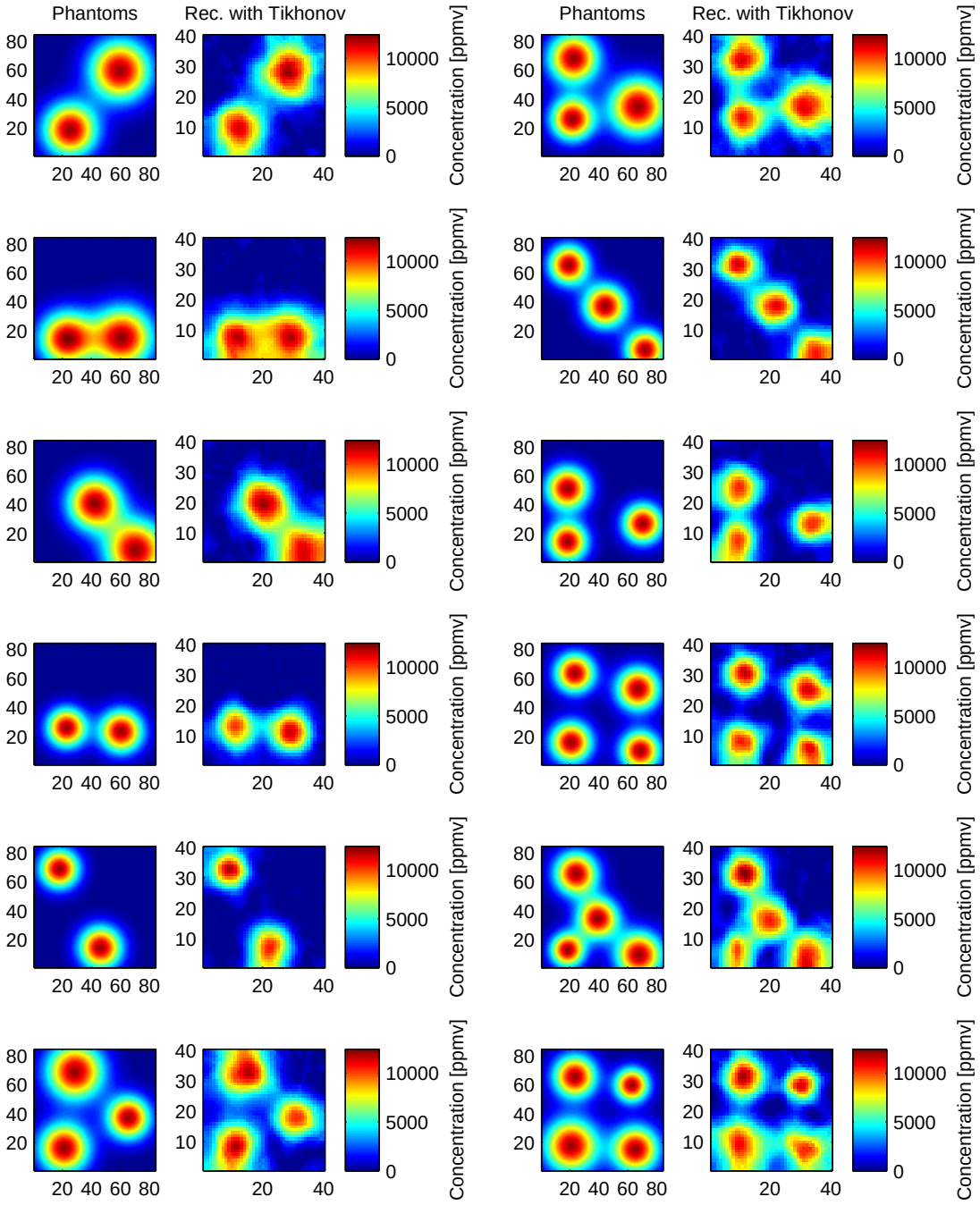

Figure F.19 Virtual experiment study: Reconstructions with Tikhonov algorithm – Part I

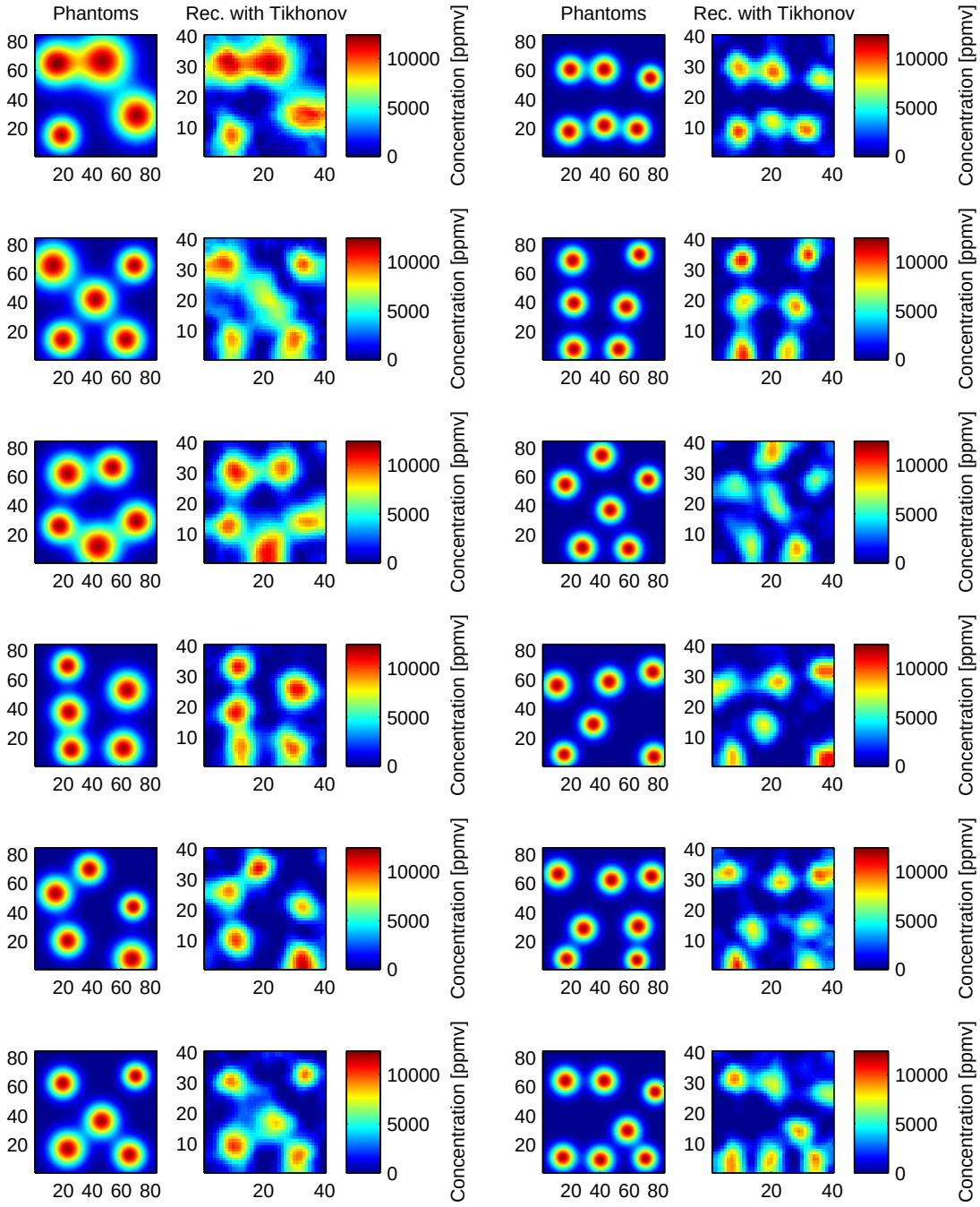

Figure F.20 Virtual experiment study: Reconstructions with Tikhonov algorithm – Part II

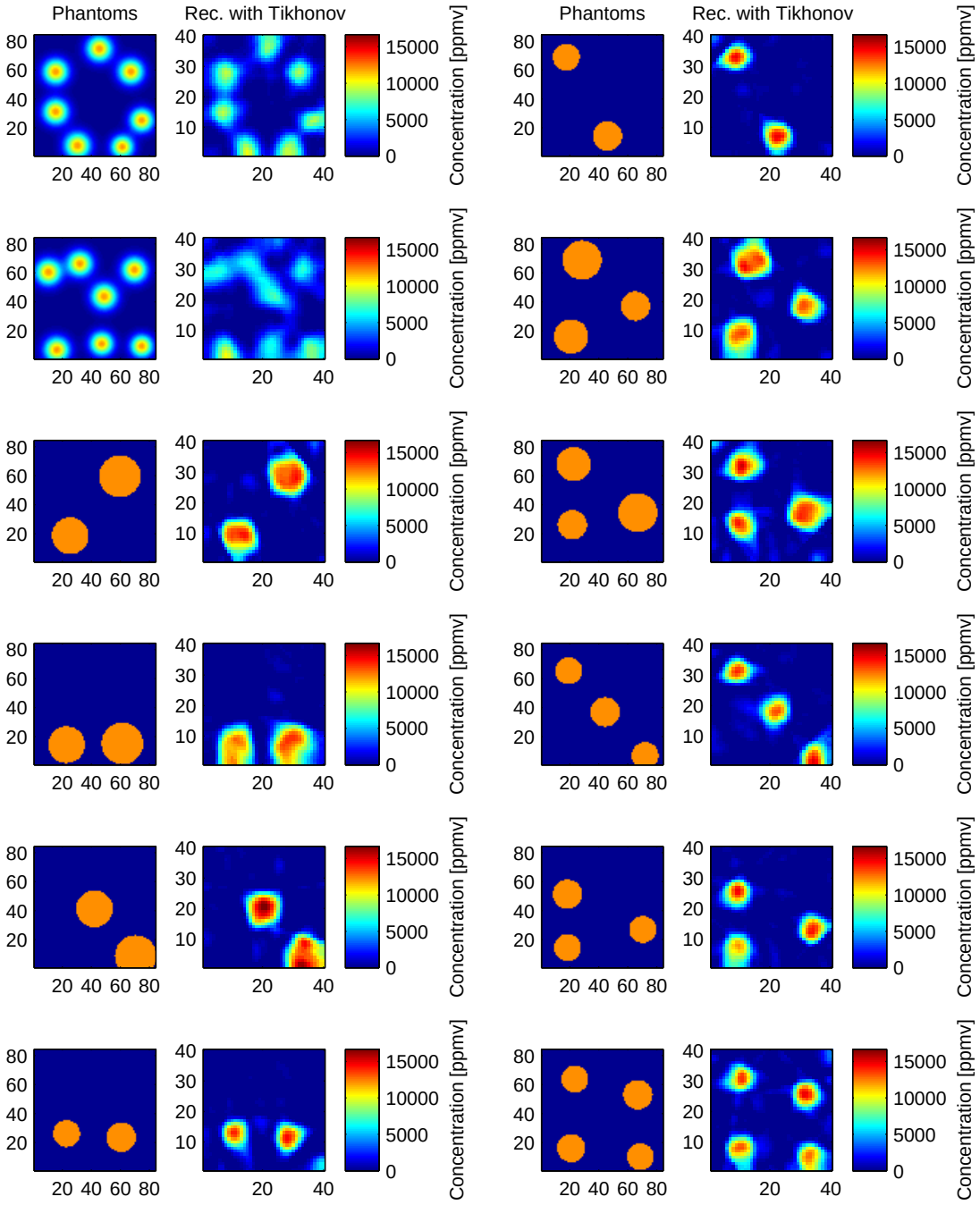

Figure F.21 Virtual experiment study: Reconstructions with Tikhonov algorithm – Part III

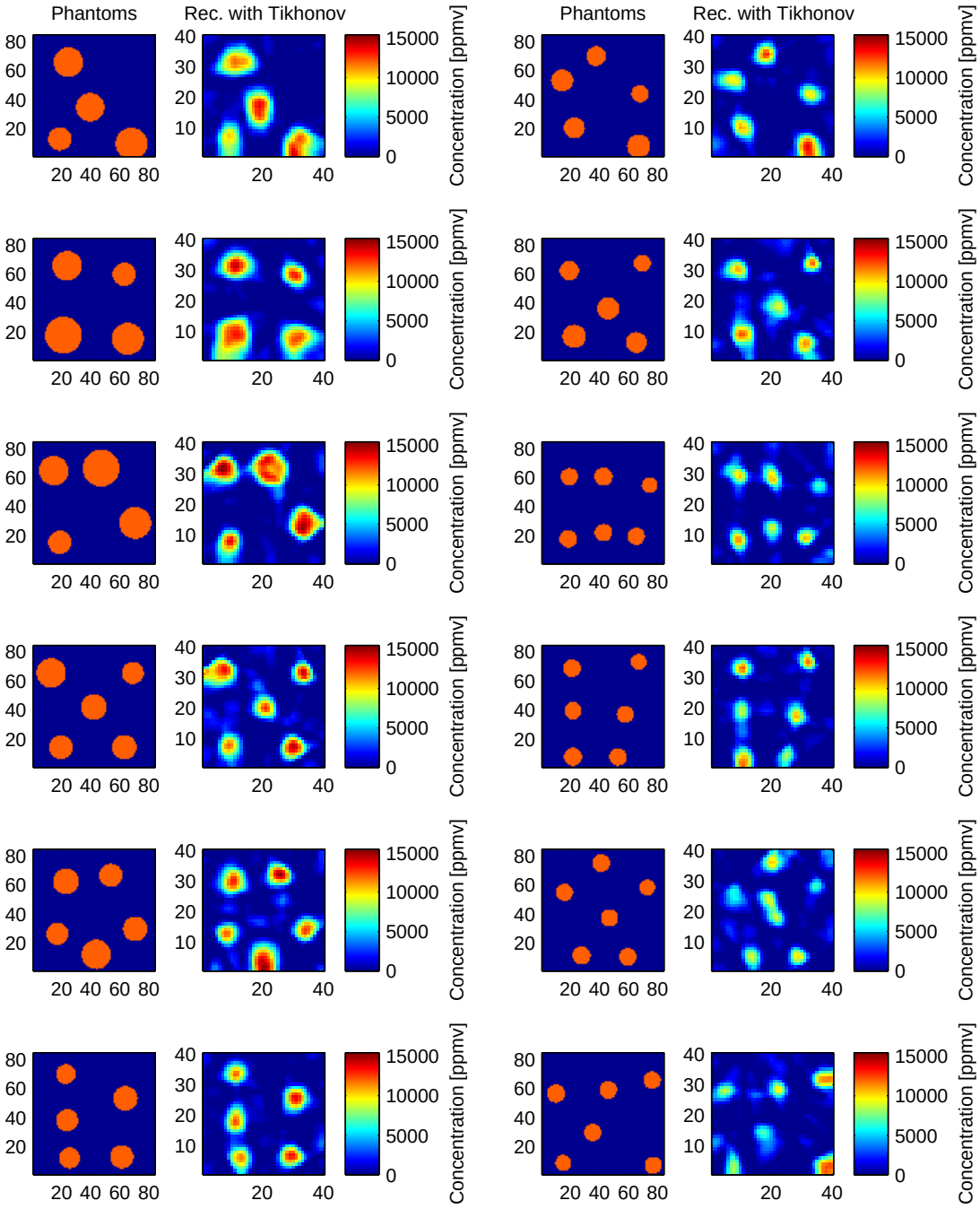

Figure F.22 Virtual experiment study: Reconstructions with Tikhonov algorithm – Part IV

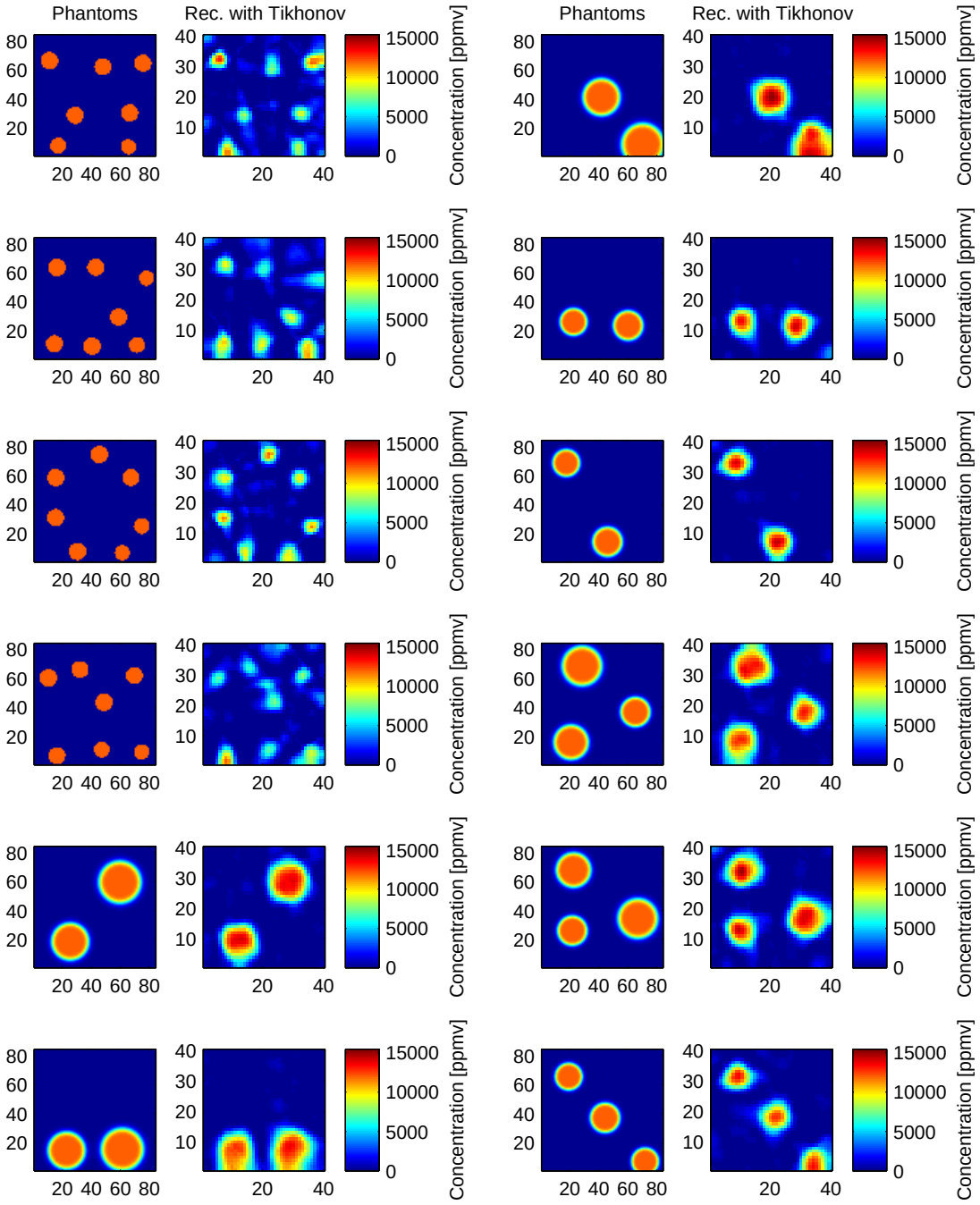

Figure F.23 Virtual experiment study: Reconstructions with Tikhonov algorithm – Part V

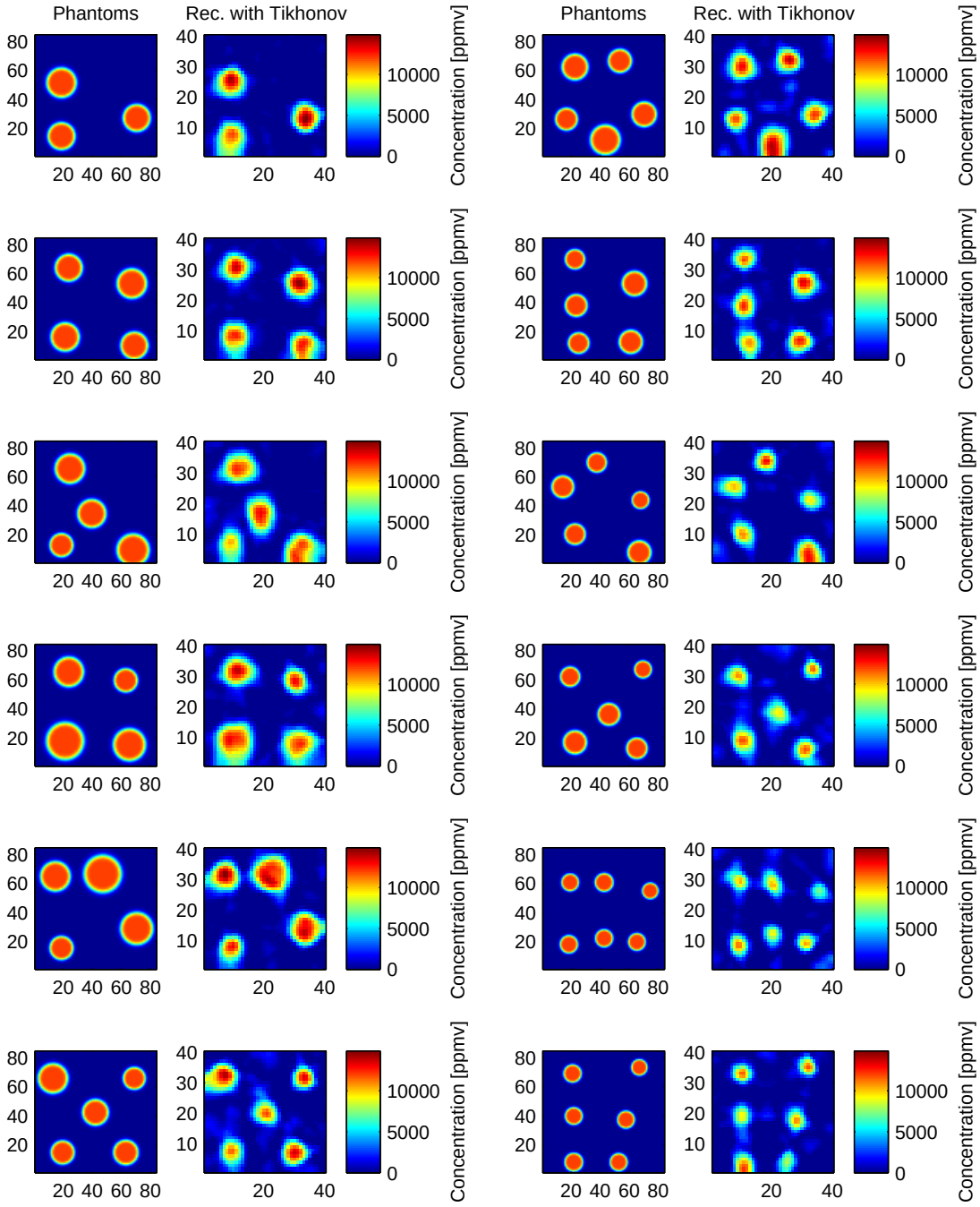

Figure F.24 Virtual experiment study: Reconstructions with Tikhonov algorithm – Part VI

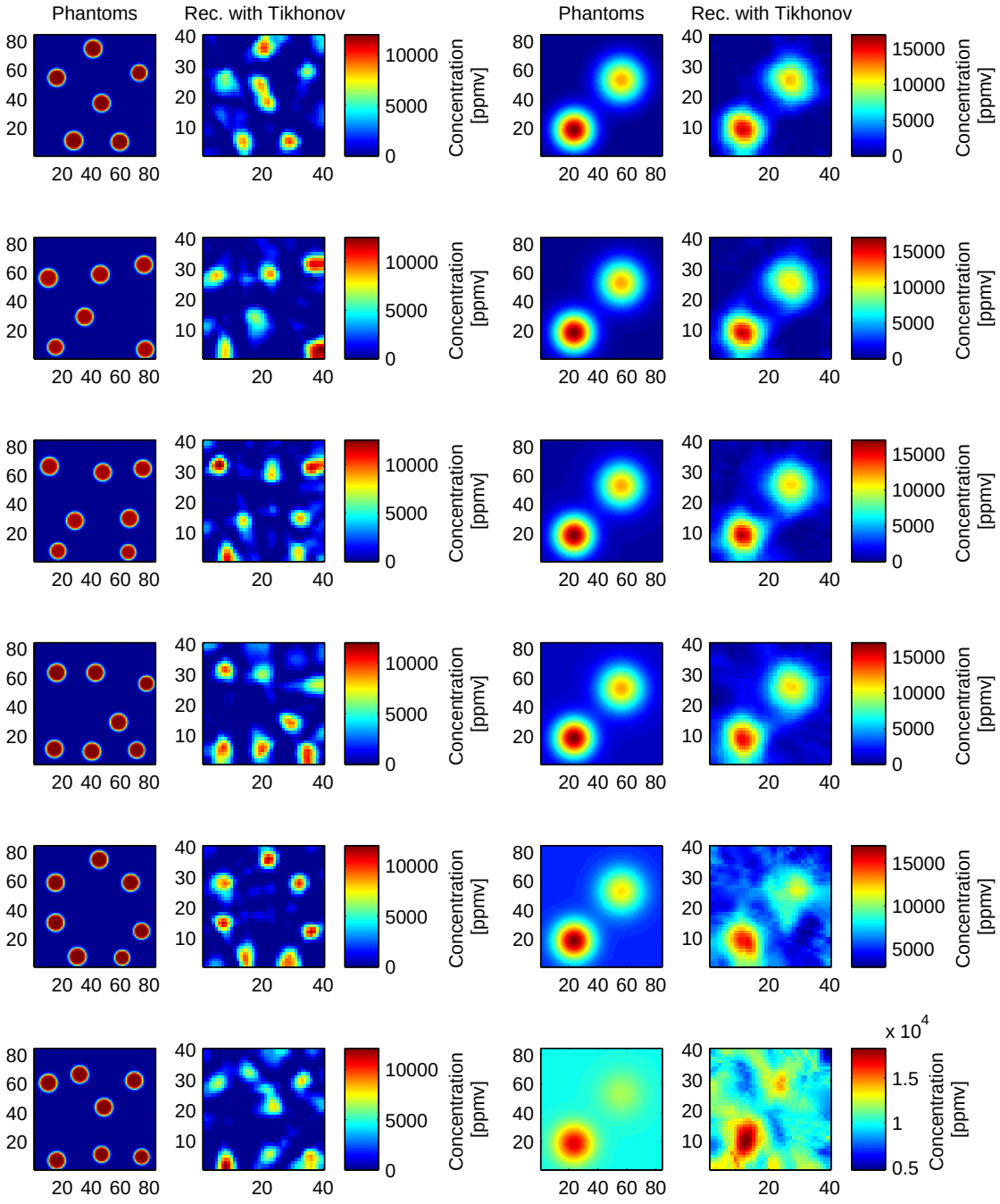

Figure F.25 Virtual experiment study: Reconstructions with Tikhonov algorithm – Part VII

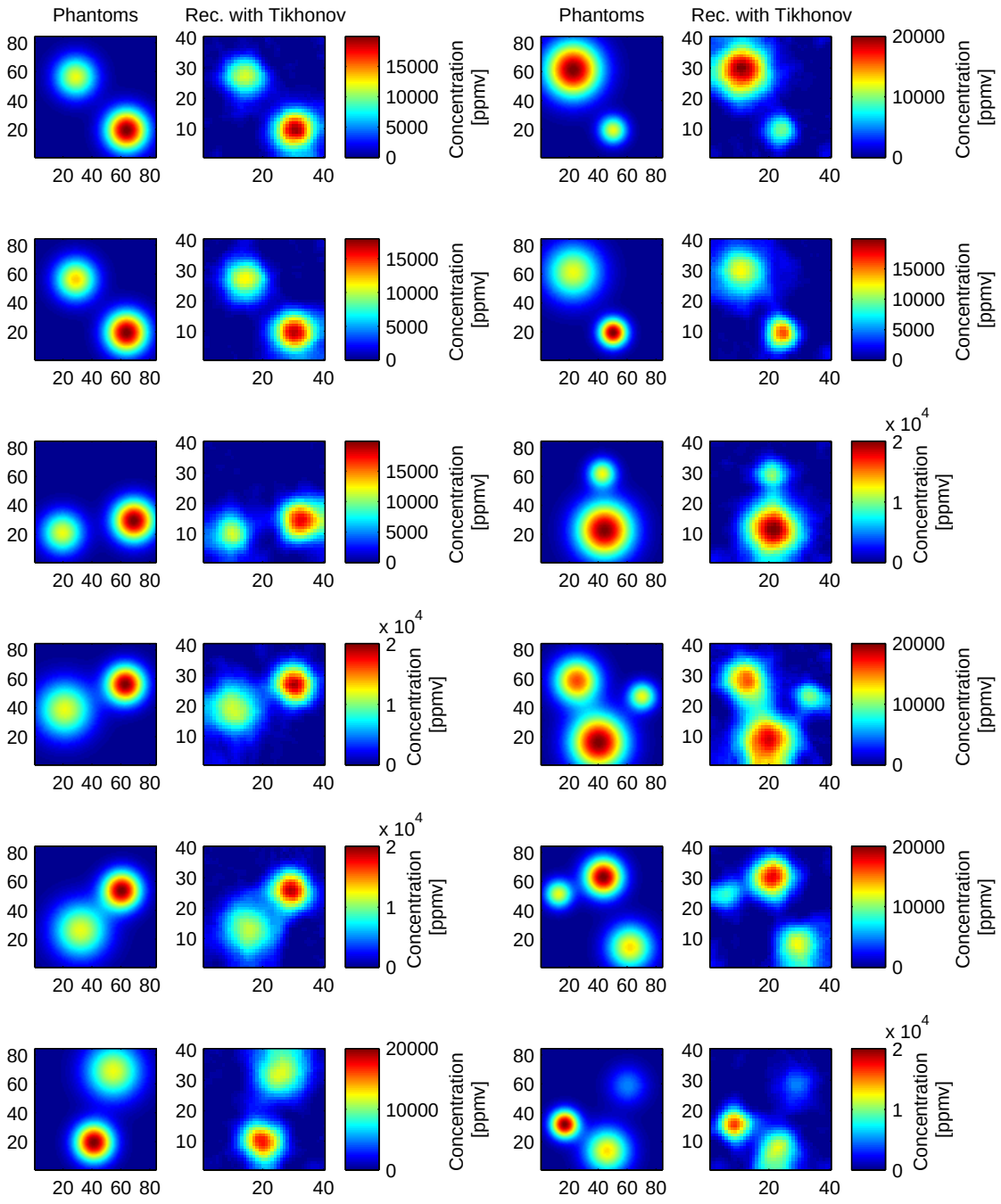

Figure F.26 Virtual experiment study: Reconstructions with Tikhonov algorithm – Part VIII

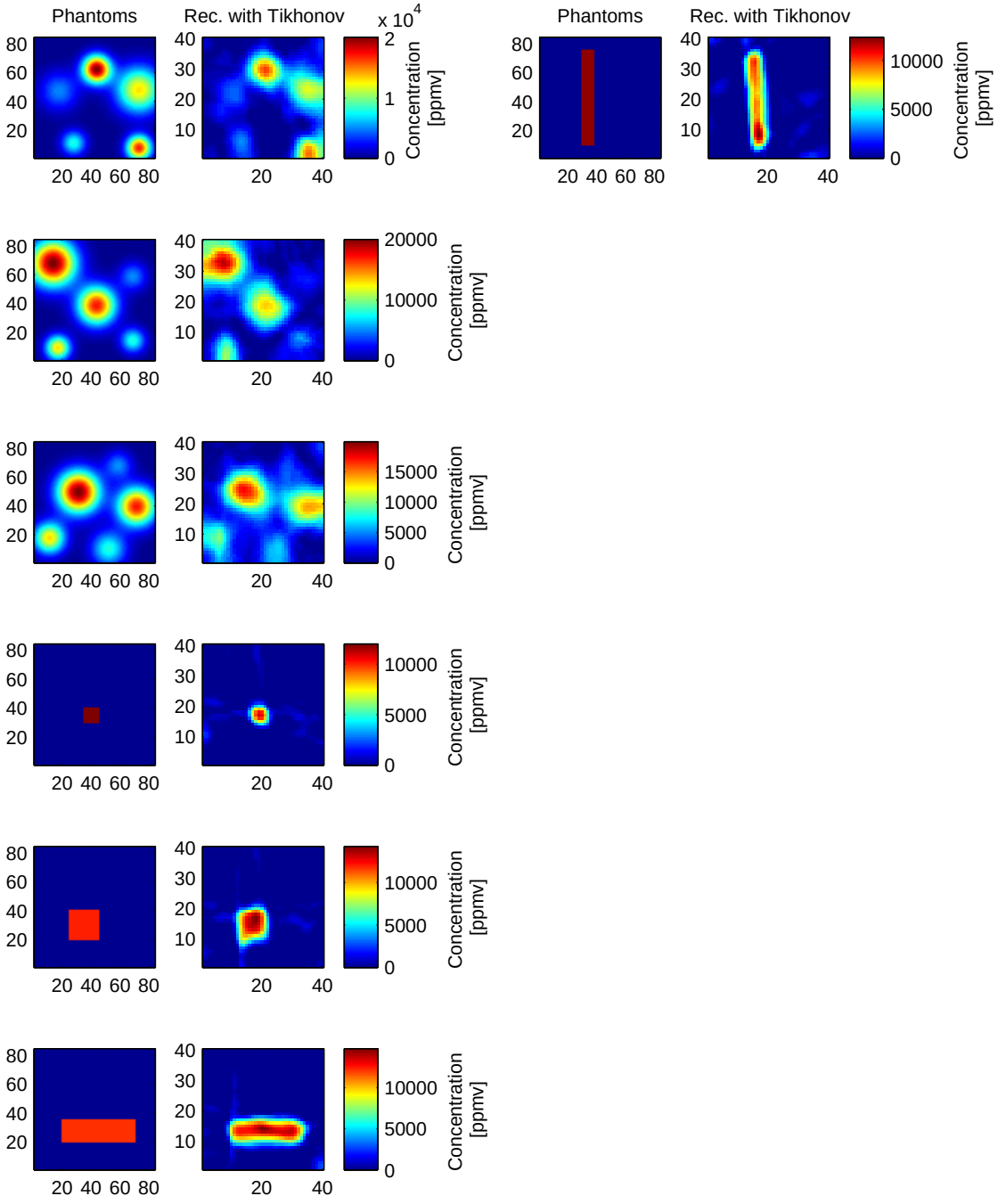

Figure F.27 Virtual experiment study: Reconstructions with Tikhonov algorithm – Part IX

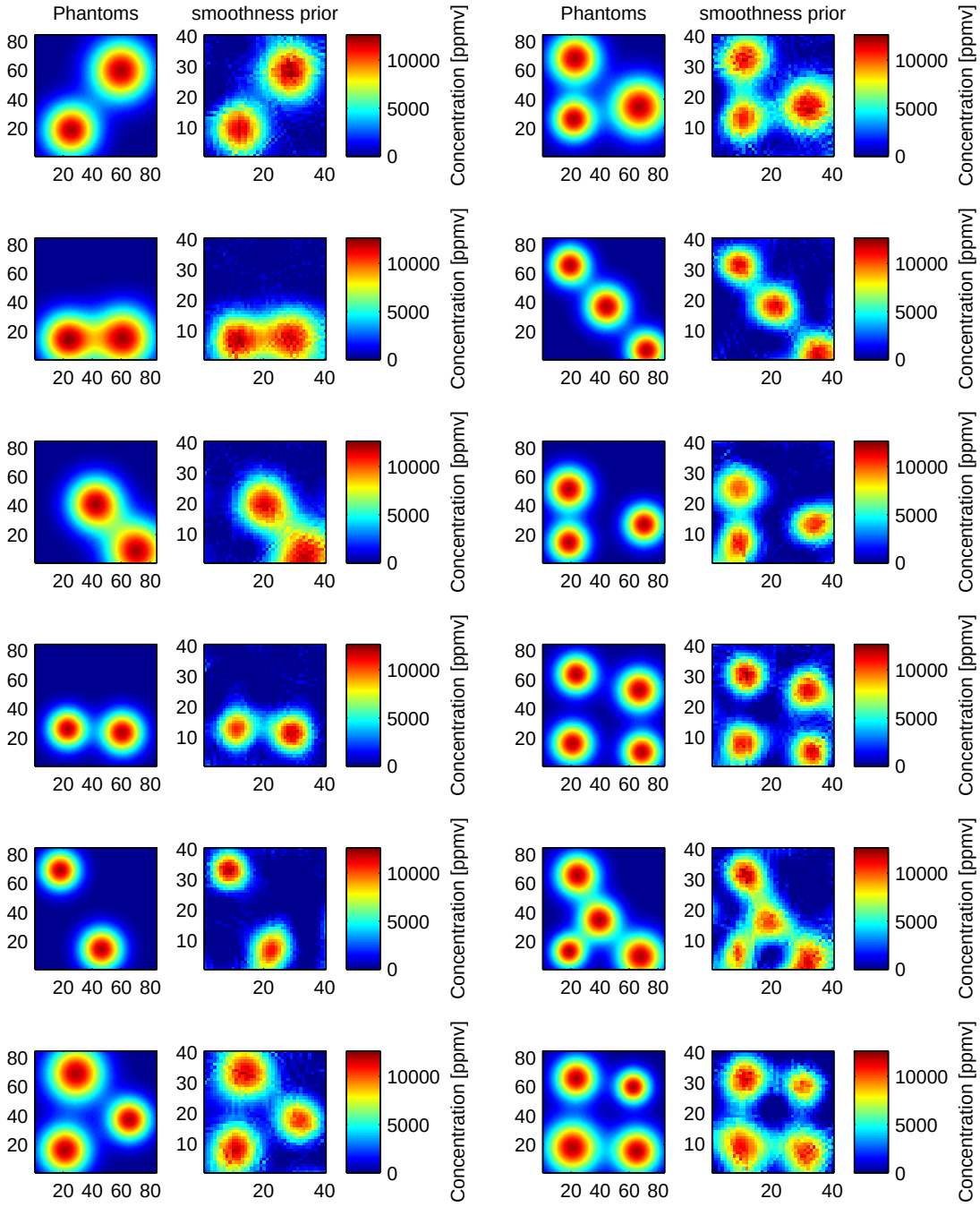

Figure F.28 Virtual experiment study: Reconstructions with informative smoothness prior – Part I

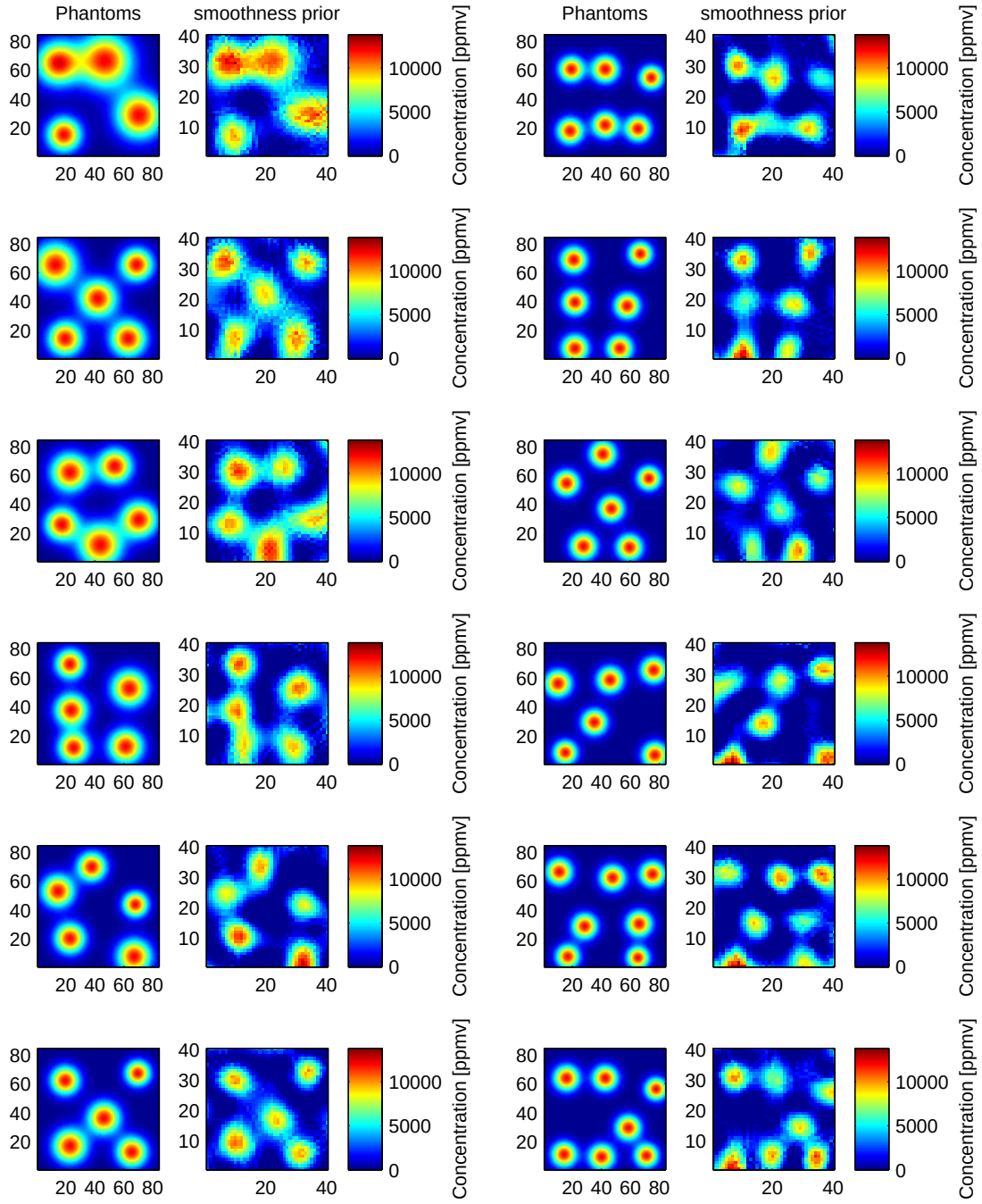

Figure F.29 Virtual experiment study: Reconstructions with informative smoothness prior – Part II

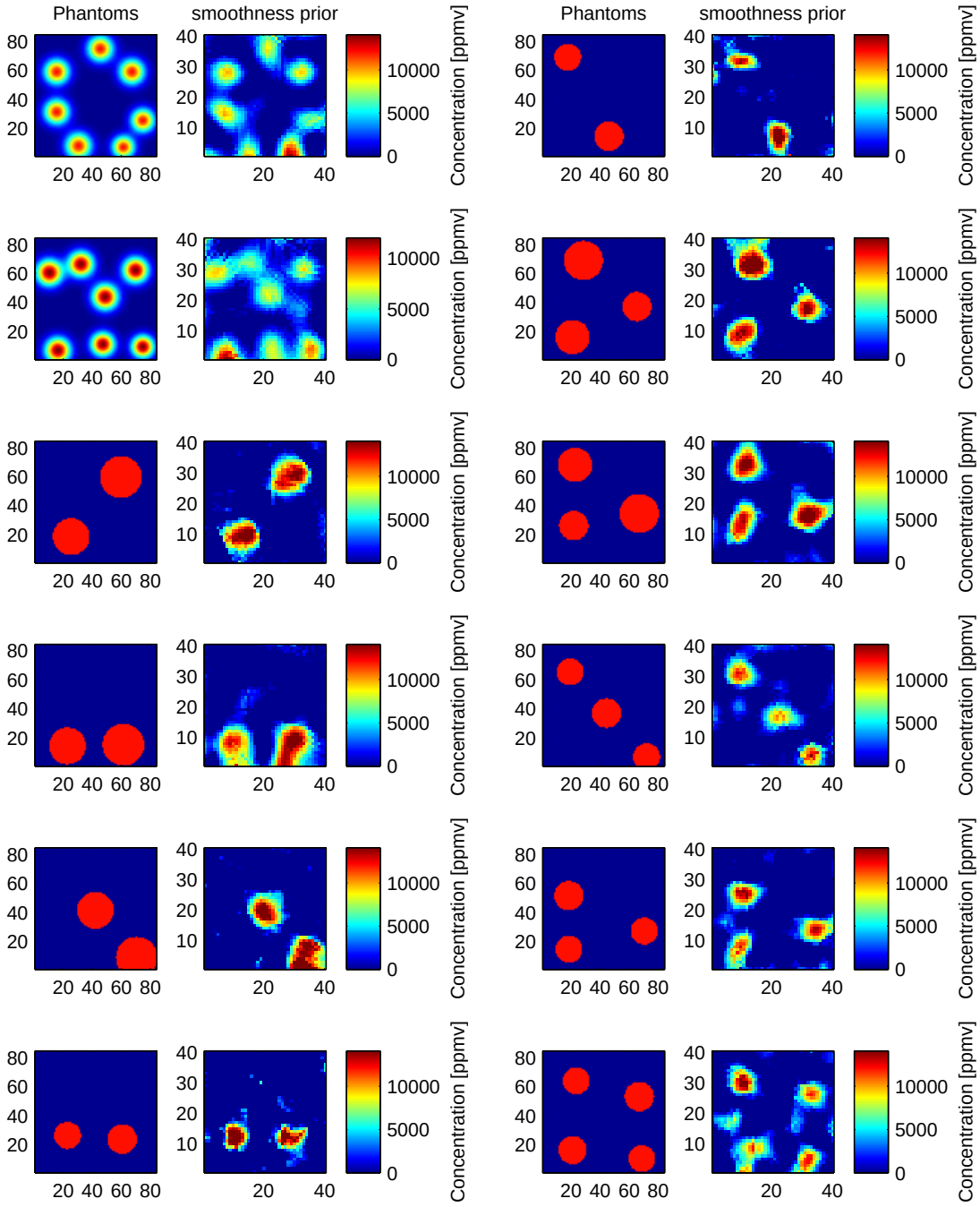

Figure F.30 Virtual experiment study: Reconstructions with informative smoothness prior – Part III

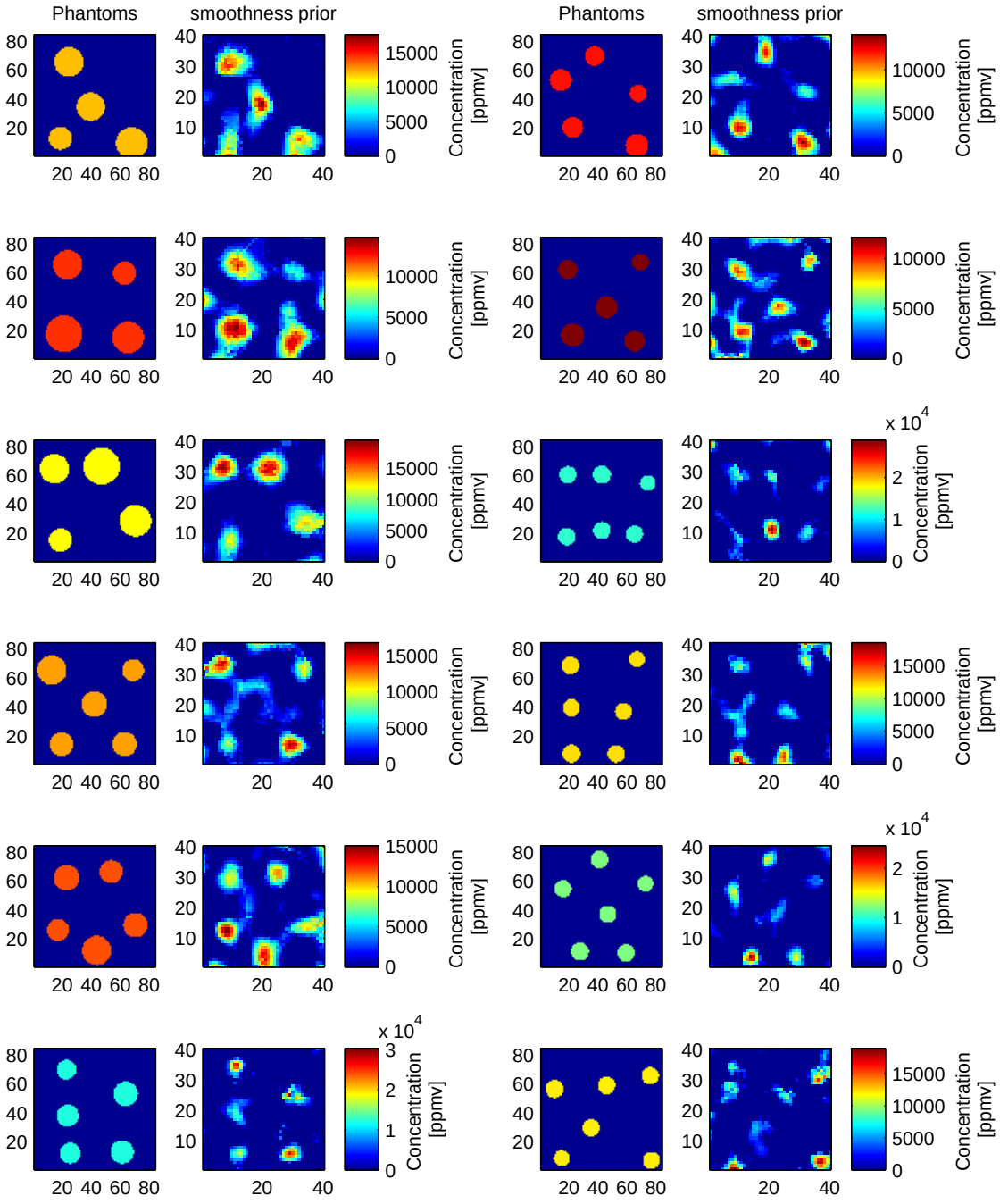

Figure F.31 Virtual experiment study: Reconstructions with informative smoothness prior – Part IV

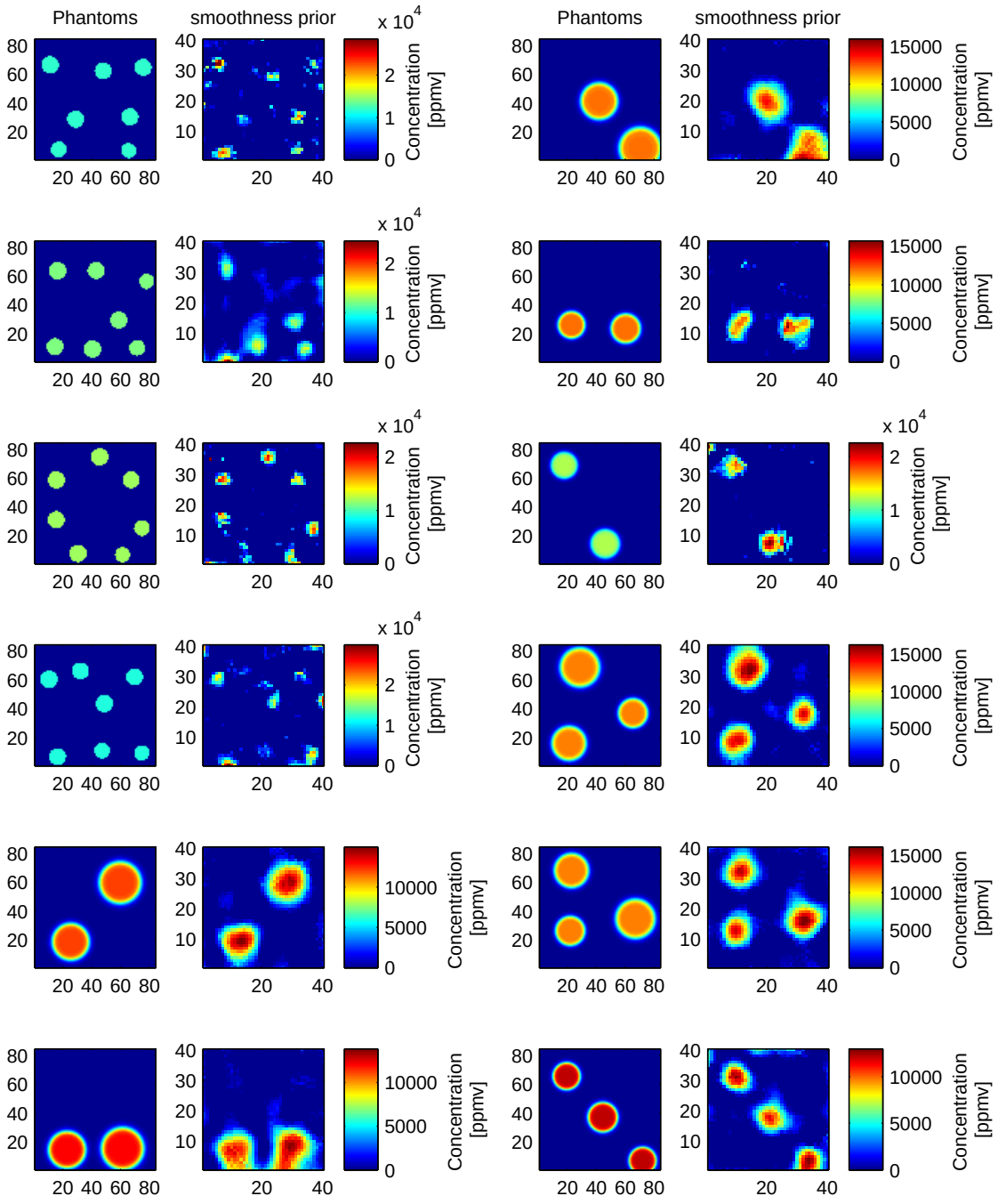

Figure F.32 Virtual experiment study: Reconstructions with informative smoothness prior – Part V

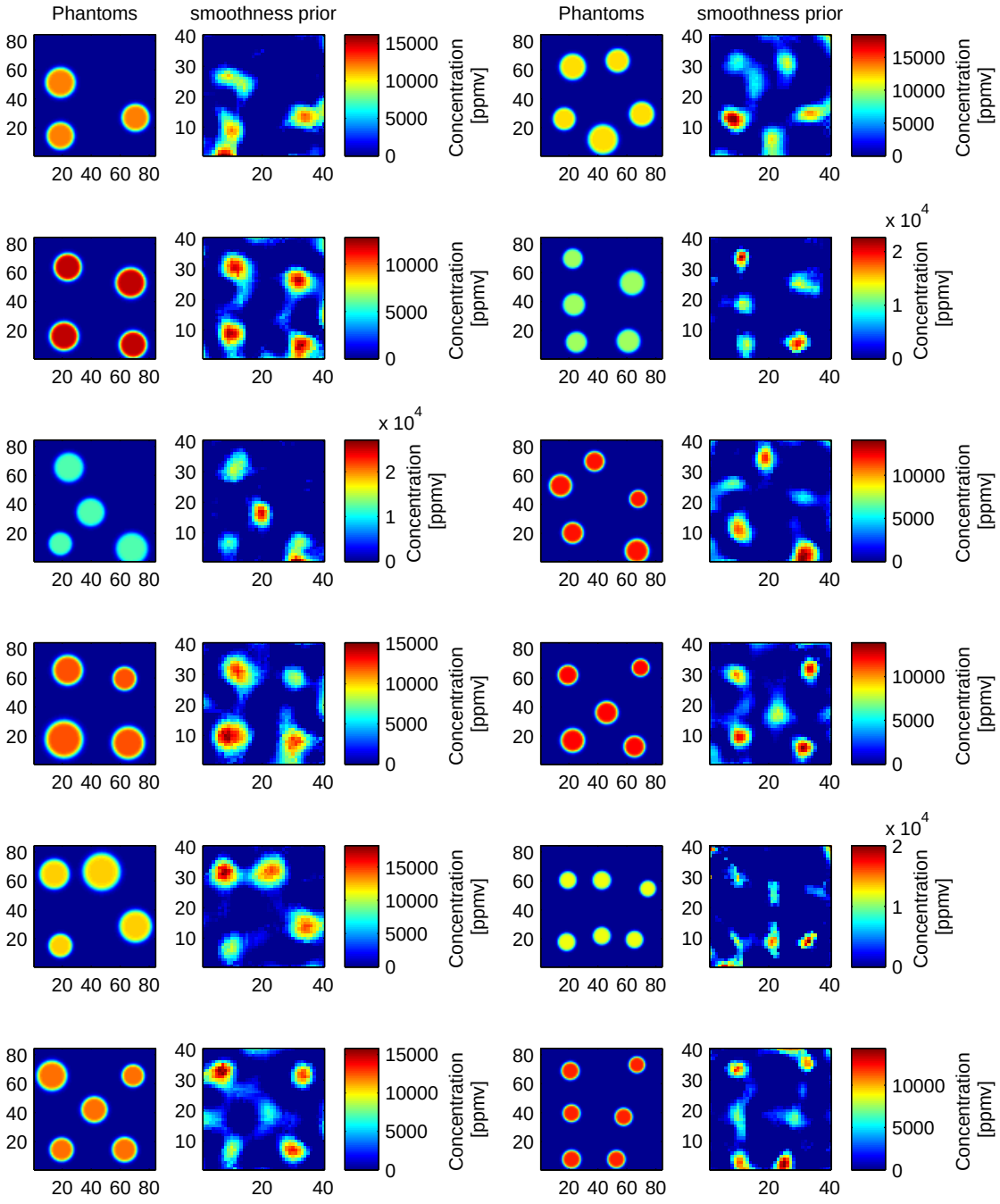

Figure F.33 Virtual experiment study: Reconstructions with informative smoothness prior – Part VI

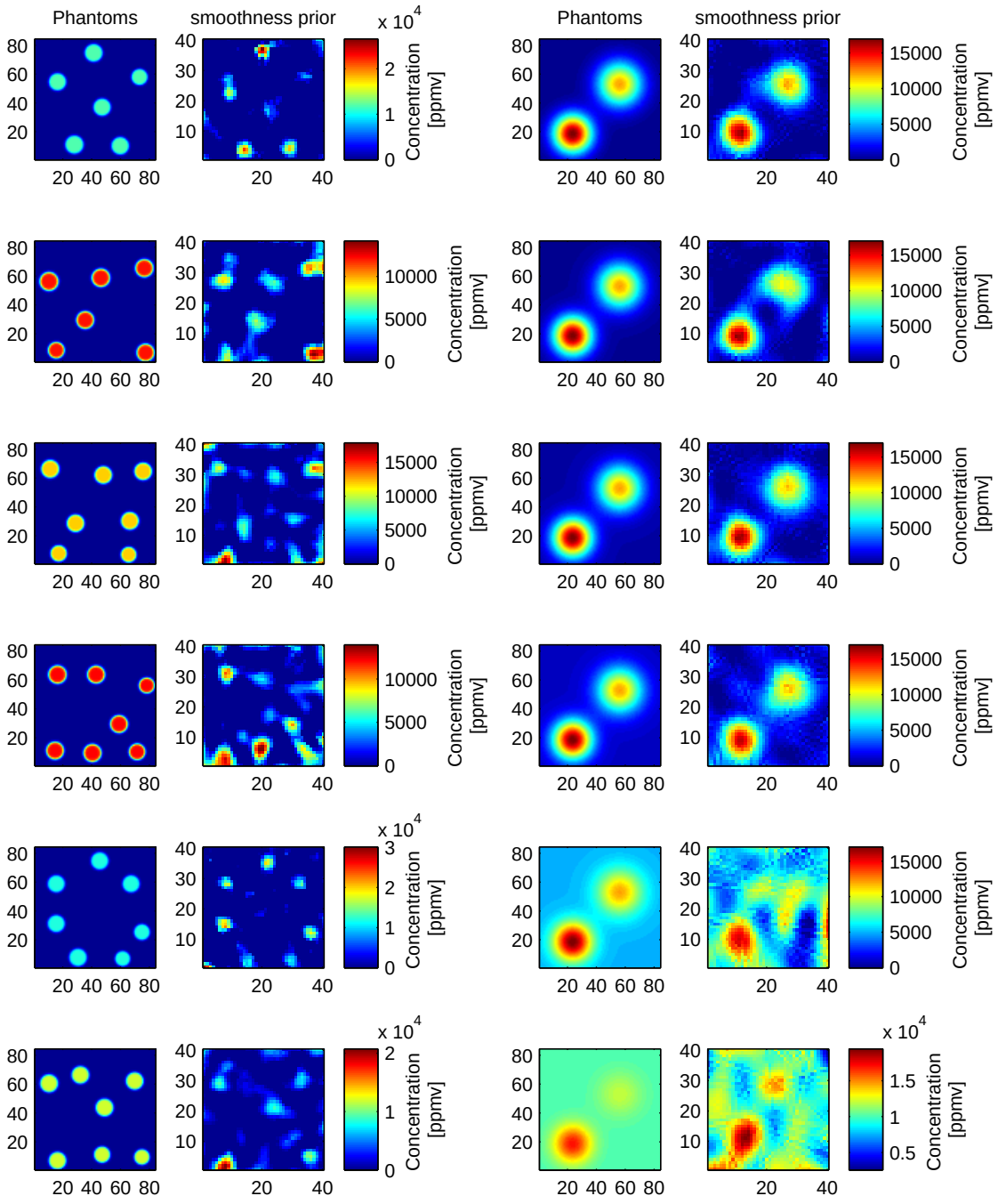

Figure F.34 Virtual experiment study: Reconstructions with informative smoothness prior – Part VII

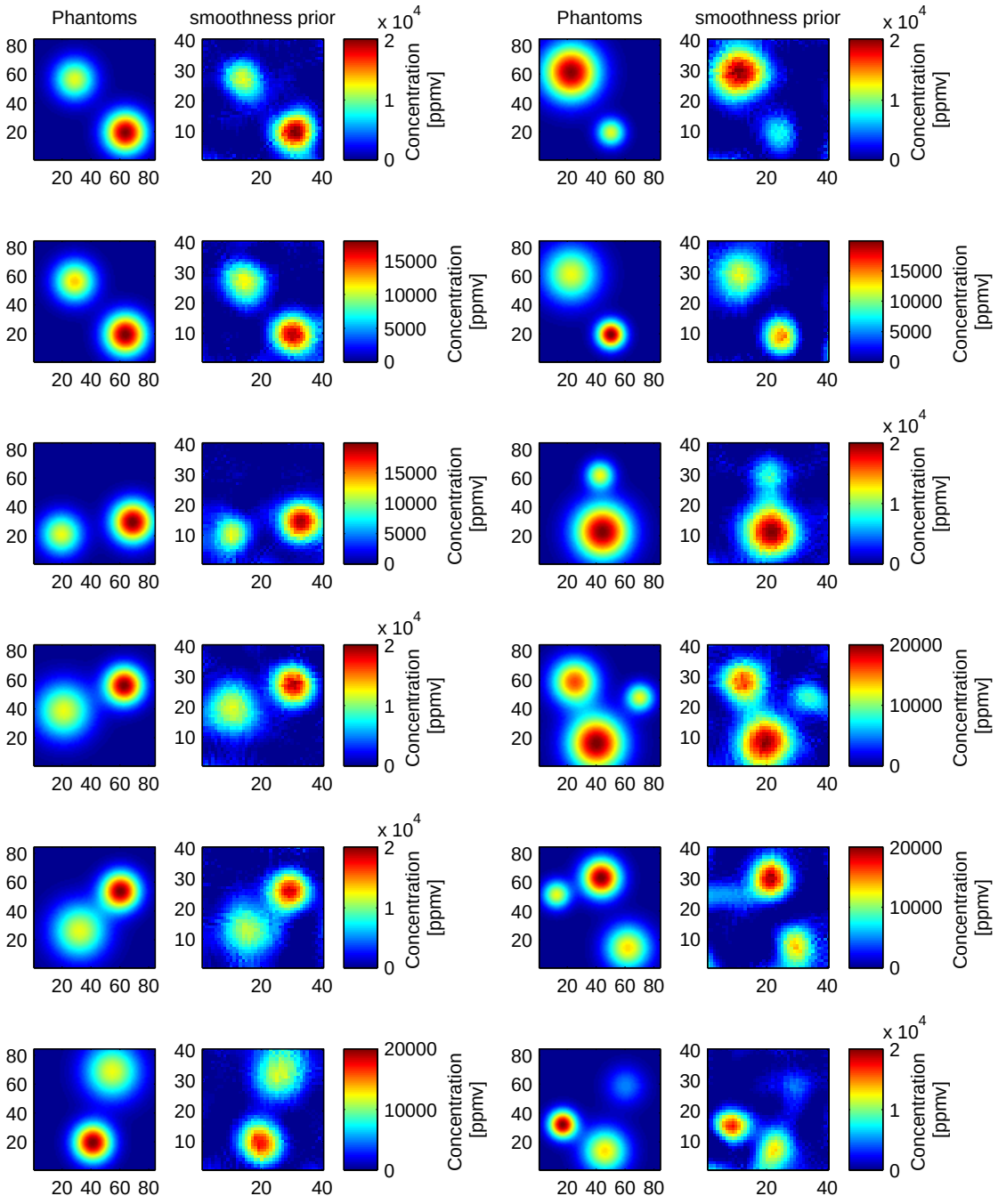

Figure F.35 Virtual experiment study: Reconstructions with informative smoothness prior – Part VIII

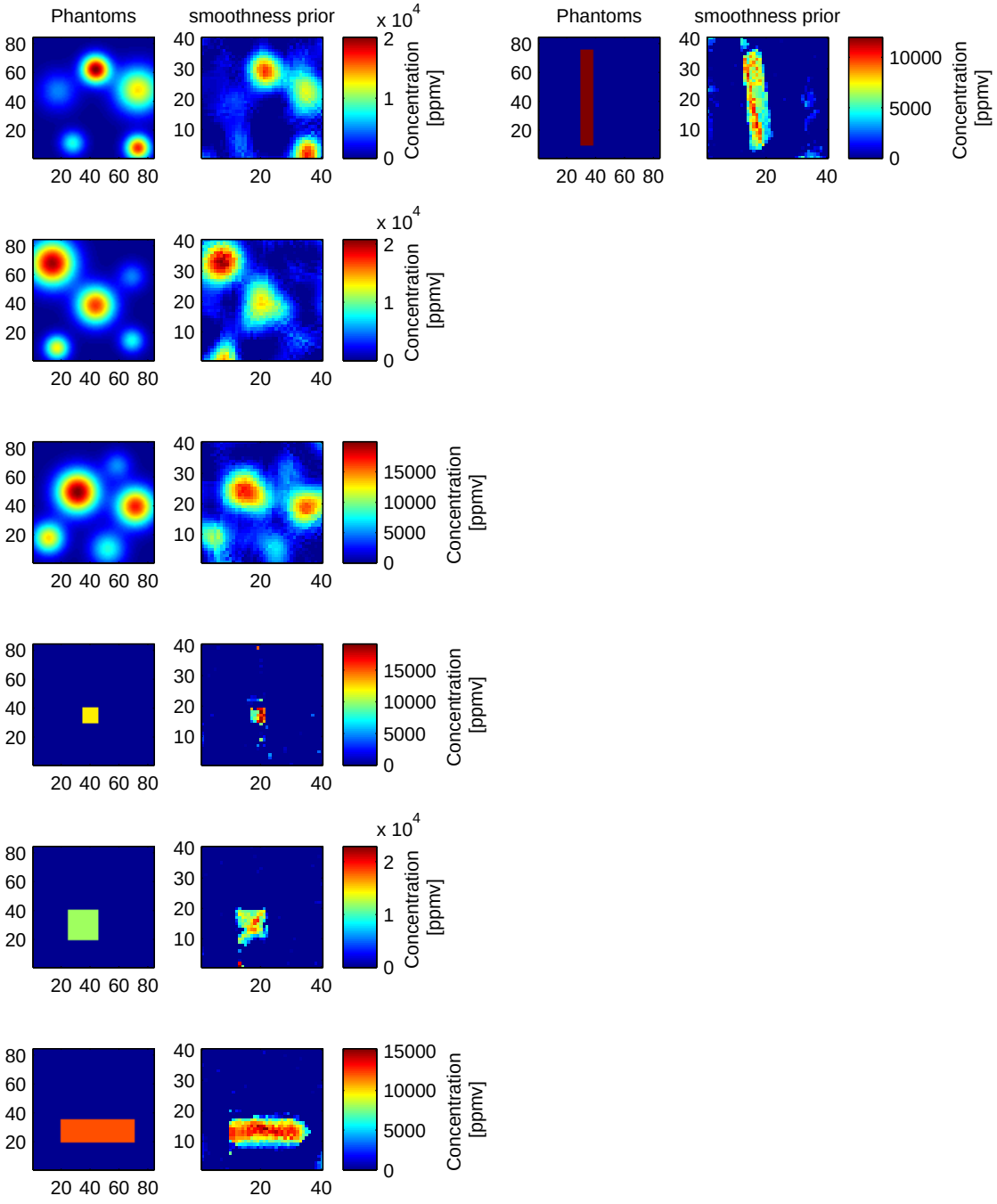

Figure F.36 Virtual experiment study: Reconstructions with informative smoothness prior – Part IX

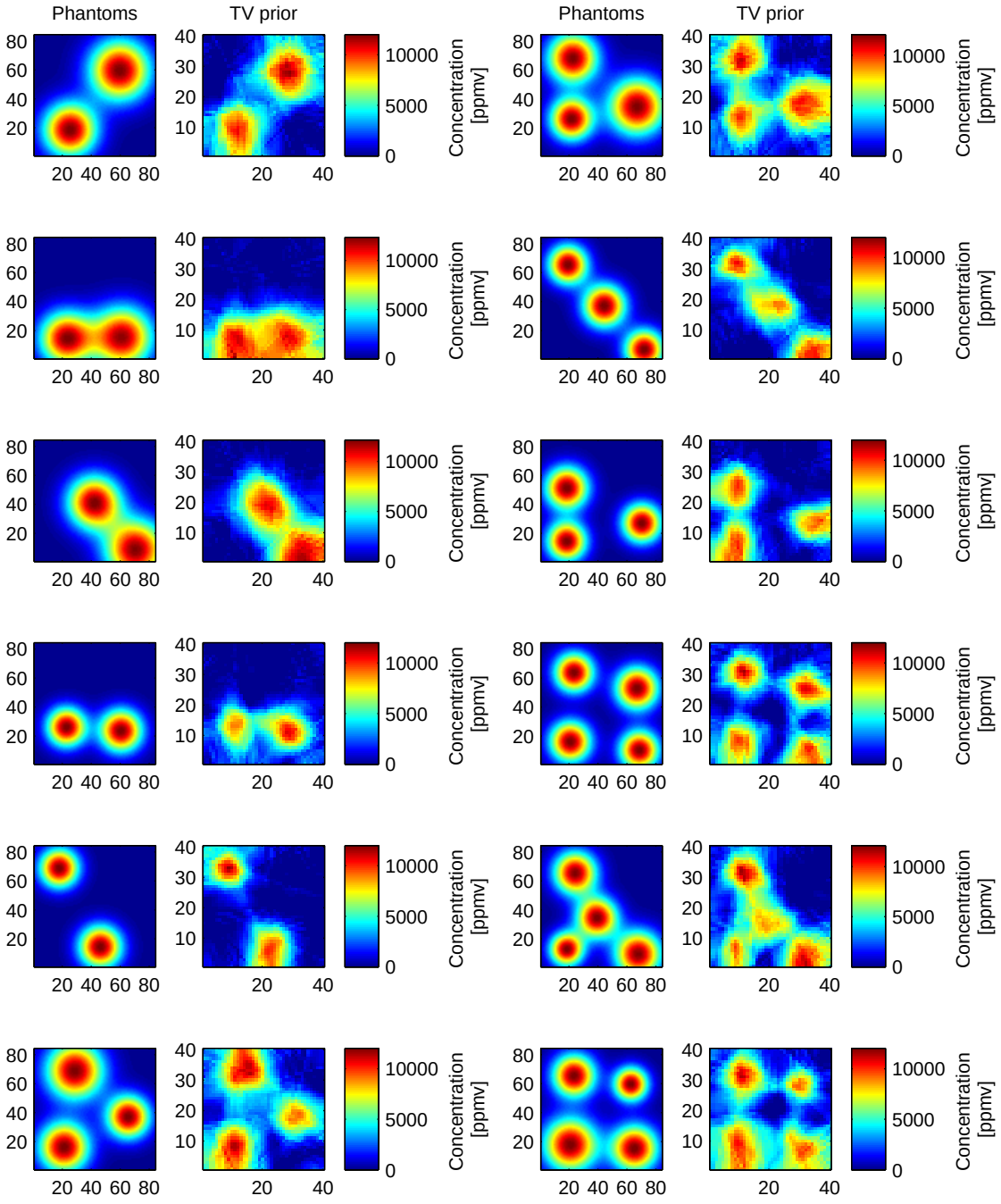

Figure F.37 Virtual experiment study: Reconstructions with total variation prior – Part I

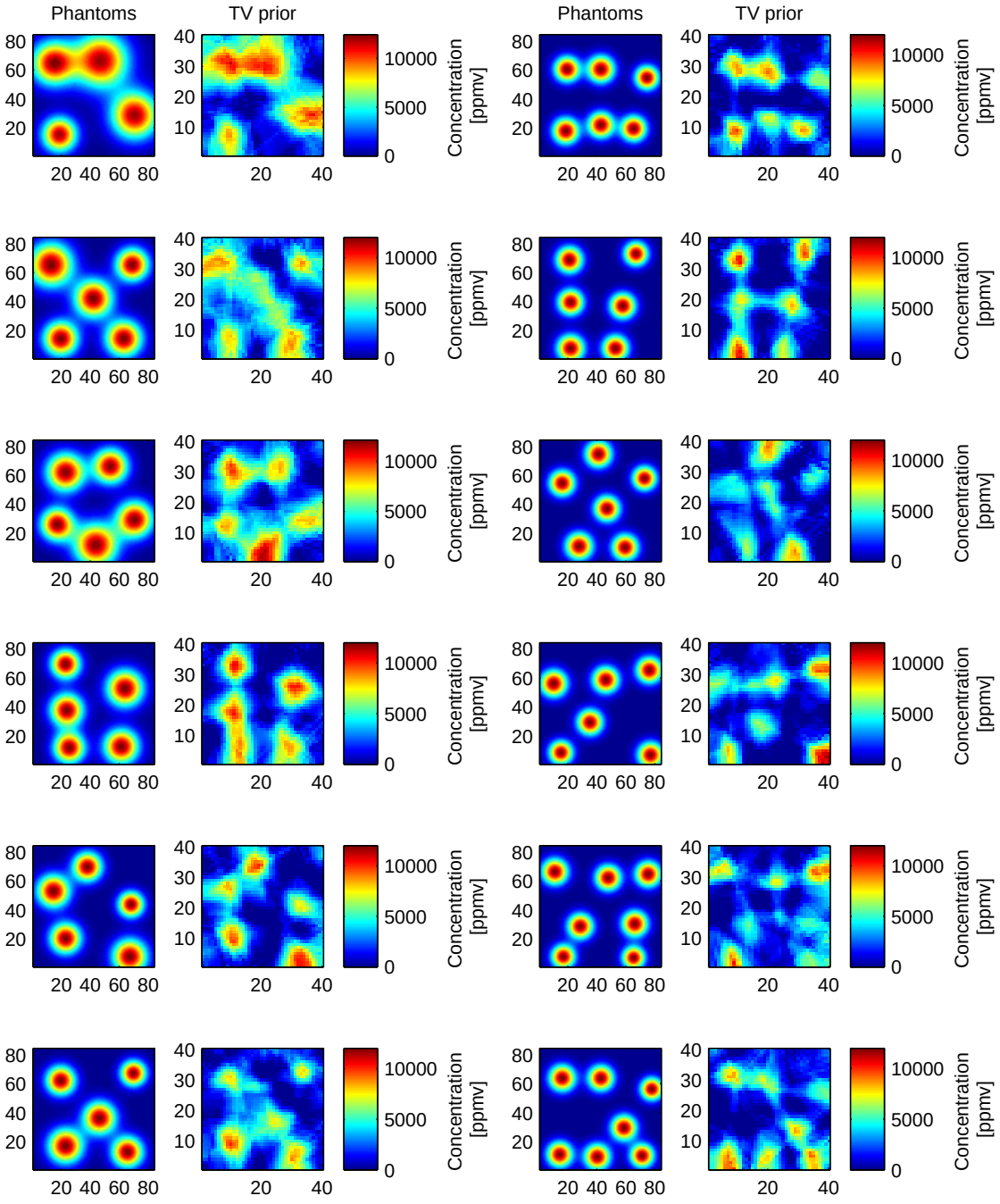

Figure F.38 Virtual experiment study: Reconstructions with total variation prior – Part II

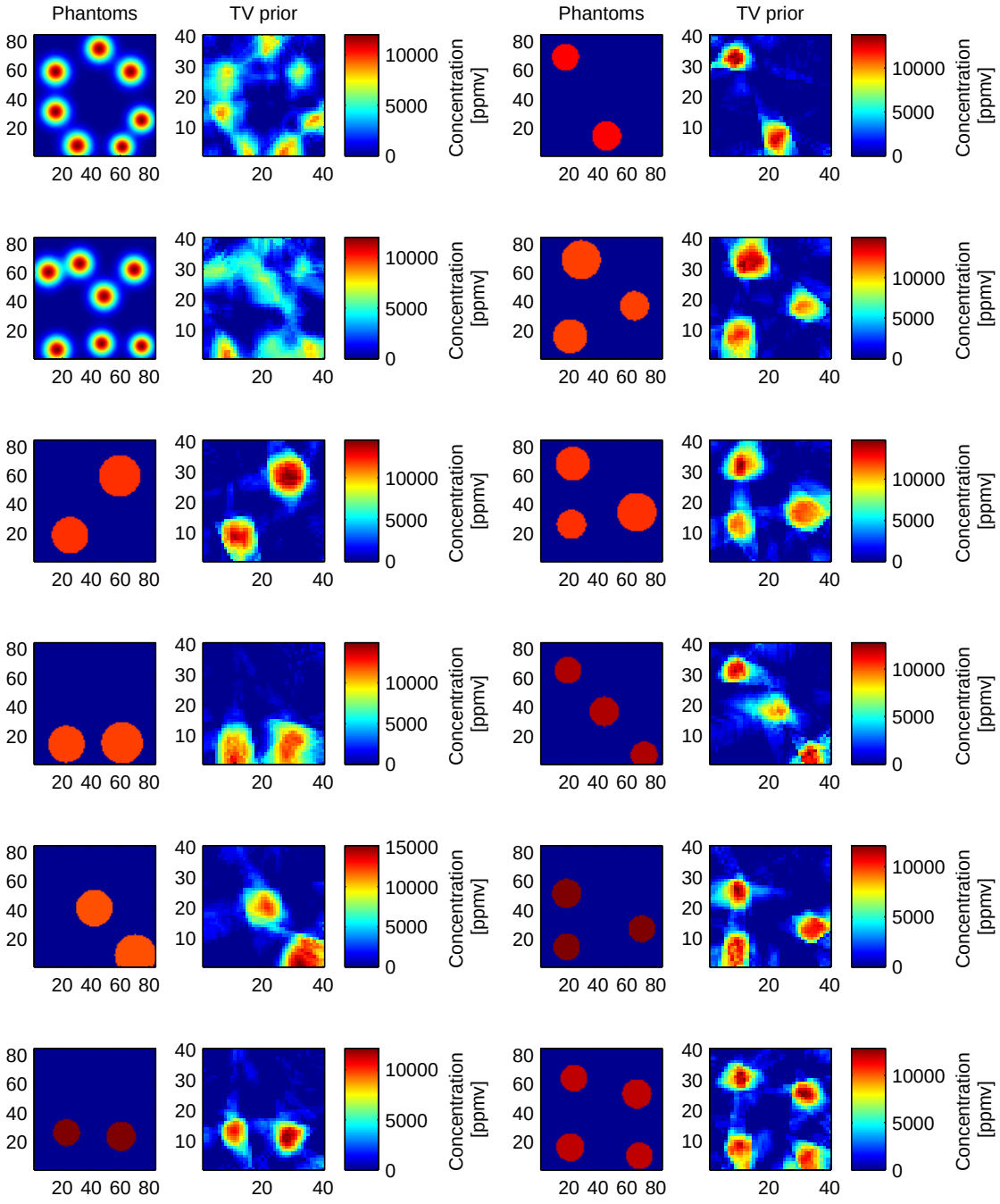

Figure F.39 Virtual experiment study: Reconstructions with total variation prior – Part III

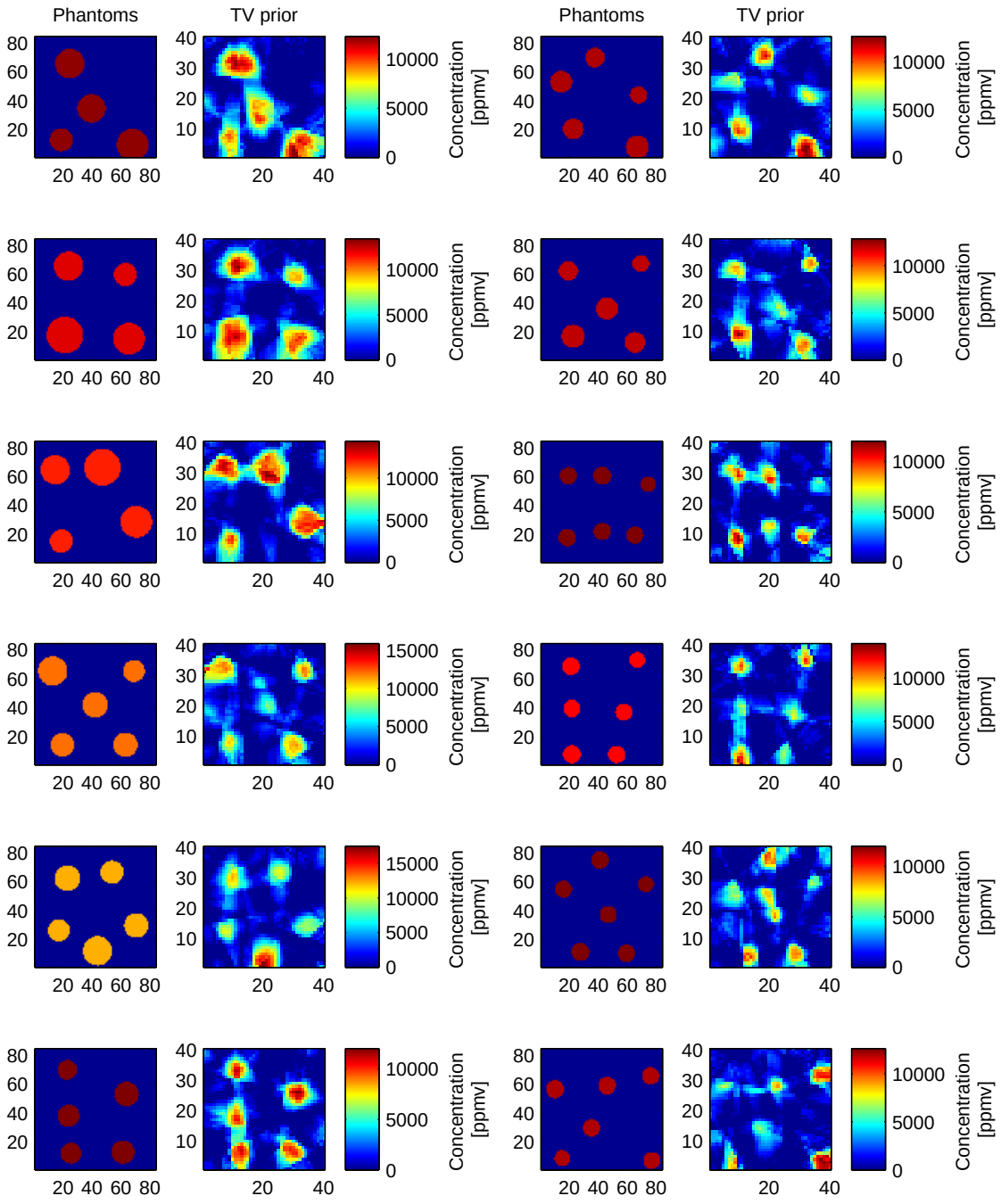

Figure F.40 Virtual experiment study: Reconstructions with total variation prior – Part IV

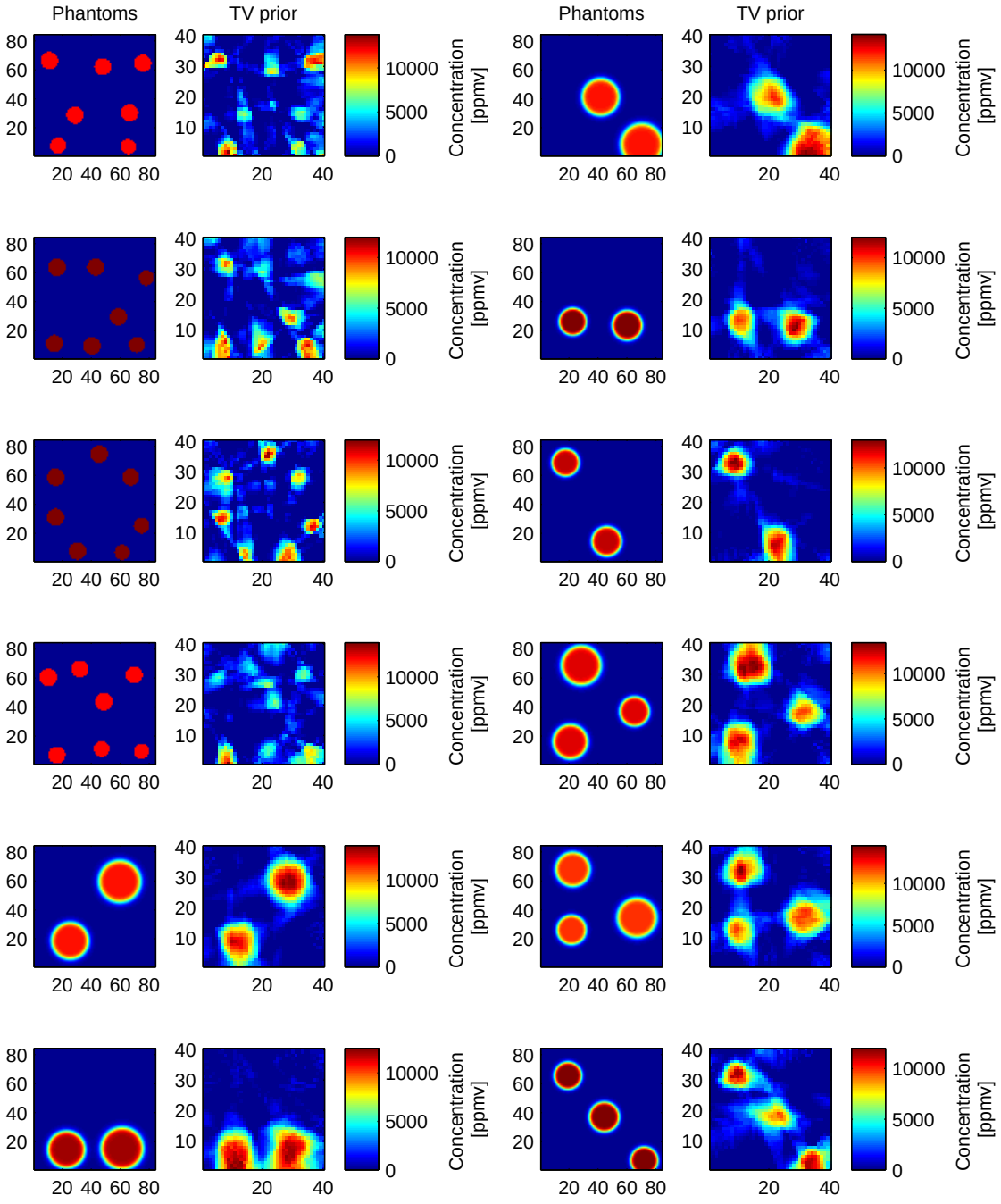

Figure F.41 Virtual experiment study: Reconstructions with total variation prior – Part V

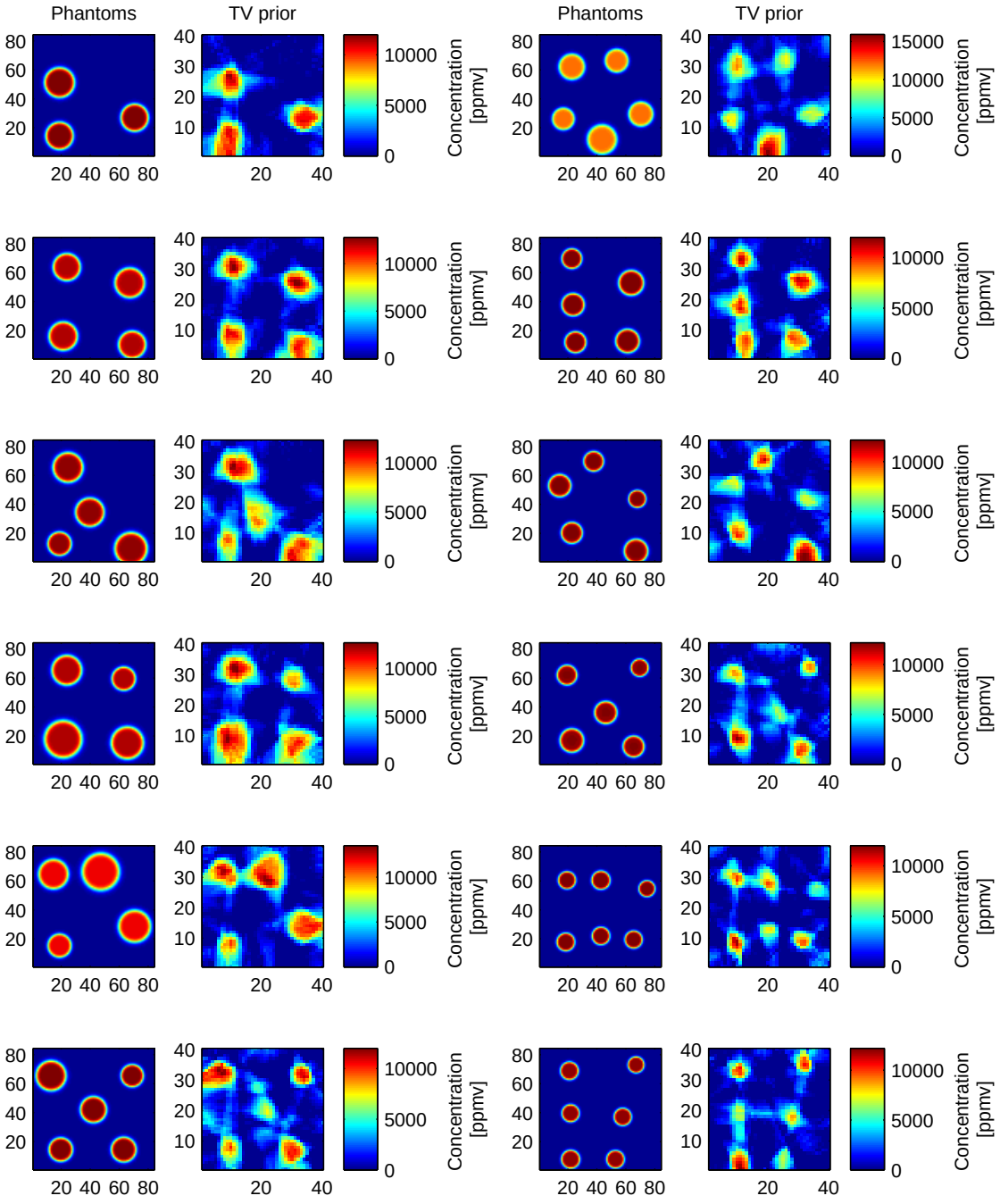

Figure F.42 Virtual experiment study: Reconstructions with total variation prior – Part VI

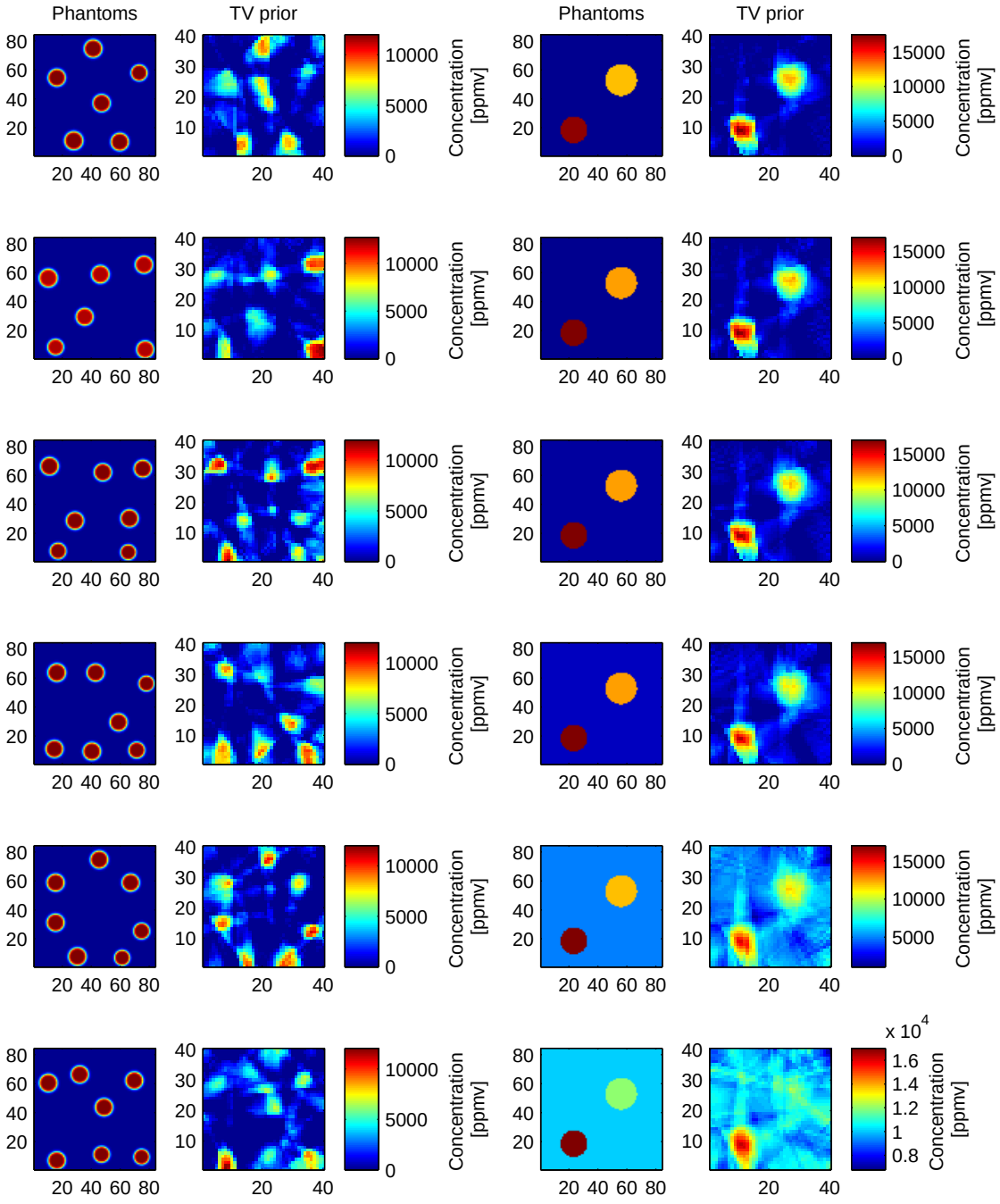

Figure F.43 Virtual experiment study: Reconstructions with total variation prior – Part VII

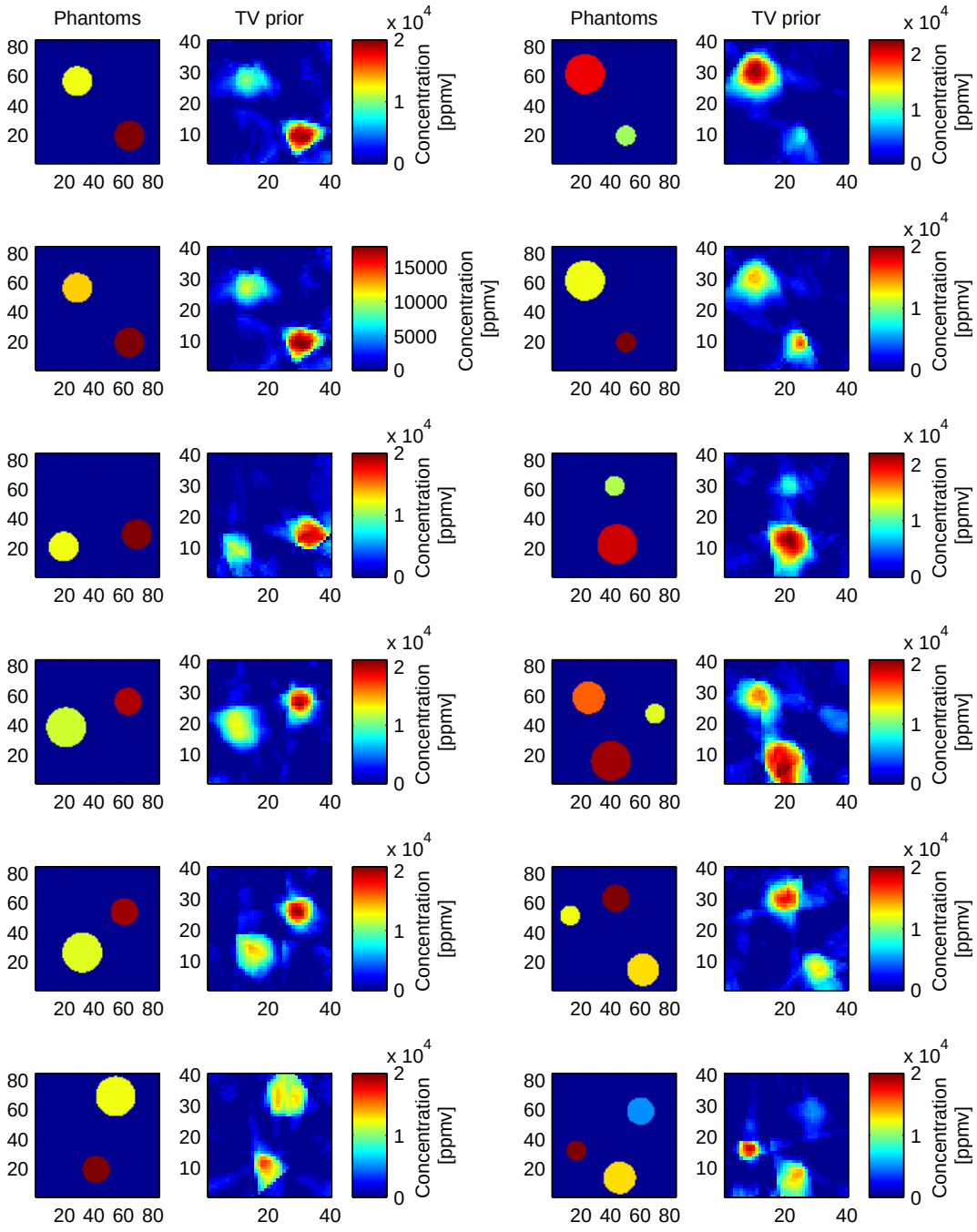

Figure F.44 Virtual experiment study: Reconstructions with total variation prior – Part VIII

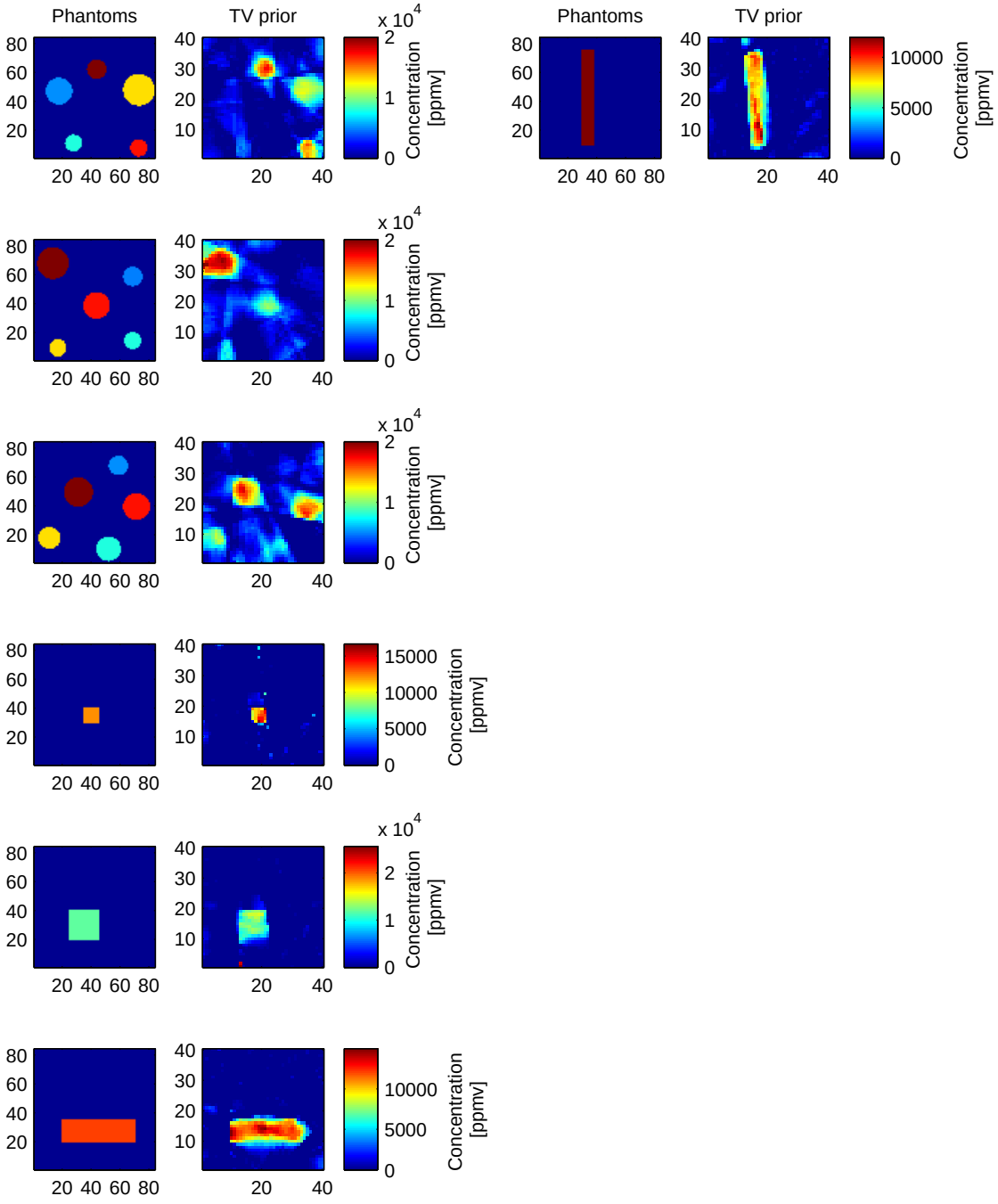

Figure F.45 Virtual experiment study: Reconstructions with total variation prior – Part IX

Appendix G

Tikhonov reconstruction of real experiments

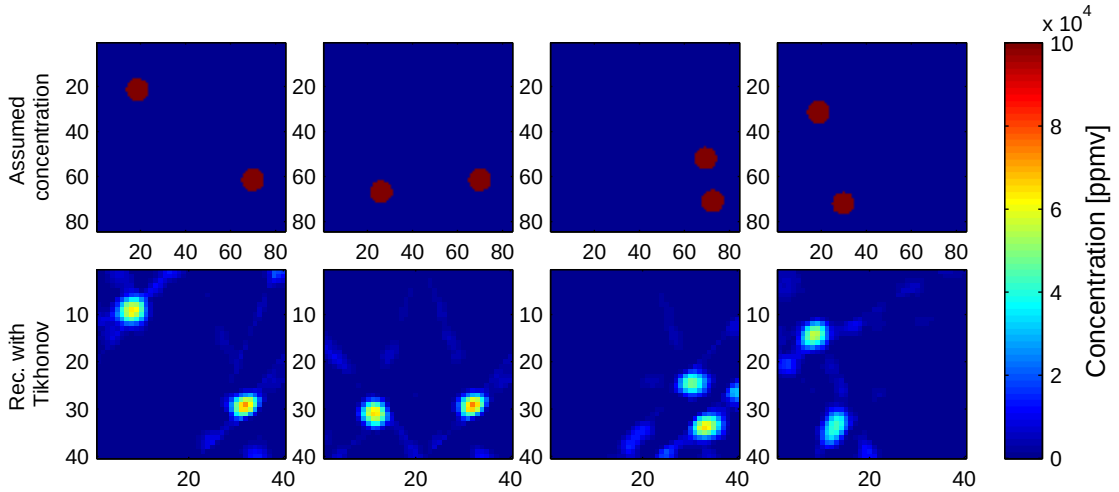

Figure G.1 A few examples of reconstructed measurements with Tikhonov algorithm. Above are the assumed real concentration fields.

Bibliography

[1] Wolfgang Demtröder. *Laser Spectroscopy*. Springer, Berlin, Heidelberg, 2008.

[2] B. Buchholz, N. Böse, and V. Ebert. Absolute validation of a diode laser hygrometer via intercomparison with the German national primary water vapor standard. *Applied Physics B*, February 2014.

[3] B. Buchholz, B. Kühnreich, H. G. J. Smit, and V. Ebert. Validation of an extractive, airborne, compact TDL spectrometer for atmospheric humidity sensing by blind intercomparison. *Applied Physics B*, 110(2):249–262, September 2012.

[4] Steven Wagner, Brian T Fisher, JamesW. Fleming, and Volker Ebert. TDLAS-based in situ measurement of absolute acetylene concentrations in laminar 2D diffusion flames. *Proceedings of the Combustion Institute*, 32(1):839–846, 2009.

[5] Steven Wagner, Moritz Klein, Trupti Kathrotia, Uwe Riedel, Thilo Kissel, Andreas Dreizler, and Volker Ebert. Absolute, spatially resolved, in situ CO profiles in atmospheric laminar counter-flow diffusion flames using 2.3 μm TDLAS. *Applied Physics B*, 109(3):533–540, October 2012.

[6] O. Witzel, A. Klein, C. Meffert, S. Wagner, S. Kaiser, C. Schulz, and V. Ebert. VCSEL-based, high-speed, in situ TDLAS for in-cylinder water vapor measurements in IC engines. *Optics Express*, 21(17):19951, August 2013.

[7] O. Witzel, a. Klein, S. Wagner, C. Meffert, C. Schulz, and V. Ebert. High-speed tunable diode laser absorption spectroscopy for sampling-free in-cylinder water vapor concentration measurements in an optical IC engine. *Applied Physics B*, 109(3):521–532, October 2012.

[8] Pascal Ortwein, Wolfgang Woiwode, S Fleck, and Mark Eberhard. Absolute diode laser-based in situ detection of HCl in gasification processes. *Experiments in Fluids*, 49:961–968, 2010.

[9] Karl Wunderle, Steven Wagner, Igor Pasti, Roland Pieruschka, Uwe Rascher, Ulrich Schurr, and Volkert Ebert. Distributed feedback diode laser spectrometer at 2.7 μ for sensitive, spatially resolved H_2O vapor detection. *Applied optics*, 48(4):B172–82, February 2009.

[10] Stefan Hunsmann, Karl Wunderle, Steven Wagner, Uwe Rascher, Ulrich Schurr, and Volker Ebert. Absolute, high resolution water transpiration rate measurements on single plant leaves via tunable diode laser absorption spectroscopy (TDLAS) at 1.37 μm. *Applied Physics B*, 92(3):393–401, July 2008.

[11] Willi A. Kalender. *Computed Tomography: Fundamentals, System Technology, Image Quality, Applications*. Publicis, Erlangen, 2011.

[12] Alexander G. Ramm. *Inverse Problems*. Springer-Verlag, New York, 2005.

[13] O.A. Anisimov and F.E. Nelson. Permafrost zonation and climate change in the northern hemisphere: results from transient general circulation models. *Climatic Change*, 35(2):241–258, 1997.

[14] Christopher B Field, David B. Lobell, Halton Peters, and Nona R. Chiariello. Feedbacks of Terrestrial Ecosystems to Climate Change *. *Annual Review of Environment and Resources*, 32(1):1–29, November 2007.

[15] C. M. Luke and P. M. Cox. Soil carbon and climate change: from the Jenkinson effect to the compost-bomb instability. *European Journal of Soil Science*, 62(1):5–12, February 2011.

[16] Caitlin E Hicks Pries, Edward a G Schuur, and Kathryn G Crummer. Thawing permafrost increases old soil and autotrophic respiration in tundra: partitioning ecosystem respiration using δ(13) C and â^†(14) C. *Global change biology*, 19(2):649–61, February 2013.

[17] Daniel Riseborough, Nikolay Shiklomanov, Bernd Etzelmüller, Stephan Gruber, and Sergei Marchenko. Recent advances in permafrost modelling. *Permafrost and Periglacial Processes*, 19:137–156, 2008.

[18] Sergey Zimov, Edward Schuur, and F Stuart Chapin. Climate change. Permafrost and the global carbon budget. *Science*, 312(5780):1612–3, June 2006.

[19] Tomoko Nakano, Shunich Kuniyoshi, and Masami Fukuda. Temporal variation in methane emission from tundra wetlands in a permafrost area, northeastern Siberia. *Atmospheric Environment*, 34(8):1205–1213, January 2000.

[20] Edward Schuur, Jason G Vogel, Kathryn G Crummer, Hanna Lee, James O Sickman, and T E Osterkamp. The effect of permafrost thaw on old carbon release and net carbon exchange from tundra. *Nature*, 459(7246):556–9, May 2009.

[21] Martin Heimann and Markus Reichstein. Terrestrial ecosystem carbon dynamics and climate feedbacks. *Nature*, 451(7176):289–92, January 2008.

[22] FM O'Connor and O Boucher. Possible role of wetlands, permafrost, and methane hydrates in the methane cycle under future climate change: A review. *Reviews of Geophysics*, 48(4):RG4005, 2010.

[23] KA Smith, T Ball, and F Conen. Exchange of greenhouse gases between soil and atmosphere: interactions of soil physical factors and biological processes. *European Journal of Soil Science*, 54:779–791, 2003.

[24] EAG Schuur. High risk of permafrost thaw. *Nature*, 480:32–33, 2011.

[25] Wolfgang Demtröder. *Experimentalphysik 3*. Springer-Lehrbuch. Springer, Berlin, Heidelberg, 2009.

[26] Dieter Meschede, editor. *Gerthsen Physik*. Springer-Lehrbuch. Springer, Berlin, Heidelberg, 2010.

[27] Volker Ebert and Jürgen Wolfrum. Absorption. In F. Mayinger, editor, *Optical measurements - techniques and applications*, chapter Absorption, pages 227–265. Springer, Berlin, 2nd edition, 2011.

[28] Franz Schreier. Optimized implementations of rational approximations for the Voigt and complex error function. *Journal of Quantitative Spectroscopy and Radiative Transfer*, 112(6):1010–1025, April 2011.

[29] S.M. Abrarov, B.M. Quine, and R.K. Jagpal. A simple interpolating algorithm for the rapid and accurate calculation of the Voigt function. *Journal of Quantitative Spectroscopy and Radiative Transfer*, 110(6-7):376–383, April 2009.

[30] S.M. Abrarov, B.M. Quine, and R.K. Jagpal. Rapidly convergent series for high-accuracy calculation of the Voigt function. *Journal of Quantitative Spectroscopy and Radiative Transfer*, 111(3):372–375, February 2010.

[31] BH Armstrong. Spectrum line profiles: the Voigt unction. *Journal of Quantitative Spectroscopy and Radiative Transfer*, 7(2):61–88, 1967.

[32] Kendra L. Letchworth and D. Chris Benner. Rapid and accurate calculation of the Voigt function. *Journal of Quantitative Spectroscopy and Radiative Transfer*, 107(1):173–192, September 2007.

[33] J Puerta and P Martin. Three and four generalized Lorentzian approximations for the Voigt line shape: errata. *Applied optics*, 22(1):19, January 1983.

[34] E.E. Whiting. An empirical approximation to the Voigt profile. *Journal of Quantitative Spectroscopy and Radiative Transfer*, 8:1379–1384, 1968.

[35] M Kuntz. A new implementation of the Humlicek algorithm for the calculation of the Voigt profile function. *Journal of Quantitative Spectroscopy and Radiative Transfer*, 51(6):819–824, 1997.

[36] Hermann Haken and Hans Christian Wolf. *Molekülphysik und Quantenchemie*. Springer-Verlag, Berlin/Heidelberg, 2006.

[37] Pascal Ortwein, Steven Wagner, and Volker Ebert. Absolute diode laser based spectral data for the in situ detection of CO in high pressure combustion and gasification processes. In *Proceedings of the European Combustion Meeting 2011*, pages 1–5, 2011.

[38] Thomas Rießinger. *Mathematik für Ingenieure*. Springer-Lehrbuch. Springer Berlin Heidelberg, Berlin, Heidelberg, 2009.

[39] Jürgen Warnatz and Robert Dibble. *Combustion*. Springer Berlin Heidelberg, 2006.

[40] Thorsten M. Buzug. *Computed Tomography*. Springer, Berlin, Heidelberg, 2008.

[41] Avinash C. Kak and Malcolm Slaney. *Principles of Computerized Tomographic Imaging*. Society for Industrial and Applied Mathematics, January 2001.

[42] A Lipponen, A Seppänen, and J P Kaipio. Reduced-order estimation of nonstationary flows with electrical impedance tomography. *Inverse Problems*, 26(7):074010, July 2010.

[43] A Lipponen, a Seppänen, and J P Kaipio. Nonstationary approximation error approach to imaging of three-dimensional pipe flow: experimental evaluation. *Measurement Science and Technology*, 22(10):104013, October 2011.

[44] Jérémi Dardé, Nuutti Hyvönen, Aku Seppänen, and Stratos Staboulis. Simultaneous recovery of admittivity and body shape in electrical impedance tomography: an experimental evaluation. *Inverse Problems*, 29(8):085004, August 2013.

[45] Kimmo Karhunen, Aku Seppänen, Anssi Lehikoinen, Paulo J.M. Monteiro, and Jari P. Kaipio. Electrical Resistance Tomography imaging of concrete. *Cement and Concrete Research*, 40(1):137–145, January 2010.

[46] Lu Ma and Manuchehr Soleimani. Limited angle and limited data electromagnetic induction tomography: experimental evaluation of the effect of missing data. *Measurement Science and Technology*, 23(12):125406, December 2012.

[47] Gabor T. Herman. *Fundamentals of Computerized Tomography*. Advances in Pattern Recognition. Springer London, London, 2009.

[48] Frank Natterer. *The Mathematics of Computerized Tomography*. B.G. Teubner, Stuttgart, 1986.

[49] Gabor T. Herman and Attila Kuba, editors. *Advances in Discrete Tomography and Its Applications*. Applied and Numerical Harmonic Analysis. Birkhäuser, Boston, MA, 2007.

[50] Stefan Kaczmarz. Angenäherte auflösung von systemen linearer gleichungen. *Bulletin International de l'Academie Polonaise des Sciences et des Lettres*, 35:355–357, 1937.

[51] Kunio Tanabe. Projection method for solving a singular system of linear equations and its applications. *Numerische Mathematik*, 17(3):203–214, 1971.

[52] N Terzija, J L Davidson, C Garcia-Stewart, P Wright, K B Ozanyan, S Pegrum, T J Litt, and H McCann. Image optimization for chemical species tomography with an irregular and sparse beam array. *Measurement Science and Technology*, 19(9):094007, September 2008.

[53] WQ Yang, DM Spink, TA York, and H. McCann. An image-reconstruction algorithm based on Landweber's iteration method for electrical-capacitance tomography. *Measurement Science and Technology*, 10:1065, 1999.

[54] Stefan Tappe. *Einführung in die Wahrscheinlichkeitstheorie*. Springer, Berlin, Heidelberg, 2013.

[55] Claudia Czado and Thorsten Schmidt. *Mathematische Statistik*. Springer, Berlin, Heidelberg, 2011.

[56] Jari P. Kaipio and Erkki Somersalo. *Statistical and Computational Inverse Problems*, volume 160 of *Applied Mathematical Sciences*. Springer-Verlag, New York, 2005.

[57] Eberhard Zeidler, editor. *Springer-Taschenbuch der Mathematik*. Springer, Wiesbaden, 2013.

[58] K.J. Daun. Infrared species limited data tomography through Tikhonov reconstruction. *Journal of Quantitative Spectroscopy and Radiative Transfer*, 111(1):105–115, January 2010.

[59] Kyle J Daun, Steven L Waslander, and Brandon B Tulloch. Infrared species tomography of a transient flow field using Kalman filtering. *Applied Optics*, 50(6):891–900, 2011.

[60] T Lahivaara, A Seppanen, and JP Kaipio. Bayesian Approach to Tree Detection Based on Airborne Laser Scanning Data. *IEEE transactions on geoscience and remote sensing*, 52(5):2690–2699, 2014.

[61] Jari P. Kaipio, V. Kolehmainen, M. Vauhkonen, and Erkki Somersalo. Inverse problems with structural prior information. *Inverse problems*, 15:713–729, 1999.

[62] David Strong and Tony Chan. Edge-preserving and scale-dependent properties of total variation regularization. *Inverse problems*, 19:165–187, 2003.

[63] Jörg Feldhusen and Karl-Heinrich Grote, editors. *Pahl/Beitz Konstruktionslehre*. Springer, Berlin, Heidelberg, 2013.

[64] Gerald F. Marshall, editor. *Handbook of Optical and Laser Scanning*. Marcel Dekker, Inc., New York, 2004.

[65] A. Seidel, S. Wagner, and V. Ebert. TDLAS-based open-path laser hygrometer using simple reflective foils as scattering targets. *Applied Physics B*, 109(3):497–504, October 2012.

[66] Matthew G Twynstra and Kyle J Daun. Laser-absorption tomography beam arrangement optimization using resolution matrices. *Applied optics*, 51(29):7059–68, October 2012.

[67] Hans Wilhelm Alt. *Lineare Funktionalanalysis*. Springer, Berlin, Heidelberg, 2012.

[68] Rüdiger Reinhardt, Armin Hoffmann, and Tobias Gerlach. *Nichtlineare Optimierung*. Springer, Berlin, Heidelberg, 2013.

[69] S. Schäfer, M. Mashni, J. Sneider, A. Miklos, P. Hess, H. Pitz, K.-U. Pleban, and V. Ebert. Sensitive detection of methane with a 1.65 μm diode laser by photoacoustic and absorption spectroscopy. *Applied Physics B: Lasers and Optics*, 66(4):511–516, 1998.

[70] C. Frankenberg, T. Warneke, A. Butz, I. Aben, F. Hase, P. Spietz, and L. R. Brown. Pressure broadening in the $2\nu_3$ band of methane and its implication on atmospheric retrievals. *Atmospheric Chemistry and Physics*, 8(17):5061–5075, September 2008.

[71] L.S. Rothman, I.E. Gordon, Y. Babikov, a. Barbe, D. Chris Benner, P.F. Bernath, M. Birk, L. Bizzocchi, V. Boudon, L.R. Brown, a. Campargue, K. Chance, E.a. Cohen, L.H. Coudert, V.M. Devi, B.J. Drouin, a. Fayt, J.-M. Flaud, R.R. Gamache, J.J. Harrison, J.-M. Hartmann, C. Hill, J.T. Hodges, D. Jacquemart, a. Jolly, J. Lamouroux, R.J. Le Roy, G. Li, D.a. Long, O.M. Lyulin, C.J. Mackie, S.T. Massie, S. Mikhailenko, H.S.P. Müller, O.V. Naumenko, a.V. Nikitin, J. Orphal, V. Perevalov, a. Perrin, E.R. Polovtseva, C. Richard, M.a.H. Smith, E. Starikova, K. Sung, S. Tashkun, J. Tennyson, G.C. Toon, Vl.G. Tyuterev, and G. Wagner. The HITRAN2012 molecular spectroscopic database. *Journal of Quantitative Spectroscopy and Radiative Transfer*, 130:4–50, November 2013.

[72] Horst Stöcker, editor. *Taschenbuch der Physik*, volume 75. Verlag Harri Deutsch, Frankfurt am Main, November 2005.

[73] N Terzija and H. McCann. Wavelet-Based Image Reconstruction for Hard-Field Tomography with Severely Limited Data. *IEEE Sensors Journal*, 11(9):1885–1893, 2011.

[74] Paul Wright, CA Garcia-Stewart, and SJ Carey. Toward in-cylinder absorption tomography in a production engine. *Applied Optics*, 44(31):6578–6592, 2005.

[75] S Pal, K B Ozanyan, and H McCann. A computational study of tomographic measurement of carbon monoxide at minor concentrations. *Measurement Science and Technology*, 19(9):094018, September 2008.

[76] Wim Verkruysse and Lori a Todd. Novel algorithm for tomographic reconstruction of atmospheric chemicals with sparse sampling. *Environmental science & technology*, 39(7):2247–54, April 2005.

[77] V. L. Kasyutich and P. Martin. Towards a two-dimensional concentration and temperature laser absorption tomography sensor system. *Applied Physics B*, 102(1):149–162, July 2010.

[78] Yoshihiro Deguchi, Daisuke Yasui, and Akira Adachi. Development of 2D Temperature and Concentration Measurement Method Using Tunable Diode Laser Absorption Spectroscopy. *Journal of Mechanics Engineering and Automation*, 2:543–549, 2012.

[79] Lin Ma and Weiwei Cai. Numerical investigation of hyperspectral tomography for simultaneous temperature and concentration imaging. *Applied optics*, 47(21):3751–9, July 2008.

[80] Lin Ma and Weiwei Cai. Determination of the optimal regularization parameters in hyperspectral tomography. *Applied optics*, 47(23):4186–92, August 2008.

[81] Lin Ma, Weiwei Cai, Andrew W Caswell, Thilo Kraetschmer, Scott T Sanders, Sukesh Roy, and James R Gord. Tomographic imaging of temperature and chemical species based on hyperspectral absorption spectroscopy. *Optics express*, 17(10):8602–13, May 2009.

[82] Weiwei Cai and Lin Ma. Hyperspectral tomography based on proper orthogonal decomposition as motivated by imaging diagnostics of unsteady reactive flows. *Applied optics*, 49(4):601–10, February 2010.

[83] Lin Ma, Xuesong Li, Scott T. Sanders, Andrew W. Caswell, Sukesh Roy, David H. Plemmons, and James R. Gord. 50-kHz-rate 2D imaging of temperature and H_2O concentration at the exhaust plane of a J85 engine using hyperspectral tomography. *Optics Express*, 21(1):1152, January 2013.

[84] F Wang, K F Cen, N Li, Jay B Jeffries, Q X Huang, J H Yan, and Y Chi. Two-dimensional tomography for gas concentration and temperature distributions based on tunable diode laser absorption spectroscopy. *Measurement Science and Technology*, 21(4):045301, April 2010.

[85] Junling Song, Yanji Hong, Guangyu Wang, and Hu Pan. Algebraic tomographic reconstruction of two-dimensional gas temperature based on tunable diode laser absorption spectroscopy. *Applied Physics B*, 112(4):529–537, April 2013.

[86] M. Spiegel. *Schaum's Easy Outline of Mathematical Handbook of Formulas and Tables*. McGraw-Hill Companies, 2001.

Abstract

The scope of this work was to develop and implement instrumentation and mathematical methods for two-dimensional, spatially resolved absorption spectroscopic tomography based on a drastically reduced amount of measurement data.
Very soon it turned out that design has to be purpose-specific due to the strongly varying boundary conditions of technical and scientific systems.
Therefore, it was focussed onto an application from environmental soil science. An instrument for monitoring climate gas concentration in the soil-air boundary layer of thawing permafrost was developed. The spatial distribution of gas that is emitted from soil structures shall enhance the understanding and modelling of positive feedback processes in climate research.
The device is based on continuously scanned laser beams and inexpensive retro-reflecting foil. Currently, an area of 0.8×0.8 m^2 is covered and can be imaged with up to 2.5 Hz rate.
The spectroscopic method *Tunable Diode Laser Absorption Spectroscopy* (TDLAS) allows for absolute measurements of path-integrated concentrations without the need for any reference-gas measurement. The accuracy of concentrations retrieved from the scanning reflective instrument is investigated with measurements of an homogeneous H_2O field.
A selection of promising reconstruction techniques is examined regarding reconstructed image quality, spatial resolution and calculation time.
Eventually, tomographic measurements of a defined concentration field that is generated by a controlled flow from circular laminar jets are presented. The reconstructed images are compared to the approximately known concentration fields. Aspects of the instruments' dynamic range of concentrations, structure sizes and measurement speed are illuminated.

Kurzfassung

Das Ziel dieser Arbeit war es, ein Messinstrument und mathematische Methoden für die zweidimensionale, räumlich aufgelöste Absorptionsspektroskopie auf der Grundlage sehr stark reduzierter Messdaten zu entwickeln.
Es stellte sich sehr schnell heraus, dass die Gestaltung wegen der stark variierenden Randbedingungen technischer und wissenschaftlicher Systeme zweckspezifisch sein muss. Deshalb wurde der Schwerpunkt auf eine Anwendung aus dem Bereich der Umweltphysik, genauer der Bodenphysik, gelegt. Es wurde ein Instrument für die Erfassung von Treibhausgaskonzentrationen in der Boden-Luft-Grenzschicht von tauenden Permafrostböden entwickelt. Die räumliche Verteilung der Gase, die aus den Bodenstrukturen austreten, soll das Verständnis und die Modellbildung von positiven Rückkopplungsprozessen in der Klimaforschung verbessern.
Das Instrument besteht aus kontinuierlich gescannten Laserstrahlen und kostengünstigen retroreflektierenden Folien. Momentan kann eine Fläche von 0.8×0.8 m^2 abgedeckt und mit einer Bildfrequenz von bis zu 2.5 Hz dargestellt werden. Die spektroskopische Methode *Tunable Diode Laser Absorption Spectroscopy* (TDLAS) ermöglicht absolute Messungen von Pfad-integrierten Konzentrationen ohne auf Referenz-Gasmessungen zurückgreifen zu müssen. Die Akkuratheit der Konzentrationen, die mit dem scannenden, reflektierenden Instrument gemessen wurden, wird anhand von Messungen eines homogenen H_2O - Feldes ermittelt.
Es wird eine Auswahl vielversprechender Rekonstruktionstechniken hinsichtlich der Qualität des rekonstruierten Bildes, der räumlichen Auflösung und der notwendigen Rechenzeit untersucht.
Schließlich werden tomographische Messungen eines definierten Konzentrationsfeldes präsentiert, das durch eine kontrollierte Strömung aus kreisförmigen laminaren Jets generiert wird. Zuletzt werden einige Aspekte des Dynamikumfangs der Konzentrationen, der Strukturgrößen und der Messgeschwindigkeit aufgezeigt.